Theoretical and Numerical study of the electric activity of the heart. Modeling and Numerical simulation of electrocardiograms.

Nejib Zemzemi

N° d'ordre:

THÈSE

Présentée pour obtenir

LE GRADE DE DOCTEUR EN SCIENCES
DE L'UNIVERSITÉ PARIS-SUD XI

Spécialité: Mathématiques

par

Néjib ZEMZEMI

Étude théorique et numérique de l'activité électrique du cœur: Applications aux électrocardiogrammes

Soutenue le 14 décembre 2009 devant la Commission d'examen:

M.	François ALOUGES	
M.	Habib AMMARI	
M.	Miguel Angel FERNÁNDEZ	(Directeur de thèse)
M.	Jean-Frédéric GERBEAU	(Directeur de thèse)
M.	Yvon MADAY	(Président du jury)
M.	Bertrand MAURY	
M.	Joakim SUNDNES	

Rapporteurs:

M.	Piero Colli Franzone
M.	Joakim Sundnes

Thèse préparée dans
l'Équipe-Projet REO
INRIA Paris-Rocquencourt Bât. 16
B.P 105
78 153 Le Chesnay CEDEX

Résumé

La modélisation du vivant, en particulier la modélisation de l'activité cardiaque, est devenue un défi scientifique majeur. Le but de cette thématique est de mieux comprendre les phénomènes physiologiques et donc d'apporter des solutions à des problèmes cliniques. Nous nous intéressons dans cette thèse à la modélisation et à l'étude numérique de l'activité électrique du cœur, en particulier l'étude des électrocardiogrammes (ECGs). L'onde électrique dans le cœur est gouvernée par un système d'équations de réaction-diffusion appelé *modèle bidomaine* ce système est couplé à une EDO représentant l'activité cellulaire. Afin simuler des ECGs, nous tenons en compte la propagation de l'onde électrique dans le thorax qui est décrite par une équation de diffusion.

Nous commençons par une démonstrer l'existence d'une solution faible du système couplé cœur-thorax pour une classe de modèles ioniques phénoménologiques. Nous prouvons ensuite l'unicité de cette solution sous certaines conditions.

Le plus grand apport de cette thèse est l'étude et la simulation numérique du couplage électrique cœur-thorax. Les résultats de simulations sont représentés à l'aide des ECGs. Dans une première partie, nous produisons des simulations pour un cas normal et pour des cas pathologiques (blocs de branche gauche et droit et des arhythmies). Nous étudions également l'impact de certaines hypothèses de modélisation sur les ECGs (couplage faible, utilisation du modèle monodomaine, isotropie, homogénéité cellulaire, comportement résistance-condensateur du péricarde,...). Nous étudions à la fin de cette partie la sensibilité des ECGs par apport aux paramètres du modèle. En deuxième partie, nous effectuons l'analyse numérique de schémas du premier ordre en temps découplant les calculs du potentiel d'action et du potentiel extérieur. Puis, nous combinons ces schémas en temps avec un traîtement explicite du type Robin-Robin des conditions de couplage entre le cœur et le thorax. Nous proposons une analyse de stabilité de ces schémas et nous illustrons les résultats avec des simulations numériques d'ECGs.

La dernière partie est consacrée à trois applications. Nous commençons par l'estimation de certains paramètres du modèle (conductivité du thorax et paramètres ioniques). Dans la deuxième application, qui est d'originie industrielle, nous utilisons des méthodes d'apprentissage statistique pour reconstruire des ECGs à partir de mesures ('électrogrammes). Enfin, nous présentons des simulations électro-mécaniques du coeur sur une géométrie réelle dans diverses situations physiologiques et pathologiques. Les indicateurs cliniques, électriques et mécaniques, calculés à partir de ces simulations sont très similaires à ceux observés en réalité.

Remerciements

Ces pages sont dédiés à tous ceux qui m'ont permis de mener à bien mes travaux de recherche pendant ma thèse thèse.

D'abord, j'aimerais exprimer mes plus profonds remerciements à mes deux directeurs Jean-Frédéric Gerbeau et Miguel Fernández pour avoir su m'initier au monde de la recherche. Avec leur confiance et leur soutien durant les trois ans de thèse j'ai appris à aimer les mathématiques. En plus de m'avoir permis d'entreprende cette thèse, en me proposant cet intéressant sujet, ils m'ont donner la grande satisfaction et le grand honneur de partager leurs connaissances et leurs amitiés. Le travail avec eux était pour moi une grande source d'inspiration.

Je suis très honoré que M. Piero Colli-Franzone et M. Joakim Sundnes, deux références de l'électro-physiologie cardiaque, aient accepté la lourde tâche de rapporter ma thèse.

Je suis également honoré par la présence de M. François Alouges, M. Habib Ammari, M. Yvon Maday et M. Betrand Maury dans mon jury de thèse. Je les en remercie chaleureusement.

Un grand merci à tout les chercheur avec qui j'ai eu de la chance de collaborer et sans eux je n'aurais pas pu aborder certains sujets si intéressants. Merci à Muriel Boulakia, Géraldine Ebrard, Dominique Chapelle , Philippe Moireau, Fabrice Rossi, Adnane Azouzi, Yves Coudière, Rodolphe Turpault et Serge Caseau qui nous a accueilli chez lui pour nous donner son avis médical sur nos résultats de simulation.

Je tiens à remercier nos collaborateurs de ELA Medical qui nous ont accueilli dans leur locaux à la Boursidière et avec qui nous ont proposé le sujet sur la reconstruction des électrocardiogrammes à partir de mesures sur le cœur et avec qui on a eu beaucoup de discussions constructives.

Je remercie mes collègues thésards du bâtiment 16 à l'INRIA particulièrement mes collègue de bureau Matteo Astorino, Cristobal Bertoglio Anne-Claire Egloffe et nos voisin de bureau chercheurs, postdocs et ingénieurs Vincent Martin, Alfonso Caiazzo, Julien Castelneau, Joaquin Mura, Maryse Desnous et Elsie Phe.

Je tiens aussi à remercier les permanents du bâtiment 16 et particulièrement ceux du projet REO. Un merci spécial pour Maryse Desnous et Valérie Lavigne.

Je ne pourrais pas oublier tous mes amis qui m'ont toujours soutenu Montacer, Mohamed, Mehdi, Foued, Hatem, Belkacem, Amine, Adnane, Imen, Néfissa, Najeh, Ahmed, Wided, Wajih, Ines, Anis, Youssef, Skander, Monther, Abdelkarim, Lasaad, Hichem, Tarek, Khalil, Sylvie, Claire, Danielle...

Je remercie finalement ma famille. Mes parents Jallouli et Najet mes frères et sœur Khaled Soumaya Amel et le petit Wassim qui m'ont soutenu, m'ont encouragé sans cesse tout au long de mes études, et plus spécialement pendant ma thèse.

Contents

Chapter 1

Introduction

Le cœur est l'un des organes vitaux du corps humain, son rôle est de faire circuler le sang dans tous les tissus de l'organisme. Malgré son petit volume (entre 50 et 60 cm^3), il est chargé de pomper 8000 litres de sang par jour. Pour faire circuler cette grande quantité, il doit battre sans s'arrêter plus de 100 000 fois par jour. Son arrêt peut être fatal. Comme tous les organes du corps humain, il peut être affecté de nombreuses pathologies. Ces dernières peuvent être sans danger, comme certaines tachycardies par exemple, ou bien s'avérer très sérieuses, comme les fibrillations et les blocs de branches. L'évolution des technologies a permis au médecin d'observer l'état du cœur à travers des outils d'imagerie médicale. Ceux-ci peuvent être basés sur des ultrasons (echocardiographie), de la résonance magnétique (IRM) ou des rayons X. Ces technologies sont incontournables pour dresser un diagnostic du cœur, mais leur utilisation demeure complexe et coûteuse. En 2006, il y avait seulement 370 IRM installées dans toute la France, le coût d'un appareil est de 1,5 M d'euros et le coût d'un examen est en moyenne de 315 euros (d'après l'institut Curie).

L'électrocardiogramme (ECG) est un outil clinique performant, non invasif, peu coûteux et facile à mettre en œuvre. Il est l'examen le plus couramment utilisé en électrocardiologie. Les travaux dans cette thèse concernent la modélisation et la simulation numérique de l'activité électrique du cœur, en particulier la modélisation et la simulation numérique des électrocardiogrammes. Nous avons choisi de nous concentrer sur l'ECG pour deux raisons. La première est la performance de cet outil et son importance auprès des médecins (il s'agit du premier élément du diagnostic du cœur). La deuxième raison est que cet outil nous permet de dialoguer avec les cardiologues, ce qui nous permet d'avoir un retour critique sur nos résultats de simulation. Il est en effet plus familier pour un médecin d'évaluer un ECG que la propagation de l'onde électrique dans le myocarde.

La modélisation du vivant est devenue un défi scientifique très important. Elle pourrait aider à mieux comprendre les phénomènes physiologiques et apporter des solutions à des problèmes cliniques. En effet, les expériences *in vivo* ne sont parfois pas réalisables à cause de contraintes pratiques ou morales. Avoir un outil numérique prédictif capable de reproduire le phénomène physiologique fournirait en quelque sorte un *"cobaye virtuel"*. Ce cobaye pourrait servir à réaliser des expériences dans le but de résoudre des problèmes biomédicaux ou industriels. L'étude de ces phénomènes permet aussi de faire évoluer les sciences physique mathématiques en proposant des nouvelles problé-

matiques et peut en même temps inciter le chercheur à trouver des nouvelles méthodes pour résoudre les problèmes soulevés.

1.1 Contexte de la thèse

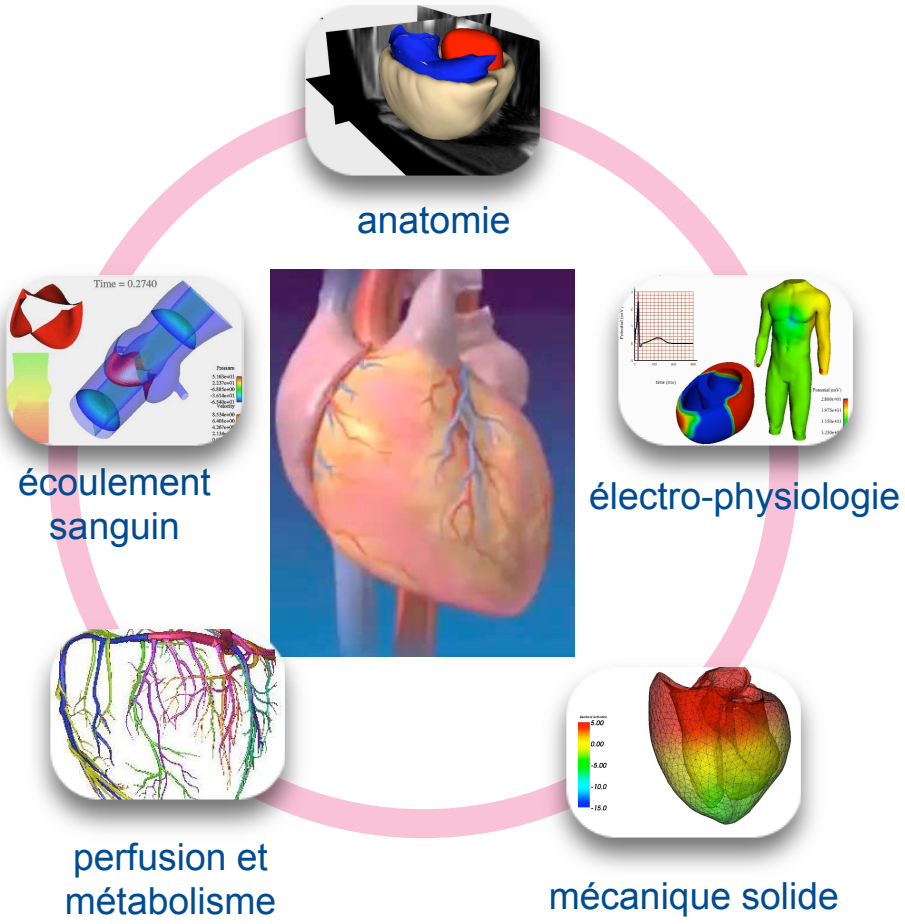

Figure 1.1: Représentation de la chaîne de travail de CARDIOSENSE3D.

Les objectifs de cette thèse ont été fixés dans le cadre de l'action d'Envergure nationale CardioSense3D de l'INRIA, un projet national financé par l'INRIA dont le but est la modélisation et la simulation du coeur. Les outils et les modèles développés dans ce cadre doivent contribuer à la compréhension de la physiologie cardiaque et à l'amélioration de la pratique médicale autour des maladies cardio-vasculaires. En plus de l'équipe-projet REO, cette action regroupe des chercheurs des équipes MACS et SISYPHE situées dans le centre de recherche INRIA Paris - Rocquencourt et l'équipe ASCLEPIOS située dans le centre de recherche INRIA Sophia Antipolis - Méditerranée. Ces équipes travaillent sur trois axes de recherche. Le premier axe est la construction d'un simulateur de l'activité cardiaque couplant les 4 phénomènes physiologiques suivants: l'électrophysiologie, la contraction mécanique, l'ecoulement sanguin dans les ventricules et la perfusion et le métabolisme cardiaque. Le deuxième axe concerne la création de modèles personnalisés du coeur grâce à l'estimation de paramètres à partir

des signaux électriques ou des images médicales d'un patient. Le troisième axe est la construction d'applications pour résoudre des problèmes cliniques et industriels. Cette action implique plusieurs centres cliniques comme l'Hôpital Européen Georges Pompidou, le Guy's Hospital situé à Londres (en partenariat avec King's College London), le laboratoire de Cardiac Energetics du National Institutes of Health situé à Washington. Elle implique également l'université de Nantes ainsi que des partenaires industriels (PHILIPS, ELA Medical).

1.2 Etat de l'art et principales contributions

Le but de cette thèse est de modéliser et simuler des électrocardiogrammes réalistes en se basant sur un modèle macroscopique gouvernant la propagation de l'onde électrique du coeur. Le modèle le plus adopté dans la littérature pour représenter la propagation de l'onde électrique dans le cœur est le *modèle bidomaine* [Tun78, CFS02, SLC$^+$06, PBC05], ce modèle, qui consiste en un système d'équations de réaction diffusion non linéaire, est couplé à un système dynamique modélisant les courants ioniques cellulaires. La propagation de l'onde électrique sur le thorax est réduite à un phénomène de diffusion. Le modèle cœur-thorax [SLC$^+$06, PBC05, Lin99, Pie05] que nous allons utiliser pour simuler des électrocardiogrammes est donné par le système suivant

$$\chi_{\mathrm{m}}\partial_t V_{\mathrm{m}} + I_{\mathrm{ion}}(V_{\mathrm{m}}, w) - \mathrm{div}(\boldsymbol{\sigma}_{\mathrm{i}}\boldsymbol{\nabla} V_{\mathrm{m}}) - \mathrm{div}(\boldsymbol{\sigma}_{\mathrm{i}}\boldsymbol{\nabla} u_{\mathrm{e}}) = I_{\mathrm{app}}, \text{ dans } \Omega_{\mathrm{H}} \times (0,T), \quad (1.2.1)$$

$$-\mathrm{div}((\boldsymbol{\sigma}_{\mathrm{i}} + \boldsymbol{\sigma}_{\mathrm{e}})\boldsymbol{\nabla} u_{\mathrm{e}}) - \mathrm{div}(\boldsymbol{\sigma}_{\mathrm{i}}\boldsymbol{\nabla} V_{\mathrm{m}}) = 0, \text{ dans } \Omega_{\mathrm{H}} \times (0,T), \quad (1.2.2)$$

$$\partial_t w + g(V_{\mathrm{m}}, w) = 0, \text{ dans } \Omega_{\mathrm{H}} \times (0,T), \quad (1.2.3)$$

$$-\mathrm{div}(\boldsymbol{\sigma}_{\mathrm{T}}\boldsymbol{\nabla} u_{\mathrm{T}}) = 0, \text{ dans } \Omega_{\mathrm{T}} \times (0,T), \quad (1.2.4)$$

$$\boldsymbol{\sigma}_{\mathrm{T}}\boldsymbol{\nabla} u_{\mathrm{T}} \cdot \boldsymbol{n}_{\mathrm{T}} = 0, \text{ sur } \Gamma_{\mathrm{ext}} \times (0,T), \quad (1.2.5)$$

$$\boldsymbol{\sigma}_{\mathrm{i}}\boldsymbol{\nabla} V_{\mathrm{m}} \cdot \boldsymbol{n} + \boldsymbol{\sigma}_{\mathrm{i}}\boldsymbol{\nabla} u_{\mathrm{e}} \cdot \boldsymbol{n} = 0, \text{ sur } \Sigma \times (0,T), \quad (1.2.6)$$

$$u_{\mathrm{T}} = u_{\mathrm{e}}, \text{ sur } \Sigma \times (0,T), \quad (1.2.7)$$

$$\boldsymbol{\sigma}_{\mathrm{e}}\boldsymbol{\nabla} u_{\mathrm{e}} \cdot \boldsymbol{n} = -\boldsymbol{\sigma}_{\mathrm{T}}\boldsymbol{\nabla} u_{\mathrm{T}} \cdot \boldsymbol{n}_{\mathrm{T}}, \text{ sur } \Sigma \times (0,T), \quad (1.2.8)$$

$$V_{\mathrm{m}}(\boldsymbol{x}, 0) = V_{\mathrm{m}}^0(\boldsymbol{x}), \quad w(\boldsymbol{x}, 0) = w^0(\boldsymbol{x}), \quad \forall \boldsymbol{x} \in \Omega_{\mathrm{H}}. \quad (1.2.9)$$

où Ω_{H}, Ω_{T} et Σ désignent respectivement les domaines cardiaque, thoracique et l'interface cœur-thorax. Le domaine temporel est donné par l'interval (0,T). Les variables d'états $V_{\mathrm{m}}, u_{\mathrm{i}}$, u_{e} et u_{T} désignent respectivement le potentiel d'action, les potentiels intra-cellulaire , extra-cellulaire et thoracique, avec $V_{\mathrm{m}} \overset{\mathrm{def}}{=} u_{\mathrm{i}} - u_{\mathrm{e}}$. La constate χ_{m} représente la capacité membranaire multipliée par une constante géométrique (le taux de surface membranaire par unité de volume). Les tenseurs de conductivités intra-, extracellulaire et thoracique sont respectivement notés $\boldsymbol{\sigma}_{\mathrm{i}}$, $\boldsymbol{\sigma}_{\mathrm{e}}$ et $\boldsymbol{\sigma}_{\mathrm{T}}$. Le courant ionique $I_{\mathrm{ion}}(V_{\mathrm{m}}, w)$ et la fonction $g(V_{\mathrm{m}}, w)$ dépendent du modèle ionique utilisé. Les détails de la modélisation du système (1.2.1)-(1.2.9) sont donnés dans la section 3.2 du chapitre 3.

Dans le cas ou le cœur est supposé *isolé*, la propagation de l'onde électrique dans le myocarde est décrite par le système d'équations (1.2.1)-(1.2.3), la donnée initiale (1.2.9) et les conditions aux limites suivantes

$$\begin{cases} \boldsymbol{\sigma}_{\mathrm{i}}\boldsymbol{\nabla} V_{\mathrm{m}} \cdot \boldsymbol{n} = 0, \quad \text{sur} \quad \Sigma \\ \boldsymbol{\sigma}_{\mathrm{e}}\boldsymbol{\nabla} u_{\mathrm{e}} \cdot \boldsymbol{n} = 0, \quad \text{sur} \quad \Sigma, \end{cases} \quad (1.2.10)$$

Dans la littérature, beaucoup de travaux théoriques ont porté sur l'étude de ce dernier système. Un premier résultat d'existence, d'unicité et de régularité pour le problème cœur *isolé* a été produit par Colli Franzone et Savaré [CFS02]. Le modèle ionique considéré pour définir $I_{\text{ion}}(V_{\text{m}}, w)$ et $g(V_{\text{m}}, w)$ est celui de FitzHugh-Nagumo [NAY62]. La preuve est basée sur une reformulation abstraite du système en terme d'une inégalité variationnelle d'évolution dans des espaces de Hilbert. Une analyse pour des modèles ioniques plus simplifiés, notamment dans le cas où $I_{\text{ion}}(V_{\text{m}}, w) \stackrel{\text{def}}{=} I_{\text{ion}}(V_{\text{m}})$, a été traitée par Bendahmane et Karlsen [BK06]. Dans un travail plus récent, Bourgault Coudière et Pierre [BCP09], se basant sur une approche de semi-groupes, montrent un résultat d'existence, d'unicité et de régularité local en temps. Ce résultat concerne une classe de modèles ioniques incluant les modèles de FitzHugh-Nagumo [NAY62], Aliev-Panfilov [AP96] et Roger-MacCulloch [RM94]. Un dernier résultat d'existence et de unicité pour le modèle bidomaine couplé avec le modèle ionique de Luo-Rudy (phase-I) [LR91] a été démontré par Veneroni [Ven09].

1.2.1 Résultats théoriques: Existence et unicité du problème couplé cœur-thorax

À notre connaissance aucun travail dans la littérature n'a fait l'objet d'une preuve d'existence d'une solution pour du problème couplé cœur-thorax (1.2.1)-(1.2.9). Dans le chapitre 4, nous analysons l'existence, l'unicité et la régularité d'une solution faible de ce problème. En posant

$$u \stackrel{\text{def}}{=} \begin{cases} u_{\text{e}} \text{ dans } \Omega_{\text{H}}, \\ u_{\text{T}} \text{ dans } \Omega_{\text{T}}, \end{cases} \qquad \Omega = \Omega_{\text{H}} \cup \Omega_{\text{T}} \quad \text{et } V \stackrel{\text{def}}{=} \left\{ \phi \in H^1(\Omega) \,:\, \int_{\Omega_{\text{H}}} \phi = 0 \right\},$$

une solution faible du problème couplé cœur-thorax (1.2.1)-(1.2.9) est donnée par le quadruplet de fonctions $(V_{\text{m}}, u_{\text{i}}, u, w)$ satisfaisant la régularité

$$\begin{aligned} &V_{\text{m}} \in L^\infty(0,T; H^1(\Omega_H)) \cap H^1(0,T; L^2(\Omega_{\text{H}})), \\ &u \in L^\infty(0,T;V), \quad w \in W^{1,\infty}(0,T, L^\infty(\Omega_{\text{H}})), \end{aligned} \tag{1.2.11}$$

vérifiant les conditions initiales (1.2.9) et

$$C_{\text{m}} \int_{\Omega_{\text{H}}} \partial_t V_{\text{m}} \phi_{\text{i}} + \int_{\Omega_{\text{H}}} \boldsymbol{\sigma}_{\text{i}} \boldsymbol{\nabla} u_{\text{i}} \cdot \boldsymbol{\nabla} \phi_{\text{i}} + \int_{\Omega_{\text{H}}} I_{\text{ion}}(V_{\text{m}}, w) \phi_{\text{i}} = \int_{\Omega_{\text{H}}} I_{\text{app}} \phi_{\text{i}}, \tag{1.2.12}$$

$$C_{\text{m}} \int_{\Omega_{\text{H}}} \partial_t V_{\text{m}} \psi - \int_{\Omega} \boldsymbol{\sigma} \boldsymbol{\nabla} u \cdot \boldsymbol{\nabla} \psi + \int_{\Omega_{\text{H}}} I_{\text{ion}}(V_{\text{m}}, w) \psi = \int_{\Omega_{\text{H}}} I_{\text{app}} \psi, \tag{1.2.13}$$

dans $\mathcal{D}'(0,T)$, pour tout $(\phi_{\text{i}}, \psi) \in H^1(\Omega_{\text{H}}) \times V$. La variable w doit verifier

$$\partial_t w + g(v_{\text{m}}, w) = 0, \text{p.p. dans } \Omega_{\text{H}} \times (0,T).$$

L'existence d'une solution faible du problème cœur-thorax est donnée par le théorème suivant:

Théorème (Theorem 4.2.0.4) *Sous des conditions précisées dans le chapitre 4 (section 4.2) le système* (1.2.1)-(1.2.9) *admet une unique solution faible.*

La preuve de ce théorème fait l'objet du chapitre 4. Notons que le résultat d'existence concerne une classe de modèles ioniques qui contient le modèle de Mitchell-Schaeffer. Ceci est intéressant puisque ce modèle ionique sera utilisé dans la suite de cette thèse pour génèrer des ECGs réalistes.

1.2.2 Résultats numériques: Simulations des ECGs

L'électrocardiogramme (ECG) est un examen non invasif de l'activité électrique du cœur, il consiste à enregistrer 12 différences de potentiel entre différentes positions de la surface de corps. Cet enregistrement de 12 "dérivations" est l'examen le plus utilisé chez les médecins pour faire le diagnostic de l'activité cardiaque [Aeh06, Gol06]. Malgré cela, certains éléments d'interprétation de l'ECG ne sont pas encore entièrement compris. La simulation des ECGs (normaux et pathologiques) à partir du modèle (1.2.1)-(1.2.9), peut être considérée comme un outil précieux pour l'amélioration de ces connaissances. La génération des ECGs peut également être utile dans la construction d'une base de données virtuelle de cas pathologiques, afin de tester des algorithmes de traitement du signal destinés à des dispositifs médicaux [EFG$^+$09]. De plus la simulation des ECGs réalistes est une étape indispensable pour aborder le problème d'adaptation du modèle à des patients en utilisant des données cliniques d'ECG (probème inverse).

Bien que de nombreux travaux aient été consacrés à la simulation numérique en électrophysiologie cardiaque (voir par exemple les monographies [Sac04, PBC05, SLC$^+$06] et les références qu'elles contiennent), seul un petit nombre [Hui98, PDG03, LBG$^+$03, KSW$^+$07, TDP$^+$04, PDV09] traite la simulation numérique des ECGs basée sur des modèles de réaction-diffusion. Parmi eux, seul un très petit nombre [PDG03, PDV09] fournit des simulations significatives des 12 dérivations de l'ECG. Ces simulations utilisent le modèle monodomaine pour décrire l'activité électrique du cœur, un découplage entre le cœur et le thorax (hypothèse de cœur isolé) et une approximation multi-dipolaire de la source électrique dans le torse (voir [LBG$^+$03, Section 4.6] et [Gul88]). À notre connaissance, aucune des approches existantes basées sur des équations aux dérivés partielles (EDP) et d'un cœur couplé au thorax par les équations (1.2.7)-(1.2.8) n'a montré des simulations réalistes de l'ECG pour les 12 dérivations (voir par exemple [LBG$^+$03, Section 4.6] et la monographie récente [SLC$^+$06]).

Contributions en simulation numérique (Chapitre 5) *L'une des contributions les plus importantes de cette thèse est la production d'un outil de simulation permettant d'obtenir des ECGs réalistes. La difficulté principale a consisté à choisir convenablement la complexité des nombreux compartiments du modèle. L'outil obtenu est non seulement capable de simuler correctement des situations "saines" mais également certaines situations pathologiques,* en ne modifiant que les paramètres censés représenter ces pathologies. *Ceci montre, au moins dans certains cas, que le modèle proposé possède des capacités prédictives.*

En plus du modèle (1.2.1)-(1.2.9), plusieurs autres hypothèses de modélisation sont prises en considération, afin de simuler des ECGs. Des hypothèses proviennent de

la nature du domaine cardiaque comme l'anisotropie du myocarde [RS82, CNLH04a, PDV09, CFPST09] et l'hétérogénéité cellulaire [FBR+87, FPST08, YA98, Ant06], ou de la nature du domaine thoracique comme l'hétérogénéité des conductivités sur le thorax [BP03, BFGZ07].

Pour résoudre numériquement le système (1.2.1)-(1.2.9), nous utilisons la méthode des éléments finis pour la discrétisation en espace. Cette méthode est appliquée à la formulation faible (1.2.12)-(1.2.13), où les espaces des fonctions sont remplacés par des espaces de dimensions finies de fonctions affines par morceaux, $V_h \subset H^1(\Omega_{\mathrm{H}})$ et $W_h \subset H^1(\Omega)$.

Pour la discrétisation en temps, nous utilisons les méthodes BDF (backward differentiation formulae, voir [QSS07]) d'ordre 2, avec une extrapolation d'ordre 2 du terme non-linéaire (terme de réaction). D'autres types de schémas sont proposés dans [EB08]. Soit $N \in \mathbb{N}^*$ un entier donné, on considère $\{[t_n, t_{n+1}]\}_{0\leq n\leq N-1}$ avec $t_n \overset{\text{def}}{=} n\tau$ la partition de l'intervalle $[0,T]$ et où $\tau \overset{\text{def}}{=} T/N$ le pas de temps. On note $(V_{\mathrm{m}}^n, u^n, w^n)$ l'approximation de la solution au temps t_n. Au temps t_{n+1} la solution $(V_{\mathrm{m}}^{n+1}, u^{n+1}, w^{n+1})$ est calculée comme suit: Pour $0 \leq n \leq N-1$

1. On calcule une extrapolation d'ordre 2 de V_{m} : $\widetilde{V}_{\mathrm{m}}^{n+1} \overset{\text{def}}{=} 2V_{\mathrm{m}}^n - V_{\mathrm{m}}^{n-1}$;

2. On cherche $w^{n+1} \in V_h$:

$$\frac{1}{\tau}\left(\frac{3}{2}w^{n+1} - 2w^n + \frac{1}{2}w^{n-1}\right) + g(\widetilde{V}_{\mathrm{m}}^{n+1}, w^{n+1}) = 0, \quad \text{(par nœud)};$$

3. Evaluation du courant ionique: $I_{\mathrm{ion}}(\widetilde{V}_{\mathrm{m}}^{n+1}, w^{n+1})$;

4. On cherche $(V_{\mathrm{m}}^{n+1}, u^{n+1}) \in V_h \times W_h$, avec $\displaystyle\int_{\Omega_{\mathrm{H}}} u^{n+1} = 0$:

$$\begin{cases} A_{\mathrm{m}}\displaystyle\int_{\Omega_{\mathrm{H}}} \frac{C_{\mathrm{m}}}{\tau}\left(\frac{3}{2}V_{\mathrm{m}}^{n+1} - 2V_{\mathrm{m}}^n + \frac{1}{2}V_{\mathrm{m}}^{n-1}\right)\phi + \displaystyle\int_{\Omega_{\mathrm{H}}} \boldsymbol{\sigma}_{\mathrm{i}}\boldsymbol{\nabla}(V_{\mathrm{m}}^{n+1} + u^{n+1})\cdot\boldsymbol{\nabla}\phi \\ \qquad\qquad = A_{\mathrm{m}}\displaystyle\int_{\Omega_{\mathrm{H}}} \Big(I_{\mathrm{app}}(t_{n+1}) - I_{\mathrm{ion}}(\widetilde{V}_{\mathrm{m}}^{n+1}, w^{n+1})\Big)\phi, \\ \displaystyle\int_{\Omega_{\mathrm{H}}} (\boldsymbol{\sigma}_{\mathrm{i}} + \boldsymbol{\sigma}_{\mathrm{e}})\boldsymbol{\nabla}u^{n+1}\cdot\boldsymbol{\nabla}\psi + \int_{\Omega_{\mathrm{H}}} \boldsymbol{\sigma}_{\mathrm{i}}\boldsymbol{\nabla}V_{\mathrm{m}}^{n+1}\cdot\boldsymbol{\nabla}\psi + \int_{\Omega_{\mathrm{T}}} \boldsymbol{\sigma}_{\mathrm{T}}\boldsymbol{\nabla}u^{n+1}\cdot\boldsymbol{\nabla}\psi = 0, \end{cases} \tag{1.2.14}$$

pour tout $(\phi,\psi) \in V_h \times W_h$, avec $\displaystyle\int_{\Omega_{\mathrm{H}}} \psi = 0$. Finallement, on pose $u_{\mathrm{e}}^{n+1} = u_{|\Omega_{\mathrm{H}}}^{n+1}$ et $u_{\mathrm{T}}^{n+1} = u_{|\Omega_{\mathrm{T}}}^{n+1}$.

On peut remarquer que l'équation $(1.2.14)_2$ impose de façon naturelle les conditions de couplage (1.2.7)-(1.2.8). En pratique nous ne résolvons pas le système (1.2.14) dans un seul système linéaire. Nous utilisons une technique de décomposition de domaines (voir [QV99, TW05]): nous utilisons l'algorithme Dirichlet-Neumann avec une accélération d'Aitken (voir [IT69]). Plus de détails sur ces méthodes sont donnés dans le Chapitre 5 (section 5.3.2).

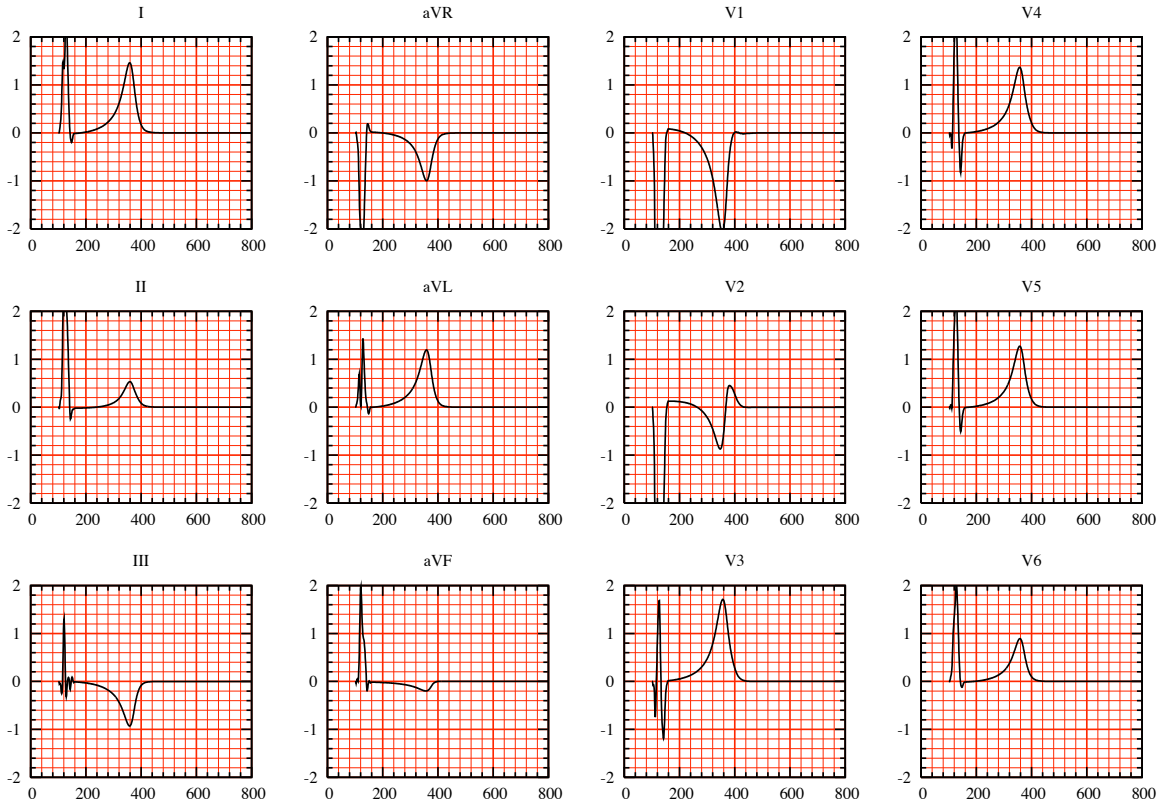

Figure 1.2: Simulation numérique des 12 dérivations de l'ECG pour un cas sain.

Dans le chapitre 5, nous fournissons des simulation des ECGs pour un cas sain (voir Figure 1.2) et des cas pathologiques. La simulation des cas pathologiques montre l'aspect prédictif du modèle. En effet, les simulations des blocs de branches et des arythmies cardiaques sont en de nombreux points semblables à des enregistrements cliniques, et surtout, les principaux critères utilisés par les médecins pour détecter ces pathologies (durée du QRS, polarité des différentes ondes, fréquence,*etc.*) sont vérifiés dans les simulations.

Nous montrons, à travers des simulations numériques, que certaines des hypothèses de modélisation que nous avons faites sont indispensables. Ainsi, en accord avec d'autres études, nous montrons que l'homogénéité cellulaire cause une inversion de la polarité de l'onde T; l'isotropie du muscle cardiaque affecte d'une manière significative l'ECG en cas de pathologie de blocs des branches, *etc.* Les relations de couplage entre le cœur et le thorax sont aussi étudiées. Nous commençons par montrer que la relaxation des conditions de continuité du potentiel et de courant (1.2.7)-(1.2.8) en seulement une condition de continuité de potentiel (1.2.7) affecte l'amplitude de l'ECG. Par contre la forme générale de l'ECG reste conservée. Dans ce cas, le calcul des potentiels cardiaques (potentiel d'action et potentiel extra-cellulaire) est découplé du potentiel thoracique et le calcul est bien moins coûteux. Le coût de la simulation des potentiels cardiaque et thoracique est encore moins élevé lors de l'utilisation de l'approximation monodomaine [CNLH04b, CFPT05]. En effet, cette approximation permet, au cas où le cœur est supposé isolé et que le couplage du cœur avec le thorax est assuré par la relation (1.2.7), de découpler le calcul du potentiel d'action du calcul du potentiel extérieur. Par suite, les trois champs sont calculés de façon séquentielle (V_{m}, puis u_{e}, ensuite u_{T}). Nous montrons

que l'ECG est légèrement affecté par l'approximation monodomaine: l'erreur relative de l'ECG calculé en utilisant le modèle bidomaine et celui obtenu avec l'approximation monodomaine est de 4% en norme l^2. Ces résultats sont en accord avec [CNLH04b] et [PDR$^+$06] où il est montré que la vitesse de propagation de l'onde en cas du modèle bidomaine est 2% plus rapide que celle calculée avec l'approximation monodomaine. Nous soulignons aussi que dans le cas de l'utilisation de couplage fort (couplage assuré par les équations (1.2.7)-(1.2.8)) entre le cœur et le thorax, il n'est plus possible de découpler le calcul des trois champs ($V_{\rm m}$, $u_{\rm e}$ et $u_{\rm T}$). Dans ce cas, le modèle bidomaine conduit à un coût de calcul similaire.

Pour les relations de couplage, nous considérons aussi l'effet des conditions *résistance-capacité* que nous avons introduites dans [BFGZ07] et montrons que, dans le cas où le péricarde est très résistif et faiblement capacitif, l'amplitude de l'ECG devient très faible. Dans le cas où la capacité est relativement plus importante, le segment S-T de l'ECG est "décalé". Ce phénomène, connu en électrocardiologie sous le nom de *sus-décalage ST*, est visible en cas de *péricardites* (inflammation du péricarde) [CCAS08]. On peut émettre l'hypothèse que la péricardite introduit effectivement un effet capacitif au niveau de l'interface myocarde/torse, ce qui justifierait dans certains cas l'introduction des conditions de transmission que nous avons proposées.

1.2.3 Méthodes numériques: Analyse de stabilité

Afin de réduire le coût de calcul des ECGs nous proposons une série de schémas numériques pemettant de découpler le calcul des différentes variables d'état. Nous avons mentionné dans la section précédente que l'approximation monodomaine permet de faire ce découplage en cas de résolution du problème *cœur isolé*. Mais en cas de couplage fort cette approximation ne permet pas de réduire le coût des calculs. Nous proposons dans le Chapitre 6 des schémas temporels de premier ordre permettant de découpler les deux potentiels cardiaques tout en gardant le modèle bidomaine.

Notons, pour une fonction X dependante du temps, par X^n l'approximation de $X(t_n)$ et $D_\tau X^n \stackrel{\rm def}{=} (X^n - X^{n-1})/\tau$ une approximation d'ordre un de la dérivée de X au temps t_n.

Cœur isolé: (découplage de $V_{\rm m}$ et $u_{\rm e}$)

Les schémas numériques consistent à combiner un traîtement semi-implicite d'ordre 1 du courant ionique avec des schémas explicites (de type Gauss-Seidel ou Jacobi) pour traîter le couplage entre $V_{\rm m}$ et $u_{\rm e}$. Les shemas qui en résultent peuvent s'écrire d'une façon génerale comme suit:

Pour $0 \leq n \leq N-1$, nous résolvons

1. La variable ionique: chercher $w^{n+1} \in L^\infty(\Omega_{\rm H})$ tel que

$$\int_{\Omega_{\rm H}} \big(D_\tau w^{n+1} + g(V_{\rm m}^n, w^{n+1})\big)\xi = 0 \tag{1.2.15}$$

pour tout $\xi \in L^2(\Omega_{\rm H})$.

2. Potentiel transmembranaire: trouver $V_{\mathrm{m}}^{n+1} \in H^1(\Omega_{\mathrm{H}})$ tel que

$$\chi_{\mathrm{m}} \int_{\Omega_{\mathrm{H}}} D_\tau V_{\mathrm{m}}^{n+1} \phi + \int_{\Omega_{\mathrm{H}}} \boldsymbol{\sigma}_{\mathrm{i}} \boldsymbol{\nabla} V_{\mathrm{m}}^{n+1} \cdot \boldsymbol{\nabla} \phi + \int_{\Omega_{\mathrm{H}}} \boldsymbol{\sigma}_{\mathrm{i}} \boldsymbol{\nabla} u_{\mathrm{e}}^{\star} \cdot \boldsymbol{\nabla} \phi = \int_{\Omega_{\mathrm{H}}} \left(I_{\mathrm{app}}^{n+1} - I_{\mathrm{ion}}(V_{\mathrm{m}}^{n}, w^{n+1}) \right) \phi \quad (1.2.16)$$

pour tout $\phi \in H^1(\Omega_{\mathrm{H}})$.

3. Potentiel extracellulaire: trouver $u_{\mathrm{e}}^{n+1} \in H^1(\Omega_{\mathrm{H}}) \cap L_0^2(\Omega_{\mathrm{H}})$ tel que

$$\int_{\Omega_{\mathrm{H}}} (\boldsymbol{\sigma}_{\mathrm{i}} + \boldsymbol{\sigma}_{\mathrm{e}}) \boldsymbol{\nabla} u_{\mathrm{e}}^{n+1} \cdot \boldsymbol{\nabla} \psi + \int_{\Omega_{\mathrm{H}}} \boldsymbol{\sigma}_{\mathrm{i}} \boldsymbol{\nabla} V_{\mathrm{m}}^{\star} \cdot \boldsymbol{\nabla} \psi = 0 \quad (1.2.17)$$

pour tout $\psi \in H^1(\Omega_{\mathrm{H}}) \cap L_0^2(\Omega_{\mathrm{H}})$.

Pour $(u_{\mathrm{e}}^{\star}, V_{\mathrm{m}}^{\star}) = (u_{\mathrm{e}}^{n+1}, V_{\mathrm{m}}^{n+1})$, les potentiels inconnus V_{m}^{n+1} et u_{e}^{n+1} sont couplés d'une façon implicite. Les équations (1.2.16) et (1.2.17) doivent être résolues dans le même système (voir [KB98, SLT05, EB08, EB08, BCF$^+$09]). Une analyse de stabilité de ce schéma semi-implicite a été récemment proposée par Ethier et Bourgault [EB08].

Par contre, pour $(u_{\mathrm{e}}^{\star}, V_{\mathrm{m}}^{\star}) = (u_{\mathrm{e}}^{n}, V_{\mathrm{m}}^{n+1})$ ou $(u_{\mathrm{e}}^{\star}, V_{\mathrm{m}}^{\star}) = (u_{\mathrm{e}}^{n}, V_{\mathrm{m}}^{n})$, le couplage electrodiffusif devient explicite, par suite les équations (1.2.16) et (1.2.17) peuvent être résolues séparément: ou bien séquentiellement (Gauss-Seidel) ou d'une manière parallèle (Jacobi). Le schéma Gauss-Seidel a été proposé et appliqué avec succés dans des différents travaux [SLT01, LGT03, ATP06, VWdSP$^+$08]. En revanche, aucune étude théorique de stabilité n'a été établie pour ce schéma. À notre connaissance, le schéma Jacobi n' a jamais été considéré dans la littérature.

Le résultat de stabilité des différents schémas est donné par le théorème suivant

Théorème (Theorem 6.3.3.1) *Sous des conditions précisées dans le chapitre 6 (section 6.3.3), on a les résultats de stabilité suivants*

- *Pour* $(u_{\mathrm{e}}^{\star}, V_{\mathrm{m}}^{\star}) = (u_{\mathrm{e}}^{n+1}, V_{\mathrm{m}}^{n+1})$*:*

$$\left\|w^n\right\|_{0,\Omega_{\mathrm{H}}}^2 + \chi_{\mathrm{m}} \left\|V_{\mathrm{m}}^n\right\|_{0,\Omega_{\mathrm{H}}}^2 + 2\sum_{m=0}^{n-1} \tau \left\|\boldsymbol{\sigma}_{\mathrm{e}}^{\frac{1}{2}} \boldsymbol{\nabla} u_{\mathrm{e}}^{m+1}\right\|_{0,\Omega_{\mathrm{H}}}^2 + 2\sum_{m=0}^{n-1} \tau \left\|\boldsymbol{\sigma}_{\mathrm{i}}^{\frac{1}{2}} \boldsymbol{\nabla} (V_{\mathrm{m}}^{m+1} + u_{\mathrm{e}}^{m+1})\right\|_{0,\Omega_{\mathrm{H}}}^2$$
$$\leq C(T, \alpha, \beta) \left(\left\|w^0\right\|_{0,\Omega_{\mathrm{H}}}^2 + \chi_{\mathrm{m}} \left\|V_{\mathrm{m}}^0\right\|_{0,\Omega_{\mathrm{H}}}^2 + \sum_{m=0}^{n-1} \tau \left\|I_{\mathrm{app}}^{m+1}\right\|_{0,\Omega_{\mathrm{H}}}^2 \right), \quad (1.2.18)$$

pour $1 \leq n \leq N$.

- *Pour* $(u_{\mathrm{e}}^{\star}, V_{\mathrm{m}}^{\star}) = (u_{\mathrm{e}}^{n}, V_{\mathrm{m}}^{n+1})$*:*

$$\begin{aligned}
&\left\|w^{n}\right\|_{0,\Omega_{\mathrm{H}}}^{2} + \chi_{\mathrm{m}}\left\|V_{\mathrm{m}}^{n}\right\|_{0,\Omega_{\mathrm{H}}}^{2} + \tau\left\|\boldsymbol{\sigma}_{\mathrm{i}}^{\frac{1}{2}}\boldsymbol{\nabla} u_{\mathrm{e}}^{n}\right\|_{0,\Omega_{\mathrm{H}}}^{2} \\
&\qquad + 2\sum_{m=0}^{n-1}\tau\left\|\boldsymbol{\sigma}_{\mathrm{e}}^{\frac{1}{2}}\boldsymbol{\nabla} u_{\mathrm{e}}^{m+1}\right\|_{0,\Omega_{\mathrm{H}}}^{2} + \sum_{m=0}^{n-1}\tau\left\|\boldsymbol{\sigma}_{\mathrm{i}}^{\frac{1}{2}}\boldsymbol{\nabla}(V_{\mathrm{m}}^{m+1} + u_{\mathrm{e}}^{m+1})\right\|_{0,\Omega_{\mathrm{H}}}^{2} \\
&\leq C(T,\alpha,\beta)\left(\left\|w^{0}\right\|_{0,\Omega_{\mathrm{H}}}^{2} + \chi_{\mathrm{m}}\left\|V_{\mathrm{m}}^{0}\right\|_{0,\Omega_{\mathrm{H}}}^{2} + \tau\left\|\boldsymbol{\sigma}_{\mathrm{i}}^{\frac{1}{2}}\boldsymbol{\nabla} u_{\mathrm{e}}^{0}\right\|_{0,\Omega_{\mathrm{H}}}^{2} + \sum_{m=0}^{n-1}\tau\left\|I_{\mathrm{app}}^{m+1}\right\|_{0,\Omega_{\mathrm{H}}}^{2}\right),
\end{aligned} \tag{1.2.19}$$

pour $1 \leq n \leq N$*.*

- *Pour* $(u_{\mathrm{e}}^{\star}, V_{\mathrm{m}}^{\star}) = (u_{\mathrm{e}}^{n}, V_{\mathrm{m}}^{n})$*:*

$$\begin{aligned}
&\left\|w^{n}\right\|_{0,\Omega_{\mathrm{H}}}^{2} + \chi_{\mathrm{m}}\left\|V_{\mathrm{m}}^{n}\right\|_{0,\Omega_{\mathrm{H}}}^{2} + \tau\left\|\boldsymbol{\sigma}_{\mathrm{i}}^{\frac{1}{2}}\boldsymbol{\nabla} u_{\mathrm{e}}^{n}\right\|_{0,\Omega_{\mathrm{H}}}^{2} + \tau\left\|\boldsymbol{\sigma}_{\mathrm{i}}^{\frac{1}{2}}\boldsymbol{\nabla} V_{\mathrm{m}}^{n}\right\|_{0,\Omega_{\mathrm{H}}}^{2} \\
&+2\sum_{m=0}^{n-1}\tau\left\|\boldsymbol{\sigma}_{\mathrm{e}}^{\frac{1}{2}}\boldsymbol{\nabla} u_{\mathrm{e}}^{m+1}\right\|_{0,\Omega_{\mathrm{H}}}^{2} \leq C(T,\alpha,\beta)\left(\left\|w^{0}\right\|_{0,\Omega_{\mathrm{H}}}^{2} + \chi_{\mathrm{m}}\left\|V_{\mathrm{m}}^{0}\right\|_{0,\Omega_{\mathrm{H}}}^{2} + \tau\left\|\boldsymbol{\sigma}_{\mathrm{i}}^{\frac{1}{2}}\boldsymbol{\nabla} V_{\mathrm{m}}^{0}\right\|_{0,\Omega_{\mathrm{H}}}^{2}\right. \\
&\qquad\qquad\left. +\tau\left\|\boldsymbol{\sigma}_{\mathrm{i}}^{\frac{1}{2}}\boldsymbol{\nabla} u_{\mathrm{e}}^{0}\right\|_{0,\Omega_{\mathrm{H}}}^{2} + \sum_{m=0}^{n-1}\tau\left\|I_{\mathrm{app}}^{m+1}\right\|_{0,\Omega_{\mathrm{H}}}^{2}\right),
\end{aligned} \tag{1.2.20}$$

pour $1 \leq n \leq N$*.*

Cœur-thorax: (découplage de V_{m}, u_{e} et u_{T})

Afin de découpler le calcul de V_{m}, u_{e} et u_{T}, nous proposons de combiner les techniques de découplage de V_{m} et u_{e} introduites ci-dessus avec les conditions de découplage entre le cœur et le thorax de type Robin-Robin suivant [ACF09, BF09]

$$\begin{aligned}
\boldsymbol{\sigma}_{\mathrm{e}}\boldsymbol{\nabla} u_{\mathrm{e}}^{n+1}\cdot\boldsymbol{n} + \frac{\gamma\sigma_{\mathrm{t}}}{h}u_{\mathrm{e}}^{n+1} &= -\boldsymbol{\sigma}_{\mathrm{T}}\boldsymbol{\nabla} u_{\mathrm{T}}^{n}\cdot\boldsymbol{n}_{\mathrm{T}} + \frac{\gamma\sigma_{\mathrm{t}}}{h}u_{\mathrm{T}}^{n}, \quad \text{sur} \quad \Sigma, \\
\boldsymbol{\sigma}_{\mathrm{T}}\boldsymbol{\nabla} u_{\mathrm{T}}^{n+1}\cdot\boldsymbol{n}_{\mathrm{T}} + \frac{\gamma\sigma_{\mathrm{t}}}{h}u_{\mathrm{T}}^{n+1} &= \boldsymbol{\sigma}_{\mathrm{T}}\boldsymbol{\nabla} u_{\mathrm{T}}^{n}\cdot\boldsymbol{n}_{\mathrm{T}} + \frac{\gamma\sigma_{\mathrm{t}}}{h}u_{\mathrm{e}}^{n+1}, \quad \text{sur} \quad \Sigma,
\end{aligned} \tag{1.2.21}$$

où $\gamma > 0$ est le paramètre de Robin à préciser, et σ_{t} est tel que $\boldsymbol{\sigma}_{\mathrm{T}|\Sigma} = \sigma_{\mathrm{t}}\boldsymbol{I}$. Il en résulte les schémas suivants: pour $0 \leq n \leq N-1$, nous résolvons

1. La variable ionique: chercher $w^{n+1} \in X_h$ tel que

$$\int_{\Omega_{\mathrm{H}}}\left(D_{\tau}w^{n+1} + g(V_{\mathrm{m}}^{n}, w^{n+1})\right)\xi = 0 \tag{1.2.22}$$

pour tout $\xi \in X_h$.

2. Le potentiel transmembranaire: trouver $V_{\mathrm{m}}^{n+1} \in X_h$ tel que

$$\begin{aligned}
\chi_{\mathrm{m}}\int_{\Omega_{\mathrm{H}}}D_{\tau}V_{\mathrm{m}}^{n+1}\phi + \int_{\Omega_{\mathrm{H}}}\boldsymbol{\sigma}_{\mathrm{i}}\boldsymbol{\nabla} V_{\mathrm{m}}^{n+1}\cdot\boldsymbol{\nabla}\phi + \int_{\Omega_{\mathrm{H}}}\boldsymbol{\sigma}_{\mathrm{i}}\boldsymbol{\nabla} u_{\mathrm{e}}^{\star}\cdot\boldsymbol{\nabla}\phi \\
= \int_{\Omega_{\mathrm{H}}}\left(I_{\mathrm{app}}^{n+1} - I_{\mathrm{ion}}(V_{\mathrm{m}}^{n}, w^{n+1})\right)\phi
\end{aligned} \tag{1.2.23}$$

pour tout $\phi \in X_h$.

3. Le potentiel extracellulaire : trouver $u_{\mathrm{e}}^{n+1} \in X_h$ tel que

$$\begin{aligned}\int_{\Omega_{\mathrm{H}}} (\boldsymbol{\sigma}_{\mathrm{i}} + \boldsymbol{\sigma}_{\mathrm{e}}) \boldsymbol{\nabla} u_{\mathrm{e}}^{n+1} \cdot \boldsymbol{\nabla} \psi + \int_{\Omega_{\mathrm{H}}} \boldsymbol{\sigma}_{\mathrm{i}} \boldsymbol{\nabla} V_{\mathrm{m}}^{\star} \cdot \boldsymbol{\nabla} \psi + \frac{\gamma \sigma_{\mathrm{t}}}{h} \int_{\Sigma} u_{\mathrm{e}}^{n+1} \psi \\ = - \int_{\Sigma} \boldsymbol{\sigma}_{\mathrm{T}} \boldsymbol{\nabla} u_{\mathrm{T}}^{n} \cdot \boldsymbol{n}_{\mathrm{T}} \psi + \frac{\gamma \sigma_{\mathrm{t}}}{h} \int_{\Sigma} u_{\mathrm{T}}^{n} \psi\end{aligned} \tag{1.2.24}$$

pour tout $\psi \in X_h$.

4. Le potentiel thoracique: trouver $u_{\mathrm{T}}^{n+1} \in X_h$

$$\int_{\Omega_{\mathrm{T}}} \boldsymbol{\sigma}_{\mathrm{T}} \boldsymbol{\nabla} u_{\mathrm{T}}^{n+1} \cdot \boldsymbol{\nabla} \zeta + \frac{\gamma \sigma_{\mathrm{t}}}{h} \int_{\Sigma} u_{\mathrm{T}}^{n+1} \zeta = \int_{\Sigma} \boldsymbol{\sigma}_{\mathrm{T}} \boldsymbol{\nabla} u_{\mathrm{T}}^{n} \cdot \boldsymbol{n}_{\mathrm{T}} \zeta + \frac{\gamma \sigma_{\mathrm{t}}}{h} \int_{\Sigma} u_{\mathrm{e}}^{n+1} \zeta \tag{1.2.25}$$

pour tout $\zeta \in X_h$.

Contrairement à la formulation (1.2.14) la formulation (1.2.22)-(1.2.24) permet de résoudre indépendamment le potentiel extérieur et le potentiel thoracique. En particulier, les choix $(u_{\mathrm{e}}^{\star}, V_{\mathrm{m}}^{\star}) = (u_{\mathrm{e}}^{n}, V_{\mathrm{m}}^{n+1})$ ou $(u_{\mathrm{e}}^{\star}, V_{\mathrm{m}}^{\star}) = (u_{\mathrm{e}}^{n}, V_{\mathrm{m}}^{n})$ permettent de découpler totalement le calcul de w^{n+1}, V_{m}^{n+1}, u_{e}^{n+1} et u_{T}^{n+1} et de les calculer de façon séquentielle.

En notant $E_{\mathrm{H}}^{0}\big(u_{\mathrm{e}}^{\star}, V_{\mathrm{m}}^{\star}\big)$ (resp. $E_{\mathrm{H}}^{n}\big(u_{\mathrm{e}}^{\star}, V_{\mathrm{m}}^{\star}\big)$) l'énergie discrète au pas 0 (resp. n) estimée dans le théoreme précédent. Dans le cas où $(u_{\mathrm{e}}^{\star}, V_{\mathrm{m}}^{\star}) = (u_{\mathrm{e}}^{n}, V_{\mathrm{m}}^{n})$ par exemple, on a

$$\begin{aligned}E_{\mathrm{H}}^{0}\big(u_{\mathrm{e}}^{\star}, V_{\mathrm{m}}^{\star}\big) &\stackrel{\mathrm{def}}{=} \big\|w^{0}\big\|_{0,\Omega_{\mathrm{H}}}^{2} + \chi_{\mathrm{m}} \big\|V_{\mathrm{m}}^{0}\big\|_{0,\Omega_{\mathrm{H}}}^{2} + \tau \big\|\boldsymbol{\sigma}_{\mathrm{i}}^{\frac{1}{2}} \boldsymbol{\nabla} V_{\mathrm{m}}^{0}\big\|_{0,\Omega_{\mathrm{H}}}^{2} + \tau \big\|\boldsymbol{\sigma}_{\mathrm{i}}^{\frac{1}{2}} \boldsymbol{\nabla} u_{\mathrm{e}}^{0}\big\|_{0,\Omega_{\mathrm{H}}}^{2}, \\ E_{\mathrm{H}}^{n}\big(u_{\mathrm{e}}^{\star}, V_{\mathrm{m}}^{\star}\big) &\stackrel{\mathrm{def}}{=} \big\|w^{n}\big\|_{0,\Omega_{\mathrm{H}}}^{2} + \chi_{\mathrm{m}} \big\|V_{\mathrm{m}}^{n}\big\|_{0,\Omega_{\mathrm{H}}}^{2} + \tau \big\|\boldsymbol{\sigma}_{\mathrm{i}}^{\frac{1}{2}} \boldsymbol{\nabla} u_{\mathrm{e}}^{n}\big\|_{0,\Omega_{\mathrm{H}}}^{2} + \tau \big\|\boldsymbol{\sigma}_{\mathrm{i}}^{\frac{1}{2}} \boldsymbol{\nabla} V_{\mathrm{m}}^{n}\big\|_{0,\Omega_{\mathrm{H}}}^{2} \\ &\quad + 2 \sum_{m=0}^{n-1} \tau \big\|\boldsymbol{\sigma}_{\mathrm{e}}^{\frac{1}{2}} \boldsymbol{\nabla} u_{\mathrm{e}}^{m+1}\big\|_{0,\Omega_{\mathrm{H}}}^{2},\end{aligned}$$

La stabilité du schéma (1.2.22)-(1.2.25) est assurée par le théorème suivant

Théorème (Theorem 6.4.3.1) *Sous des conditions précisées dans le chapitre 6 (section 6.4.3), si* $\big\{\big(w^{n}, V_{\mathrm{m}}^{n}, u_{\mathrm{e}}^{n}, u_{\mathrm{T}}^{n}\big)\big\}_{n=0}^{N}$ *est solution de* (1.2.22)-(1.2.25)*, on a les résultats de stabilité suivants*

$$\begin{aligned}&E_{\mathrm{H}}^{n}\big(u_{\mathrm{e}}^{\star}, V_{\mathrm{m}}^{\star}\big) + \tau \frac{\gamma \sigma_{\mathrm{t}}}{h} \big\|u_{\mathrm{T}}^{n}\big\|_{0,\Sigma}^{2} + \sum_{m=0}^{n-1} \tau \big\|\boldsymbol{\sigma}_{\mathrm{T}}^{\frac{1}{2}} \boldsymbol{\nabla} u_{\mathrm{T}}^{m+1}\big\|_{0,\Omega_{\mathrm{T}}}^{2} + \sum_{m=0}^{n-1} \tau \frac{\gamma \sigma_{\mathrm{t}}}{2h} \big\|u_{\mathrm{T}}^{m+1} - u_{\mathrm{e}}^{m+1}\big\|_{0,\Sigma}^{2} \\ &\leq C(T, \alpha, \beta) \left(E_{\mathrm{H}}^{0}\big(u_{\mathrm{e}}^{\star}, V_{\mathrm{m}}^{\star}\big) + \tau \frac{\gamma \sigma_{\mathrm{t}}}{h} \big\|u_{\mathrm{T}}^{0}\big\|_{0,\Sigma}^{2} + \tau \big\|\boldsymbol{\sigma}_{\mathrm{T}}^{\frac{1}{2}} \boldsymbol{\nabla} u_{\mathrm{T}}^{0}\big\|_{0,\Omega_{\mathrm{T}}}^{2} + \sum_{m=0}^{n-1} \tau \|I_{\mathrm{app}}^{m+1}\|_{0,\Omega_{\mathrm{H}}}^{2} \right),\end{aligned} \tag{1.2.26}$$

avec $1 \leq n \leq N$*. En particulier,* (1.2.26) *assure la stabilité du couplage explicite entre le cœur et le thorax* (1.2.22)-(1.2.25) *sous la condition* $\tau = O(h)$*.*

Les résultats de stabilité sont illustrés par des simulations sur une géomeétrie réaliste du cœur et du torse. Pour le cas du cœur isolé nous comparons le potentiel d'action (Figure 1.3, gauche) entre les différents schémas numériques: bidomaine couplé ($(u_{\mathrm{e}}^{\star}, V_{\mathrm{m}}^{\star}) = (u_{\mathrm{e}}^{n+1}, V_{\mathrm{m}}^{n+1})$), le schéma Gauss-Seidel ($(u_{\mathrm{e}}^{\star}, V_{\mathrm{m}}^{\star}) = (u_{\mathrm{e}}^{n}, V_{\mathrm{m}}^{n+1})$) et le

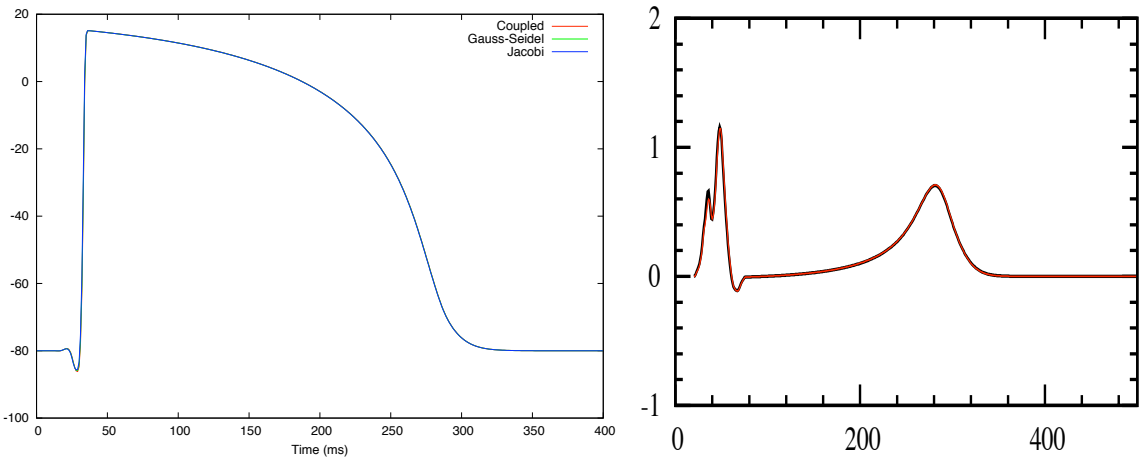

Figure 1.3: Gauche: Comparaison du potentiel d'action entre les shemas: bidomaine couplé ($(u_{\mathrm{e}}^{\star}, V_{\mathrm{m}}^{\star}) = (u_{\mathrm{e}}^{n+1}, V_{\mathrm{m}}^{n+1})$), le schéma de Gauss-Seidel ($(u_{\mathrm{e}}^{\star}, V_{\mathrm{m}}^{\star}) = (u_{\mathrm{e}}^{n}, V_{\mathrm{m}}^{n+1})$) et le schéma de Jacobi ($(u_{\mathrm{e}}^{\star}, V_{\mathrm{m}}^{\star}) = (u_{\mathrm{e}}^{n}, V_{\mathrm{m}}^{n})$). Droite: Comparaison de la première dérivation d'un ECG calculé avec un couplage fort (noir) et un ECG calculé en utilisant le schéma de Jacobi avec Robin-Robin pour découpler le cœur du thorax (rouge).

schéma de Jacobi ($(u_{\mathrm{e}}^{\star}, V_{\mathrm{m}}^{\star}) = (u_{\mathrm{e}}^{n}, V_{\mathrm{m}}^{n})$). Le resultat confirme le résultat de stabilité théorique. On constate également que les schémas de Gauss-Seidel et de Jacobi offrent une bonne précision de calcul. La simulation des ECGs confirme également la stabilité de la solution quand on utilise le découplage explicite (Robin-Robin). Les ECGs obtenus avec un couplage fort entre le thorax et ceux résultant d'un découplage complet entre les variables d'états (schéma de Jacobi avec conditions Robin-Robin pour découpler le cœur du thorax) sont quasi-identiques (Figure 1.3, droite). La simulation des conditions pathologiques (bloc de branche gauche) et la simulation des ECGs sur une géométrie analytique reportées dans le chapitre 6 (section 6.5.3) confirment l'efficacité de ces méthodes.

1.2.4 Applications: Utilisations de l'ECG

Dans la dernière partie de la thèse, nous considérons quelques applications en relation avec l'ECG. La première concerne l'estimation de certains paramètres du modèle. Nous cherchons à estimer les conductivités $\sigma_{\mathrm{t}}, \sigma_{\mathrm{l}}, \sigma_{\mathrm{b}}$ définissant le tenseur de conductivité thoracique. Ce tenseur, supposé scalaire, est donné par

$$\boldsymbol{\sigma}_{\mathrm{T}} = \begin{cases} \sigma_l, & \text{dans les poumons,} \\ \sigma_b, & \text{dans le squelette,} \\ \sigma_t, & \text{dans le reste du tissu thoracique.} \end{cases} \tag{1.2.27}$$

Dans le cas où le thorax n'affecte pas le cœur, la propagation de l'onde électrique dans le thorax est donnée par

$$\begin{cases} \operatorname{div}(\boldsymbol{\sigma}_{\mathrm{T}} \boldsymbol{\nabla} u_{\mathrm{T}}) = 0, \text{ dans } \Omega_{\mathrm{T}}, \\ \qquad\qquad u_{\mathrm{T}} = u_{\mathrm{e}}, \quad \text{sur} \quad \Sigma, \\ \boldsymbol{\sigma}_{\mathrm{T}} \boldsymbol{\nabla} u_{\mathrm{T}} \cdot \boldsymbol{n}_{\mathrm{T}} = 0, \text{ sur } \Gamma_{\mathrm{ext}}, \end{cases} \tag{1.2.28}$$

En multipliant le tenseur de conductivité $\boldsymbol{\sigma}_{\mathrm{T}}$ par une constante γ, la solution ne change pas. Par suite, la solution du problème (1.2.28) est la même que celle du problème suivant

$$(\mathrm{P}_\gamma)\begin{cases} \operatorname{div}(\gamma\boldsymbol{\sigma}_{\mathrm{T}}\boldsymbol{\nabla}u_{\mathrm{T}}) = 0, \text{ dans } \Omega_{\mathrm{T}}, \\ \qquad\qquad u_{\mathrm{T}} = u_{\mathrm{e}}, \quad \text{sur} \quad \Sigma, \\ \gamma\boldsymbol{\sigma}_{\mathrm{T}}\boldsymbol{\nabla}u_{\mathrm{T}}\cdot\boldsymbol{n}_{\mathrm{T}} = 0, \text{ sur } \Gamma_{\mathrm{ext}}, \end{cases} \tag{1.2.29}$$

Ce qui fait qu'en posant $\gamma = \dfrac{1}{\sigma_i}$, où $\sigma_i \in \{\sigma_{\mathrm{t}}, \sigma_{\mathrm{l}}, \sigma_{\mathrm{b}}\}$, nous avons besoin d'estimer deux ratios au lieu de trois paramètres. Un des problèmes que nous rencontrons ici est que la valeur de u_{e} sur l'interface cœur-thorax est supposée être une donnée du problème, alors qu'en pratique il n'est pas facile d'accéder à cette quantité. Nous proposons dans le chapitre 7 une solution à ce problème basée sur un principe de superposition. Les détails de l'expérience numérique sont données dans la section 7.3.1 du chapitre 7. En choisissant $\gamma = \dfrac{1}{\sigma_{\mathrm{b}}}$ le problème d'identification des paramètres est formulé en un problème de minimisation comme suit

$$\min_{\sigma} I(\sigma),$$

avec

$$I(\sigma) = J(\sigma, \xi(\sigma))$$

où,

pour tout $\sigma = \begin{cases} \alpha_1, & \text{dans le tissu,} \\ \alpha_2, & \text{dans les poumons,} \\ 1, & \text{dans le squelette,} \end{cases}$

la fonction $\xi(\sigma)$ est la solution du problème suivant:

$$\begin{cases} \operatorname{div}(\boldsymbol{\sigma}_{\mathrm{T}}\boldsymbol{\nabla}\xi) = 0, \text{ dans } \Omega_{\mathrm{T}}, \\ \qquad\qquad \xi = 0, \text{ sur } \Sigma, \\ \qquad\qquad \xi = \bar{\xi}, \text{ sur } S, \\ \boldsymbol{\sigma}_{\mathrm{T}}\boldsymbol{\nabla}\xi\cdot\boldsymbol{n}_{\mathrm{T}} = 0, \text{ sur } \Gamma_{\mathrm{ext}}\backslash S. \end{cases} \tag{1.2.30}$$

où S est le domaine où on applique un potentiel source. La fonction J est donnée par

$$J(\sigma, \xi) = \frac{1}{2} \parallel \xi - \bar{\xi} \parallel^2_{L^2(\omega)} + \frac{\beta}{2}\big(|\alpha_1 - \bar{\alpha_1}|^2 + |\alpha_2 - \bar{\alpha_2}|^2\big),$$

ici $\beta > 0$ est un paramètre de regularization, ω est le domaine de mesure et

$$\boldsymbol{\sigma}_{\mathrm{M}} = \begin{cases} \bar{\alpha_1}, & \text{dans le tissu,} \\ \bar{\alpha_2}, & \text{dans les poumons,} \\ 1, & \text{dans le squelette,} \end{cases}$$

est dans la moyenne des ratios de conductivité. Nous utilisons des méthodes classiques d'optimisation et une approche duale pour le calcul du gradient. Les résultats obtenus sont satisfaisants, en particulier en choisissant comme domaine de mesure ω les position classiques des électrodes de l'ECG.

Pour le modèle ionique nous avons choisi de commencer par l'estimation de deux paramètres du modèle de Mitchell-Shaeffer $(\tau^{RV}_{\mathrm{close}}, \tau^{Epi}_{\mathrm{close}})$. Nous utiliserons la toolbox

d'optimisation de matlab pour résoudre le problème de minimisation. La fonction coût, dans ce cas, utilise les ECGs comme opérateur d'observation du modèle. Le problème d'identification des paramètres est transformer en un problème de minimisation donné par

$$\min_{\tau_{\text{close}}^{RV},\tau_{\text{close}}^{Epi}} \| ECG_{ref} - ECG(\tau_{\text{close}}^{RV},\tau_{\text{close}}^{Epi}) \|_{L^p(0,T)},$$

Le gradient de la fonction coût est calculé par difference finie dans le toolbox de matlab. Les résultats obtenus sont aussi satisfaisants.

Dans la deuxième application, nous utilisons des méthodes d'apprentissage statistique (*machine learning*) dans le but de reconstruire des électrocardiogrammes à partir des électrogrammes (des mesures de différences de potentiel prises sur le cœur, appelées aussi EGMs). Ce sujet a été soulevé par un industriel fabriquant des pacemakers (ELA Medical). Nous utilisons des techniques de métamodélisation basées sur les méthodes d'apprentissage à noyau (Reproducing Kernel Hilbert Spaces ou RKHS, voir [HTF01])). Nous présentons brièvement le principe de la méthode et nous proposons différentes approches de son application. Ces approches concernent le choix et la gestion des espaces de données. Nous présentons les résultats de reconstructions des ECGs sur des données simulées et des données cliniques. Nous comparons ensuite les approches utilisées. L'utilisation du simulateur des ECGs permet d'enrichir la base de données sur laquelle nous faisons l'apprentissage. Nous générons une base de données qui contient divers stades d'une pathologie (bloc de branche droit). Ceci nous permet d'évaluer la qualité de la méthode de reconstruction, ainsi que ces limites.

La dernière application concerne le couplage électro-mécanique. Nous présentons dans cette section le modèle mécanique [SMCCS06] couplé avec le modèle électrique à travers le potentiel transmembranaire [Moi08]. Nous produisons des résultats de simulations des cas sain et pathologiques (blocs de branches et arythmies). Les simulations sont faites sur une géométrie physiologique du cœur. Les indicateurs médicaux (l'ECG pour la partie électrique et les courbes de volume et de pression pour la partie mécanique) montrent des résultats comparables à des données physiologiques.

1.3 Plan de de la thèse

Dans la première partie, nous nous intéressons à la modélisation de l'activité électrique du cœur et du thorax afin d'introduire la simulation des électrocardiogrammes.

Dans la deuxième partie, nous démontrons un résultat d'existence d'une solution faible du système couplé cœur-thorax. Nous prouvons l'unicité de cette solution sous certaines conditions.

La troisième partie comporte deux sous-parties. La première est consacrée à l'étude et la simulation numérique du couplage électrique cœur-thorax. Des résultats de simulations sont présentés pour un cas normal et pour des cas pathologiques (blocs de branche gauche et droit). Nous étudions également l'impact de certaines hypothèses de modélisation sur les ECGs (couplage faible, utilisation du modèle monodomaine, isotropie, homogéneité cellulaire, comportement résistance-condensateur du péricarde,...). Nous étudions à la fin de cette sous-partie la sensibilité des électrocardiogrammes par apport aux paramètres du modèle. Dans la deuxième sous-partie, nous effectuons l'analyse

numérique de schémas du premier ordre en temps découplant les calculs du potentiel d'action et du potentiel extérieur. Puis, nous combinons ces schémas en temps avec un traîtement explicite du type Robin-Robin des conditions de couplage entre le cœur et le thorax. Nous proposons une analyse de stabilité de ces schémas et nous illustrons les résultats avec des simulations numériques.

La dernière partie est consacrée à trois applications. Nous commençons par l'estimation de certains paramètres du modèle (conductivité du thorax et paramètres ioniques). Dans la deuxième application, qui est d'originie industrielle, nous utilisons des méthodes d'apprentissage statistique pour reconstruire des électrocardiogrammes à partir d'électrogrammes. Enfin, nous présentons des simulations électro-mécaniques du coeur sur géométrie réelle dans diverses situations physiologiques et pathologiques. Les indicateurs cliniques, électriques et mécaniques, calculés à partir de ces simulations sont très similaires à ceux observés en réalité.

PUBLICATIONS ET COMMUNICATIONS

Les travaux présentés dans ce mémoire ont donné lieu à différentes publications dans des journaux et des communications dans des Conférences internationales.

Journaux

Parus

- M. Boulakia, M.A. Fernández, J.-F. Gerbeau, N. Zemzemi. A coupled system of PDEs and ODEs arising in electrocardiograms modelling. AMRX. Appl. Math. Res. Express, (2008) Vol. 2008. DOI: 10.1093/amrx/abn002

Soumis

- M. Boulakia, S. Cazeau, M.A. Fernández, J.-F. Gerbeau, N. Zemzemi. Mathematical Modeling Of Electrocardiograms: A Numerical Study. Accepted for publishing in *Annals of Biomedical Engineering*.
- M.A. Fernández, N. Zemzemi. Time decoupling techniques in electrocardiography simulation: Stability analysis and numerics. To appear in *Mathematical Biosciences*.

En preparation

- D. Chapelle, M.A. Fernández, J−F. Gerbeau, P. Moireau, N. Zemzemi. A 3D model for the electromechanical activity of the heart.

Proceedings

Parus

- G. Ebrard, M.A. Fernández, J.-F Gerbeau, F. Rossi, N. Zemzemi. From intracardiac electrograms to electrocardiograms. Models and metamodels. In Proceedings of the Fifth International Conference on Functional Imaging and Modeling of the Heart FIMH 2009, N, Ayache, H. Delingette, M. Sermesant Eds. pp. 524-533, Springer, 2009.
- D. Chapelle, M.A. Fernández, J.-F. Gerbeau, P. Moireau, J. Sainte-Marie, N. Zemzemi. Numerical simulation of the electromechanical activity of the heart, n Proceedings of the Fifth International Conference on Functional Imaging and Modeling of the Heart (FIMH09), N, Ayache, H. Delingette, M. Sermesant Eds. pp. 357-365, Springer, 2009.
- M. Boulakia and M.A. Fernández and J. F. Gerbeau and N. Zemzemi. Direct and Inverse problems in Electrocardiography. AIP Conference Proceedings, pp. 113-117, AIP 2008.
- M. Boulakia, M.A. Fernández, J.-F. Gerbeau, N. Zemzemi. Towards the numerical simulation of electrocardiograms. In Proceedings of the Fourth International Conference on Functional Imaging and Modeling of the Heart (FIMH07), F.B. Sachse, G. Seemann Eds., pp. 420-429, Springer, 2007.

Part I

Éléments d'électrophysiologie et modélisation

Summary

Chapter 2

Anatomie cardiaque et électrocardiogramme

2.1 Le cœur

Le cœur est un muscle creux formé principalement de fibres enroulés (voir Figure 2.1), une pompe composée de tissu musculaire, qui recueille sans cesse le sang et le propulse dans les artères. C'est le seul muscle qui peut se contracter régulièrement sans fatigue, tandis que les autres muscles ont besoin d'une période de repos. Il se trouve au milieu de la cage thoracique délimitée par les deux poumons, le sternum et la colonne vertébrale, il se situe un peu à gauche du centre du thorax au-dessus du diaphragme.

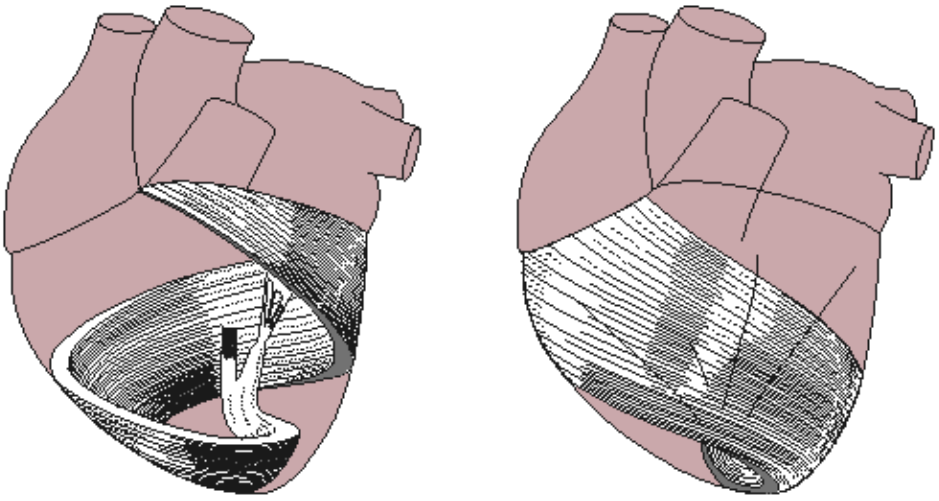

Figure 2.1: Orientation des fibres (d'après bembook [MP95]).

Alors que la masse du cœur (350 g) n'excède pas 0,5 % de la masse du corps, il prélève 10% de la consommation totale d'oxygène; il est alimenté en oxygène et nutriments par les vaisseaux coronaires, qui forment autour de lui une sorte de couronne. Le cœur est composé de quatre chambres (deux oreillettes et deux ventricules), équipées de valves qui empêchent les reflux sanguins. Il pompe le sang grâce à une série de systoles

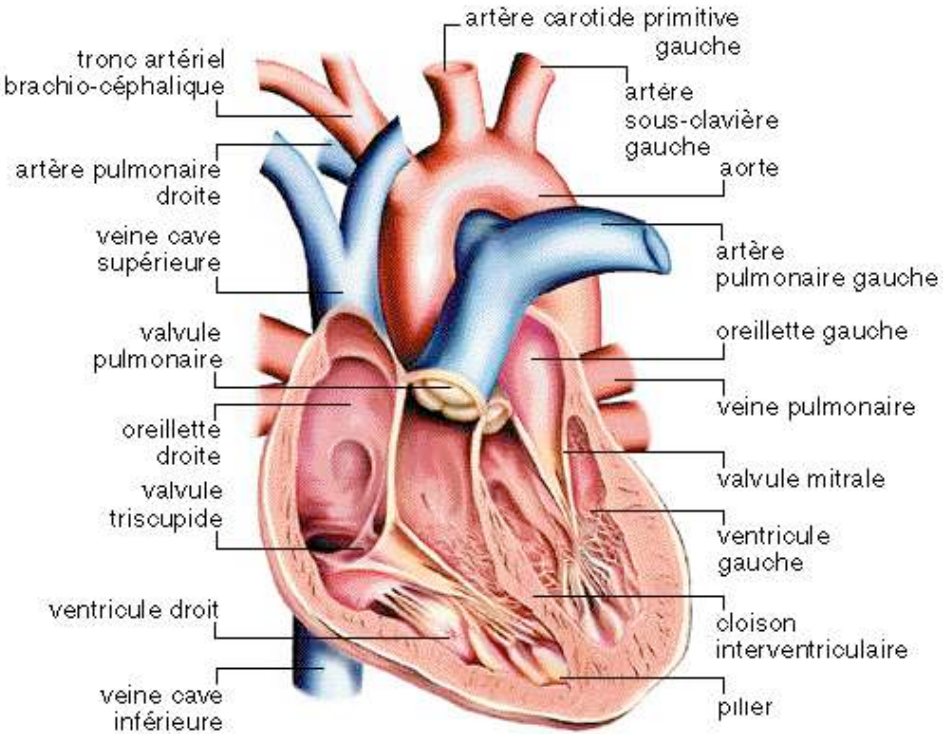

Figure 2.2: Anatomie du coeur (Source: Encyclopédie Larousse)

(contractions) et diastoles (relâchements) des oreillettes et ventricules. La circulation sanguine étant à sens unique, les valves ont pour but d'empêcher le sang de revenir en arrière: la valve tricuspide sépare l'oreillette droite du ventricule droit, la valve mitrale sépare l'oreillette gauche du ventricule gauche. Les artères sont séparés des ventricules par les valves sigmoides: le ventricule gauche est séparé de l'artère pulmonaire par les valves pulmonaires et le ventricule gauche est séparé de l'aorte par les valves aortiques. Par contre il n'existe pas de séparation entre les veines et les oreillettes.

2.2 Fonctionnement du cœur

2.2.1 Rôle du coeur

Le cœur se contracte très régulièrement et la continuité de ses battements est essentielle à la vie: un arrêt de la pulsation cardiaque est l'un des signes les plus évidents d'un décès. Ces pulsations, qui permettent à du sang frais, oxygéné, d'irriguer les organes, ne peuvent s'arrêter, même durant une période très courte: certains organes peuvent survivre à une brève interruption des pulsations cardiaques, d'autres non. C'est le cas du cerveau, qui est extrêmement sensible à toute anomalie circulatoire: 10 minutes d'interruption de l'irrigation sanguine du cerveau suffisent pour endommager l'organe de façon irréversible et la mort s'ensuit. Un cœur au repos se contracte normalement environ 70 fois par minute, période au cours de laquelle il chasse 5 litres de sang (le volume sanguin total d'un Homme). La contraction du cœur se fait d'une manière intrinsèque, c'est-à-dire qu'aucune stimulation d'origine nerveuse n'intervient. Une cellule

musculaire cardiaque isolée continue à battre spontanément et rythmiquement. Ensemble, les cellules musculaires constituent la paroi du cœur ou myocarde. Bien que le cœur génère son propre rythme contractile (le pouls), celui-ci est régulé par le système nerveux et deux hormones : L'adrénaline et la noradrénaline, hormones sécrétées par les glandes surrénales en cas de peur ou de colère, augmentent le rythme des contractions cardiaques; la noradrénaline est aussi libérée par les fibres nerveuses sympathiques arrivant au myocarde, l'acétylcholine, substance libérée par les nerfs parasympathiques, agit au contraire sur le cœur en ralentissant le pouls. Le rythme cardiaque varie de 70 battements par minutes (au repos) à 180, voire 210 battements par minute lors d'efforts intenses.

2.2.2 Les battements cardiaques en électrophysiologie

Les battements cardiaques sont sous le contrôle d'un pacemaker naturel, sorte de groupement de cellules du myocarde qui constituent le nœud sinusal ou nœud sino-auriculaire (SA), situé en haut de l'oreillette droite. Le nœud SA donne naissance à une onde d'excitation tous les 0.8 seconde. Cette onde parcourt, pendant 0.1 seconde, le tissu musculaire des deux oreillettes, qui se contractent d'abord lorsque les ventricules sont au repos. Cette periode correspond dans l'ECG à la duré de l'onde P. Puis l'onde gagne le second nœud, le nœud auriculo-ventriculaire (ou nœud AV) situé plus bas entre les deux oreillettes, lequel transmet l'onde d'excitation aux parois des deux ventricules via le faisceau auriculo-ventriculaire (ou le faisceau de His) puis les fibres de Purkinje. Ces dernières, en contact direct avec le myocarde, lui transmettent le courant ce qui entraine la dépolarisation et la contraction des cellules. Cette periode correspond au complexe QRS de l'ECG. Lorsque les ventricules se contractent, les oreillettes sont au repos. Le bruit du coeur provient de la brusque fermeture des valves à chaque contraction.

2.3 La circulation sanguine

L'Homme possède un système circulatoire clos: le sang part du cœur en empruntant les artères puis les artérioles, il traverse le réseau capillaire soit au niveau des poumons (petite circulation ou circulation pulmonaire), soit au niveau des autres organes (grande circulation ou circulation systémique), puis il retourne au coeur par les veinules puis les veines. Les artères sont des vaisseaux sanguins qui vont du cœur vers les organes, les veines ramenant inversement le sang des organes vers le cœur. Dans la grande circulation, les artères, partant du ventricule gauche, transportent du sang oxygéné (rouge) et les veines, revenant à l'oreillette droite, transportent du sang chargé en dioxyde de carbone (bleu), voir Figure 2.4. Par contre, dans la petite circulation, les artères pulmonaires, partant du ventricule droit, transportent du sang chargé en dioxyde de carbone vers les poumons, et les veines pulmonaires ramènent à l'oreillette gauche du sang oxygéné.

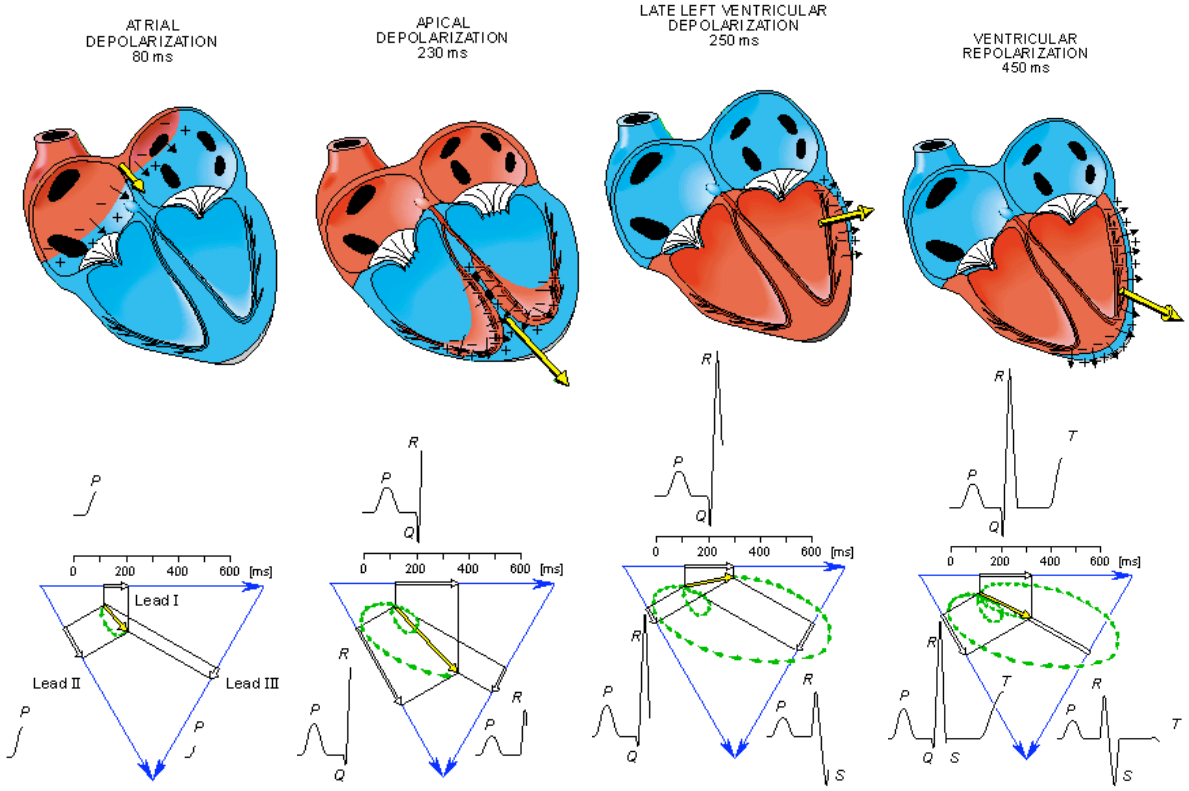

Figure 2.3: Etapes de la progression de la contraction cardiaque et composantes correspondantes d'un électrocardiogramme (d'après Bembook [MP95]).

2.3.1 Petite circulation

Le myocarde étant dans sa phase de décontraction, la pression sanguine est plus élevée dans les artères que dans le cœur en diastole, de sorte que les valves sigmoides (valves pulmonaire et aortique) sont fermées, entre-temps les oreillettes se remplissent de sang provenant des veines. Le sang qui vient de l'oreillette droite passe, à travers la valve triscupide, dans le ventricule droit. Les contractions du ventricule droit envoient le sang dans l'artère pulmonaire qui pénètre dans les poumons et s'y ramifie en capillaires pulmonaires. Ces derniers se rassemblent en veines pulmonaires qui aboutissent à l'oreillette gauche. Le cycle est ainsi bouclé.

2.3.2 Grande circulation

Quand la stimulation contractile atteint le myocarde, ceci provoque la contraction des ventricules: cette systole ferme les valves tricuspide et mitrale. La pression dans les ventricules devient tellement élevée que les valves sigmoides s'ouvrent: le sang afflue dans les artères. En particulier, le sang sortant du ventricule gauche passe à travers la valve aortique vers l'aorte. Les organes sont généralement vascularisés par une artère provenant d'une ramification de l'aorte. Le sang qui pénètre dans le foie provient de deux sources: l'artère hépatique apporte du sang oxygéné par la circulation systémique, et la veine porte hépatique apporte du sang carbonaté mais riche en nutriments, provenant des organes digestifs. Le système porte hépatique rassemble le sang veineux venant de

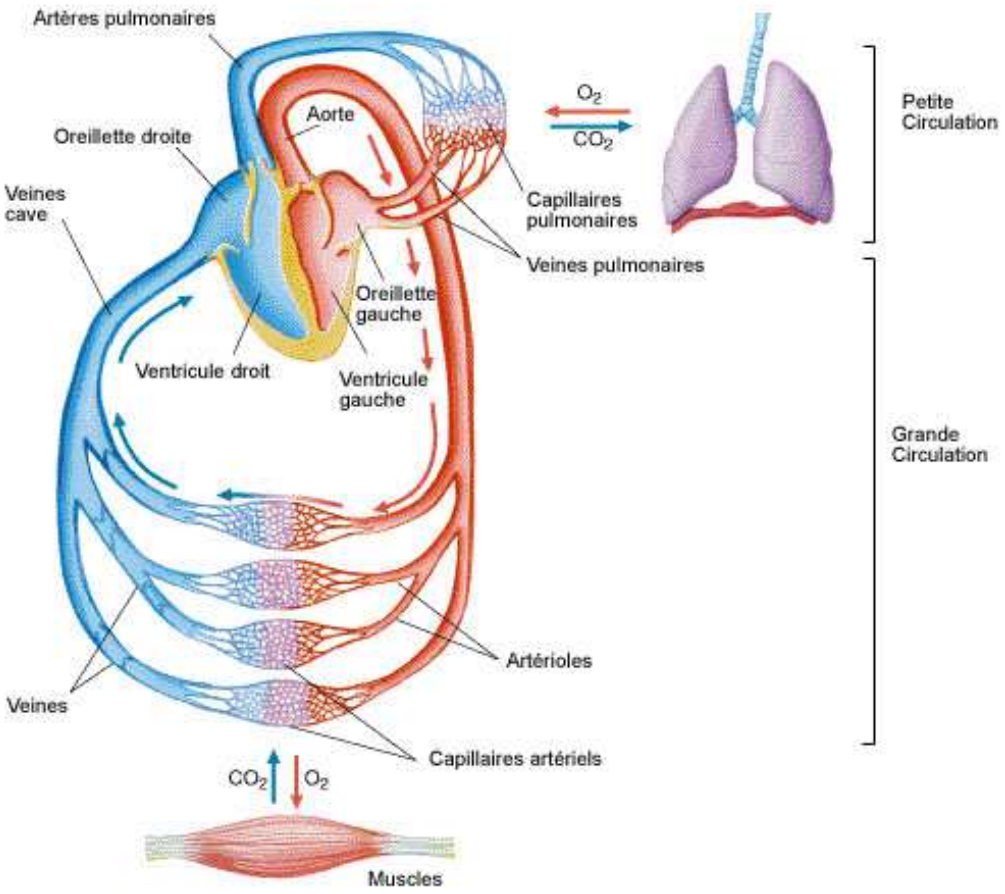

Figure 2.4: Représentation schématique de la petite et la grande circulations sanguines: Les flèches rouges designe le sens de circulation du sang oxygéné et les flèches bleus designe le sens de circulation du sang riche en CO_2. Source: `http://www-rocq.inria.fr/Marc.Thiriet/Glosr/Bio/AppCircul/Circul.html`

l'estomac (via la veine gastrique), du pancréas (via la veine pancréatique), de l'intestin (via les veines mésentériques) et aussi de la rate (via la veine splénique). Le foie contrôle les nutriments ainsi apportés, emmagasine le glucose (sous forme de glycogène) et filtre certaines substances nocives comme l'alcool ou la caféine ou la théobromine du cacao. Enfin, le sang quitte le foie par la veine sus-hépatique, qui se jette dans la veine cave inférieure. De façon comparable, d'autres veines provenant de membres supérieurs, de la tête et du cou se jettent semblablement, dans la veine cave supérieure. Les deux veines caves supérieure et inférieure ramènent le sang vers l'oreillette droite.

2.4 L'électrocardiogramme

2.4.1 Définition

L'électrocardiogramme est une représentation graphique de l'activité électrique du coeur. L'électrocardiographe qui est l'appareil permettant de faire un ECG, mesure la différence de potentiel entre différentes positions de la surface du corps. Ce qui permet d'avoir une

description non invasive de l'état du cœur. Le médecin peut visualiser ces différences de potentiel sur un écran appelé électrocardioscope. L'électrocardiogramme peut aussi être tracé sur un papier millimétré. Ce papier appelé "papier pour ECG" est tracé en petits et grands carrés de tailles respectives 1mm et 5mm (voir Figure. 2.5). Horizontalement, un petit carreau (respectivement, un grand carreau) représente 40 ms (respectivement, 200 ms) et verticalement 1 mv (respectivement, 5 mv). L'électrocardiogramme affiché sur la Figure. 2.5 représente la première dérivation de l'ECG d'un cœur en situation normale. Les différentes fluctuations qu'on regarde sur cet ECG s'appellent, dans l'ordre de gauche à droite, les ondes P, Q, R, S, T et U.

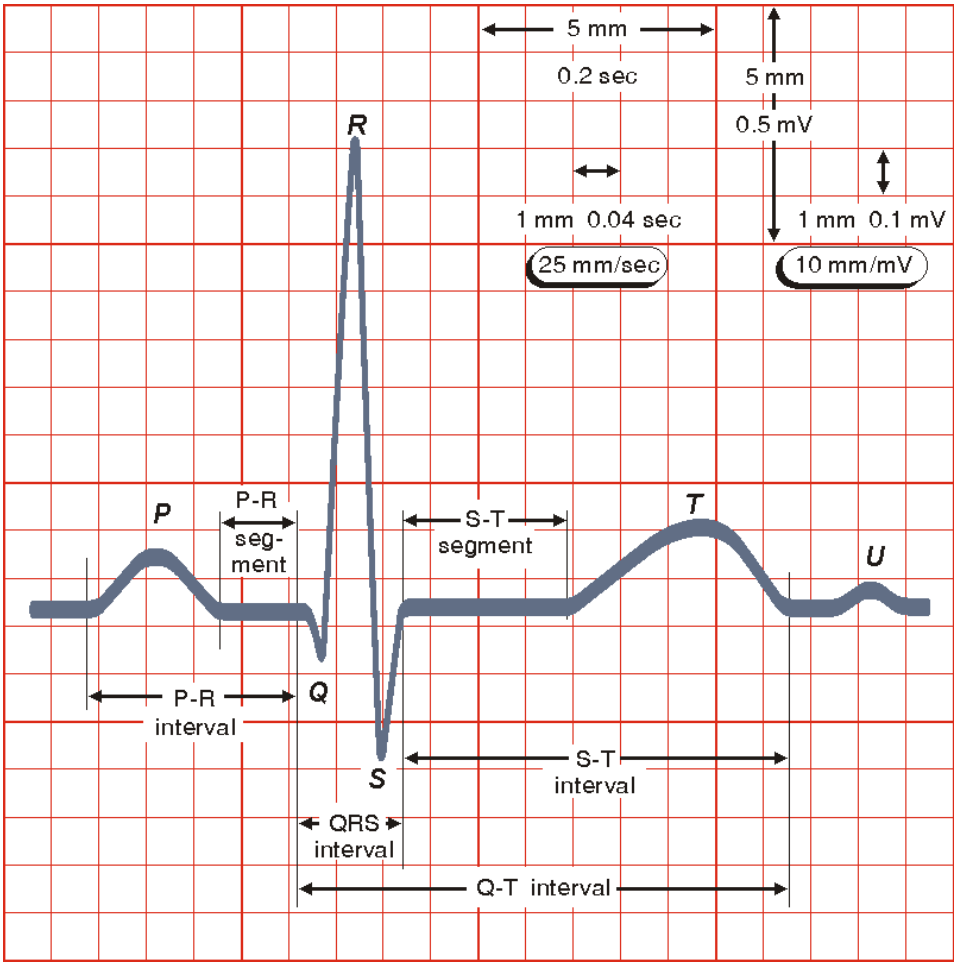

Figure 2.5: L'ECG d'un cycle cardiaque normale.

- L'onde P, représente la dépolarisation auriculaire,
- le complexe QRS, représente la dépolarisation des ventricules,
- le segment QT, représente le plateau des potentiels d'action ventriculaire,
- L'onde T, correspond à la repolarisation des ventricules,
- L'onde U, généralement absente, est provoquée par une repolarisation prolongée des cellules M ou par un facteur mécanique correspondant à la relaxation du myocarde.

2.4.2 Cadre historique

L'ECG est un outil médical récent. Son histoire a commencé à la fin du XVIII ème siècle. Au cour d'un siècle et demi les chercheurs ont trouvé la forme "idéale" de l'ECG. L'ECG qu'utilisent actuellement les cliniciens date du début du XX ème siècle.

Historiquement, la première personne qui a remarqué que le muscle bouge quand il est excité est le médecin et physicien italien Luigi Galvani. Il découvre en 1771 que les muscles d'une grenouille morte bougent lorsqu'elles sont mises en contact avec des métaux telsque le cuivre et le zinc (voir Figure. 2.6). Mais jusqu'à cette date, personne ne connaît l'origine de l'onde électrique qui traverse le corps d'un animal.

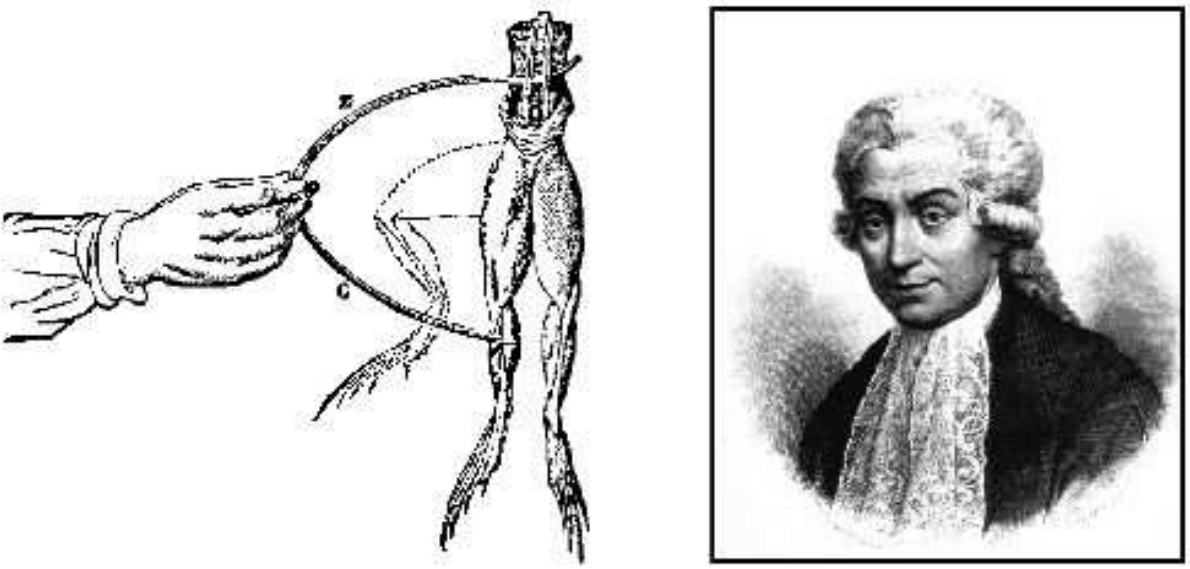

Figure 2.6: Représentation de l'expérience de Galvani, qui lui a permis de découvrir l'électricité animale (gauche). Photo de Luigi Galvani (droite). Source: Wikipedia.

Ce n'est qu'après l'invention d'un outil de mesure du signal électrique, "le Galvanomètre[1]", que les physiciens et les médecins commencent à relier les battements cardiaques à un signal électrique. En effet, le physicien italien Carlo Matteucci [Mat42], montre en 1842, pour la première fois, que chaque contraction du coeur est accompagnée par un courant électrique. Un an après, le physiologiste allemand Emil Dubois Reymond confirme les travaux de Matteucci et décrit un potentiel d'action accompagnant chaque contraction musculaire. Ce potentiel d'action a été enregistré pour la première fois en 1856 par les chercheurs allemand Rudolph von Koelliker et Heinrich Muller. Après l'invention de l'électromètre capillaire[2] par le physicien français Gabriel Lippmann, en 1872, cet appareil a été utilisé par le physiologiste français Étienne-Jules Marey [Mar76] en 1876 pour enregistrer l'activité électrique du coeur d'une grenouille. Deux ans plus tard, les physiologistes britanniques John Burden Sanderson et Frederick Page [SP76] enregistrent le courant électrique cardiaque avec l'électromètre capillaire et montrent qu'il est composé de deux phases (dépolarisation et repolarisation). Ces deux chercheurs publient en 1884 des enregistrements électriques faits sur le cœur d'une grenouille [SP84].

[1] Appareil de mesure du signal électrique inventé par Johan Salomo et Christoph Schweigger en 1821.
[2] C'est un tube de verre à colonne de mercure et d'acide sulfurique.

Trois ans après, le premier électrocardiogramme humain a été enregistré par le physiologiste britannique Augustus D. Waller de St Mary's Medical School, à Londres [Wal87]. Il est enregistré sur Thomas Goswell, un technicien du laboratoire. En 1889, le physiologiste allemand Willem Einthoven (voir Figure. 2.7)[3] démontre sa technique au Premier Congrès International de Physiologie. En 1890, G.J. Burch d'Oxford imagine une correc-

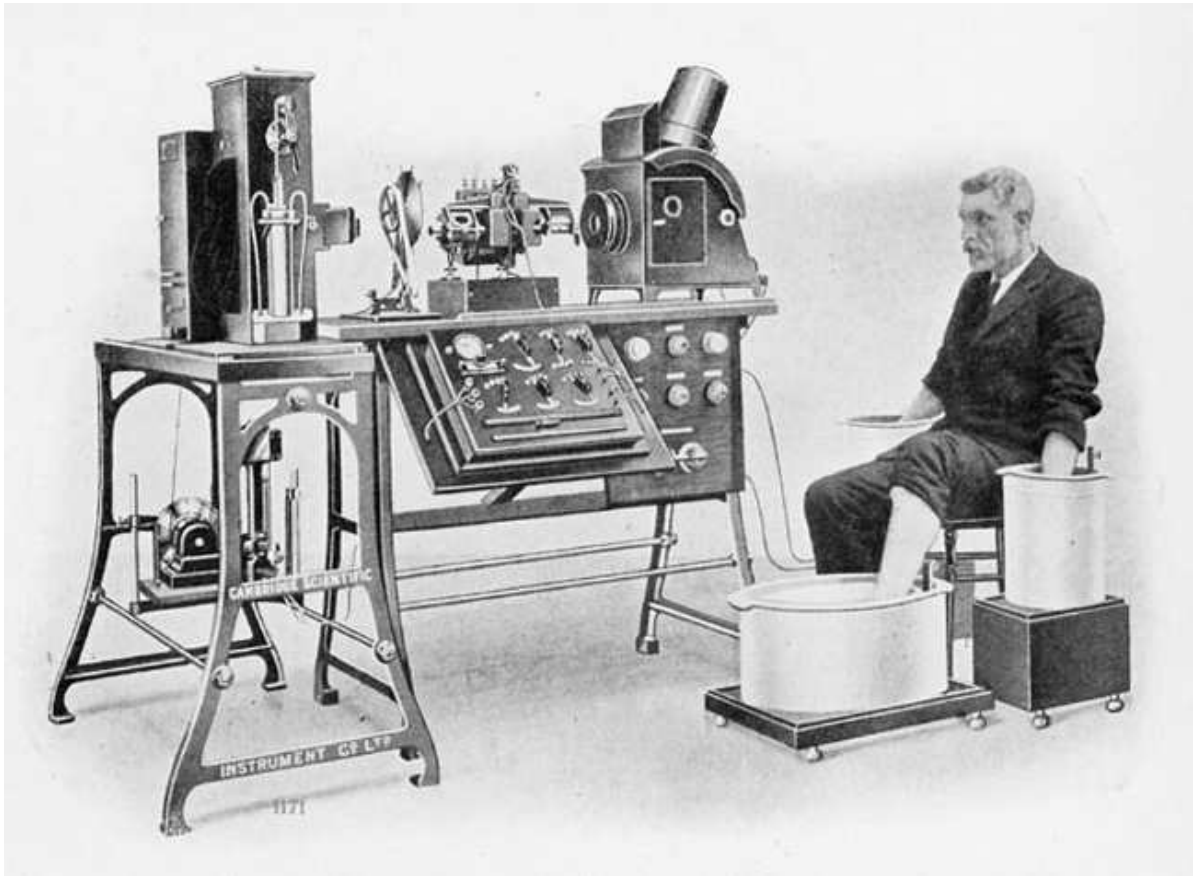

Figure 2.7: Photo de l'électrographe d'Einthoven montrant la technique qu'il a utilisé: Les deux mains et le pied gauche sont plongés dans des jarres contenant de l'eau salée. Les trois jarres sont reliées à l'appareil avec des fils électriques.

tion arithmétique pour les observations de fluctuation de l'électromètre. Celui-ci permet de voir le vrai tracé de l'électrocardiogramme [Bur90].

Cinq ans plus tard, Einthoven, utilisant un électromètre amélioré ainsi qu'une formule de correction développée indépendamment par Burch, met en évidence cinq déflexions qu'il appelle P, Q, R, S and T [Ein95].

En 1901, Einthoven modifie cet enregistreur pour produire des électrocardiogrammes. Son appareil pèse 300 kg (voir Figure. 2.7) [Ein01]. L'année qui suit, Einthoven publie le premier électrocardiogramme enregistré avec cet appareil. Il publie, en 1906, la première classification des électrocardiogrammes normaux et anormaux: Hypertrophies ventriculaires gauches et droites, hypertrophies auriculaires gauches et droites, ondes U, éléments sur le QRS, contractions ventriculaires prématurées, bigéminisme ventriculaire, flutter auriculaire et bloc auriculo-ventriculaire complet [Ein06]. Six ans plus tard, il décrit un

[3]Source: wikipedia.

triangle équilatéral formé par les dérivations standards D1, D2, D3, appelé plus tard "triangle d'Einthoven". C'est aussi la première fois qu'il utilise dans un article l'abréviation anglo-saxonne de l'électrocardiogramme EKG (ECG). En 1920, Hubert Mann du laboratoire de cardiologie de l'hôpital du Mont Sinaï de New York, décrit la dérivation d'un "monocardiogramme" plus tard appelé "vectocardiogramme" [Man20]. En 1924, Willem Einthoven obtient le prix Nobel pour l'invention de l'électrocardiographe.

L'American Heart Association et The Cardiac Society de Grande Bretagne définissent, en 1938, les positions standards des dérivations précordiales V1, V2,...,V6 [RPW$^+$38]. Enfin, en 1942, Emanuel Goldberger ajoute aux dérivations frontales d'Einthoven les dérivations aVR, aVL, aVF. Ceci lui permet, avec les 6 dérivations précordiales V1,V2,...,V6, de réaliser le premier électrocardiogramme sur 12 dérivations, qui est encore utilisé aujourd'hui.

Chapter 3

Modèles mathématiques

On peut distinguer deux échelles de modélisation en électrophysiologie cardiaque. On trouve d'une part des modèles s'intéressant à l'échelle microscopique, dont le but est de produire une description fine de ce qui est à l'origine de l'onde électrique dans les cellules. On trouve d'autre part des modèles à l'échelle de l'organe, dont le but est de décrire la propagation de l'onde électrique dans le cœur et le reste du corps. Dans ce qui suit, nous proposons de présenter les éléments principaux de ces deux catégories. Nous avons choisi de nous limiter aux approches basées sur des équations différentielles et aux dérivées partielles (nous ne présenterons donc pas de modèles basés sur des automates cellulaires).

3.1 Modèle OD: échelle cellulaire

Les cellules (en particulier les cellules cardiaques) sont entourées par une membrane limitant l'unité cellulaire, cette membrane est percée par des protéines dont le rôle est d'assurer le flux des différentes substances intra et extra-cellulaires à travers la membrane (voir figure 3.1).

Ces protéines peuvent avoir un comportement passif ou actif selon l'état de la cellule, leur activité permet le passage de certaines substances chimiques à l'intérieur ou à l'extérieur de la cellule, ce qui provoque la dépolarisation ou la répolarisation cellulaire. On peut classifier le processus du transport ionique en trois modes de transfert: les canaux ioniques, les pompes et les échangeurs.

3.1.1 Les canaux ioniques

Un canal ionique (Figure 3.2, gauche) laisse passer dans un sens donné une espèce conformément à son gradient électrochimique. Son comportement est simplement modélisé par une résistance. Un canal ionique est cependant actif dans la mesure où sa conductivité est variable selon les conditions extérieures: en particulier il peut être fermé.

La dépolarisation de la cellule est généralement causée par l'ouverture d'un canal ionique. Ce canal est celui du sodium Na^+. Son ouverture se fait dans le sens de son gradient électrochimique, par conséquent, il ne nécessite aucun apport d'énergie de

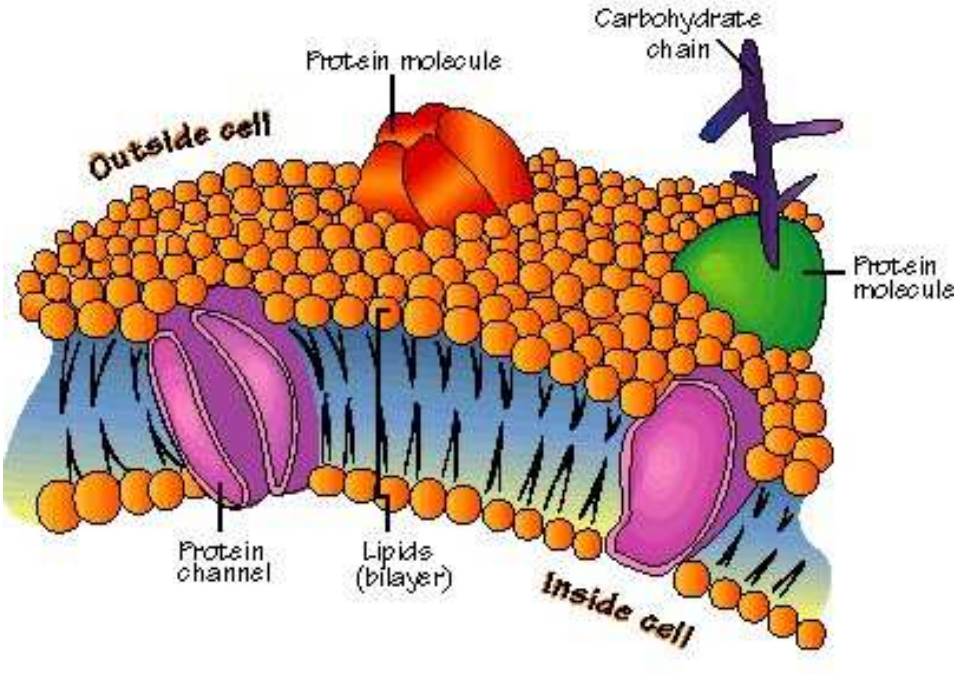

Figure 3.1: Représentation schématique de la membrane cellulaire. Source: `www.bio-energetik.ca/images/cell_membrane.jpg`

la cellule. Ce genre de transport ionique est appelé transport passif. L'ouverture d'un canal de sodium provoque la création d'un courant ionique i_{Na} de l'ordre du pico-ampère (pA). Ce courant est proportionnel au gradient électrochimique du sodium $(V_{\mathrm{m}} - E_{Na})$ et à une variable qui représente l'ouverture et la fermeture de ce canal G_{Na}. Le potentiel transmembranaire V_{m} est la différence entre le potentiel intra et extra-cellulaire. Le potentiel électrochimique E_{Na} est donné par la loi de Nernst

$$E_{Na} = \frac{RT}{F} ln \frac{[Na]_{\mathrm{e}}}{[Na]_{\mathrm{i}}}, \tag{3.1.1}$$

où $[Na]_{\mathrm{e}}$ (respectivement $[Na]_{\mathrm{i}}$) est la concentration extra-cellulaire (respectivement intra-cellulaire) de l'ion sodium Na^+. Les constantes R, T et F indiquent respectivement, la constante de gaz parfait, la temperature et la constante de Faraday.

Le courant i_{Na} d'ions Na^+ à travers ce canal, décrit par Hodgkin et Huxley (voir [HH52]) est donné par

$$i_{Na} = G_{Na}(V_{\mathrm{m}} - E_{Na}). \tag{3.1.2}$$

Ce canal ionique n'est pas toujours ouvert. Sa fermeture et son ouverture suivent la loi de conductivité des portes des canaux ioniques G_{Na} qui peut être réprésentée de la manière suivante:

$$G_{Na} = \overline{G}_{Na} H, \tag{3.1.3}$$

où $\overline{G}_{Na}$ est la conductivité maximale du canal ionique représentant son ouverture maximale. La fonction H est comprise entre 0 et 1, elle est donnée par,

$$H = H(V_{\mathrm{m}}, [Na_{\mathrm{i}}], [Na_{\mathrm{e}}]...). \tag{3.1.4}$$

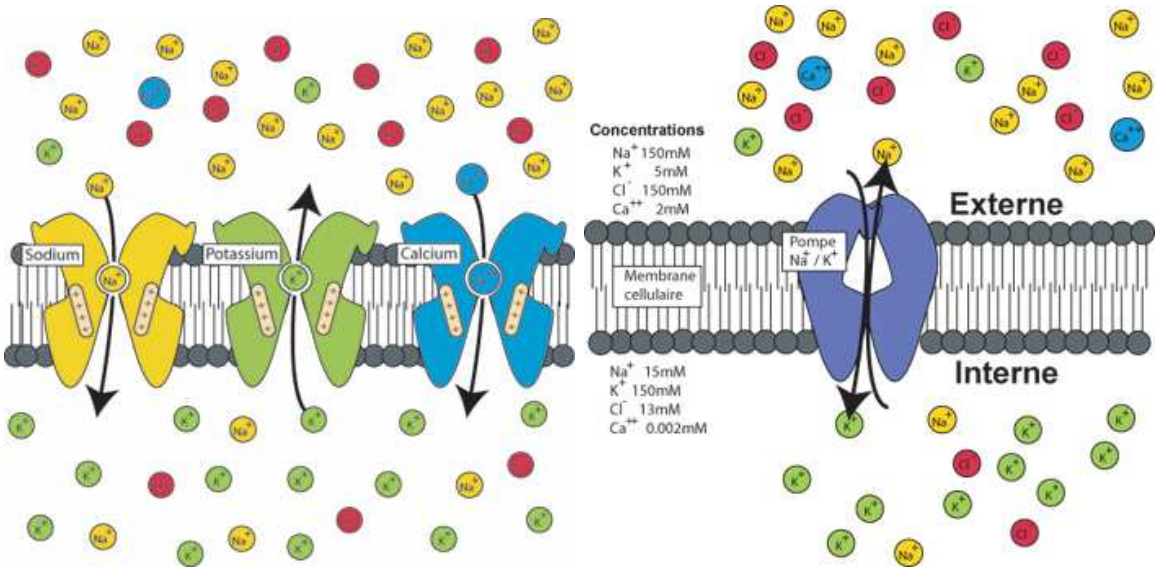

Figure 3.2: Représentation schématique des canaux ioniques Na^+, K^+ et Ca^{2+} (gauche) et de la pompe Na^+/K^+ (droite). Source: `http://www.apteronote.com/revue/neurone/article_79.shtml`

Le canal ionique Na^+ a été le premier élément de la modélisation de l'activité électrique de la membrane cellulaire. Hodgkin et Huxley ont proposé en 1952 le premier modèle de potentiel d'action. Dans leur article [HH52], ils proposent trois types de courants membranaires :

- Le courant I_{Na} responsable de la dépolarisation cellulaire. Il est dû, comme modélisé ci-dessus, à l'ouverture du canal du sodium.

- Le courant I_K qui provoque la repolarisation de la cellule est dû à un autre type de transport ionique: les pompes ioniques (voir 3.1.2)

- I_L est le courant qui représente le courant provenant des autres types d'espèces chimiques.

3.1.2 Les pompes

Contrairement aux canaux ioniques les pompes peuvent faire entrer ou sortir des espèces chimiques dans le sens contraire de leur gradient électrochimique. Ce sont les protéines (voir Figure 3.2) qui font cette fonction grâce au métabolisme cellulaire, et plus précisément par les molécules d'Adénosine Tri Phosphate (ATP).

L'exemple le plus intéressant des pompes est celui de la pompe Na/K. Cette pompe permet de faire rentrer deux ions potassium K^+ contre trois ions sodium Na^+ qui sortent en même temps. Au repos, la cellule est fortement concentrée en potassium et faiblement concentrée en sodium, pendant la dépolarisation les canaux ioniques s'ouvrent

pour faire entrer le sodium et faire sortir le potassium. Une fois dépolarisée, la cellule est enrichie en sodium et appauvrie en potassium, l'activation de la pompe Na/K permet à la cellule de retrouver ses concentrations initiales en sodium et en potassium.

Lors de son activation la pompe Na/K crée un courant électrique noté $i_{Na/K}$. Ce courant est une fonction du potentiel transmembranaire, des concentrations de potassium de sodium ainsi que des molécules ATP:

$$i_{Na/K} = F(V_{\mathrm{m}}, [Na]_{\mathrm{i,e}}, [K]_{\mathrm{i,e}}, \mathrm{ATP}) \tag{3.1.5}$$

Comme ce courant est dû au déplacement de deux ions à travers la membrane on aura:

$$i_{Na/K} = i_{Na,Na/K} + i_{K,Na/K} \tag{3.1.6}$$

avec

$$i_{Na,Na/K} = 3i_{Na/K}; \qquad i_{K,Na/K} = -2i_{Na/K}. \tag{3.1.7}$$

3.1.3 Les échangeurs

Comme l'indiquent leurs noms, les échangeurs permettent de transporter les ions et de les échanger entre les milieux intra et extra-cellulaires. Le ions sont échangés en utilisant une énergie provenant du gradient élecrochimique d'un autre type d'ion. L'existence de ce gradient électrochimique est due à la dépolarisation cellulaire réalisée par la pompe Na/K. On peut donc considérer que cette énergie est propre à la cellule. L'exemple typique déchangeur de ce genre de transport ionique est l'échangeur Na^+/Ca^{2+}. Ce transporteur permet aux concentrations des ions Na^+ et Ca^{2+} de retrouver leurs conditions initiales.

3.1.4 Modélisation de la membrane cellulaire cardiaque

Modèles physiologiques

Dix ans après la publication du modèle de Hodgkin et Huxley, en 1962, Noble propose une modification de ce modèle afin de produire le premier modèle de l'activité électrique de la membrane d'une cellule cardiaque. Ce modèle a été adapté aux cellules du réseau de Purkinje et des cellules pacemakers (cellules auto-excitables) [Nob62]. La modélisation des cellules ventriculaires a été introduite par Beeler et Reuter [BR77], en 1977. En 1985, Di Francesco et Noble [DFN85] proposent un modèle qui prend en compte les pompes ioniques, ce qui permet aux différentes espèces chimiques telles que le sodium le potassium et le calcium de retrouver leurs états stables. Ceci qui n'était pas pris en considération dans les modèles précédents puisqu'ils se basaient sur la modélisation des canaux ioniques.

Ces modèles ont été améliorés par Luo et Rudy une première fois en 1991(Luo-Rudy I [LR91]) et une deuxième fois en 1994 (Luo-Rudy II [LR94]). Le développement de ces modèles continue et l'adaptaion à des conditions spécifiques telles que le type de la pathologie ou l'espèce du sujet étudié est devenue le but des études récentes.

Citons à titre d'exemple les travaux de Shaw et Rudy [SR97] qui ont étudié l'effet d'une ischémie sur la durée du potentiel d'action, les travaux de Zeng *et al.* [ZLRR95] qui ont développé un modèle de cellule ventriculaire d'un cochon. Des travaux plus récents sont destinés à la modélisation du potentiel d'action des ventricules humains (voir par exemple [TTNNP04, BOCF08]).

Modèles phénoménologiques

Les modèles cités ci-dessus sont tous des modèles physiologiques représentant les échanges ioniques à travers la membrane cellulaire. D'autres types de modèles, appelés les modèle phénoménologiques décrivent une approximation des canaux ioniques. Ces modèles permettent de décrire le phénomène d'exitabilité tout en gardant une faible complexité. Avec seulement deux variables d'état, le potentiel d'action V_{m} et une variable de recouvrement w, ces modèles sont capables de reproduire la dépolarisation et la repolarisation cellulaire. Le premier modèle phénoménologique décrivant un potentiel d'action est celui de Fizhugh et Nagumo [Fit61, NAY62] date depuis 1961. D'autres versions de ce modèle adaptées aux cellules cardiaques ont été développées par Roger et McCulloch [RM94], Aliev et Panfilov [AP96] ou récement le modèle de Mitchell et Schaeffer [MS03].

- FitzHugh-Nagumo:

$$I_{\mathrm{ion}}(v,w) = kv(v-a)(v-1)+w, \quad g(v,w) = -\epsilon(\gamma v - w).$$

- Roger-McCulloch:

$$I_{\mathrm{ion}}(v,w) = kv(v-a)(v-1)+vw, \quad g(v,w) = -\epsilon(\gamma v - w).$$

- Aliev-Panfilov:

$$I_{\mathrm{ion}}(v,w) = kv(v-a)(v-1)+vw, \quad g(v,w) = \epsilon(\gamma v(v-1-a)+w).$$

- Mitchell-Schaeffer:

$$I_{\mathrm{ion}}(v,w) = \frac{w}{\tau_{\mathrm{in}}}v^2(v-1) - \frac{v}{\tau_{\mathrm{out}}},$$
$$g(v,w) = \begin{cases} \dfrac{w-1}{\tau_{\mathrm{open}}} & \text{si } v \le v_{\mathrm{gate}}, \\ \dfrac{w}{\tau_{\mathrm{close}}} & \text{si } v > v_{\mathrm{gate}}. \end{cases}$$

Les paramètres $0 < a < 1$, k, ϵ, γ, $\tau_{\mathrm{in}} < \tau_{\mathrm{out}} < \tau_{\mathrm{open}}$, τ_{close} and $0 < v_{\mathrm{gate}} < 1$ sont des constantes positives.

3.2 Le modèle 3D: échelle macroscopique

La modélisation de l'activité électrique du cœur à l'échelle de l'organe a évolué depuis l'invention de l'appareil de mesure de l'ECG par Einthoven. Ce dernier et Waller ont

proposé le premier modèle en électrophysiologie cardiaque à l'échelle macroscopique en considérant que le cœur se comporte comme un dipôle et que l'ECG n'est que la projection d'un vecteur cardiaque sur les trois vecteurs formant le triangle d'Einthoven. Le vecteur cardiaque est défini comme étant le moment dipolaire du champ électrique du cœur, il a été supposé, dans un premier temps, fixe puis, mobile suivant le front de l'onde de dépolarisation. Nous renvoyons à [MP95] pour plus de détails sur cet aspect de modélisation. L'approche "milieu continu" de la modélisation de la propagation de l'onde électrique dans le cœur a été introduite par Schmitt [Sch69] en 1969. Cette approche appelée le modèle *bidomaine* a été fomulée mathématiquement par Tung [Tun78] en 1978. Depuis sa formulation (voir la section 3.2.1), ce modèle est devenu la référence adoptée par la majorité des chercheurs pour la modélisation de l'activité électique du cœur. D'autres travaux concernent uniquement la propagation du front d'onde de dépolarisation sur le myocarde. Ces travaux utilisent le modèle *eikonal* [CFGPT98b, CFGPT98a] ou [Tom00]. Ce modèle permet de suivre le front d'onde de dépolarisation (donner la position du front d'onde à un instant donné) sans faire face au lourd calcul des équations du modèle bidomaine. Nous renvoyons aux travaux de Colli Franzone *et al.* [CFG93, CFGPT98a, CFGPT98b, CFGT04] pour plus de détails sur ces modèles.

3.2.1 Le modèle bidomaine

Nous introduisons ici le modèle bidomaine pour représenter l'activité électrique du cœur [Tun78, CFS02, SLC$^+$06, PBC05, Lin99, SLC$^+$06, Pie05]. Ce modèle est établi à partir des bilans électriques au niveau d'une cellule cardiaque. A l'échelle microscopique, le tissu cardiaque est composé de deux milieux distincts : le milieu intra-cellulaire, composé des cellules musculaires cardiaques, et le milieu extra-cellulaire, composé du reste du volume cardiaque. Nous notons respectivement $\Omega_{\mathrm{H,i}}$, $\Omega_{\mathrm{H,e}}$ et Ω_{H} le domaine intra-cellulaire, le domaine extra-cellulaire et le domaine total occupé par le cœur (voir la Figure 3.3). Ainsi, nous avons:

$$\overline{\Omega_{\mathrm{H}}} = \overline{\Omega_{\mathrm{H,i}}} \cup \overline{\Omega_{\mathrm{H,e}}}.$$

Notons $\boldsymbol{j}_{\mathrm{i}}$, $\boldsymbol{j}_{\mathrm{e}}$ et u_{i}, u_{e} respectivement la densité de courant et le potentiel électrique intra- et extra-cellulaire. Puisque les milieux intra- et extra-cellulaire sont assimilés à des conducteurs passifs à l'état quasi-statique, ces termes sont reliés par la loi d'Ohm:

$$\begin{aligned} \boldsymbol{j}_{\mathrm{i}} &= -\boldsymbol{\sigma}_{\mathrm{i}} \boldsymbol{\nabla} u_{\mathrm{i}}, \\ \boldsymbol{j}_{\mathrm{e}} &= -\boldsymbol{\sigma}_{\mathrm{e}} \boldsymbol{\nabla} u_{\mathrm{e}}, \end{aligned} \tag{3.2.8}$$

où $\boldsymbol{\sigma}_{\mathrm{i}}$ et $\boldsymbol{\sigma}_{\mathrm{e}}$ sont les tenseurs de conductivité des milieux intra et extra-cellulaires. Les milieux intra et extra-cellulaires sont séparés par une membrane $\Gamma_{\mathrm{m}} = \partial\Omega_{\mathrm{H,i}} \cap \partial\Omega_{\mathrm{H,e}}$ et nous définissons I_{m} la densité surfacique de courant sur Γ_{m} mesurée de $\Omega_{\mathrm{H,i}}$ vers $\Omega_{\mathrm{H,e}}$. La conservation de la charge implique que, sur Γ_{m},

$$I_{\mathrm{m}} = \boldsymbol{j}_{\mathrm{i}} \cdot \boldsymbol{n} = -\boldsymbol{j}_{\mathrm{e}} \cdot \boldsymbol{n}, \tag{3.2.9}$$

où $\boldsymbol{n}$ est la normale unitaire extérieure à $\Omega_{\mathrm{H,i}}$.

La membrane cellulaire se comporte à la fois comme une résistance et une capacité. En effet, d'une part, la membrane est formée d'une double couche de lipides isolante

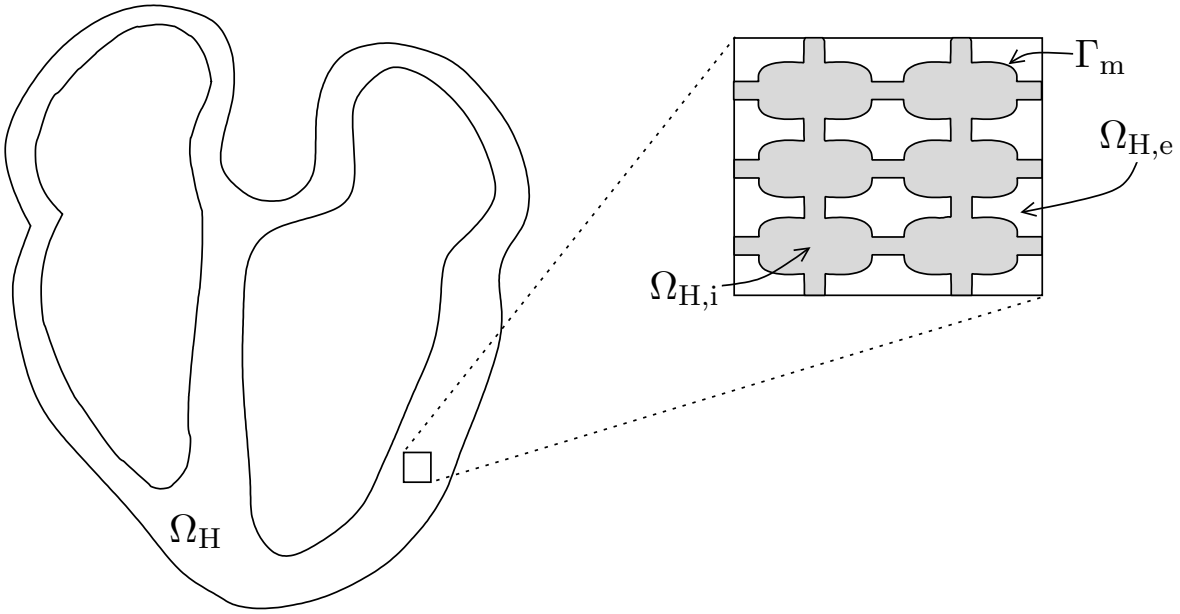

Figure 3.3: Coupe du cœur avec les domaines intra et extra-celullaire : $\Omega_{\mathrm{H,i}}$ et $\Omega_{\mathrm{H,e}}$

ce qui lui confère son comportement capacitif. D'autre part, le caractère résistif est lié à des protéines membranaires qui transportent différents types d'ions à travers la membrane (voir Figure 3.1). Celle-ci est donc traversée par un courant ionique I_{ion}. Ainsi, la densité surfacique de courant peut s'écrire

$$I_{\mathrm{m}} = I_{\mathrm{ion}} + C_{\mathrm{m}} \frac{\partial V_{\mathrm{m}}}{\partial t} + i_{\mathrm{app}}, \tag{3.2.10}$$

où C_{m} représente la capacité par unité de surface de la membrane, i_{app} est le courant appliqué (ou exterieur) et V_{m} représente le potentiel transmembranaire qui est défini par

$$V_{\mathrm{m}} = u_{\mathrm{i}} - u_{\mathrm{e}}. \tag{3.2.11}$$

La définition de la fonction I_{ion} dépend des modèles ionique utilisés (voir [SLC+06, PBC05] et les réferences qu'ils contiennent). Ces modèles peuvent être de type phénomènologique ([Fit61, vCD80, FK98, MS03]) ou de type physiologique ([BR77, LR91, LR94, NVKN98, DS05]). Dans les deux cas, le courant ionique dépond de V_{m} et d'un champs de variables qu'on note $\boldsymbol{w}$, on a donc $I_{\mathrm{ion}} = I_{\mathrm{ion}}(V_{\mathrm{m}}, \boldsymbol{w})$. Le champs de variables $\boldsymbol{w}$ représente les concentrations de différentes espèces chimiques et des variables représentant l'ouvertures ou la fermetures des certaines portes de canaux ionniques. Cette représentation est généralement donnée par le système dynamique suivant

$$\partial_t \boldsymbol{w} + \boldsymbol{g}(V_{\mathrm{m}}, \boldsymbol{w}) = 0,$$

où $\boldsymbol{g}$ est un champs de fonctions ayant la même dimension que $\boldsymbol{w}$, cette dimension est généralement réduite à un dans le cas où le modèle ionique utilisé est phénoménologique.

Ensuite, une étape d'homogénéisation permet de passer d'un point de vue microscopique et discret à une représentation continue du courant électrique. Chaque variable définie au niveau discret sur les domaines $\Omega_{\mathrm{H,i}}$ ou $\Omega_{\mathrm{H,e}}$ est remplacée par sa valeur moyenne définie sur le domaine global Ω_{H}. Cette démarche permet de prolonger les

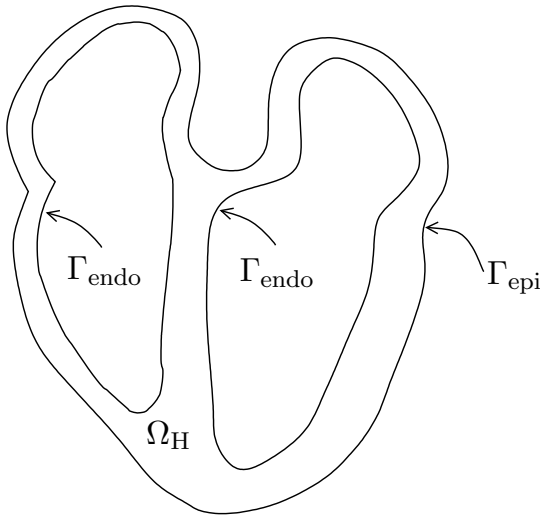

Figure 3.4: Coupe du domaine cardiaque : Ω_{H}

équations satisfaites sur les domaines discrets au domaine global Ω_{H}. Pour des détails sur le processus d'homogénéisation, nous renvoyons à l'article [KN93] ou à la thèse [Pie05]. L'équation homogenéisée associée à (3.2.9) est:

$$\operatorname{div}(\boldsymbol{j}_{\text{i}} + \boldsymbol{j}_{\text{e}}) = 0, \quad \text{dans} \quad \Omega_{\text{H}}. \tag{3.2.12}$$

Cette équation peut être réécrite en fonction de u_{i} et u_{e} d'après (3.2.8)

$$\operatorname{div}(\boldsymbol{\sigma}_{\text{i}} \boldsymbol{\nabla} u_{\text{i}} + \boldsymbol{\sigma}_{\text{e}} \boldsymbol{\nabla} u_{\text{e}}) = 0, \quad \text{dans} \quad \Omega_{\text{H}},$$

ou, en termes de V_{m} et u_{e},

$$\operatorname{div}\left((\boldsymbol{\sigma}_{\text{i}} + \boldsymbol{\sigma}_{\text{e}}) \boldsymbol{\nabla} u_{\text{e}}\right) = -\operatorname{div}(\boldsymbol{\sigma}_{\text{i}} \boldsymbol{\nabla} V_{\text{m}}), \quad \text{dans} \quad \Omega_{\text{H}}, \tag{3.2.13}$$

Finalement, l'équation (3.2.10) combinée avec (3.2.9) devient, après homogénéisation,

$$A_{\text{m}} \left(C_{\text{m}} \frac{\partial V_{\text{m}}}{\partial t} + I_{\text{ion}}(V_{\text{m}}, \boldsymbol{w}) \right) = \operatorname{div}(\boldsymbol{\sigma}_{\text{i}} \boldsymbol{\nabla} u_{\text{i}}) + I_{\text{app}}, \quad \text{dans} \quad \Omega_{\text{H}}.$$

ou en termes de V_{m} et u_{e},

$$A_{\text{m}} \left(C_{\text{m}} \frac{\partial V_{\text{m}}}{\partial t} + I_{\text{ion}}(V_{\text{m}}, \boldsymbol{w}) \right) - \operatorname{div}(\boldsymbol{\sigma}_{\text{i}} \boldsymbol{\nabla} V_{\text{m}}) = \operatorname{div}(\boldsymbol{\sigma}_{\text{i}} \boldsymbol{\nabla} u_{\text{e}}) + I_{\text{app}}, \quad \text{dans} \quad \Omega_{\text{H}}. \tag{3.2.14}$$

Ici, A_{m} est une constante géométrique représentant le taux moyen de surface membranaire par unité de volume et C_{m} est la capacité membranaire. La fonction I_{ion}, représente le courant dû aux échanges ioniques et I_{app} le courant appliqué.

Le bord $\partial\Omega_{\text{H}}$ du domaine Ω_{H}, c'est-à-dire la frontière entre le cœur et la région extra-cardiaque (le tissu thoracique et le sang intra-cardiaque), est divisé en deux parties : une interne, l'endocarde notée Γ_{endo}, et une externe, l'épicarde notée Γ_{epi} (voir la Figure 3.4). Nous définissons $\Sigma \stackrel{\text{def}}{=} \Gamma_{\text{endo}} \cup \Gamma_{\text{epi}}$. Au niveau cellulaire, on observe expérimentalement que le courant intra-cellulaire $\boldsymbol{j}_{\text{i}}$ ne se propage pas à l'extérieur du cœur (voir [Pag62]). Par conséquent, sur le bord du cœur on impose:

$$\boldsymbol{\sigma}_{\text{i}} \boldsymbol{\nabla} u_{\text{i}} \cdot \boldsymbol{n} = 0, \quad \text{sur} \quad \Sigma, \tag{3.2.15}$$

avec $\boldsymbol{n}$ la normale unitaire extérieure sur $\partial\Omega_{\mathrm{H}}$. Cette equation a été proposée par Tung [Tun78] et confirmée par Krassowska [KN94]. D'après (3.2.11), cette condition s'écrit, en terme de V_{m} et u_{e}

$$\boldsymbol{\sigma}_{\mathrm{i}}\boldsymbol{\nabla}u_{\mathrm{e}}\cdot\boldsymbol{n}=-\boldsymbol{\sigma}_{\mathrm{i}}\boldsymbol{\nabla}V_{\mathrm{m}}\cdot\boldsymbol{n},\quad\text{sur}\quad\Sigma. \tag{3.2.16}$$

Enfin, lorsque l'on suppose que le cœur est électriquement isolé du milieu environnant (pas de couplage avec le thorax) on a

$$\boldsymbol{\sigma}_{\mathrm{e}}\boldsymbol{\nabla}u_{\mathrm{e}}\cdot\boldsymbol{n}=0,\quad\text{sur}\quad\Sigma. \tag{3.2.17}$$

Cette condition est adoptée dans la littérature pour tous les travaux basés sur l'étude du cœur isolé. En combinant (3.2.13)-(3.2.17), on obtient le *modèle bidomaine* dit *isolé*:

$$\begin{cases} A_{\mathrm{m}}\left(C_{\mathrm{m}}\dfrac{\partial V_{\mathrm{m}}}{\partial t}+I_{\mathrm{ion}}(V_{\mathrm{m}},\boldsymbol{w})\right)-\operatorname{div}(\boldsymbol{\sigma}_{\mathrm{i}}\boldsymbol{\nabla}V_{\mathrm{m}})=\operatorname{div}(\boldsymbol{\sigma}_{\mathrm{i}}\boldsymbol{\nabla}u_{\mathrm{e}})+I_{\mathrm{app}},\quad\text{dans}\quad\Omega_{\mathrm{H}},\\ \operatorname{div}\left((\boldsymbol{\sigma}_{\mathrm{i}}+\boldsymbol{\sigma}_{\mathrm{e}})\boldsymbol{\nabla}u_{\mathrm{e}}\right)=-\operatorname{div}(\boldsymbol{\sigma}_{\mathrm{i}}\boldsymbol{\nabla}V_{\mathrm{m}}),\quad\text{dans}\quad\Omega_{\mathrm{H}},\\ \partial_t\boldsymbol{w}+\boldsymbol{g}(V_{\mathrm{m}},\boldsymbol{w})=0,\quad\text{dans}\quad\Omega_{\mathrm{H}},\\ \boldsymbol{\sigma}_{\mathrm{i}}\boldsymbol{\nabla}V_{\mathrm{m}}\cdot\boldsymbol{n}=-\boldsymbol{\sigma}_{\mathrm{i}}\boldsymbol{\nabla}u_{\mathrm{e}}\cdot\boldsymbol{n},\quad\text{sur}\quad\Sigma,\\ (\boldsymbol{\sigma}_{\mathrm{i}}+\boldsymbol{\sigma}_{\mathrm{e}})\boldsymbol{\nabla}u_{\mathrm{e}}\cdot\boldsymbol{n}=-\boldsymbol{\sigma}_{\mathrm{i}}\boldsymbol{\nabla}V_{\mathrm{m}}\cdot\boldsymbol{n},\quad\text{sur}\quad\Sigma. \end{cases} \tag{3.2.18}$$

3.3 Modèle du thorax

Un des objectifs de ce travail est de simuler un électrocardiogramme, ceci consiste à mesurer des différences de potentiel sur la surface du corps humain. Nous avons donc besoin de coupler le modèle du cœur avec un modèle électrique du tissu environnant. Le domaine thoracique est noté Ω_{T} (voir Figure 3.5) et u_{T} désigne le potentiel dans Ω_{T}. Le thorax est considéré dans un état quasistatique (voir [MP95]), il se comporte donc comme un conducteur passif c'est-à-dire le champ électrique E_{T} dans le thorax dérive du potentiel u_{T}, $E_{\mathrm{T}}=-\boldsymbol{\nabla}u_{\mathrm{T}}$. Ainsi, d'après la loi d'Ohm, la densité volumique du courant dans le thorax noté $\boldsymbol{j}_{\mathrm{T}}$ satisfait l'équation suivante,

$$\boldsymbol{j}_{\mathrm{T}}=-\boldsymbol{\sigma}_{\mathrm{T}}\boldsymbol{\nabla}u_{\mathrm{T}},\quad\text{dans}\quad\Omega_{\mathrm{T}}, \tag{3.3.19}$$

où $\boldsymbol{\sigma}_{\mathrm{T}}$ représente le tenseur de conductivité du thorax qui est en réalité très anisotrope. Dans la suite de la thèse on néglige cet aspect anisotrope à cause de sa complexitée. En effet, et à titre d'exemple, il est difficile d'avoir une description fine de l'orientation de tout les tissus musculaires du corps humain. C'est pour cela qu'on a supposé la conductivité scalaire. Cependant on prend en compte l'hétérogénéité en distinguant trois zones dans le thorax: les poumons, le squelette et le reste du tissu [BP03] (voir Figure 3.5).

La non création de charges électriques est modélisée par une divergence nulle de la densité du courant thoracique $\boldsymbol{j}_{\mathrm{T}}$,

$$\operatorname{div}(\boldsymbol{\sigma}_{\mathrm{T}}\boldsymbol{\nabla}u_{\mathrm{T}})=0,\quad\text{dans}\quad\Omega_{\mathrm{T}}, \tag{3.3.20}$$

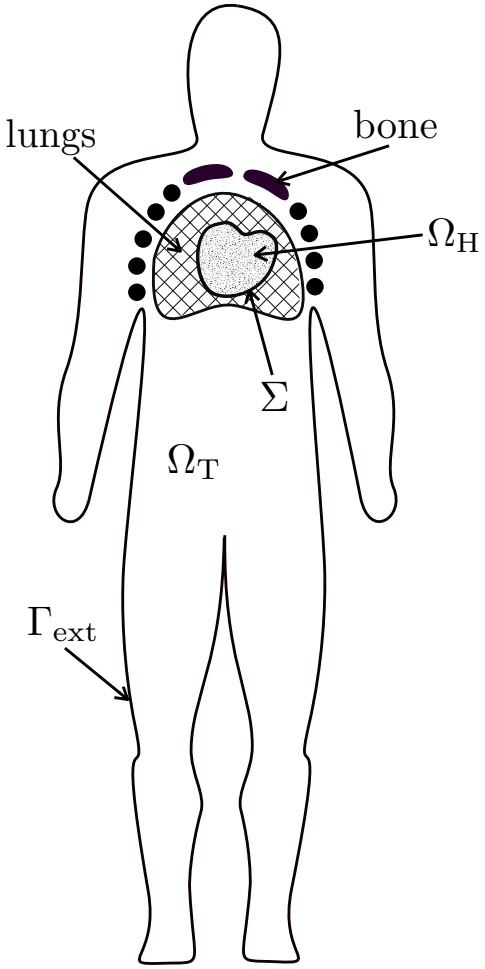

Figure 3.5: Description géomeétrique: Le domaine cardiaque Ω_H et le domaine thoracique Ω_T incluant les poumons le squelette et le reste du tissu thoracique.

Le bord du thorax Ω_T est divisé en deux parties : l'une interne Σ en contact avec le cœur et l'autre externe Γ_{ext} représentant la surface extérieure du thorax (voir la Figure 3.5). La frontière Γ_{ext} est supposée isolée, on impose donc

$$\boldsymbol{\sigma}_T \boldsymbol{\nabla} u_T \cdot \boldsymbol{n}_T = 0, \quad \text{sur} \quad \Gamma_{ext}, \tag{3.3.21}$$

avec $\boldsymbol{n}_T$ la normale unitaire extérieure sur Γ_{ext}. Ce choix est généralement adopté dans la littérature ([SLC+06, PBC05, Lin99, SLC+06, Pie05]). En revanche, d'autres conditions aux limites sur Γ_{ext} peuvent être imposées dans des conditions particulières. Notamment, en cas de modélisation d'une défibrillation, on peut imposer une différence de potentiel entre deux zones différentes du bord Γ_{ext}.

3.4 Couplage avec le thorax

Afin de transmettre les informations (potentiel et courant) du cœur au thorax et vice-versa, nous avons besoin de définir des conditions de transmission (ou couplage) sur l'interface cœur-thorax. Sur le bord Σ, on suppose que l'on a continuité du potentiel et

du courant entre le milieu extra-cellulaire et le milieu thoracique, c'est-à-dire,

$$\begin{aligned} u_{\mathrm{e}} &= u_{\mathrm{T}}, \quad \text{sur} \quad \Sigma, \\ \boldsymbol{\sigma}_{\mathrm{e}} \boldsymbol{\nabla} u_{\mathrm{e}} \cdot \boldsymbol{n} &= \boldsymbol{\sigma}_{\mathrm{T}} \boldsymbol{\nabla} u_{\mathrm{T}} \cdot \boldsymbol{n}, \quad \text{sur} \quad \Sigma. \end{aligned} \tag{3.4.22}$$

La composante normale du flux de courant intra-cellulaire sur le bord Σ est supposée nulle $\boldsymbol{\sigma}_{\mathrm{i}} \boldsymbol{\nabla} u_{\mathrm{i}} \cdot \boldsymbol{n} = 0$. Ces conditions on été formellement obtenues dans [KN94] par un procédé d'homogénéisation et sont adoptées dans beaucoup de travaux dans la littérature [Lin99, SLC$^+$06, PBC05, CPT06]. La continuité entre u_{e} et u_{T} a été aussi considérée dans l'approche *eikonale* présentée dans [CFGT04], mais d'autres conditions sont utilisées pour modéliser le flux de courant à l'interface.

Pour des raisons de coût de calculs les conditions (3.4.23) sont relaxées dans certains travaux ([PDG03, PDV09, LBG$^+$03, BCF$^+$09]) par les conditions suivantes

$$\begin{aligned} u_{\mathrm{e}} &= u_{\mathrm{T}}, \quad \text{sur} \quad \Sigma, \\ \boldsymbol{\sigma}_{\mathrm{e}} \boldsymbol{\nabla} u_{\mathrm{e}} \cdot \boldsymbol{n} &= 0, \quad \text{sur} \quad \Sigma. \end{aligned} \tag{3.4.23}$$

Ces conditions permettent de découpler le calcul des potentiels cardiaques de celui du thorax, leur utilisation sera discutée dans la section 5.5.1. En revanche, il est à noter que ces conditions ne peuvent pas être utilisées pour modéliser des phénomènes pour lesquels le thorax influence le cœur (par exemple la défibrillation). Il est nécessaire dans ces cas d'utiliser les conditions au bord (3.4.23).

En combinant (3.2.13)-(3.2.16) et (3.3.21)-(3.4.23), on obtient le système couplé suivant (*cf.* [SLC$^+$06, PBC05, CPT06]):

- Équations bidomaine-thorax:

$$\begin{cases} A_{\mathrm{m}} \left(C_{\mathrm{m}} \dfrac{\partial V_{\mathrm{m}}}{\partial t} + I_{\mathrm{ion}}(V_{\mathrm{m}}, \boldsymbol{w}) \right) - \operatorname{div}(\boldsymbol{\sigma}_{\mathrm{i}} \boldsymbol{\nabla} V_{\mathrm{m}}) = \operatorname{div}(\boldsymbol{\sigma}_{\mathrm{i}} \boldsymbol{\nabla} u_{\mathrm{e}}) + I_{\mathrm{app}}, & \text{dans} \quad \Omega_{\mathrm{H}}, \\ \operatorname{div}\left((\boldsymbol{\sigma}_{\mathrm{i}} + \boldsymbol{\sigma}_{\mathrm{e}}) \boldsymbol{\nabla} u_{\mathrm{e}} \right) = - \operatorname{div}(\boldsymbol{\sigma}_{\mathrm{i}} \boldsymbol{\nabla} V_{\mathrm{m}}), & \text{dans} \quad \Omega_{\mathrm{H}}, \\ \partial_t \boldsymbol{w} + \boldsymbol{g}(V_{\mathrm{m}}, \boldsymbol{w}) = 0, & \text{dans} \quad \Omega_{\mathrm{H}}, \\ \operatorname{div}(\boldsymbol{\sigma}_{\mathrm{T}} \boldsymbol{\nabla} u_{\mathrm{T}}) = 0, & \text{dans} \quad \Omega_{\mathrm{T}}. \end{cases} \tag{3.4.24}$$

- Conditions aux limites:

$$\begin{cases} \boldsymbol{\sigma}_{\mathrm{i}} \boldsymbol{\nabla} u_{\mathrm{e}} \cdot \boldsymbol{n} = -\boldsymbol{\sigma}_{\mathrm{i}} \boldsymbol{\nabla} V_{\mathrm{m}} \cdot \boldsymbol{n}, & \text{sur} \quad \Sigma \cup \Gamma_{\mathrm{endo}}, \\ (\boldsymbol{\sigma}_{\mathrm{i}} + \boldsymbol{\sigma}_{\mathrm{e}}) \boldsymbol{\nabla} u_{\mathrm{e}} \cdot \boldsymbol{n} = -\boldsymbol{\sigma}_{\mathrm{i}} \boldsymbol{\nabla} V_{\mathrm{m}} \cdot \boldsymbol{n}, & \text{sur} \quad \Gamma_{\mathrm{endo}}, \\ \boldsymbol{\sigma}_{\mathrm{T}} \boldsymbol{\nabla} u_{\mathrm{T}} \cdot \boldsymbol{n}_{\mathrm{T}} = 0, & \text{sur} \quad \Gamma_{\mathrm{ext}}, \end{cases} \tag{3.4.25}$$

- Conditions de couplage:

$$\begin{cases} u_{\mathrm{e}} = u_{\mathrm{T}}, & \text{sur} \quad \Sigma, \\ (\boldsymbol{\sigma}_{\mathrm{i}} + \boldsymbol{\sigma}_{\mathrm{e}}) \boldsymbol{\nabla} u_{\mathrm{e}} \cdot \boldsymbol{n} = \boldsymbol{\sigma}_{\mathrm{T}} \boldsymbol{\nabla} u_{\mathrm{T}} \cdot \boldsymbol{n} - \boldsymbol{\sigma}_{\mathrm{i}} \boldsymbol{\nabla} V_{\mathrm{m}} \cdot \boldsymbol{n}, & \text{sur} \quad \Sigma. \end{cases} \tag{3.4.26}$$

Dans la suite de la thèse, nous nous intéressons à l'etude théorique et à la simulation numérique de l'ECG. Nous analysons l'éxistence et l'unicité d'une solution faible du système couplé cœur-thorax (3.4.24)-(3.4.26). Nous utilisons ce système comme base d'un modèle qui nous permettra de simuler des électrocardiogrammes dans des cas normaux et pathologiques. La simulation numérique nous permettra de souligner l'importance de certaines hypothèses de modélisation. Enfin, nous exposerons quelques applications de l'utilisation de cet outil au niveau médical et industriel.

Part II

Mathematical analysis: Existence and uniqueness of the bidomain-torso coupled problem

Summary

Chapter 4

Existence and uniqueness of the bidomain-torso coupled problem

This chapter addresses the well-posedness analysis of the coupled heart-torso system (3.4.24)-(3.4.26) arising in the numerical simulation of electrocardiograms (ECG). Global existence of weak solutions is proved for an abstract class of ionic models including Mitchell-Schaeffer, FitzHugh-Nagumo, Aliev-Panfilov and MacCulloch. Uniqueness is proved in the case of the FitzHugh-Nagumo ionic model. The proof is based on the combination of a regularization argument with a Faedo-Galerkin/compactness procedure.

This chapter is part of a joint work with M. Boulakia, M.A. Fernández and J.-F. Gerbeau, reported in [BFGZ08b].

4.1 Introduction

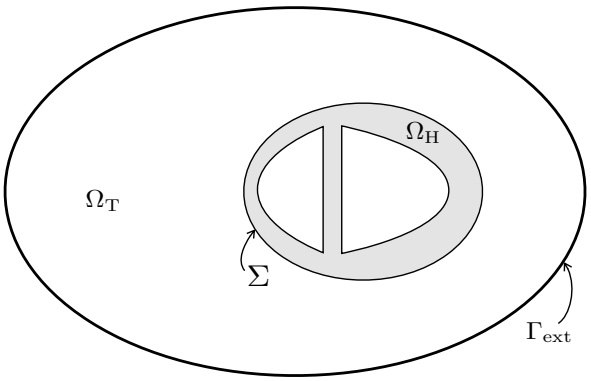

Figure 4.1: The heart and torso domains: Ω_H and Ω_T

We assume the cardiac tissue to be located in a domain (an open bounded subset with locally Lipschitz continuous boundary) Ω_H of $\mathbb{R}^3$. The surrounding tissue within the torso occupies a domain Ω_T. We denote by $\Sigma \stackrel{\text{def}}{=} \overline{\Omega_H} \cap \overline{\Omega_T} = \partial\Omega_H$ the interface

between both domains, and by Γ_{ext} the external boundary of Ω_{T}, *i.e.* $\Gamma_{\text{ext}} \stackrel{\text{def}}{=} \partial\Omega_{\text{T}} \backslash \Sigma$, see figure 4.1. At last, we define Ω the global domain $\overline{\Omega_{\text{H}}} \cup \Omega_{\text{T}}$.

A widely accepted model of the macroscopic electrical activity of the heart is the so-called *bidomain model* (see *e.g.* the monographs [Sac04, PBC05, SLC$^+$06]). It consists of two degenerate parabolic reaction-diffusion PDEs coupled to a system of ODEs:

$$\begin{cases} C_{\text{m}}\partial_t v_{\text{m}} + I_{\text{ion}}(v_{\text{m}}, w) - \operatorname{div}(\boldsymbol{\sigma}_{\text{i}} \boldsymbol{\nabla} u_{\text{i}}) = I_{\text{app}}, & \text{in} \quad \Omega_{\text{H}} \times (0,T), \\ C_{\text{m}}\partial_t v_{\text{m}} + I_{\text{ion}}(v_{\text{m}}, w) + \operatorname{div}(\boldsymbol{\sigma}_{\text{e}} \boldsymbol{\nabla} u_{\text{e}}) = I_{\text{app}}, & \text{in} \quad \Omega_{\text{H}} \times (0,T), \\ \partial_t w + g(v_{\text{m}}, w) = 0, & \text{in} \quad \Omega_{\text{H}} \times (0,T). \end{cases} \tag{4.1.1}$$

The two PDEs describe the dynamics of the averaged intra- and extracellular potentials u_{i} and u_{e}, whereas the ODE, also known as *ionic model*, is related to the electrical behavior of the myocardium cells membrane, in terms of the (vector) variable w representing the averaged ion concentrations and gating states. In (4.1.1), the quantity $v_{\text{m}} \stackrel{\text{def}}{=} u_{\text{i}} - u_{\text{e}}$ stands for the transmembrane potential, C_{m} is the membrane capacitance, $\boldsymbol{\sigma}_{\text{i}}, \boldsymbol{\sigma}_{\text{e}}$ are the intra- and extra-cellular conductivity tensors and I_{app} is an external applied volume current. The nonlinear reaction term $I_{\text{ion}}(v_{\text{m}}, w)$ and the vector-valued function $g(v_{\text{m}}, w)$ depend on the ionic model under consideration (*e.g.* Mitchell-Schaeffer [MS03], FitzHugh-Nagumo [NAY62] or Luo-Rudy [LR91, LR94]).

The PDE part of (4.1.1) has to be completed with boundary conditions for u_{i} and u_{e}. The intracellular domain is assumed to be electrically isolated, so we prescribe

$$\boldsymbol{\sigma}_{\text{i}} \boldsymbol{\nabla} u_{\text{i}} \cdot \boldsymbol{n} = 0, \quad \text{on} \quad \Sigma,$$

where $\boldsymbol{n}$ stands for the outward unit normal on Σ. Conversely, the boundary conditions for u_{e} will depend on the interaction with the surrounding tissue.

The numerical simulation of the ECG signals requires a description of how the surface potential is perturbed by the electrical activity of the heart. In general, such a description is based on the coupling of (4.1.1) with a diffusion equation in Ω_{T}:

$$\operatorname{div}(\boldsymbol{\sigma}_{\text{T}} \boldsymbol{\nabla} u_{\text{T}}) = 0, \quad \text{in} \quad \Omega_{\text{T}}, \tag{4.1.2}$$

where u_{T} stands for the torso potential and $\boldsymbol{\sigma}_{\text{T}}$ for the conductivity tensor of the torso tissue. The boundary Γ_{ext} can be supposed to be insulated, which corresponds to the condition

$$\boldsymbol{\sigma}_{\text{T}} \boldsymbol{\nabla} u_{\text{T}} \cdot \boldsymbol{n}_{\text{T}} = 0 \text{ on } \Gamma_{\text{ext}},$$

where $\boldsymbol{n}_{\text{T}}$ stands for the outward unit normal on Γ_{ext}.

The coupling between (4.1.1) and (4.1.2) is operated at the heart-torso interface Σ. Generally, by enforcing the continuity of potentials and currents (see *e.g* [KN94, Gul03, Pie05, PBC05, SLC$^+$06]):

$$\begin{cases} u_{\text{e}} = u_{\text{T}}, & \text{on} \quad \Sigma, \\ \boldsymbol{\sigma}_{\text{e}} \boldsymbol{\nabla} u_{\text{e}} \cdot \boldsymbol{n} = \boldsymbol{\sigma}_{\text{T}} \boldsymbol{\nabla} u_T \cdot \boldsymbol{n}, & \text{on} \quad \Sigma. \end{cases} \tag{4.1.3}$$

These conditions represent a perfect electrical coupling between the heart and the surrounding tissue. More general coupling conditions, which take into account the impact

of the pericardium (a double-walled sac which separates the heart and the surrounding tissue), have been reported in chapter 5 section 5.5.5.

In summary, from (4.1.1), (4.1.2) and (4.1.3) we obtain the following coupled heart-torso model (see *e.g* [Gul03, Pie05, PBC05, SLC+06]):

$$\begin{cases} C_{\mathrm{m}}\partial_t v_{\mathrm{m}} + I_{\mathrm{ion}}(v_{\mathrm{m}}, w) - \mathrm{div}(\boldsymbol{\sigma}_{\mathrm{i}}\boldsymbol{\nabla} u_{\mathrm{i}}) = I_{\mathrm{app}}, & \text{in} \quad \Omega_{\mathrm{H}}, \\ C_{\mathrm{m}}\partial_t v_{\mathrm{m}} + I_{\mathrm{ion}}(v_{\mathrm{m}}, w) + \mathrm{div}(\boldsymbol{\sigma}_{\mathrm{e}}\boldsymbol{\nabla} u_{\mathrm{e}}) = I_{\mathrm{app}}, & \text{in} \quad \Omega_{\mathrm{H}}, \\ \partial_t w + g(v_{\mathrm{m}}, w) = 0, & \text{in} \quad \Omega_{\mathrm{H}}, \\ \mathrm{div}(\boldsymbol{\sigma}_{\mathrm{T}}\boldsymbol{\nabla} u_{\mathrm{T}}) = 0, & \text{in} \quad \Omega_{\mathrm{T}}, \\ \boldsymbol{\sigma}_{\mathrm{i}}\boldsymbol{\nabla} u_{\mathrm{i}} \cdot \boldsymbol{n} = 0, & \text{on} \quad \Sigma \\ \boldsymbol{\sigma}_{\mathrm{e}}\boldsymbol{\nabla} u_{\mathrm{e}} \cdot \boldsymbol{n} = \boldsymbol{\sigma}_{\mathrm{T}}\boldsymbol{\nabla} u_{\mathrm{T}} \cdot \boldsymbol{n}, & \text{on} \quad \Sigma, \\ u_{\mathrm{e}} = u_{\mathrm{T}}, & \text{on} \quad \Sigma, \\ \boldsymbol{\sigma}_{\mathrm{T}}\boldsymbol{\nabla} u_{\mathrm{T}} \cdot \boldsymbol{n}_{\mathrm{T}} = 0, & \text{on} \quad \Gamma_{\mathrm{ext}}. \end{cases} \tag{4.1.4}$$

Problem (4.1.4) is completed with initial conditions:

$$v_{\mathrm{m}}(0, x) = v_0(x) \text{ and } w(0, x) = w_0(x) \quad \forall\, x \in \Omega_{\mathrm{H}}, \tag{4.1.5}$$

and the identity

$$v_{\mathrm{m}} \stackrel{\mathrm{def}}{=} u_{\mathrm{i}} - u_{\mathrm{e}}, \quad \text{in} \quad \Omega_{\mathrm{H}}. \tag{4.1.6}$$

Finally, let us notice that u_{e} and u_{T} are defined up to the same constant. This constant can be fixed, for instance, by enforcing the following condition

$$\int_{\Omega_{\mathrm{H}}} u_{\mathrm{e}} = 0,$$

on the extra-cellular potential.

Introduced in the late 70's [Tun78], the system of equations (4.1.1) can be derived mathematically using homogenization techniques. Typically, by assuming that the myocardium has periodic structure at the cell scale [KN93] (see also [CFS02, PSF06]). A first well-posedness analysis of (4.1.1), with $I_{\mathrm{ion}}(v_{\mathrm{m}}, w)$ and $g(v_{\mathrm{m}}, w)$ given by the FitzHugh-Nagumo ionic model [NAY62], has been reported in [CFS02]. The proof is based on a reformulation of (4.1.1) in terms of an abstract evolutionary variational inequality. The analysis for a simplified ionic model, namely $I_{\mathrm{ion}}(v_{\mathrm{m}}, w) \stackrel{\mathrm{def}}{=} I_{\mathrm{ion}}(v_{\mathrm{m}})$, has been addressed in [BK06]. In the recent work [BCP09], existence, uniqueness and regularity of a local, in time, solution are proved for the bidomain model with a general ionic model, using a semi-group approach. Existence of a global, in time, solution of the bidomain problem is also proved in [BCP09] for a wide class of ionic models (including FitzHugh-Nagumo, Aliev-Panfilov [AP96] and MacCulloch [RM94]) through a compactness argument. Uniqueness, however, is achieved only for the FitzHugh-Nagumo ionic model. Finally, in [Ven09], existence, uniqueness and some regularity results are proved with a generalized phase-I Luo-Rudy ionic model [LR91].

None of the above mentioned works consider the coupled bidomain-torso problem (4.1.4). The aim of this chapter is to provide a well-posedness analysis of this coupled problem. Our main result states the existence of global weak solutions for (4.1.4) with an abstract class of ionic models, including: FitzHugh-Nagumo [Fit61, NAY62], Aliev-Panfilov [AP96], Roger-McCulloch [RM94] and Mitchell-Schaeffer [MS03]. For the sake of completeness, we give here the expressions of I_{ion} and g for these models.

- FitzHugh-Nagumo model:

$$I_{\text{ion}}(v,w) = kv(v-a)(v-1) + w, \quad g(v,w) = -\epsilon(\gamma v - w). \tag{4.1.7}$$

- Aliev-Panfilov model:

$$I_{\text{ion}}(v,w) = kv(v-a)(v-1) + vw, \quad g(v,w) = \epsilon(\gamma v(v-1-a) + w). \tag{4.1.8}$$

- Roger-McCulloch model:

$$I_{\text{ion}}(v,w) = kv(v-a)(v-1) + vw, \quad g(v,w) = -\epsilon(\gamma v - w). \tag{4.1.9}$$

- Mitchell-Schaeffer model:

$$\begin{aligned} I_{\text{ion}}(v,w) &= \frac{w}{\tau_{\text{in}}}v^2(v-1) - \frac{v}{\tau_{\text{out}}}, \\ g(v,w) &= \begin{cases} \dfrac{w-1}{\tau_{\text{open}}} \text{ if } v \le v_{\text{gate}}, \\ \dfrac{w}{\tau_{\text{close}}} \text{ if } v > v_{\text{gate}}. \end{cases} \end{aligned} \tag{4.1.10}$$

Here $0 < a < 1$, k, ϵ, γ, $\tau_{\text{in}} < \tau_{\text{out}} < \tau_{\text{open}}$, τ_{close} and $0 < v_{\text{gate}} < 1$ are given positive constants.

To the best of our knowledge, the ionic model (4.1.10) has not yet been considered within a well-posedness study of the bidomain equations (4.1.1). Compared to models (4.1.7)-(4.1.9), the Mitchell-Schaeffer model has different structure that makes the proof of our results slightly more involved. As far as the ECG modeling is concerned, in chapter 5 (see also [BFGZ07, BCF$^+$09]), we point out that realistic ECG signals can be obtained with this model, whereas it seems to be not the case for standard FitzHugh-Nagumo type models (4.1.7).

The remainder of the chapter is organized as follows. In the next section we state our main existence result for problem (4.1.4), under general assumptions on the ionic model. In Section 3 we provide the proof of this result. We use a regularization argument and a standard Faedo-Galerkin/compactness procedure based on a specific spectral basis in Ω. Uniqueness is proved for the FitzHugh-Nagumo ionic model.

4.2 Main result

We assume that the conductivities of the intracellular, extracellular and thoracic media $\boldsymbol{\sigma}_{\text{i}}$, $\boldsymbol{\sigma}_{\text{e}}$, $\boldsymbol{\sigma}_{\text{T}} \in [L^\infty(\Omega_{\text{H}})]^{3\times 3}$ are symmetric and uniformly positive definite, *i.e.* there exist $\alpha_{\text{i}} > 0$, $\alpha_{\text{e}} > 0$ and $\alpha_{\text{T}} > 0$ such that, $\forall\, \boldsymbol{x} \in \mathbb{R}^3$, $\forall\, \boldsymbol{\xi} \in \mathbb{R}^3$,

$$\boldsymbol{\xi}^T \boldsymbol{\sigma}_{\text{i}}(\boldsymbol{x})\boldsymbol{\xi} \ge \alpha_{\text{i}}|\boldsymbol{\xi}|^2, \quad \boldsymbol{\xi}^T \boldsymbol{\sigma}_{\text{e}}(\boldsymbol{x})\boldsymbol{\xi} \ge \alpha_{\text{e}}|\boldsymbol{\xi}|^2, \quad \boldsymbol{\xi}^T \boldsymbol{\sigma}_{\text{T}}(\boldsymbol{x})\boldsymbol{\xi} \ge \alpha_{\text{T}}|\boldsymbol{\xi}|^2. \tag{4.2.11}$$

Moreover, we shall use the notation $\alpha \stackrel{\text{def}}{=} \min\{\alpha_{\text{e}}, \alpha_{\text{T}}\}$.

For the reaction terms we consider two kinds of (two-variable) ionic models:

- **I1**: Generalized FitzHugh-Nagumo models, where functions I_{ion} and g are given by

$$\begin{aligned} I_{\text{ion}}(v,w) &= f_1(v) + f_2(v)w, \\ g(v,w) &= g_1(v) + c_1 w. \end{aligned} \tag{4.2.12}$$

  Here, f_1, f_2 and g_1 are given real functions and c_1 is a real constant.

- **I2**: A regularized version of the Mitchell-Schaeffer model (see *e.g.* [DSL07]), for which the functions I_{ion} and g are given by:

$$\begin{aligned} I_{\text{ion}}(v,w) &= \frac{w}{\tau_{\text{in}}} f_1(v) - \frac{v}{\tau_{\text{out}}}, \\ g(v,w) &= \Big(\frac{1}{\tau_{\text{close}}} + \frac{\tau_{\text{close}} - \tau_{\text{open}}}{\tau_{\text{close}}\tau_{\text{open}}} h_\infty(v)\Big)(w - h_\infty(v)), \end{aligned} \tag{4.2.13}$$

  where f_1 is a real function given by

$$f_1(v) = v^2(v-1), \tag{4.2.14}$$

  the function h_∞ is given by

$$h_\infty(v) = \frac{1}{2}\left[1 - \tanh\left(\frac{v - v_{\text{gate}}}{\eta_{\text{gate}}}\right)\right], \tag{4.2.15}$$

  and τ_{in}, τ_{out}, $\tau_{\text{open}}, \tau_{\text{close}}$, v_{gate}, η_{gate} are positive constants.

In what follows we will consider the following two problems:

- **P1**: System (4.1.4) with the ionic model (**I1**) given by (4.2.12).
- **P2**: System (4.1.4) with the ionic model (**I2)** given by (4.2.13)-(4.2.15).

In order to analyze the well-posedness of these problems, we shall make use of the following assumptions on the behavior of the reaction terms.

- **A1**: We assume that f_1, f_2 and g_1 belong to $C^1(\mathbb{R})$ and that, $\forall\, v \in \mathbb{R}$,

$$\begin{aligned} |f_1(v)| &\le c_2 + c_3|v|^3, \\ f_2(v) &= c_4 + c_5 v, \\ |g_1(v)| &\le c_6 + c_7|v|^2, \end{aligned} \tag{4.2.16}$$

  with $\{c_i\}_{i=2}^7$ given real constants and c_2, c_3, c_6, c_7 are positives.
  For any $v \in \mathbb{R}$,

$$f_1(v)v \ge a|v|^4 - b|v|^2, \tag{4.2.17}$$

  with $a > 0$ and $b \ge 0$ given constants.

- **A2**: $(4.2.16)_1$ and (4.2.17).

The next assumption will be also used in order to prove uniqueness of the solution of problem **P1**.

- **A3**: For all $\mu > 0$, we introduce F_μ as

$$\begin{aligned} F_\mu \ : \ & \mathbb{R}^2 \longrightarrow \mathbb{R}^2 \\ & (v,w) \mapsto (\mu I_{\text{ion}}(v,w), g(v,w)), \end{aligned}$$

and Q_μ as:

$$Q_\mu(z) \stackrel{\text{def}}{=} \frac{1}{2}\left(\boldsymbol{\nabla} F_\mu(z) + \boldsymbol{\nabla} F_\mu(z)^{\mathrm{T}}\right), \forall\, z \in \mathbb{R}^2.$$

In addition, we assume that there exist $\mu_0 > 0$ and a constant $C_{\text{ion}} \leq 0$ such that the eigenvalues $\lambda_{1,\mu_0}(z) \leq \lambda_{2,\mu_0}(z)$ of $Q_{\mu_0}(z)$, satisfy

$$C_{\text{ion}} \leq \lambda_{1,\mu_0}(z) \leq \lambda_{2,\mu_0}(z), \quad \forall\, z \in \mathbb{R}^2. \tag{4.2.18}$$

Remark 4.2.0.1. *One can check that models* (4.1.7)-(4.1.9) *enter the general framework* (4.2.12) *and satisfy the assumption* **A1** *and the model given by* (4.2.13)-(4.2.15) *satisfies assumption* **A2**. *In addition,* **A3** *holds true for the FitzHugh-Nagumo model. We refer to [BCP09], for the details.*

In what follows, we shall make use of the following function spaces

$$\begin{aligned} V_{\text{i}} &\stackrel{\text{def}}{=} H^1(\Omega_{\text{H}}), \\ V_{\text{e}} &\stackrel{\text{def}}{=} \left\{ \phi \in H^1(\Omega_{\text{H}}) \ : \ \int_{\Omega_{\text{H}}} \phi = 0 \right\}, \\ V_{\text{HT}} &\stackrel{\text{def}}{=} \left\{ \phi \in H^1(\Omega_{\text{T}}) \ : \ \phi_{|\Sigma} = 0 \right\}, \\ V &\stackrel{\text{def}}{=} \left\{ \phi \in H^1(\Omega) \ : \ \int_{\Omega_{\text{H}}} \phi = 0 \right\}. \end{aligned}$$

For times T, t and t_n we introduce the cylindrical time-space domains $Q_T \stackrel{\text{def}}{=} (0,T)\times\Omega_{\text{H}}$, $Q_t \stackrel{\text{def}}{=} (0,t)\times\Omega_{\text{H}}$, $Q_{t_n} \stackrel{\text{def}}{=} (0,t_n)\times\Omega_{\text{H}}$, and we define u as the extracellular cardiac potential in Ω_{H}, and the thoracic potential in Ω_{T}, *i.e.*:

$$u \stackrel{\text{def}}{=} \begin{cases} u_{\text{e}} \text{ in } \Omega_{\text{H}}, \\ u_{\text{T}} \text{ in } \Omega_{\text{T}}. \end{cases}$$

From the first coupling condition in (4.1.3), it follows that $u \in H^1(\Omega)$ provided that $u_{\text{e}} \in H^1(\Omega_{\text{H}})$ and $u_{\text{T}} \in H^1(\Omega_{\text{T}})$. Similarly, we define the global conductivity tensor $\boldsymbol{\sigma} \in [L^\infty(\Omega)]^{3\times 3}$ as

$$\boldsymbol{\sigma} \stackrel{\text{def}}{=} \begin{cases} \boldsymbol{\sigma}_{\text{e}} \text{ in } \Omega_{\text{H}}, \\ \boldsymbol{\sigma}_{\text{T}} \text{ in } \Omega_{\text{T}}. \end{cases}$$

Definition 4.2.0.2. *A weak solution of problem* **P1** *is a quadruplet of functions* $(v_{\text{m}}, u_{\text{i}}, u, w)$ *with the regularity*

$$\begin{aligned} & v_{\text{m}} \in L^\infty(0,T; H^1(\Omega_H)) \cap H^1(0,T; L^2(\Omega_{\text{H}})), \\ & u \in L^\infty(0,T;V), \quad w \in H^1(0,T; L^2(\Omega_{\text{H}})), \end{aligned} \tag{4.2.19}$$

and satisfying (4.1.5), (4.1.6) *and*

$$C_{\text{m}} \int_{\Omega_{\text{H}}} \partial_t v_{\text{m}} \phi_{\text{i}} + \int_{\Omega_{\text{H}}} \boldsymbol{\sigma}_{\text{i}} \boldsymbol{\nabla} u_{\text{i}} \cdot \boldsymbol{\nabla} \phi_{\text{i}} + \int_{\Omega_{\text{H}}} I_{\text{ion}}(v_{\text{m}}, w)\phi_{\text{i}} = \int_{\Omega_{\text{H}}} I_{\text{app}} \phi_{\text{i}}, \tag{4.2.20}$$

$$C_{\text{m}} \int_{\Omega_{\text{H}}} \partial_t v_{\text{m}} \psi - \int_{\Omega} \boldsymbol{\sigma} \boldsymbol{\nabla} u \cdot \boldsymbol{\nabla} \psi + \int_{\Omega_{\text{H}}} I_{\text{ion}}(v_{\text{m}}, w)\psi = \int_{\Omega_{\text{H}}} I_{\text{app}} \psi, \tag{4.2.21}$$

$$\partial_t w + g(v_{\text{m}}, w) = 0. \tag{4.2.22}$$

for all $(\phi_{\rm i}, \psi, \theta) \in H^1(\Omega_{\rm H}) \times V \times L^2(\Omega_{\rm H})$. *Equations* (4.2.20) *and* (4.2.21) *holds in* $\mathcal{D}'(0,T)$ *and equation* (4.2.22) *holds almost everywhere. On the other hand, a weak solution of problem* **P2** *is a quadruplet* $(u_{\rm i}, u, v_{\rm m}, w)$ *satisfying* (4.2.19) (4.1.5), (4.1.6), (4.2.20)-(4.2.21) *and*

$$w \in W^{1,\infty}(0,T,L^\infty(\Omega_{\rm H})), \quad \partial_t w + g(v_{\rm m}, w) = 0, \, a.e. \text{ on } Q_T.$$

Remark 4.2.0.3. *Since* $w \in H^1(0,T;L^2(\Omega_{\rm H}))$ *it follows that* $w \in C^0(0,T;L^2(\Omega_{\rm H}))$, *which gives a sense to the initial data of* w. *In the same manner, the initial condition on* $v_{\rm m}$ *makes sense.*

The next theorem provides the main result of this chapter, it states the existence of solution for problems **P1** and **P2**.

Theorem 4.2.0.4. *Let* $T > 0$, $I_{\rm app} \in L^2(Q_T)$, $\boldsymbol{\sigma}_{\rm i}, \boldsymbol{\sigma}_{\rm e} \in [L^\infty(\Omega_{\rm H})]^{3\times 3}$ *symmetric and satisfying* (4.2.11), $w_0 \in L^2(\Omega_{\rm H})$ *and* $v_0 \in H^1(\Omega_{\rm H})$ *be given data.*

- *If* **A1** *holds, then problem* **P1** *has a weak solution in the sense of Definition 4.2.0.2. Moreover, if assumption* **A3** *holds true, the solution is unique.*
- *If* **A2** *holds and* $w_0 \in L^\infty(\Omega_{\rm H})$ *with a positive lower bound* $r > 0$, *such that*

$$r < w_0 \leq 1 \quad in \quad \Omega_{\rm H}, \tag{4.2.23}$$

  then, problem **P2** *has a weak solution in the sense of Definition 4.2.0.2.*

The next section is fully devoted to the proof of this theorem.

4.3 Existence of weak solution of the bidomain-torso problem

Two main issues arise in the analysis of problem (4.1.4). Firstly, the non-linear reaction-diffusion equations $(4.1.4)_{1,2}$ are degenerate in time. And secondly, we have a coupling with a diffusion equation through the interface Σ. The first issue is overcome here by adding a couple of regularization terms, making bidomain equations parabolic. The method we propose simplifies the approach used in [BK06] by merging regularization and approximation of the solution . Then, the resulting regularized system can be analyzed by standard arguments, namely, through a Faedo-Galerkin/compactness procedure and a specific treatment of the non-linear terms. On the other hand, the second matter can be handled through a specific definition of the Galerkin basis.

In paragraph 4.3.1, regularization and Faedo-Galerkin techniques are merged by introducing a regularized problem in finite dimension n. In the next paragraph, existence of solution for this problem is proved. In paragraph 4.3.3, energy estimates are derived, independent of the regularization parameter $\frac{1}{n}$. Existence of solution for the continuous problem is addressed in section 4.3.4 whereas, in 4.4, uniqueness is proved for problem **P1**, under the additional assumption **A3**.

4.3.1 A regularized problem in finite dimension

Let $\{h_k\}_{k\in\mathbb{N}^*}$ be a Hilbert basis of $V_{\rm i}$, $\{f_k\}_{k\in\mathbb{N}^*}$ be a Hilbert basis of $V_{\rm e}$ and $\{g_k\}_{k\in\mathbb{N}^*}$ a Hilbert basis of $V_{\rm HT}$, see *e.g.,* [DL85]. We assume that these basis functions are (sufficiently) smooth and that $\{h_k\}_{k\in\mathbb{N}^*}$ is an orthogonal basis in $L^2(\Omega_{\rm H})$ (see, *e.g.,* [RR04] page 268). We introduce a Galerkin basis of V by defining, for all $k\in\mathbb{N}^*$, $\tilde{f}_k\in H^1(\Omega)$ as an extension of f_k in $H^1(\Omega)$, given by an arbitrary continuous extension operator. We also extend, for all $k\in\mathbb{N}^*$, g_k by $\tilde{g_k}\in H^1(\Omega)$ such that $\tilde{g_k}=0$ in $\Omega_{\rm H}$. One can check straightforwardly that $\{e_k\}_{k\in\mathbb{N}^*}$, defined as, $e_{2k-1}=\tilde{f}_k,\quad e_{2k}=\tilde{g_k},\quad \forall\, k\in\mathbb{N}^*$, is a Galerkin basis of V.

Finally, for all $n\in\mathbb{N}^*$, we can define the finite dimensional spaces $V_{{\rm i},n}$, $V_{{\rm e},n}$, $V_{{\rm T},n}$ and V_n generated, respectively, by $\{h_k\}_{k=1}^n$,$\{f_k\}_{k=1}^n$, $\{g_k\}_{k=1}^n$ and $\{e_k\}_{k=1}^{2n}$, *i.e*

$$
\begin{aligned}
&V_{{\rm i},n}\stackrel{\rm def}{=}<\{h_k\}_{k=1}^n>,\quad V_{{\rm e},n}\stackrel{\rm def}{=}<\{f_k\}_{k=1}^n>,\\
&V_{{\rm T},n}\stackrel{\rm def}{=}<\{g_k\}_{k=1}^n>,\quad V_n\stackrel{\rm def}{=}<\{e_k\}_{k=1}^{2n}>.
\end{aligned}
$$

Hence, we can introduce, for each $n\in\mathbb{N}^*$, the following two discrete problems $\mathbf{P1}_n$ and $\mathbf{P2}_n$ associated to problems **P1** and **P2**, respectively:

- $\mathbf{P1}_n$: Find $(u_{{\rm i},n},u_n)\in C^1(0,T;V_{{\rm i},n}\times V_{\rm n})$, $w_n\in C^1(0,T;V_{{\rm i},n})$ such that, for $v_n=u_{{\rm i},n}-u_{n/\Omega_{\rm H}}$ and for all $(h,e,\theta)\in V_{{\rm i},n}\times V_{\rm n}\times V_{{\rm i},n}$ we have,

$$
\begin{aligned}
C_{\rm m}\int_{\Omega_{\rm H}}\partial_t v_n h+\frac{1}{n}\int_{\Omega_{\rm H}}\partial_t u_{{\rm i},n}h+\int_{\Omega_H}\boldsymbol{\sigma}_{\rm i}\boldsymbol{\nabla}u_{{\rm i},n}\cdot\boldsymbol{\nabla}h&\\
+\int_{\Omega_H}I_{\rm ion}(v_n,w_n)h=\int_{\Omega_H}I_{\rm app}h,&\\
C_{\rm m}\int_{\Omega_{\rm H}}\partial_t v_n e-\frac{1}{n}\int_{\Omega}\partial_t u_n e-\int_{\Omega}\boldsymbol{\sigma}\boldsymbol{\nabla}u_n\cdot\boldsymbol{\nabla}e&\\
+\int_{\Omega_H}I_{\rm ion}(v_n,w_n)e=\int_{\Omega_H}I_{\rm app}e,&\\
\int_{\Omega_{\rm H}}\partial_t w_n\theta+\int_{\Omega_{\rm H}}g(v_n,w_n)\theta=0,&
\end{aligned}
\tag{4.3.24}
$$

  with $v_n\stackrel{\rm def}{=}u_{{\rm i},n}-u_{n|\Omega_{\rm H}}$ and verifying the initial conditions

$$
\begin{aligned}
&v_n(0)=v_{0,n},\quad u_{{\rm i},n}(0)=u_{{\rm i},0,n},\quad \text{in}\quad \Omega_{\rm H};\quad u_n(0)=u_{0,n}\quad\text{in}\quad\Omega,\\
&w_n(0)=w_{0,n},\quad \text{in}\quad\Omega_{\rm H},
\end{aligned}
\tag{4.3.25}
$$

  Here, $v_{0,n},w_{0,n}$ are suitable approximations of v_0 and w_0 in $V_{{\rm i},n}$, and $u_{{\rm i},0,n},u_{0,n}$ are *auxiliary* initial conditions to be specified later on.

- $\mathbf{P2}_n$: Find $(u_{{\rm i},n},u_n)\in C^1(0,T;V_{{\rm i},n}\times V_{\rm n})$ and $w_n\in C^1(0,T,L^\infty(\Omega_{\rm H}))$ such that, for $v_n=u_{{\rm i},n}-u_{n/\Omega_{\rm H}}$, the triplet $(v_n,u_{{\rm i},n},u_n)$ satisfy $(4.3.24)_{1,2}$-$(4.3.25)_1$ and

$$
\begin{aligned}
\partial_t w_n+g(v_n,w_n)=0,\quad &\text{a.e. in}\quad Q_T,\\
w_n(0)=w_0,\quad &\text{a.e. in}\quad\Omega_{\rm H}.
\end{aligned}
\tag{4.3.26}
$$

The (auxiliary) initial conditions for $u_{\mathrm{i},n}$ and u_n, needed by the two problems below, are defined by introducing two arbitrary functions $u_{\mathrm{i},0} \in H^1(\Omega_{\mathrm{H}})$ and $u_0 \in V$ such that $v_0 = u_{\mathrm{i},0} - u_0$ in Ω_{H}. Then, for $n \in \mathbb{N}^*$, we define $(u_{\mathrm{i},0,n}, u_{0,n}, w_{0,n})$ as the orthogonal projections, on $V_{\mathrm{i},n} \times V_{\mathrm{n}} \times V_{\mathrm{i},n}$, of $(u_{\mathrm{i},0}, u_0, w_0)$. Clearly, by construction of these sequences, we have

$$(v_{0,n}, u_{\mathrm{i},0,n}, u_{0,n}, w_{0,n}) \longrightarrow (v_0, u_{\mathrm{i},0}, u_0, w_0), \tag{4.3.27}$$

in $V_{\mathrm{i}}^2 \times V \times L^2(\Omega_{\mathrm{H}})$.

4.3.2 Local existence of the discretized solution

Lemma 4.3.2.1. *Suppose that there exists C_0 such that*

$$\|u_{\mathrm{i},0,n}\|_{H^1(\Omega_{\mathrm{H}})} + \|u_{0,n}\|_{H^1(\Omega)} + \|w_{0,n}\|_{L^2(\Omega_{\mathrm{H}})} \leq C_0. \tag{4.3.28}$$

For all $n \in \mathbb{N}^*$ there exists a positive time $0 < t_n \leq T$ which only depends on C_0 such that problems $\mathbf{P1}_n$ and $\mathbf{P2}_n$ admit a unique solution over the time interval $[0, t_n]$.

Proof. For the sake of conciseness we only give here the details of the proof for problem $\mathbf{P1}_n$, the proof for problem $\mathbf{P2}_n$ follows with minor modifications. Since $\{h_l\}_{1 \leq l \leq n}$ and $\{e_l\}_{1 \leq l \leq 2n}$ are basis of $V_{\mathrm{i},n}$ and V_{n}, respectively, we can write

$$\begin{aligned} &u_{\mathrm{i},n}(t) = \sum_{l=1}^{n} c_{\mathrm{i},l}(t) h_l, \quad u_n(t) = \sum_{l=1}^{2n} c_l(t) e_l, \quad w_n(t) = \sum_{l=1}^{n} c_{\mathrm{w},l}(t) h_l, \\ &u_{\mathrm{i},0,n} = \sum_{l=1}^{n} c_{\mathrm{i},l}^0 h_l, \quad u_{0,n} = \sum_{l=1}^{2n} c_l^0 e_l, \quad w_{0,n} = \sum_{l=1}^{n} c_{\mathrm{w},l}^0 h_l. \end{aligned} \tag{4.3.29}$$

Thus, introducing the notations

$$\begin{aligned} &\boldsymbol{c}_{\mathrm{i}} \stackrel{\mathrm{def}}{=} \{c_{\mathrm{i},l}\}_{l=1}^n, \quad \boldsymbol{c} \stackrel{\mathrm{def}}{=} \{c_l\}_{l=1}^{2n}, \quad \boldsymbol{c}_{\mathrm{w}} \stackrel{\mathrm{def}}{=} \{c_{\mathrm{w},l}\}_{l=1}^n, \\ &\boldsymbol{c}_{\mathrm{i}}^0 \stackrel{\mathrm{def}}{=} \{c_{\mathrm{i},l}^0\}_{l=1}^n, \quad \boldsymbol{c}^0 \stackrel{\mathrm{def}}{=} \{c_l^0\}_{l=1}^{2n}, \quad \boldsymbol{c}_{\mathrm{w}}^0 \stackrel{\mathrm{def}}{=} \{c_{\mathrm{w},l}^0\}_{l=1}^n, \end{aligned}$$

it follows that problem $\mathbf{P1}_n$ is equivalent to the following non-linear system of ordinary differential equations (ODE)

$$\boldsymbol{M} \begin{bmatrix} \boldsymbol{c}_{\mathrm{i}}' \\ \boldsymbol{c}' \\ \boldsymbol{c}_{\mathrm{w}}' \end{bmatrix} = \begin{bmatrix} \boldsymbol{G}_{\mathrm{i}}\big(t, \boldsymbol{c}_{\mathrm{i}}, \boldsymbol{c}, \boldsymbol{c}_{\mathrm{w}}\big) \\ \boldsymbol{G}\big(t, \boldsymbol{c}_{\mathrm{i}}, \boldsymbol{c}, \boldsymbol{c}_{\mathrm{w}}\big) \\ \boldsymbol{G}_{\mathrm{w}}\big(t, \boldsymbol{c}_{\mathrm{i}}, \boldsymbol{c}, \boldsymbol{c}_{\mathrm{w}}\big) \end{bmatrix}, \quad \begin{bmatrix} \boldsymbol{c}_{\mathrm{i}}(0) \\ \boldsymbol{c}(0) \\ \boldsymbol{c}_{\mathrm{w}}(0) \end{bmatrix} = \begin{bmatrix} \boldsymbol{c}_{\mathrm{i}}^0 \\ \boldsymbol{c}^0 \\ \boldsymbol{c}_{\mathrm{w}}^0 \end{bmatrix}. \tag{4.3.30}$$

Here, the *mass* matrix $\boldsymbol{M} \in \mathbb{R}^{4n \times 4n}$ is given by

$$\boldsymbol{M} \stackrel{\mathrm{def}}{=} \begin{bmatrix} (C_{\mathrm{m}} + \frac{1}{n})\boldsymbol{M}_{V_{\mathrm{i}}} & \vdots & -C_{\mathrm{m}}\boldsymbol{M}_{V_{\mathrm{ie}}} & \vdots & 0 \\ \cdots\cdots\cdots & \vdots & \cdots\cdots\cdots\cdots\cdots & \vdots & \cdots\cdots\cdots \\ & \vdots & & \vdots & \\ -C_{\mathrm{m}}\boldsymbol{M}_{V_{\mathrm{ie}}}{}^T & \vdots & C_{\mathrm{m}}\boldsymbol{M}_{V_{\mathrm{e}}} + \frac{1}{n}\boldsymbol{M}_{V_{\mathrm{HT}}} & \vdots & 0 \\ & \vdots & & \vdots & \\ \cdots\cdots\cdots & \vdots & \cdots\cdots\cdots\cdots\cdots & \vdots & \cdots\cdots\cdots \\ 0 & \vdots & 0 & \vdots & \boldsymbol{M}_{V_{\mathrm{i}}} \end{bmatrix},$$

with $\boldsymbol{M}_{V_\mathrm{i}} \in \mathbb{R}^{n\times n}$, $\boldsymbol{M}_{V_\mathrm{ie}} \in \mathbb{R}^{n\times 2n}$ and $\boldsymbol{M}_{V_\mathrm{e}}, \boldsymbol{M}_{V_\mathrm{HT}} \in \mathbb{R}^{2n\times 2n}$

$$\boldsymbol{M}_{V_\mathrm{i}} \stackrel{\text{def}}{=} \Big(\int_{\Omega_\mathrm{H}} h_k h_l\Big)_{1\le k,l\le n}, \quad \boldsymbol{M}_{V_\mathrm{ie}} \stackrel{\text{def}}{=} \Big(\int_{\Omega_\mathrm{H}} h_k e_l\Big)_{1\le k\le n,\, 1\le l\le 2n},$$
$$\boldsymbol{M}_{V_\mathrm{e}} \stackrel{\text{def}}{=} \Big(\int_{\Omega_\mathrm{H}} e_k e_l\Big)_{1\le k,l\le 2n}, \quad \boldsymbol{M}_{V_\mathrm{HT}} \stackrel{\text{def}}{=} \Big(\int_{\Omega} e_k e_l\Big)_{1\le k,l\le 2n}.$$

On the other hand, from the notations

$$\boldsymbol{G}_\mathrm{i} \stackrel{\text{def}}{=} \{G_{\mathrm{i},k}\}_{k=1}^{n}, \quad \boldsymbol{G} \stackrel{\text{def}}{=} \{G_k\}_{k=1}^{2n}, \quad \boldsymbol{G}_\mathrm{w} \stackrel{\text{def}}{=} \{G_{\mathrm{w},k}\}_{k=1}^{n},$$

the right-hand side of (4.3.30) is given by

$$G_{\mathrm{i},k}(t, \boldsymbol{c}_\mathrm{i}, \boldsymbol{c}, \boldsymbol{c}_\mathrm{w}) \stackrel{\text{def}}{=} -\int_{\Omega_H} \boldsymbol{\sigma}_\mathrm{i} \boldsymbol{\nabla} u_{\mathrm{i},n} \cdot \boldsymbol{\nabla} h_k - \int_{\Omega_H} I_\mathrm{ion}(v_n, w_n) h_k + \int_{\Omega_H} I_\mathrm{app} h_k,$$

for all $1 \le k \le n$,

$$G_k(t, \boldsymbol{c}_\mathrm{i}, \boldsymbol{c}, \boldsymbol{c}_\mathrm{w}) \stackrel{\text{def}}{=} -\int_{\Omega} \boldsymbol{\sigma} \boldsymbol{\nabla} u_n \cdot \boldsymbol{\nabla} e_k + \int_{\Omega_H} I_\mathrm{ion}(v_n, w_n) e_k - \int_{\Omega_H} I_\mathrm{app} e_k,$$

for all $1 \le k \le 2n$, and finally,

$$G_{\mathrm{w},k}(t, \boldsymbol{c}_\mathrm{i}, \boldsymbol{c}, \boldsymbol{c}_\mathrm{w}) \stackrel{\text{def}}{=} -\int_{\Omega_H} g(v_n, w_n) h_k,$$

for all $1 \le k \le n$.
According to Lemma 4.3.2.2, given below, the mass matrix $\boldsymbol{M}$ is positive definite and hence invertible and, on the other hand, the right-hand side of (4.3.30) is a C^1 function with respect to the arguments $\boldsymbol{c}_\mathrm{i}$, $\boldsymbol{c}$ and $\boldsymbol{c}_\mathrm{w}$. Thus, thanks to Cauchy-Lipschitz theorem (we refer, for instance, to [Car67]), we obtain the existence of a local solution for the ODE system (4.3.30) defined on $[0, t_n]$ where t_n only depends on C_0 (introduced in (4.3.28)). This completes the proof. □

Lemma 4.3.2.2. *For all $n \in \mathbb{N}^*$, the matrix $\boldsymbol{M}$ is positive definite.*

Proof. We can decompose $\boldsymbol{M}$ as $\boldsymbol{M} = C_\mathrm{m}\boldsymbol{N} + \dfrac{1}{n}\boldsymbol{D}$, with

$$\boldsymbol{D} \stackrel{\text{def}}{=} \begin{bmatrix} \boldsymbol{M}_{V_\mathrm{i}} & \vdots & 0 & \vdots & 0 \\ \cdots\cdots & \vdots & \cdots\cdots\cdots & \vdots & \cdots\cdots \\ & \vdots & & \vdots & \\ 0 & \vdots & \boldsymbol{M}_{V_\mathrm{HT}} & \vdots & 0 \\ & \vdots & & \vdots & \\ \cdots\cdots & \vdots & \cdots\cdots\cdots & \vdots & \cdots\cdots \\ 0 & \vdots & 0 & \vdots & n\boldsymbol{M}_{V_\mathrm{i}} \end{bmatrix},$$

and

$$\boldsymbol{N} \overset{\text{def}}{=} \left[\begin{array}{c:c:c} \boldsymbol{M}_{V_{\mathrm{i}}} & -\boldsymbol{M}_{V_{\mathrm{ie}}} & 0 \\ \hdashline -\boldsymbol{M}_{V_{\mathrm{ie}}}{}^{T} & \boldsymbol{M}_{V_{\mathrm{e}}} & 0 \\ \hdashline 0 & 0 & 0 \end{array}\right].$$

Since the matrices $\boldsymbol{M}_{V_{\mathrm{i}}}$, $\boldsymbol{M}_{V_{\mathrm{HT}}}$ and $\boldsymbol{M}_{V_{\mathrm{i}}}$ are mass matrices, we obtain that the block-diagonal matrix D is positive definite. On the other hand, for each $\begin{bmatrix}\boldsymbol{c}_{\mathrm{i}} & \boldsymbol{c} & \boldsymbol{c}_{\mathrm{w}}\end{bmatrix}^{\mathrm{T}} \in \mathbb{R}^{4n}$ we have

$$\begin{aligned}\begin{bmatrix}\boldsymbol{c}_{\mathrm{i}}\\ \boldsymbol{c}\\ \boldsymbol{c}_{\mathrm{w}}\end{bmatrix}^{\mathrm{T}} \boldsymbol{N} \begin{bmatrix}\boldsymbol{c}_{\mathrm{i}}\\ \boldsymbol{c}\\ \boldsymbol{c}_{\mathrm{w}}\end{bmatrix} &= \sum_{l,k=1}^{n} \left(\int_{\Omega_{\mathrm{H}}} c_{\mathrm{i},l} c_{\mathrm{i},k} h_l h_k - 2 \int_{\Omega_{\mathrm{H}}} c_{\mathrm{i},l} c_{2k-1} h_l f_k + \int_{\Omega_{\mathrm{H}}} c_{2l-1} c_{2k-1} f_l f_k \right) \\ &= \left\| \sum_{l,1}^{n} \left(c_{\mathrm{i},l} h_l - c_{2l-1} f_l \right) \right\|^2_{L^2(\Omega_{\mathrm{H}})} \\ &\geq 0,\end{aligned}$$

so that $\boldsymbol{N}$ is positive. It then follows that $\boldsymbol{M}$ is positive definite. □

Remark 4.3.2.3. *The above lemma points out the role of the regularization term* $\frac{1}{n}\boldsymbol{D}$. *It allows to obtain a matrix* $\boldsymbol{M}$ *in* (4.3.30) *which is non-singular, so that the resulting system of ODE is nondegenerate.*

4.3.3 Energy estimates

In the next lemma, we state some uniform estimates (with respect to n) of the solution of problems $\mathbf{P1}_n$ and $\mathbf{P2}_n$. We also provide similar estimates for the time derivative, which will be useful for the passage to the limit. For the sake of clarity, in what follows, $c > 0$ stands for a generic constant which depends on T, on the initial conditions and on the physical parameters, but which is independent of n.

Lemma 4.3.3.1. *Let* $u_{\mathrm{i},0} \in H^1(\Omega_{\mathrm{H}})$, $u_0 \in V$, $w_0 \in L^2(\Omega_{\mathrm{H}})$ *and* $I_{\mathrm{app}} \in L^2(Q_T)$ *be given data and let* $(u_{\mathrm{i},n}, u_n, w_n)$ *be a solution of* $\mathbf{P1}_n$ *defined on* $[0,T']$ *for* $0 < T' < T$. *Assume that* **A1** *holds true. Then, for* $v_n = u_{\mathrm{i},n} - u_{n/\Omega_{\mathrm{H}}}$ *and for all* $n \in \mathbb{N}^*$ *and* $t \in [0,T']$, *we have*

$$\begin{aligned}&\|v_n\|_{L^\infty(0,t;L^2(\Omega_{\mathrm{H}}))} + \|v_n\|_{L^4(Q_t)} + \frac{1}{\sqrt{n}} \left(\|u_{\mathrm{i},n}\|_{L^\infty(0,t;L^2(\Omega_{\mathrm{H}}))} + \|u_n\|_{L^\infty(0,t;L^2(\Omega))} \right) \\ &\qquad + \|\boldsymbol{\nabla} u_{\mathrm{i},n}\|_{L^2(Q_t)} + \|\boldsymbol{\nabla} u_n\|_{L^2((0,t)\times\Omega)} \leq c, \\ &\|\partial_t v_n\|_{L^2(Q_t)} + \|v_n\|_{L^\infty(0,t;H^1(\Omega_{\mathrm{H}}))} + \frac{1}{\sqrt{n}} \left(\|\partial_t u_{\mathrm{i},n}\|_{L^2(Q_t)} + \|\partial_t u_n\|_{L^2((0,t)\times\Omega)} \right) \\ &\qquad + \|\boldsymbol{\nabla} u_{\mathrm{i},n}\|_{L^\infty(0,t;L^2(\Omega_{\mathrm{H}}))} + \|\boldsymbol{\nabla} u_n\|_{L^\infty(0,t;L^2(\Omega))} \leq c,\end{aligned} \tag{4.3.31}$$

and

$$\|w_n\|_{L^\infty(0,t;L^2(\Omega_{\rm H}))} \le c, \quad \|\partial_t w_n\|_{L^2(Q_t)} \le c. \tag{4.3.32}$$

If **A2** *is satisfied and* $w_0 \in L^\infty(\Omega_{\rm H})$ *with* (4.2.23)*, there exists a positive constant* $w_{\min}$ *(independent of* T'*) such that a solution* $(u_{{\rm i},n}, u_n, w_n)$ *of* $\mathbf{P2}_n$ *defined on* $[0,T']$ *for* $T' > 0$ *satisfies* (4.3.31) *and, for all* $t \in [0,T']$

$$\|w_n\|_{W^{1,\infty}(0,t,L^\infty(\Omega_{\rm H}))} \le c, \quad w_{\min} \le w_n \le 1, \quad \textit{in} \quad Q_{T'}. \tag{4.3.33}$$

Proof. We start by proving the estimates for problem $\mathbf{P1}_n$. Taking $h = u_{{\rm i},n}$, $e = -u_n$, $\theta = w_n$ in (4.3.24) and using the uniform coercivity of the conductivity tensors (4.2.11), we obtain:

$$\begin{aligned}\frac{1}{2}\frac{\rm d}{{\rm d}t}\left[\|w_n\|^2_{L^2(\Omega_{\rm H})} + C_{\rm m}\|v_n\|^2_{L^2(\Omega_{\rm H})} + \frac{1}{n}\left(\|u_{{\rm i},n}\|^2_{L^2(\Omega_{\rm H})} + \|u_n\|^2_{L^2(\Omega)}\right)\right] \\ + \alpha_{\rm i}\|\boldsymbol{\nabla} u_{{\rm i},n}\|^2_{L^2(\Omega_{\rm H})} + \alpha\|\boldsymbol{\nabla} u_n\|^2_{L^2(\Omega)} + \int_{\Omega_{\rm H}} I_{\rm ion}(v_n,w_n)v_n \\ + \int_{\Omega_{\rm H}} g(v_n,w_n)w_n \le \int_{\Omega_{\rm H}} I_{\rm app}v_n. \end{aligned} \tag{4.3.34}$$

From assumption **A1**, we get

$$I_{\rm ion}(v,w)v + g(v,w)w \ge a|v|^4 - (c_8|v|^2 + c_9|w|^2) - c_{10},$$

with $c_8, c_9, c_{10} > 0$. Thus, inserting this expression in (4.3.34) and using the Cauchy-Schwarz's inequality, it follows that

$$\begin{aligned}\frac{1}{2}\frac{\rm d}{{\rm d}t}\left[\|w_n\|^2_{L^2(\Omega_{\rm H})} + C_{\rm m}\|v_n\|^2_{L^2(\Omega_{\rm H})} + \frac{1}{n}\left(\|u_{{\rm i},n}\|^2_{L^2(\Omega_{\rm H})} + \|u_n\|^2_{L^2(\Omega)}\right)\right] \\ + \alpha_{\rm i}\|\boldsymbol{\nabla} u_{{\rm i},n}\|^2_{L^2(\Omega_{\rm H})} + \alpha\|\boldsymbol{\nabla} u_n\|^2_{L^2(\Omega)} + a\|v_n\|^4_{L^4(\Omega_{\rm H})} \\ \le \left(c_8 + \frac{1}{2}\right)\|v_n\|^2_{L^2(\Omega_{\rm H})} + c_9\|w_n\|^2_{L^2(\Omega_{\rm H})} + c_{10}|\Omega_{\rm H}| + \frac{1}{2}\|I_{\rm app}\|^2_{L^2(\Omega_{\rm H})}.\end{aligned}$$

Therefore, integrating over $(0,t)$, with $t \in [0,T']$, we have

$$\begin{aligned}\|w_n\|^2_{L^2(\Omega_{\rm H})} + C_{\rm m}\|v_n\|^2_{L^2(\Omega_{\rm H})} + \frac{1}{n}\left(\|u_{{\rm i},n}\|^2_{L^2(\Omega_{\rm H})} + \|u_n\|^2_{L^2(\Omega)}\right) \\ + \alpha_{\rm i}\|\boldsymbol{\nabla} u_{{\rm i},n}\|^2_{L^2(Q_t)} + \alpha\|\boldsymbol{\nabla} u_n\|^2_{L^2(\Omega\times(0,t))} + a\|v_n\|^4_{L^4(Q_t)} \\ \le c\int_0^t \left(\|v_n\|^2_{L^2(\Omega_{\rm H})} + \|w_n\|^2_{L^2(\Omega_{\rm H})}\right) + c_{10}|\Omega_{\rm H}|T + \frac{1}{2}\|I_{\rm app}\|^2_{L^2(Q_T)} \\ + \|w_{0,n}\|^2_{L^2(\Omega_{\rm H})} + C_{\rm m}\|v_{0,n}\|^2_{L^2(\Omega_{\rm H})} + \frac{1}{n}\left(\|u_{{\rm i},0,n}\|^2_{L^2(\Omega_{\rm H})} + \|u_{0,n}\|^2_{L^2(\Omega)}\right),\end{aligned}$$

for all $t \in [0,T']$. Estimates $(4.3.31)_1$ and $(4.3.32)_1$ follow by applying Gronwall lemma and using the fact that, from (4.3.27),

$$\|w_{0,n}\|^2_{L^2(\Omega_{\rm H})} + C_{\rm m}\|v_{0,n}\|^2_{L^2(\Omega_{\rm H})} + \frac{1}{n}\left(\|u_{{\rm i},0,n}\|^2_{L^2(\Omega_{\rm H})} + \|u_{0,n}\|^2_{L^2(\Omega)}\right),$$

is uniformly bounded with respect to n.

For the estimate of the time derivative, following [BK06], we notice that

$$\int_{\Omega_{\mathrm{H}}} f_1(v)\partial_t v = \frac{d}{dt}\int_{\Omega_{\mathrm{H}}} H(v), \quad H(v) \stackrel{\text{def}}{=} \int_0^v f_1. \tag{4.3.35}$$

On the other hand, taking $h = \partial_t u_{\mathrm{i},n}$, $e = \partial_t u_n$ and $\theta = \partial_t w_n$ in (4.3.24) and integrating over $(0,t)$, with $t \in [0,T']$, yields

$$\begin{aligned}
&\|\partial_t w_n\|^2_{L^2(Q_t)} + C_{\mathrm{m}}\|\partial_t v_n\|^2_{L^2(Q_t)} + \frac{1}{n}\left(\|\partial_t u_{\mathrm{i},n}\|^2_{L^2(Q_t)} + \|\partial_t u_n\|^2_{L^2(0,t;L^2(\Omega))}\right)\\
&+ \frac{\alpha_{\mathrm{i}}}{2}\|\boldsymbol{\nabla} u_{\mathrm{i},n}\|^2_{L^2(\Omega_{\mathrm{H}})} + \frac{\alpha}{2}\|\boldsymbol{\nabla} u_n\|^2_{L^2(\Omega)}\\
&\quad\le \frac{1}{2}\int_{\Omega_{\mathrm{H}}} \boldsymbol{\sigma}_{\mathrm{i}}\boldsymbol{\nabla} u_{\mathrm{i},0,n}\cdot\boldsymbol{\nabla} u_{\mathrm{i},0,n} + \frac{1}{2}\int_{\Omega}\boldsymbol{\sigma}\boldsymbol{\nabla} u_{0,n}\cdot\boldsymbol{\nabla} u_{0,n} + \int_{\Omega_{\mathrm{H}}} H(v_{0,n})\\
&- \int_{\Omega_{\mathrm{H}}} H(v_n) + \int_0^t\int_{\Omega_{\mathrm{H}}} I_{\mathrm{app}}\partial_t v_n - \int_0^t\int_{\Omega_{\mathrm{H}}}(f_2(v_n)w_n\partial_t v_n + g(v_n,w_n)\partial_t w_n).
\end{aligned} \tag{4.3.36}$$

It remains now to estimate the right-hand side of this expression. The first two terms can be bounded using (4.3.27). For the third term, we use $(4.2.16)_1$, the continuous embedding of $H^1(\Omega_{\mathrm{H}})$ into $L^4(\Omega_{\mathrm{H}})$ and (4.3.27) to obtain

$$\int_{\Omega_{\mathrm{H}}} |H(v_{0,n})| = \int_{\Omega_{\mathrm{H}}}\left|\int_0^{v_{0,n}} f_1(s)ds\right| \le \int_{\Omega_{\mathrm{H}}} c(v_{0,n}^4 + 1) \le c.$$

For the fourth term, according to assumption (4.2.17), we have $f_1(v)v + bv^2 \ge 0$. In other words, $f_1(v) + bv \ge 0$ for $v \ge 0$, and $f_1(v) + bv \le 0$ for $v \le 0$. As a result, integrating over $(0,v)$ yields

$$-H(v) \le \frac{b}{2}v^2. \tag{4.3.37}$$

On the other hand, the fifth term can be controlled using the Cauchy-Schwarz inequality.

In summary, from (4.3.36) and (4.2.12), we get

$$\begin{aligned}
&\|\partial_t w_n\|^2_{L^2(Q_t)} + \frac{C_{\mathrm{m}}}{2}\|\partial_t v_n\|^2_{L^2(Q_t)} + \frac{1}{n}\|\partial_t u_{\mathrm{i},n}\|^2_{L^2(Q_t)}\\
&+ \frac{1}{n}\|\partial_t u_n\|^2_{L^2(0,t;L^2(\Omega))} + \frac{\alpha_{\mathrm{i}}}{2}\|\boldsymbol{\nabla} u_{\mathrm{i},n}\|^2_{L^2(\Omega_{\mathrm{H}})} + \frac{\alpha}{2}\|\boldsymbol{\nabla} u_n\|^2_{L^2(\Omega)}\\
&\quad\le c + \frac{1}{2C_{\mathrm{m}}}\|I_{\mathrm{app}}\|^2_{L^2(Q_t)} + \frac{b}{2}\|v_n\|^2_{L^2(\Omega_{\mathrm{H}})}\\
&- \int_0^t\int_{\Omega_{\mathrm{H}}} f_2(v_n)w_n\partial_t v_n - \int_0^t\int_{\Omega_{\mathrm{H}}} g_1(v_n)\partial_t w_n - \int_0^t\int_{\Omega_{\mathrm{H}}}\frac{c_1}{2}\partial_t w_n^2.
\end{aligned} \tag{4.3.38}$$

For the last three terms of the right-hand side, we proceed as follows. First, using $(4.2.16)_2$ and Young's inequality, we notice that

$$\begin{aligned}
\left|\int_0^t\int_{\Omega_{\mathrm{H}}} f_2(v_n)w_n\partial_t v_n\right| &= \left|\int_0^t\int_{\Omega_{\mathrm{H}}} c_4\partial_t v_n w_n + c_5 v_n\partial_t v_n w_n\right|\\
&\le \frac{C_{\mathrm{m}}}{4}\|\partial_t v_n\|^2_{L^2(Q_t)} + c\|w_n\|^2_{L^2(Q_t)} + \left|\frac{c_5}{2}\int_0^t\int_{\Omega_{\mathrm{H}}} w_n\partial_t v_n^2\right|.
\end{aligned}$$

In addition, integration by parts in the last term with Young's inequality and Cauchy-Schwarz inequality yields

$$\begin{aligned}\left|\frac{c_5}{2}\int_0^t\int_{\Omega_{\mathrm{H}}} w_n\partial_t v_n^2\right| &\le \frac{|c_5|}{2}\left|\int_0^t\int_{\Omega_{\mathrm{H}}}\partial_t w_n v_n^2\right| + \frac{|c_5|}{2}\int_{\Omega_{\mathrm{H}}}\left|w_n(t)v_n^2(t) - w_{0,n}v_{0,n}^2\right| \\ &\le c\|v_n\|_{L^4(Q_t)}^4 + \frac{1}{4}\|\partial_t w_n\|_{L^2(Q_t)}^2 + c\left(\|v_{0,n}\|_{L^4(\Omega_{\mathrm{H}})}^4 + \|w_{0,n}\|_{L^2(\Omega_{\mathrm{H}})}^2\right) \\ &\quad + c\|w_n(t)\|_{L^2(\Omega_{\mathrm{H}})}\|v_n(t)\|_{L^4(\Omega_{\mathrm{H}})}^2,\end{aligned}$$

where the last term can be estimated by combining Hölder's inequality and the continuous embedding of $H^1(\Omega_{\mathrm{H}})$ in $L^6(\Omega_{\mathrm{H}})$, namely,

$$\|v_n(t)\|_{L^4(\Omega_{\mathrm{H}})}^2 \le \|v_n(t)\|_{L^2(\Omega_{\mathrm{H}})}^{\frac{1}{2}}\|v_n(t)\|_{L^6(\Omega_{\mathrm{H}})}^{\frac{3}{2}} \le c\|v_n(t)\|_{L^2(\Omega_{\mathrm{H}})}^{\frac{1}{2}}\|v_n(t)\|_{H^1(\Omega_{\mathrm{H}})}^{\frac{3}{2}}.$$

Finally, using $(4.2.16)_3$ we have,

$$\left|\int_0^t\int_{\Omega_{\mathrm{H}}} g_1(v_n)\partial_t w_n\right| \le c(|\Omega_{\mathrm{H}}|t + \|v_n\|_{L^4(Q_t)}^4) + \frac{1}{4}\|\partial_t w_n\|_{L^2(Q_t)}^2,$$

and

$$\left|\int_0^t\int_{\Omega_{\mathrm{H}}}\frac{c_1}{2}\partial_t(w_n^2)\right| = \frac{|c_1|}{2}\left|\int_{\Omega_{\mathrm{H}}} w_n^2(t) - \int_{\Omega_{\mathrm{H}}} w_{0,n}^2\right| \le \frac{|c_1|}{2}\|w_n(t)\|_{L^2(\Omega_{\mathrm{H}})}^2 + \frac{|c_1|}{2}\|w_{0,n}\|_{L^2(\Omega_{\mathrm{H}})}^2.$$

As a result, inserting these last estimates in (4.3.38), we obtain

$$\begin{aligned}&\frac{1}{2}\|\partial_t w_n\|_{L^2(Q_t)}^2 + \frac{C_{\mathrm{m}}}{4}\|\partial_t v_n\|_{L^2(Q_t)}^2 + \frac{1}{n}\|\partial_t u_{\mathrm{i},n}\|_{L^2(Q_t)}^2 + \frac{1}{n}\|\partial_t u_n\|_{L^2(0,t;L^2(\Omega))}^2 \\ &\quad + \frac{\alpha_{\mathrm{i}}}{2}\|\boldsymbol{\nabla} u_{\mathrm{i},n}\|_{L^2(\Omega_{\mathrm{H}})}^2 + \frac{\alpha}{2}\|\boldsymbol{\nabla} u_n\|_{L^2(\Omega)}^2 \le c + \frac{1}{2C_{\mathrm{m}}}\|I_{\mathrm{app}}\|_{L^2(Q_t)}^2 + c\|v_n(t)\|_{L^2(\Omega_{\mathrm{H}})}^2 \\ &\quad + c\|w_n\|_{L^2(Q_t)}^2 + c\|v_n\|_{L^4(Q_t)}^4 + c\left(\|v_{0,n}\|_{L^4(\Omega_{\mathrm{H}})}^4 + \|w_{0,n}\|_{L^2(\Omega_{\mathrm{H}})}^2\right) \\ &\quad + c\|w_n(t)\|_{L^2(\Omega_{\mathrm{H}})}\|v_n(t)\|_{L^2(\Omega_{\mathrm{H}})}^{\frac{1}{2}}\|v_n(t)\|_{H^1(\Omega_{\mathrm{H}})}^{\frac{3}{2}} + c|\Omega_{\mathrm{H}}|t + c\|w_n(t)\|_{L^2(\Omega_{\mathrm{H}})}^2, \quad (4.3.39)\end{aligned}$$

for all $t \in [0, T']$.

Therefore, using (4.3.27), the previous estimates $(4.3.31)_1$, $(4.3.32)_1$, and since $T' \le T$, inequality (4.3.39) reduces to

$$\begin{aligned}&\frac{1}{2}\|\partial_t w_n\|_{L^2(Q_t)}^2 + \frac{C_{\mathrm{m}}}{4}\|\partial_t v_n\|_{L^2(Q_t)}^2 + \frac{1}{n}\|\partial_t u_{\mathrm{i},n}\|_{L^2(Q_t)}^2 + \frac{1}{n}\|\partial_t u_n\|_{L^2(0,t;L^2(\Omega))}^2 \\ &\quad + \frac{\alpha_{\mathrm{i}}}{2}\|\boldsymbol{\nabla} u_{\mathrm{i},n}\|_{L^2(\Omega_{\mathrm{H}})}^2 + \frac{\alpha}{2}\|\boldsymbol{\nabla} u_n\|_{L^2(\Omega)}^2 \le c\left(1 + \|v_n(t)\|_{H^1(\Omega_{\mathrm{H}})}^{\frac{3}{2}}\right),\end{aligned}$$

for all $t \in [0, T']$. In particular, using estimates $(4.3.31)_1$, we obtain

$$\frac{1}{2}\min(\alpha, \alpha_i)\|v_n(t)\|_{H^1(\Omega_{\mathrm{H}})}^2 \le c\left(1 + \|v_n(t)\|_{H^1(\Omega_{\mathrm{H}})}^{\frac{3}{2}}\right),$$

so that v_n is uniformly bounded in $L^\infty(0, T'; H^1(\Omega_{\mathrm{H}}))$. Hence, we obtain the desired estimates $(4.3.31)_2$ and $(4.3.32)_2$.

Now, we consider problem $\mathbf{P2}_n$, by proving the estimate (4.3.33). From $(4.3.26)_1$ it follows that $\partial_t w_n = -g(v_n, w_n)$ and, on the other hand, according to (4.2.15), we have $0 \leq h_\infty \leq 1$. Thus, from $(4.2.13)_2$ we have, *a.e.* in $[0, T']$,

$$\begin{aligned} \partial_t w_n \geq & - w_n \Big(\frac{1}{\tau_{\text{close}}} + \frac{\tau_{\text{close}} - \tau_{\text{open}}}{\tau_{\text{close}} \tau_{\text{open}}} h_\infty(v_n) \Big), \\ \partial_t w_n \leq & (1 - w_n) \Big(\frac{1}{\tau_{\text{close}}} + \frac{\tau_{\text{close}} - \tau_{\text{open}}}{\tau_{\text{close}} \tau_{\text{open}}} h_\infty(v_n) \Big), \end{aligned} \tag{4.3.40}$$

which combined with Gronwall lemma yields

$$\begin{aligned} w_n \geq & \, w_0 \exp \left[- \int_0^t \left(\frac{1}{\tau_{\text{close}}} + \frac{\tau_{\text{close}} - \tau_{\text{open}}}{\tau_{\text{close}} \tau_{\text{open}}} h_\infty(v_n) \right) \right], \\ w_n \leq & \, 1 - (1 - w_0) \exp \left[- \int_0^t \left(\frac{1}{\tau_{\text{close}}} + \frac{\tau_{\text{close}} - \tau_{\text{open}}}{\tau_{\text{close}} \tau_{\text{open}}} h_\infty(v_n) \right) \right]. \end{aligned}$$

Using (4.2.23), we then obtain that

$$w_{\min} \stackrel{\text{def}}{=} r \exp \left(\frac{-T}{\tau_{\text{open}}} \right) \leq w_n \leq 1, \quad a.e. \text{ in } \quad Q_{T'}.$$

On the other hand, combining this estimate with (4.3.40), we get

$$\frac{-1}{\tau_{\text{open}}} \leq \partial_t w_n \leq \frac{1}{\tau_{\text{open}}}, \quad a.e. \text{ in } \quad Q_{T'}.$$

which completes the proof of (4.3.33).

Finally, the energy estimates $(4.3.31)_1$ are obtained in a standard fashion by taking $h = u_{\text{i},n}$ and $e = -u_n$ in $(4.3.24)_{1,2}$, which yields

$$\begin{aligned} \frac{1}{2} \frac{\mathrm{d}}{\mathrm{dt}} \left[C_{\text{m}} \|v_n\|^2_{L^2(\Omega_{\text{H}})} + \frac{1}{n} \left(\|u_{\text{i},n}\|^2_{L^2(\Omega_{\text{H}})} + \|u_n\|^2_{L^2(\Omega)} \right) \right] + \alpha_{\text{i}} \|\boldsymbol{\nabla} u_{\text{i},n}\|^2_{L^2(\Omega_{\text{H}})} \\ + \alpha \|\boldsymbol{\nabla} u_n\|^2_{L^2(\Omega)} + \int_{\Omega_{\text{H}}} I_{\text{ion}}(v_n, w_n) v_n \leq \int_{\Omega_{\text{H}}} I_{\text{app}} v_n. \end{aligned} \tag{4.3.41}$$

Conversely, assumption (4.2.17) and estimate (4.3.33) lead to

$$I_{\text{ion}}(v, w) v \geq \frac{a}{\tau_{\text{in}}} w_{\min} |v|^4 - \left(\frac{b}{\tau_{\text{in}}} + \frac{1}{\tau_{\text{out}}} \right) |v|^2,$$

so that, from (4.3.41), we have

$$\begin{aligned} \frac{1}{2} \frac{\mathrm{d}}{\mathrm{dt}} \left[C_{\text{m}} \|v_n\|^2_{L^2(\Omega_{\text{H}})} + \frac{1}{n} \left(\|u_{\text{i},n}\|^2_{L^2(\Omega_{\text{H}})} + \|u_n\|^2_{L^2(\Omega)} \right) \right] \\ + \alpha_{\text{i}} \|\boldsymbol{\nabla} u_{\text{i},n}\|^2_{L^2(\Omega_{\text{H}})} + \alpha \|\boldsymbol{\nabla} u_n\|^2_{L^2(\Omega)} + \frac{a}{\tau_{in}} w_{\min} \|v_n\|^4_{L^4(\Omega_{\text{H}})} \\ \leq \left(\frac{b}{\tau_{\text{in}}} + \frac{1}{\tau_{\text{out}}} + \frac{1}{2} \right) \|v_n\|^2_{L^2(\Omega_{\text{H}})} + \frac{1}{2} \|I_{\text{app}}\|^2_{L^2(\Omega_{\text{H}})}. \end{aligned}$$

We then obtain the energy estimate $(4.3.31))_1$ by applying Gronwall lemma.

For the estimate on the time derivatives, we take $h = \partial_t u_{\mathrm{i},n}$ and $e = \partial_t u_n$ in (4.3.24) and we integrate over $(0,t)$, with $t \in [0,T']$. Using Cauchy-Schwarz and Young's inequalities, we obtain

$$\begin{aligned}\frac{C_{\mathrm{m}}}{4}\|\partial_t v_n\|^2_{L^2(Q_t)} + \frac{1}{n}\left(\|\partial_t u_{\mathrm{i},n}\|^2_{L^2(Q_t)} + \|\partial_t u_n\|^2_{L^2(0,t;L^2(\Omega))}\right) + \frac{\alpha_{\mathrm{i}}}{2}\|\boldsymbol{\nabla} u_{\mathrm{i},n}\|_{L^2(\Omega_{\mathrm{H}})} \\ + \frac{\alpha}{2}\|\boldsymbol{\nabla} u_n\|_{L^2(\Omega)} \leq c\left(\|\boldsymbol{\nabla} u_{\mathrm{i},0,n}\|^2_{L^2(\Omega_{\mathrm{H}})} + \|\boldsymbol{\nabla} u_{0,n}\|^2_{L^2(\Omega)}\right) + \frac{1}{2C_{\mathrm{m}}}\|I_{\mathrm{app}}\|^2_{L^2(Q_t)} \\ + \frac{1}{\tau^2_{\mathrm{out}} C_{\mathrm{m}}}\|v_n\|^2_{L^2(Q_t)} - \frac{1}{\tau_{\mathrm{in}}}\int_0^t\int_{\Omega_{\mathrm{H}}} w_n f_1(v_n)\partial_t v_n. \quad (4.3.42)\end{aligned}$$

On the other hand, using the same notation in (4.3.35) and the fact that f_1 satisfies $(4.2.16)_1$, the same argument is used to obtain the inequality (4.3.37). Integrating by parts the last term of (4.3.42), we have

$$\begin{aligned}-\int_0^t\int_{\Omega_{\mathrm{H}}} w_n f_1(v_n)\partial_t v_n &= -\int_0^t\int_{\Omega_{\mathrm{H}}} w_n \partial_t H(v_n) \\ &= -\int_{\Omega_{\mathrm{H}}} w_n H(v_n) + \int_{\Omega_{\mathrm{H}}} w_0 H(v_{0,n}) + \int_0^t\int_{\Omega_{\mathrm{H}}} \partial_t w_n H(v_n) \\ &\leq c\|w_n(t)\|_{L^\infty(\Omega_{\mathrm{H}})}\|v_n(t)\|^2_{L^2(\Omega_{\mathrm{H}})} \\ &\quad + c\|w_0\|_{L^\infty(\Omega_{\mathrm{H}})}\left(1 + \|v_{0,n}\|^4_{L^4(\Omega_{\mathrm{H}})}\right) \\ &\quad + c\|\partial_t w_n\|_{L^\infty(Q_t)}\left(1 + \|v_n\|^4_{L^4(Q_t)}\right).\end{aligned}$$

Therefore, inserting this estimate in (4.3.42), using (4.3.27) and the previous estimates $(4.3.31)_1$ and (4.3.33), we obtain $(4.3.31)_2$, which completes the proof of Lemma 4.3.3.1. □

4.3.4 Weak solution of the bidomain-torso problem

First of all, we notice that energy estimates allow to extend the existence time of our discrete solution $(u_{i,n}, u_n, w_n)$. Indeed, according to Lemma 4.3.3.1, the solution satisfies, for all $t \in [0,T']$ where T' is the existence time,

$$\|u_{i,n}(t)\|_{H^1(\Omega_{\mathrm{H}})} + \|u_n(t)\|_{H^1(\Omega)} + \|w_n(t)\|_{L^2(\Omega_{\mathrm{H}})} \leq C_1.$$

Applying iteratively Lemma 4.3.2.1, we thus obtain the existence of solution up to an arbitrary time T.

We want now to pass to the limit when n goes to infinity. We first consider problem **P1**. Let us multiply (4.3.24) by a function $\alpha \in \mathcal{D}(0,T)$ and integrate between 0 and T. For all $k \leq n$, we have

$$\begin{aligned}C_{\mathrm{m}}\int_0^T\int_{\Omega_{\mathrm{H}}} \alpha\,\partial_t v_n h_k + \frac{1}{n}\int_0^T\int_{\Omega_{\mathrm{H}}} \alpha\,\partial_t u_{\mathrm{i},n} h_k + \int_0^T\int_{\Omega_{\mathrm{H}}} \alpha\,\boldsymbol{\sigma}_{\mathrm{i}}\boldsymbol{\nabla} u_{\mathrm{i},n}\cdot\boldsymbol{\nabla} h_k \\ + \int_0^T\int_{\Omega_{\mathrm{H}}} \alpha\, I_{\mathrm{ion}}(v_n, w_n)h_k = \int_0^T\int_{\Omega_{\mathrm{H}}} \alpha\, I_{\mathrm{app}} h_k,\end{aligned} \quad (4.3.43)$$

$$
\begin{aligned}
&C_{\mathrm{m}} \int_0^T \int_{\Omega_{\mathrm{H}}} \alpha\, \partial_t v_n e_k - \frac{1}{n} \int_0^T \int_{\Omega} \alpha\, \partial_t u_n e_k - \int_0^T \int_{\Omega} \alpha\, \boldsymbol{\sigma} \boldsymbol{\nabla} u_n \cdot \boldsymbol{\nabla} e_k \\
&+ \int_0^T \int_{\Omega_{\mathrm{H}}} \alpha\, I_{\mathrm{ion}}(v_n, w_n) e_k = \int_0^T \int_{\Omega_{\mathrm{H}}} \alpha\, I_{\mathrm{app}} e_k
\end{aligned} \tag{4.3.44}
$$

$$
\int_0^T \int_{\Omega_{\mathrm{H}}} \alpha\, \partial_t w_n h_k + \int_0^T \int_{\Omega_{\mathrm{H}}} \alpha\, g(v_n, w_n) h_k = 0. \tag{4.3.45}
$$

From Lemma 4.3.3.1, it follows that there exists four functions $u \in L^\infty(0,T;V)$, $v_{\mathrm{m}} \in L^\infty(0,T;H^1(\Omega_{\mathrm{H}})) \cap L^4(Q_T) \cap H^1(0,T;L^2(\Omega_{\mathrm{H}}))$, $u_{\mathrm{i}} \in L^\infty(0,T;H^1(\Omega_{\mathrm{H}}))$ and $w \in H^1(0,T;L^2(\Omega_{\mathrm{H}}))$ such that, up to extracted subsequences, we have:

$$
\begin{cases}
u_n \to u \text{ in } L^\infty(0,T;V) \text{ weak } *, \\
v_n \to v_{\mathrm{m}} \text{ in } L^\infty(0,T;H^1(\Omega_{\mathrm{H}})) \text{ weak } *, \\
v_n \to v_{\mathrm{m}} \text{ weakly in } L^4(Q_T), \\
v_n \to v_{\mathrm{m}} \text{ weakly in } H^1(0,T;L^2(\Omega_{\mathrm{H}})), \\
u_{\mathrm{i},n} \to u_{\mathrm{i}} \text{ in } L^\infty(0,T;H^1(\Omega_{\mathrm{H}})) \text{ weak } *, \\
w_n \to w \text{ weakly in } H^1(0,T;L^2(\Omega_{\mathrm{H}})).
\end{cases} \tag{4.3.46}
$$

Moreover, according to Lemma 4.3.3.1, we also notice that $\frac{1}{\sqrt{n}} u_{\mathrm{i},n}$ and $\frac{1}{\sqrt{n}} u_n$ are bounded in $L^\infty(0,T;L^2(\Omega_{\mathrm{H}}))$ and $L^\infty(0,T;L^2(\Omega))$, respectively. Thus, for all $k \in \mathbb{N}^*$ and $\alpha \in \mathcal{D}(0,T)$, we have

$$
\lim_{n\to+\infty} \frac{1}{n} \int_0^T \int_{\Omega_{\mathrm{H}}} \alpha\, \partial_t u_{\mathrm{i},n} h_k = 0, \quad \lim_{n\to+\infty} \frac{1}{n} \int_0^T \int_{\Omega} \alpha\, \partial_t u_n e_k = 0.
$$

Let us consider now the nonlinear terms in (4.3.43)-(4.3.45). Since $\{v_n\}$ is bounded in $L^2(0,T;H^1(\Omega_{\mathrm{H}})) \cap H^1(0,T;L^2(\Omega_{\mathrm{H}}))$, we have that $\{v_n\}$ is bounded in $H^1(Q_T)$. Hence, thanks to the compact embedding of $H^1(Q_T)$ in $L^3(Q_T)$, the sequence $\{v_n\}$ strongly converges to v_{m} in $L^3(Q_T)$. In addition, using the Lebesgue's dominated convergence theorem, we deduce that there exists a positive function $\mathcal{V} \in L^1(Q_T)$ such that, up to extraction, $v_n^3 \leq \mathcal{V}$ and that $v_n \to v_{\mathrm{m}}$ *a.e.* in Q_T. Thus, from $(4.2.16)_1$ and using once again the Lebesgue's dominated convergence theorem, it follows that $\{f_1(v_n)\}$ strongly converges to $f_1(v_{\mathrm{m}})$ in $L^1(Q_T)$. As a result,

$$
\lim_{n\to+\infty} \int_0^T \int_{\Omega_{\mathrm{H}}} \alpha\, f_1(v_n) h_k = \int_0^T \int_{\Omega_{\mathrm{H}}} \alpha\, f_1(v_{\mathrm{m}}) h_k.
$$

On the other hand, since $\{w_n\}$ is bounded in $L^2(Q_T)$ and $\{v_n\}$ strongly converges to v_{m} in $L^2(Q_T)$, we have

$$
\lim_{n\to+\infty} \int_0^T \int_{\Omega_{\mathrm{H}}} \alpha\, f_2(v_n) w_n h_k = \int_0^T \int_{\Omega_{\mathrm{H}}} \alpha\, f_2(v_{\mathrm{m}}) w h_k.
$$

Thus, in summary,

$$
\lim_{n\to+\infty} \int_0^T \int_{\Omega_{\mathrm{H}}} \alpha\, I_{\mathrm{ion}}(v_n, w_n) h_k = \int_0^T \int_{\Omega_{\mathrm{H}}} \alpha\, I_{\mathrm{ion}}(v_{\mathrm{m}}, w) h_k.
$$

Similar arguments allow to prove that

$$\lim_{n\to+\infty}\int_0^T\int_{\Omega_{\rm H}}\alpha\, g(v_n)h_k=\int_0^T\int_{\Omega_{\rm H}}\alpha\, g(v_{\rm m})h_k.$$

We can then pass to the limit in n in (4.3.43)-(4.3.45), yielding

$$\begin{aligned}C_{\rm m}\int_0^T\int_{\Omega_{\rm H}}\alpha\,\partial_t v_{\rm m}h_k+\int_0^T\int_{\Omega_H}\alpha\,\boldsymbol{\sigma}_{\rm i}\boldsymbol{\nabla}u_{\rm i}\cdot\boldsymbol{\nabla}h_k\\ +\int_0^T\int_{\Omega_H}\alpha\, I_{\rm ion}(v_{\rm m},w)h_k=\int_0^T\int_{\Omega_H}\alpha\, I_{\rm app}h_k,\end{aligned}\tag{4.3.47}$$

$$\begin{aligned}C_{\rm m}\int_0^T\int_{\Omega_{\rm H}}\alpha\,\partial_t v_{\rm m}e_k-\int_0^T\int_{\Omega}\alpha\,\boldsymbol{\sigma}\boldsymbol{\nabla}u\cdot\boldsymbol{\nabla}e_k\\ +\int_0^T\int_{\Omega_H}\alpha\, I_{\rm ion}(v_{\rm m},w)e_k=\int_0^T\int_{\Omega_H}\alpha\, I_{\rm app}e_k,\end{aligned}\tag{4.3.48}$$

$$\int_0^T\int_{\Omega_{\rm H}}\alpha\,\partial_t w h_k+\alpha\, g(v_{\rm m},w)h_k=0,\tag{4.3.49}$$

for all $k\in\mathbb{N}^*$ and $\alpha\in\mathcal{D}(0,T)$. We obtain (4.2.20)-(4.2.22) from the density properties of the spaces spanned by $\{h_k\}_{k\in\mathbb{N}^*}$ and $\{e_k\}_{k\in\mathbb{N}^*}$.

Finally, it only remains to prove that $v_{\rm m}$ and w satisfy the initial conditions (4.1.5). Since (v_n) weakly converges to $v_{\rm m}$ in $H^1(0,T;L^2(\Omega_{\rm H}))$, (v_n) strongly converges to $v_{\rm m}$ in $C(0,T;H^{-1}(\Omega_{\rm H}))$ for instance. This allows to assert that $v_{\rm m}(0)=v_0$ in $\Omega_{\rm H}$ since, by construction, $v_n(0)\to v_0$ in $L^2(\Omega_{\rm H})$. The same argument holds for w.

For problem **P2**, the arguments of passing to the limit can be adapted without major modifications. For the nonlinear terms, we can (as previously) prove that $\{v_n\}$ strongly converges to $v_{\rm m}$ in $L^3(Q_T)$. Thus $f_1(v_n)$ strongly converges to $f_1(v_{\rm m})$ in $L^1(Q_T)$. Since

$$w_n\to w \text{ in } L^\infty(Q_T) \text{ weak } *,$$

this allows to prove that

$$\lim_{n\to+\infty}\int_0^T\int_{\Omega_{\rm H}}\alpha\, I_{\rm ion}(v_n,w_n)h_k=\int_0^T\int_{\Omega_{\rm H}}\alpha\, I_{\rm ion}(v_{\rm m},w)h_k.$$

Moreover, since $h_\infty(v_n)\to h_\infty(v_{\rm m})$ a.e. in Q_T and $\{h_\infty(v_n)\}$ is bounded in $L^\infty(Q_T)$, $\{h_\infty(v_n)\}$ strongly converges in $L^2(Q_T)$ to $h_\infty(v_{\rm m})$. Thus we can also pass to the limit in equation (4.3.26). This allows to obtain a weak solution of **P2** as defined by Definition 4.2.0.2.

4.4 Uniqueness of the weak solution

In this paragraph, we prove the uniqueness of weak solution for problem **P1**, under the additional assumption **A3**. This is a direct consequence of the following *comparison Lemma*.

Lemma 4.4.0.1. *Assume that assumption* **A3** *holds and that*

$$(v_{\mathrm{m},1}, u_{\mathrm{i},1}, u_1, w_1), \quad (v_{\mathrm{m},2}, u_{\mathrm{i},2}, u_2, , w_2),$$

are two weak solutions of problem **P1** *corresponding, respectively, to the initial data* $(v_{1,0}, w_{1,0})$ *and* $(v_{2,0}, w_{2,0})$*, and right-hand sides* $I_{\mathrm{app},1}$ *and* $I_{\mathrm{app},2}$*. For all* $t \in (0,T)$*, there holds*

$$\begin{aligned}
&\|v_1(t) - v_2(t)\|^2_{L^2(\Omega_{\mathrm{H}})} + \|w_1(t) - w_2(t)\|^2_{L^2(\Omega_{\mathrm{H}})} \\
&\quad \leq \exp(K_1 t)\, K_2 \Big(\|v_{1,0} - v_{2,0}\|^2_{L^2(\Omega_{\mathrm{H}})} + |w_{1,0} - w_{2,0}|^2_{L^2(\Omega_{\mathrm{H}})} + \|I_{\mathrm{app},1} - I_{\mathrm{app},2}\|^2_{L^2(Q_t)} \Big),
\end{aligned}$$

with $K_1, K_2 > 0$ *positive constants only depending on* C_{m}*,* μ_0 *and* C_{ion}*.*

Proof. The proof follows the argument provided in [BCP09] for the isolated bidomain equations. According to Definition 4.2.0.2, we have, for all $\phi_{\mathrm{i}} \in L^2(0,T;H^1(\Omega_{\mathrm{H}}))$, $\psi \in L^2(0,T;V)$ and $\theta \in L^2(0,T;L^2(\Omega_{\mathrm{H}})$,

$$\begin{aligned}
&C_{\mathrm{m}} \int_0^t \int_{\Omega_{\mathrm{H}}} \partial_t (v_1 - v_2)\phi_{\mathrm{i}} + \int_0^t \int_{\Omega_{\mathrm{H}}} \boldsymbol{\sigma}_{\mathrm{i}} (\boldsymbol{\nabla} u_{\mathrm{i},1} - \boldsymbol{\nabla} u_{\mathrm{i},2}) \cdot \boldsymbol{\nabla} \phi_{\mathrm{i}} \\
&\qquad + \int_0^t \int_{\Omega_{\mathrm{H}}} (I_{\mathrm{ion}}(v_1, w_1) - I_{\mathrm{ion}}(v_2, w_2))\phi_{\mathrm{i}} = \int_0^t \int_{\Omega_{\mathrm{H}}} (I_{\mathrm{app},1} - I_{\mathrm{app},2})\phi_{\mathrm{i}}, \\
&C_{\mathrm{m}} \int_0^t \int_{\Omega_{\mathrm{H}}} \partial_t (v_1 - v_2)\psi - \int_0^t \int_{\Omega} \boldsymbol{\sigma} (\boldsymbol{\nabla} u_1 - \boldsymbol{\nabla} u_2) \cdot \boldsymbol{\nabla} \psi \\
&\qquad + \int_0^t \int_{\Omega_{\mathrm{H}}} (I_{\mathrm{ion}}(v_1, w_1) - I_{\mathrm{ion}}(v_2, w_2))\psi = \int_0^t \int_{\Omega_{\mathrm{H}}} (I_{\mathrm{app},1} - I_{\mathrm{app},2})\psi, \\
&\int_0^t \int_{\Omega_{\mathrm{H}}} \partial_t (w_1 - w_2)\theta + \int_0^t \int_{\Omega_{\mathrm{H}}} (g(v_1, w_1) - g(v_2, w_2))\theta = 0.
\end{aligned}$$

For $\mu > 0$, we take in this expression $\phi_{\mathrm{i}} = \mu(u_{\mathrm{i},1} - u_{\mathrm{i},2})$, $\psi = -\mu(u_1 - u_2)$ and $\theta = w_1 - w_2$. Thus, adding the resulting equalities, we have

$$\begin{aligned}
&\frac{\mu C_{\mathrm{m}}}{2} \|v_1(t) - v_2(t)\|^2_{L^2(\Omega_{\mathrm{H}})} + \frac{1}{2} \|w_1(t) - w_2(t)\|^2_{L^2(\Omega_{\mathrm{H}})} \\
&\qquad + \mu \Big(\alpha_{\mathrm{i}} \|\boldsymbol{\nabla}(u_{\mathrm{i},1} - u_{\mathrm{i},2})\|^2_{L^2(Q_t)} + \alpha \|\boldsymbol{\nabla}(u_1 - u_2)\|^2_{L^2(\Omega \times (0,t))} \Big) \\
&\qquad + \mu \int_0^t \int_{\Omega_{\mathrm{H}}} (I_{\mathrm{ion}}(v_1, w_1) - I_{\mathrm{ion}}(v_2, w_2))(v_1 - v_2) \\
&\qquad + \int_0^t \int_{\Omega_{\mathrm{H}}} (g(v_1, w_1) - g(v_2, w_2))(w_1 - w_2) \\
&\leq \frac{\mu C_{\mathrm{m}}}{2} \|v_{1,0} - v_{2,0}\|^2_{L^2(\Omega_{\mathrm{H}})} + \frac{1}{2} \|w_{1,0} - w_{2,0}\|^2_{L^2(\Omega_{\mathrm{H}})} \\
&\qquad + \frac{\mu^2}{2} \|I_{\mathrm{app},1} - I_{\mathrm{app},2}\|^2_{L^2(Q_t)} + \frac{1}{2} \|v_1 - v_2\|^2_{L^2(Q_t)}.
\end{aligned} \tag{4.4.50}$$

Let $\mu_0 > 0$ the parameter provided by assumption **A3**. We define

$$\begin{aligned}
\Phi(v_1, w_1, v_2, w_2) \overset{\text{def}}{=} &\int_{\Omega_{\mathrm{H}}} \mu_0 \big(I_{\mathrm{ion}}(v_1, w_1) - I_{\mathrm{ion}}(v_2, w_2) \big)(v_1 - v_2) \\
&+ \int_{\Omega_{\mathrm{H}}} \big(g(v_1, w_1) - g(v_2, w_2) \big)(w_1 - w_2),
\end{aligned} \tag{4.4.51}$$

Denoting $z \stackrel{\text{def}}{=} (v, w)$ and using **A3**, we have

$$\Phi(v_1, w_1, v_2, w_2) = \Phi(z_1, z_2) = \int_{\Omega_{\mathrm{H}}} \big(F_{\mu_0}(z_1) - F_{\mu_0}(z_2)\big) \cdot (z_1 - z_2).$$

Since F_{μ_0} is continuously differentiable, a Taylor expansion with integral remainder yields

$$F_{\mu_0}(z_1) - F_{\mu_0}(z_2) = \int_0^1 \boldsymbol{\nabla} F_{\mu_0}\big(\xi z_1 + (1-\xi) z_2\big) \cdot (z_1 - z_2)\, \mathrm{d}\xi, \quad \forall\, z_1, z_2 \in \mathbb{R}^2.$$

Inserting this expression in (4.4.51) and using the assumed spectral bound (4.2.18), there follows

$$\begin{aligned}
\Phi(z_1, z_2) &= \int_0^1 \int_{\Omega_{\mathrm{H}}} (z_1 - z_2) \cdot \boldsymbol{\nabla} F_{\mu_0}(\xi z_1 + (1-\xi) z_2) \cdot (z_1 - z_2)\, \mathrm{d}\xi \\
&\geq C_{\mathrm{ion}} \int_0^1 \|z_1 - z_2\|^2_{L^2(\Omega_{\mathrm{H}})}\, \mathrm{d}\xi \\
&= C_{\mathrm{ion}} (\|v_1 - v_2\|^2_{L^2(\Omega_{\mathrm{H}})} + \|w_1 - w_2\|^2_{L^2(\Omega_{\mathrm{H}})}).
\end{aligned}$$

Therefore, from (4.4.50) with $\mu = \mu_0$, we have

$$\begin{aligned}
&\frac{\mu_0 C_{\mathrm{m}}}{2} \|v_1(t) - v_2(t)\|^2_{L^2(\Omega_{\mathrm{H}})} + \frac{1}{2} \|w_1(t) - w_2(t)\|^2_{L^2(\Omega_{\mathrm{H}})} \\
&\leq \frac{\mu C_{\mathrm{m}}}{2} \|v_{1,0} - v_{2,0}\|^2_{L^2(\Omega_{\mathrm{H}})} + \frac{1}{2} \|w_{1,0} - w_{2,0}\|^2_{L^2(\Omega_{\mathrm{H}})} + \frac{\mu^2}{2} \|I_{\mathrm{app},1} - I_{\mathrm{app},2}\|^2_{L^2(Q_t)} \\
&\qquad + \left| \frac{1}{2} - C_{\mathrm{ion}} \right| \|v_1 - v_2\|^2_{L^2(Q_t)} + |C_{\mathrm{ion}}| \|w_1 - w_2\|^2_{L^2(Q_t)}.
\end{aligned} \tag{4.4.52}$$

We conclude the proof using Gronwall Lemma. □

Part III

Numerical analysis and Simulation of ECGs

Summary

Chapter 5

Mathematical modeling of Electrocardiograms: A numerical study

This chapter deals with the numerical simulation of electrocardiograms (ECG). Using the heart-torso coupled problem (3.4.24)-(3.4.26), our aim is to find the minimal modeling assumptions allowing to provide realistic 12-lead ECGs. The numerical implementation is based on state-of-the-art numerical methods: domain decomposition techniques and second order semi-implicit time marching schemes, offering a good compromise between accuracy, stability and efficiency. The numerical ECGs obtained with this approach show correct amplitudes, shapes and polarities, in all the 12 standard leads. The relevance of every modeling choice is carefully discussed and the numerical ECG sensitivity to the model parameters investigated.

This chapter is part of a joint work with M. Boulakia, S. Cazeau, M.A. Fernández and J.-F. Gerbeau, reported in [BCF+09].

5.1 Introduction

The electrocardiogram (ECG) is a noninvasive recording of the electrical activity of the heart, obtained from a standard set of skin electrodes and presented to the physician as the "12-lead ECG": that is, 12 graphs of the recorded voltage *vs.* time. The ECG can be considered as the most widely used clinical tool for the detection and diagnosis of a broad range of cardiac conditions (see *e.g.* [Aeh06, Gol06]). Despite that, the clinical significance of some ECG findings is still not fully understood. Computer based simulations of the ECG, linking models of the electrical activity of the heart (in normal or pathological condition) to the ECG signal, can therefore be a valuable tool for improving this knowledge. Such an ECG simulator can also be useful in building a virtual data base of pathological conditions, in order to test and train medical devices [EFG+09]. Moreover, being able to simulate realistic ECGs is a necessary step toward the development of patient-specific models from clinical ECG data.

The mathematical modeling of the ECG is known as the forward problem of electro-

cardiography [LBG+03]. It relies on three main ingredients: a model for the electrical activity of the heart, a model for the torso (extracardiac regions) and some specific heart-torso coupling conditions. Within each of these components, several options are possible, with different levels of complexity and realism (see [LBG+03] for a recent comprehensive review).

Although many works have been devoted to the numerical simulation of cardiac electrophysiology (see *e.g.* the monographs [Sac04, PBC05, SLC+06] and the references therein), only a small number [Hui98, PDG03, LBG+03, KSW+07, TDP+04, PDV09] addresses the numerical simulation of ECGs using a whole-heart reaction-diffusion (*i.e.* bidomain or monodomain) model. Among them, only a very few [PDG03, PDV09] provide meaningful simulations of the complete 12-lead ECG. These simulations rely on a monodomain description of the electrical activity the heart, a decoupling of the heart and the torso (isolated heart assumption) and a multi-dipole approximation of the cardiac source within the torso (see [LBG+03, Section 4.2.4] and [Gul88]). To the best of our knowledge, none of the existing approaches based on partial differential equations (PDE) and a fully coupled heart-torso formulation (see *e.g.* [LBG+03, Section 4.6] and [SLC+06]) have shown realistic 12-lead ECG simulations.

The main ingredients of our mathematical ECG model are standard (see *e.g.* [PBC05, SLC+06, LBG+03]): bidomain equations and phenomenological cell model for the heart, and a generalized Laplace equation for the torso. Nevertheless, once these ingredients have been chosen, several other critical aspects have to be elucidated: heart-torso transmission conditions, cell heterogeneity, His bundle modeling, anisotropy, *etc.*

The purpose of the present work is therefore twofold: first, provide realistic simulations of the 12-lead ECG based on a complete PDE model with a fully coupled heart-torso formulation; second, discuss through numerical simulations the impact of various modeling options and the sensitivity to the model parameters. Note that the achievement of these two goals is a fundamental step prior to addressing the inverse problem of electrocardiography, which consists in identifying the ECG model parameters from clinical ECG data.

The numerical methods proposed to solve the problem offer a good balance between efficiency, stability and accuracy. The PDE system made of the heart and torso models is solved using a finite element method and a second order semi-implicit time marching scheme (see *e.g.* [QSS07]). The coupling conditions at the heart-torso interface are enforced by a Dirichlet-Neumann domain decomposition algorithm (see *e.g.* [QV99, TW05]).

The remainder of this chapter is organized as follows. The ECG model equations are presented in section 5.2. Section 5.3 is devoted to the description of the numerical algorithm. The numerical ECGs obtained with the resulting computational model, under a healthy and a pathological (bundle branch block) condition, are presented and discussed in section 5.4. Section 5.5 investigates the impact, on the ECG, of various modeling assumptions: heart-torso uncoupling, monodomain approximation, isotropy, cell homogeneity, resistance-capacitance behavior of the pericardium. In section 5.6, we present a time and space convergence study in terms of the ECG. The sensitivity of the ECG to the main model parameters is also investigated. At last, conclusions and some lines of forthcoming research are drawn in section 5.7.

5.2 Modeling

This section contains standard material (see *e.g.* [SLC+06, Chapter 2]). It introduces notation and the coupled system of partial and ordinary differential equations (PDE/ODE) involved in the reference mathematical model considered in this chapter.

5.2.1 Heart tissue

Our reference model for the electrical activity of the heart is the so-called bidomain model [Tun78, SLC+06, PBC05]. This macroscopic model is based on the assumption that, at the cell scale, the cardiac tissue can be viewed as partitioned into two ohmic conducting media, separated by the cell membrane: intracellular, made of the cardiac cells, and extracellular which represents the space between them. After an homogenization process (see [NK93, PSF06]), the intra- and extracellular domains can be supposed to occupy the whole heart volume Ω_{H} (this also applies to the cell membrane). Hence, the averaged intra- and extracellular densities of current, $\boldsymbol{j}_{\mathrm{i}}$ and $\boldsymbol{j}_{\mathrm{e}}$, conductivity tensors, $\boldsymbol{\sigma}_{\mathrm{i}}$ and $\boldsymbol{\sigma}_{\mathrm{e}}$, and electric potentials, u_{i} and u_{e}, are defined in Ω_{H}. The electrical charge conservation becomes

$$\operatorname{div}(\boldsymbol{j}_{\mathrm{i}} + \boldsymbol{j}_{\mathrm{e}}) = 0, \quad \text{in} \quad \Omega_{\mathrm{H}}, \tag{5.2.1}$$

and the homogenized equation of the electrical activity of the cell membrane is given by

$$A_{\mathrm{m}} \left(C_{\mathrm{m}} \frac{\partial V_{\mathrm{m}}}{\partial t} + I_{\mathrm{ion}}(V_{\mathrm{m}}, w) \right) + \operatorname{div}(\boldsymbol{j}_{\mathrm{i}}) = A_{\mathrm{m}} I_{\mathrm{app}}, \quad \text{in} \quad \Omega_{\mathrm{H}}, \tag{5.2.2}$$

complemented with the Ohm's laws

$$\boldsymbol{j}_{\mathrm{i}} = -\boldsymbol{\sigma}_{\mathrm{i}} \boldsymbol{\nabla} u_{\mathrm{i}}, \quad \boldsymbol{j}_{\mathrm{e}} = -\boldsymbol{\sigma}_{\mathrm{e}} \boldsymbol{\nabla} u_{\mathrm{e}}. \tag{5.2.3}$$

Here, V_{m} stands for the transmembrane potential, defined as

$$V_{\mathrm{m}} \stackrel{\mathrm{def}}{=} u_{\mathrm{i}} - u_{\mathrm{e}}, \tag{5.2.4}$$

A_{m} is a constant representing the rate of membrane area per volume unit and C_{m} the membrane capacitance per area unit. The term $I_{\mathrm{ion}}(V_{\mathrm{m}}, w)$ represents the ionic current across the membrane and I_{app} a given applied current stimulus. Both currents are measured per membrane area unit.

In general, the ionic variable w (possibly vector valued) satisfies a system of ODE of the type:

$$\frac{\partial w}{\partial t} + g(V_{\mathrm{m}}, w) = 0, \quad \text{in} \quad \Omega_{\mathrm{H}}. \tag{5.2.5}$$

The definition of the functions g and I_{ion} depends on the considered cell ionic model (see [Tun78, SLC+06, PBC05] and the references therein). According to their degree of complexity and realism, the ionic models typically fall into one of the following categories (see [PBC05, Chapter 3]): phenomenological (*e.g.* [Fit61, vCD80, FK98, MS03]) or physiological (*e.g.* [BR77, LR91, LR94, NVKN98, DS05]).

In this study, the phenomenological two-variable model proposed by Mitchell and Schaeffer in [MS03] is considered (rescaled version). The functions g and I_{ion} are then

given by

$$I_{\text{ion}}(V_{\text{m}}, w) = -\frac{w}{\tau_{\text{in}}}\frac{(V_{\text{m}} - V_{\text{min}})^2(V_{\text{max}} - V_{\text{m}})}{V_{\text{max}} - V_{\text{min}}} + \frac{1}{\tau_{\text{out}}}\frac{V_{\text{m}} - V_{\text{min}}}{V_{\text{max}} - V_{\text{min}}},$$
$$g(V_{\text{m}}, w) = \begin{cases} \dfrac{w}{\tau_{\text{open}}} - \dfrac{1}{\tau_{\text{open}}(V_{\text{max}} - V_{\text{min}})^2} & \text{if} \quad V_{\text{m}} < V_{\text{gate}}, \\ \dfrac{w}{\tau_{\text{close}}} & \text{if} \quad V_{\text{m}} > V_{\text{gate}}, \end{cases} \tag{5.2.6}$$

where τ_{in}, τ_{out}, τ_{open}, τ_{close}, V_{gate} are given parameters and V_{min}, V_{max} scaling constants (typically -80 and 20 mV, respectively).

Despite its reduced complexity (2 state variables, 5 free parameters), the Mitchell-Schaeffer model integrates relevant physiological properties of the cell membrane: transmembrane potential, activation dynamics and two currents (inward and outward) leading to depolarization and repolarization. Moreover, owing to its planar character, the model can be understood analytically (see *e.g.* [MS03]), which allows to identify how the free parameters affect its behavior (see subsection 5.4.1).

The gate variable w depends on the change-over voltage V_{gate} and on the time constants for opening, τ_{open}, and closing, τ_{close}. The time constants τ_{in} and τ_{close} are respectively related to the length of the depolarization and repolarization (final stage) phases. Typically, these constants are such that $\tau_{\text{in}} \ll \tau_{\text{out}} \ll \tau_{\text{open}}, \tau_{\text{close}}$.

To sum up, the system of equations modeling the electrical activity within the heart is

$$\begin{cases} A_{\text{m}}\left(C_{\text{m}}\dfrac{\partial V_{\text{m}}}{\partial t} + I_{\text{ion}}(V_{\text{m}}, w)\right) - \operatorname{div}(\boldsymbol{\sigma}_{\text{i}}\boldsymbol{\nabla} V_{\text{m}}) - \operatorname{div}(\boldsymbol{\sigma}_{\text{i}}\boldsymbol{\nabla} u_{\text{e}}) = A_{\text{m}} I_{\text{app}}, & \text{in} \quad \Omega_{\text{H}}, \\ -\operatorname{div}((\boldsymbol{\sigma}_{\text{i}} + \boldsymbol{\sigma}_{\text{e}})\boldsymbol{\nabla} u_{\text{e}}) - \operatorname{div}(\boldsymbol{\sigma}_{\text{i}}\boldsymbol{\nabla} V_{\text{m}}) = 0, & \text{in} \quad \Omega_{\text{H}}, \\ \dfrac{\partial w}{\partial t} + g(V_{\text{m}}, w) = 0, & \text{in} \quad \Omega_{\text{H}}, \end{cases} \tag{5.2.7}$$

with g and I_{ion} given by (5.2.6). This system has to be complemented with appropriate initial and boundary conditions. Denoting by V_{m}^0 and w^0 given initial data for the transmembrane potential and the gate variable, the following initial condition must be enforced

$$V_{\text{m}}(\boldsymbol{x}, 0) = V_{\text{m}}^0(\boldsymbol{x}), \quad w(\boldsymbol{x}, 0) = w^0(\boldsymbol{x}) \quad \forall \boldsymbol{x} \in \Omega_{\text{H}}. \tag{5.2.8}$$

As regards the boundary conditions on $\Sigma \overset{\text{def}}{=} \partial\Omega_{\text{H}}$ (see Figure 5.1), it is widely assumed (see *e.g.* [Tun78, KN94, PBC05, SLC+06]) that the intracellular current does not propagate outside the heart. Consequently,

$$\boldsymbol{j}_{\text{i}} \cdot \boldsymbol{n} = \boldsymbol{\sigma}_{\text{i}}\boldsymbol{\nabla} u_{\text{i}} \cdot \boldsymbol{n} = 0, \quad \text{on} \quad \Sigma,$$

where $\boldsymbol{n}$ stands for the outward unit normal to Ω_{H}. Equivalently, and owing to the divergence structure of $(5.2.7)_1$, this condition can be enforced as

$$\boldsymbol{\sigma}_{\text{i}}\boldsymbol{\nabla} V_{\text{m}} \cdot \boldsymbol{n} + \boldsymbol{\sigma}_{\text{i}}\boldsymbol{\nabla} u_{\text{e}} \cdot \boldsymbol{n} = 0, \quad \text{on} \quad \Sigma. \tag{5.2.9}$$

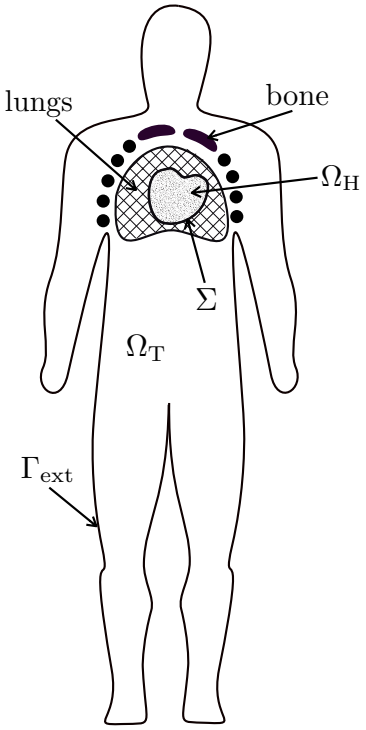

Figure 5.1: Geometry description: the heart domain Ω_H and the torso domain Ω_T (extramyocardial regions)

5.2.2 Coupling with torso

To set up boundary conditions on the extracellular potential u_e, a perfect electric transmission between the heart and the torso domains is generally assumed (see *e.g.* [Tun78, KN94, PBC05, SLC+06]):

$$\begin{cases} u_e = u_T, & \text{on} \quad \Sigma, \\ \boldsymbol{\sigma}_e \boldsymbol{\nabla} u_e \cdot \boldsymbol{n} = \boldsymbol{\sigma}_T \boldsymbol{\nabla} u_T \cdot \boldsymbol{n}, & \text{on} \quad \Sigma. \end{cases} \tag{5.2.10}$$

Here, u_T and $\boldsymbol{\sigma}_T$ stand respectively for the potential and conductivity tensor of the torso tissue, denoted by Ω_T (see Figure 5.1). Note that, with (5.2.9), the current continuity condition $(5.2.10)_2$ is consistent with the divergence structure of $(5.2.7)_2$. Other possible heart-torso transmission conditions will be discussed in sections 5.5.1 and 5.5.5.

Under the quasi-static assumption [MP95], the torso can be viewed as a passive conductor. Therefore, the potential u_T satisfies the generalized Laplace equation:

$$\operatorname{div}(\boldsymbol{\sigma}_T \boldsymbol{\nabla} u_T) = 0, \quad \text{in} \quad \Omega_T. \tag{5.2.11}$$

This equation is complemented with a boundary condition on the external boundary $\Gamma_{ext} \stackrel{\text{def}}{=} \partial\Omega_T \setminus \Sigma$ (see Figure 5.1). Moreover, assuming that no current can flow from the torso across Γ_{ext}, we enforce

$$\boldsymbol{\sigma}_T \boldsymbol{\nabla} u_T \cdot \boldsymbol{n}_T = 0, \quad \text{on} \quad \Gamma_{ext}, \tag{5.2.12}$$

where $\boldsymbol{n}_T$ stands for the outward unit normal to Ω_T.

In summary, our reference model for the ECG is based on the coupled solution of systems (5.2.7), (5.2.6) and (5.2.11), completed with the boundary conditions (5.2.9) and (5.2.12), the interface conditions (5.2.10) and the initial condition (5.2.8). Throughout this study, this system of equations will be termed **RM** (reference model), which is also known in the literature as *full bidomain model* (see *e.g.* [CNLH04b]). The interested reader is referred to Chapter 4 for a proof of the mathematical well-posedness of this system, under appropriate assumptions on the structure of I_{ion} and g.

Although additional complexity and realism can still be introduced through the ionic model (see *e.g.* [BR77, LR91, LR94, NVKN98, DS05]), this coupled system can be considered as the state-of-the-art in the PDE/ODE modeling of the ECG (see *e.g.* [LBG+03]).

5.3 Numerical methods

This section is devoted to a brief presentation of the numerical method used to solve the coupled problem **RM**.

5.3.1 Space and time discretization

The discretization in space is performed by applying the finite element method to an appropriate weak formulation of this coupled problem. Let Ω be the interior of $\overline{\Omega}_{\text{H}} \cup \overline{\Omega}_{\text{T}}$. Problem **RM** can be rewritten in weak form as follows (see Chapter 4): for $t > 0$, $V_{\text{m}}(\cdot, t) \in H^1(\Omega_{\text{H}})$, $w(\cdot, t) \in L^\infty(\Omega_{\text{H}})$ and $u(\cdot, t) \in H^1(\Omega)$, with $\int_{\Omega_{\text{H}}} u = 0$, such that

$$\left\{ \begin{array}{l} A_{\text{m}} \displaystyle\int_{\Omega_{\text{H}}} \Big(C_{\text{m}} \frac{\partial V_{\text{m}}}{\partial t} + I_{\text{ion}}(V_{\text{m}}, w) \Big) \phi + \int_{\Omega_{\text{H}}} \boldsymbol{\sigma}_{\text{i}} \boldsymbol{\nabla}(V_{\text{m}} + u) \cdot \boldsymbol{\nabla}\phi = A_{\text{m}} \int_{\Omega_{\text{H}}} I_{\text{app}} \phi, \\ \displaystyle\int_{\Omega_{\text{H}}} (\boldsymbol{\sigma}_{\text{i}} + \boldsymbol{\sigma}_{\text{e}}) \boldsymbol{\nabla} u \cdot \boldsymbol{\nabla}\psi + \int_{\Omega_{\text{H}}} \boldsymbol{\sigma}_{\text{i}} \boldsymbol{\nabla} V_{\text{m}} \cdot \boldsymbol{\nabla}\psi + \int_{\Omega_{\text{T}}} \boldsymbol{\sigma}_{\text{T}} \boldsymbol{\nabla} u \cdot \boldsymbol{\nabla}\psi = 0, \\ \displaystyle\frac{\partial w}{\partial t} + g(V_{\text{m}}, w) = 0, \quad \text{in} \quad \Omega_{\text{H}}, \end{array} \right. \tag{5.3.13}$$

for all $(\phi, \psi) \in H^1(\Omega_{\text{H}}) \times H^1(\Omega)$, with $\int_{\Omega_{\text{H}}} \psi = 0$. The potentials in the heart and the torso are recovered by setting $u_{\text{e}} = u_{|\Omega_{\text{H}}}$ and $u_{\text{T}} = u_{|\Omega_{\text{T}}}$. Note that this weak formulation (5.3.13) integrates, in a natural way, the coupling conditions (5.2.10).

The space semi-discretized formulation is based on (5.3.13) and obtained by replacing the functional spaces by finite dimensional spaces of continuous piecewise affine functions, $V_h \subset H^1(\Omega_{\text{H}})$ and $W_h \subset H^1(\Omega)$.

The resulting system is discretized in time by combining a second order implicit scheme (backward differentiation formulae, see *e.g.* [QSS07]) with an explicit treatment of the ionic current. We refer to [EB08] for a recent review which suggests the use of second order schemes. Let $N \in \mathbb{N}^*$ be a given integer and consider a uniform partition $\{[t_n, t_{n+1}]\}_{0 \le n \le N-1}$, with $t_n \stackrel{\text{def}}{=} n\delta t$, of the time interval of interest $[0, T]$, with a time-step $\delta t \stackrel{\text{def}}{=} T/N$. Denote by $(V_{\text{m}}^n, u^n, w^n)$ the approximated solution obtained at time t_n. Then, $(V_{\text{m}}^{n+1}, u^{n+1}, w^{n+1})$ is computed as follows: For $0 \le n \le N-1$

1. Second order extrapolation: $\widetilde{V}_{\mathrm{m}}^{n+1} \stackrel{\mathrm{def}}{=} 2V_{\mathrm{m}}^{n} - V_{\mathrm{m}}^{n-1}$;
2. Solve for $w^{n+1} \in V_h$:
$$\frac{1}{\delta t}\left(\frac{3}{2}w^{n+1} - 2w^{n} + \frac{1}{2}w^{n-1}\right) + g(\widetilde{V}_{\mathrm{m}}^{n+1}, w^{n+1}) = 0, \quad \text{(nodal-wise)};$$
3. Ionic current evaluation: $I_{\mathrm{ion}}(\widetilde{V}_{\mathrm{m}}^{n+1}, w^{n+1})$;
4. Solve for $(V_{\mathrm{m}}^{n+1}, u^{n+1}) \in V_h \times W_h$, with $\int_{\Omega_{\mathrm{H}}} u^{n+1} = 0$:
$$\begin{cases} A_{\mathrm{m}}\displaystyle\int_{\Omega_{\mathrm{H}}} \frac{C_{\mathrm{m}}}{\delta t}\left(\frac{3}{2}V_{\mathrm{m}}^{n+1} - 2V_{\mathrm{m}}^{n} + \frac{1}{2}V_{\mathrm{m}}^{n-1}\right)\phi + \int_{\Omega_{\mathrm{H}}} \boldsymbol{\sigma}_{\mathrm{i}}\boldsymbol{\nabla}(V_{\mathrm{m}}^{n+1} + u^{n+1})\cdot\boldsymbol{\nabla}\phi \\ \qquad\qquad = A_{\mathrm{m}}\displaystyle\int_{\Omega_{\mathrm{H}}} \left(I_{\mathrm{app}}(t_{n+1}) - I_{\mathrm{ion}}(\widetilde{V}_{\mathrm{m}}^{n+1}, w^{n+1})\right)\phi, \\ \displaystyle\int_{\Omega_{\mathrm{H}}} (\boldsymbol{\sigma}_{\mathrm{i}} + \boldsymbol{\sigma}_{\mathrm{e}})\boldsymbol{\nabla}u^{n+1}\cdot\boldsymbol{\nabla}\psi + \int_{\Omega_{\mathrm{H}}} \boldsymbol{\sigma}_{\mathrm{i}}\boldsymbol{\nabla}V_{\mathrm{m}}^{n+1}\cdot\boldsymbol{\nabla}\psi + \int_{\Omega_{\mathrm{T}}} \boldsymbol{\sigma}_{\mathrm{T}}\boldsymbol{\nabla}u^{n+1}\cdot\boldsymbol{\nabla}\psi = 0, \end{cases} \tag{5.3.14}$$
for all $(\phi, \psi) \in V_h \times W_h$, with $\displaystyle\int_{\Omega_{\mathrm{H}}} \psi = 0$. Finally, set $u_{\mathrm{e}}^{n+1} = u_{|\Omega_{\mathrm{H}}}^{n+1}$ and $u_{\mathrm{T}}^{n+1} = u_{|\Omega_{\mathrm{T}}}^{n+1}$.

The above algorithm is semi-implicit (or semi-explicit) since, owing to the extrapolation step 1, it allows the uncoupled solution of steps 2 and 4, which are computational demanding. The interested reader is referred to [LBG+03, Section 4.6] for an analogous approach, using a different time discretization scheme and to [SPM08, VWdSP+08, CFP04, GGMN+09, Sca08, PS08] for a description of various computational techniques (preconditioning, parallel computing, etc.) used for the numerical resolution of the bidomain equations.

5.3.2 Partitioned heart-torso coupling

At each time step, the linear problem (5.3.14) requires the coupled solution of the transmembrane potential V_{m}^{n+1} and the heart-torso potential u^{n+1}. This coupling can be solved monolithically, that is, after full assembling of the whole system matrix (see *e.g.* [LBG+03, Sections 4.6 and 4.5.1] and [SLMT02, SLC+06, BP02]). But this results in a increased number of unknowns with respect to the original bidomain system. Moreover, this procedure is less modular since the bidomain and torso equations cannot be solved independently.

This shortcoming can be overcome using a partitioned iterative procedure based on domain decomposition (see *e.g.* [QV99, TW05]). In this study, the heart-torso coupling is solved using the so-called Dirichlet-Neumann algorithm, combined with a specific acceleration strategy. A related approach is adopted in [BP02] (see also [LBG+03, PBC05]), using an integral formulation of the torso equation (5.2.11).

The main idea consists in (k-)iterating between the heart and torso equations via the interface conditions
$$\begin{cases} u_{\mathrm{T}}^{n+1,k+1} = u_{\mathrm{e}}^{n+1,k}, & \text{on} \quad \Sigma, \\ \boldsymbol{\sigma}_{\mathrm{e}}\boldsymbol{\nabla}u_{\mathrm{e}}^{n+1,k+1}\cdot\boldsymbol{n} = \boldsymbol{\sigma}_{\mathrm{T}}\boldsymbol{\nabla}u_{\mathrm{T}}^{n+1,k+1}\cdot\boldsymbol{n}, & \text{on} \quad \Sigma. \end{cases}$$

Hence, the monolithic solution is recovered at convergence. In the framework of $(5.3.14)_2$, this amounts to decompose the discrete test function space W_h as the direct sum $W_h = Z_{h,0} \oplus \mathcal{L}V_h$. The subspace $Z_{h,0}$ contains the functions of W_h vanishing in $\overline{\Omega_{\mathrm{H}}}$, whereas $\mathcal{L}V_h$ is the range of the standard extension operator $\mathcal{L} : V_h \to W_h$ satisfying, for all $\psi_{\mathrm{e}} \in V_h$,

$$\begin{cases} \mathcal{L}\psi_{\mathrm{e}} = \psi_{\mathrm{e}}, & \text{in} \quad \overline{\Omega_{\mathrm{H}}}, \\ \mathcal{L}\psi_{\mathrm{e}} = 0, & \text{on} \quad \Gamma_{\mathrm{ext}}. \end{cases}$$

The full algorithm used in this chapter to solve (5.3.14) reads as follows: For $k \geq 0$, until convergence,

- Torso solution (Dirichlet):

$$u_{\mathrm{T}}^{n+1,k+1} = u_{\mathrm{e}}^{n+1,k}, \quad \text{on} \quad \Sigma,$$
$$\int_{\Omega_{\mathrm{T}}} \boldsymbol{\sigma}_{\mathrm{T}} \boldsymbol{\nabla} u_{\mathrm{T}}^{n+1,k+1} \cdot \boldsymbol{\nabla} \psi_{\mathrm{T}} = 0, \quad \forall \psi_{\mathrm{T}} \in Z_{h,0}.$$

- Heart-bidomain solution (Neumann):

$$\begin{cases} A_{\mathrm{m}} \displaystyle\int_{\Omega_{\mathrm{H}}} \frac{C_{\mathrm{m}}}{\delta t} \left(\frac{3}{2} V_{\mathrm{m}}^{n+1,k+1} - 2V_{\mathrm{m}}^{n} + \frac{1}{2} V_{\mathrm{m}}^{n-1} \right) \phi \\ \qquad\qquad + \displaystyle\int_{\Omega_{\mathrm{H}}} \boldsymbol{\sigma}_{\mathrm{i}} \boldsymbol{\nabla} (V_{\mathrm{m}}^{n+1,k+1} + \widehat{u_{\mathrm{e}}^{n+1,k+1}}) \cdot \boldsymbol{\nabla} \phi \\ \qquad\qquad = A_{\mathrm{m}} \displaystyle\int_{\Omega_{\mathrm{H}}} \left(I_{\mathrm{app}}(t_{n+1}) - I_{\mathrm{ion}}(\widetilde{V}_{\mathrm{m}}^{n+1}, w^{n+1}) \right) \phi, \quad (5.3.15) \\ \displaystyle\int_{\Omega_{\mathrm{H}}} (\boldsymbol{\sigma}_{\mathrm{i}} + \boldsymbol{\sigma}_{\mathrm{e}}) \boldsymbol{\nabla} \widehat{u_{\mathrm{e}}^{n+1,k+1}} \cdot \boldsymbol{\nabla} \psi_{\mathrm{e}} + \int_{\Omega_{\mathrm{H}}} \boldsymbol{\sigma}_{\mathrm{i}} \boldsymbol{\nabla} V_{\mathrm{m}}^{n+1,k+1} \cdot \boldsymbol{\nabla} \psi_{\mathrm{e}} \\ \qquad\qquad = - \displaystyle\int_{\Omega_{\mathrm{T}}} \boldsymbol{\sigma}_{\mathrm{T}} \boldsymbol{\nabla} u_{\mathrm{T}}^{n+1,k+1} \cdot \boldsymbol{\nabla} \mathcal{L} \psi_{\mathrm{e}}, \end{cases}$$

  for all $\phi \in V_h$ and $\psi_{\mathrm{e}} \in V_h$, with $\displaystyle\int_{\Omega_{\mathrm{H}}} \psi_{\mathrm{e}} = 0$.

- Relaxation step:

$$u_{\mathrm{e}}^{n+1,k+1}{}_{|\Sigma} \longleftarrow \omega_k \widehat{u_{\mathrm{e}}^{n+1,k+1}}{}_{|\Sigma} + (1 - \omega_k) u_{\mathrm{e}}^{n+1,k}{}_{|\Sigma}.$$

The coefficient ω_k is a dynamic relaxation parameter which aims to accelerate the convergence of the iterations. In this work, the following explicit expression, based on a multidimensional Aitken formula (see *e.g.* [IT69]), has been considered

$$\omega_k = \frac{\left(\lambda^k - \lambda^{k-1}\right) \cdot \left(\lambda^k - \widehat{\lambda}^{k+1} - \lambda^{k-1} + \widehat{\lambda}^k\right)}{\left|\lambda^k - \widehat{\lambda}^{k+1} - \lambda^{k-1} + \widehat{\lambda}^k\right|^2}, \quad \lambda^k \stackrel{\text{def}}{=} u_{\mathrm{e}}^{n+1,k}{}_{|\Sigma}.$$

5.4 Numerical results

In this section, it is shown that the full PDE/ODE based model **RM**, completed by additional modeling assumptions, allows to get meaningful 12-lead ECG signals. Moreover, the predictive capabilities of the model are illustrated by providing realistic numerical ECG signals for some known pathologies, without any other calibration of the model than those directly related to the pathology.

5.4.1 Reference simulation

Throughout this chapter, the terminology "reference simulation" (or **RS**) refers to the 12-lead numerical ECG signals obtained by solving the reference model **RM** of section 5.2 with the numerical method described in section 5.3 and the modeling assumption described in the following paragraphs. The model parameters used in the **RS** are summed up in Tables 5.1–5.3 below and, as initial data, we have taken $V_{\rm m}^0 = V_{\rm min}$ and $w^0 = 1/(V_{\rm max} - V_{\rm min})^2$.

Anatomical model and computational meshes

The torso computational geometry (see Figure 5.2), including the lung and main bone regions, was obtained starting from the Zygote[1] model – a geometric model based on actual anatomical data – using the `3-matic`[2] software to obtain computationally-correct surface meshes. The heart geometry is simplified, based on intersecting ellipsoids, so that the fibers orientation can be parametrized in terms of analytical functions. We refer to [SMC+06] for the details of the geometrical definition of the heart. Note that this simplified geometry only includes the ventricles. We therefore cannot simulate the P-wave of the ECG.

The 3D computational meshes of the torso and the heart are displayed in Figures 5.2 and 5.3. They have been obtained by processing the surface meshes with the softwares `Yams` [Fre01] and `GHS3D` [GHS90]. The number of heart nodes is approximately 80 000, the number of torso nodes is approximately 120 000 and the total number of tetrahedra is approximately 1 080 000.

Heart conductivity

Cardiac muscle is made of fibers. The electrical conductivity is higher along the fiber direction than along the cross-fiber direction. The intracellular and extracellular media are therefore anisotropic. This anisotropy is included in our model defining the conductivity tensors $\boldsymbol{\sigma}_{\rm i}$ and $\boldsymbol{\sigma}_{\rm e}$ by:

$$\boldsymbol{\sigma}_{\rm i,e}(x) \stackrel{\rm def}{=} \sigma_{\rm i,e}^{\rm t}\boldsymbol{I} + (\sigma_{\rm i,e}^{\rm l} - \sigma_{\rm i,e}^{\rm t})\boldsymbol{a}(x) \otimes \boldsymbol{a}(x), \tag{5.4.16}$$

where $\boldsymbol{a}(x)$ is a unit vector parallel to the local fiber direction (Figure 5.3) and $\sigma_{{\rm i},e}^{\rm l}$ and $\sigma_{{\rm i},e}^{\rm t}$ are respectively the conductivity coefficients in the intra- and extra-cellular media

[1] `www.3dscience.com`
[2] `www.materialise.com`

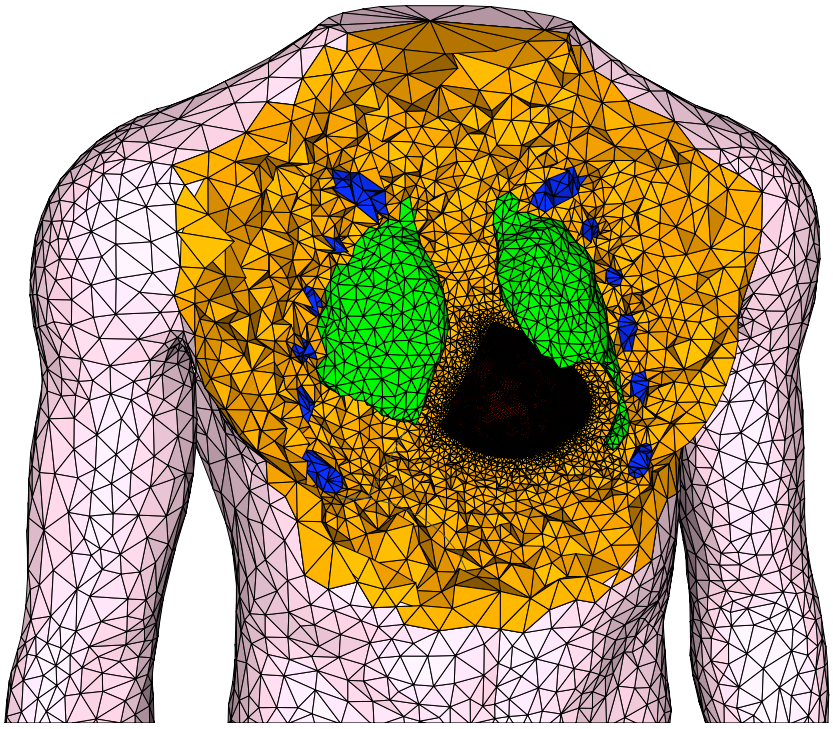

Figure 5.2: Computational torso mesh.

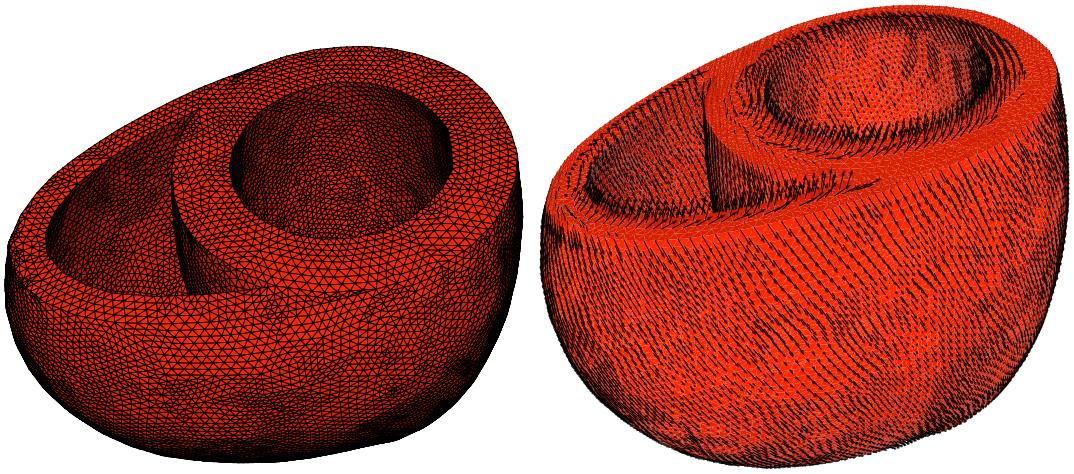

Figure 5.3: Computational heart mesh (left) and heart fiber directions (right).

measured along the fibers direction and in the transverse direction. Different conductivities values are available in the literature (see *e.g.* [SLC+06, CNLH04b, MP95]). The values used in our simulations, originally reported in [PDR+06], are given in Table 5.1. As mentioned above, the fibers directions have been set as in [SMC+06].

$\boldsymbol{\sigma}_{\mathrm{i}}^{\mathrm{l}}$ (S cm^{-1})	$\boldsymbol{\sigma}_{\mathrm{e}}^{\mathrm{l}}$ (S cm^{-1})	$\boldsymbol{\sigma}_{\mathrm{i}}^{\mathrm{t}}$ (S cm^{-1})	$\boldsymbol{\sigma}_{\mathrm{e}}^{\mathrm{t}}$ (S cm^{-1})
3.0×10^{-3}	3.0×10^{-3}	3.0×10^{-4}	1.2×10^{-3}

Table 5.1: Heart conductivity parameters.

Torso conductivity

We assume that the torso has isotropic conductivity, *i.e.* $\boldsymbol{\sigma}_{\mathrm{T}}$ is diagonal $\boldsymbol{\sigma}_{\mathrm{T}} = \sigma_{\mathrm{T}}\boldsymbol{I}$, and that the scalar heterogeneous conductivity σ_{T} takes three different values (see [BP03]):

$$\sigma_{\mathrm{T}} = \begin{cases} \sigma_{\mathrm{T}}^{\mathrm{l}}, & \text{lungs,} \\ \sigma_{\mathrm{T}}^{\mathrm{b}}, & \text{bone,} \\ \sigma_{\mathrm{T}}^{\mathrm{t}}, & \text{remaining regions,} \end{cases}$$

given in Table 5.2.

$\sigma_{\mathrm{T}}^{\mathrm{l}}$(S cm^{-1})	$\sigma_{\mathrm{T}}^{\mathrm{b}}$(S cm^{-1})	$\sigma_{\mathrm{T}}^{\mathrm{t}}$(S cm^{-1})
2.4×10^{-4}	4×10^{-5}	6×10^{-4}

Table 5.2: Torso conductivity parameters.

His bundle and Purkinje fibers

The His bundle quickly transmits the activation from the atrioventricular node to the ventricles. It is made of three main branches in the septum and gives rise to the thin Purkinje fibers in the ventricular muscle. The activation travels from the His bundle to the ventricular muscle in about 40ms. Interesting attempts at modelling the His bundle and the Purkinje fibers have been presented in the literature (see *e.g.* [VC07]). But a physiological model of this fast conduction network coupled to a 3D model of the myocardium raises many modeling and computational difficulties: the fiber network has to be manually defined whereas it cannot be non-invasively obtained from classical imaging techniques; the results are strongly dependent on the density of fibers which is a quantity difficult to determine; the time and the space scales are quite different in the fast conduction network and in the rest of the tissue which can be challenging from the computational standpoint.

To circumvent these issues, we propose to roughly model the Purkinje system by initializing the activation with a (time-dependent) external volume current, acting on a thin subendocardial layer (both left and right parts). The propagation speed of this initial activation is a parameter of the model (see the details in appendix 5.4.1). Although this approach involves a strong simplification of the reality, it allows a simple and quite accurate control of the activation initialization, which is a fundamental aspect in the simulation of correct ECGs.

External stimulus

Physiologically, the activation wave begins at the sinusal node in the right atria, it propagates to ventricles through the atrioventricular node and join the Hiss-bundle, which activates the septum and the Purkinje fibers to stimulate all the endocardium (see [MP95]). At the cellular scale, several models have been developed to describe the propagation of the électrical wave in the his bundle and the purkinje fibers, the most known one is the DiFrancesco-Noble (DN) model [DFN85]. But at the macroscopic level, there is a problem of localizing the pukinje fibers due to their scale. In order to model the electric activation wave in an appropriate and simple way, we propose to follow its time course within the heart. Our model does not include the atria, so we suppose that only the endocardium is stimulated. The spread of excitation is initiated within the myocardium: We apply a given volume current density to a thin subendocardial layer of the ventricles during a small period of time t_{act}. In the left ventricle, this thin layer

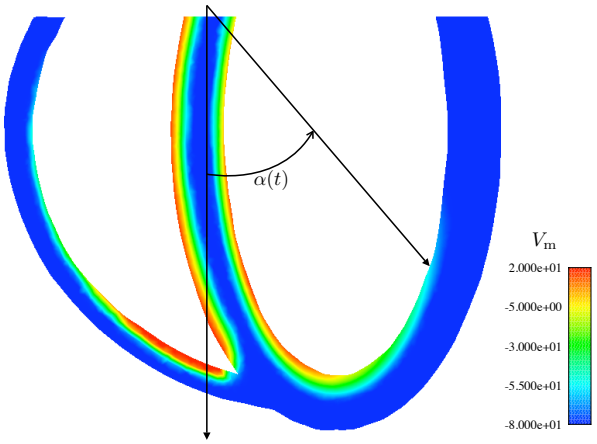

Figure 5.4: Geometrical description of the external stimulus (plane cut $y = 0$).

(1.6 mm) of external activation is given by

$$S \stackrel{\text{def}}{=} \{(x, y, z) \in \Omega_{\text{H}} \,/\, c_1 \leq ax^2 + by^2 + cz^2 \leq c_2\},$$

where a, b, c, c_1 and c_2 are given constants, with $c_1 < c_2$, see Figure 5.4. The source current I_{app}, involved in (5.2.7), is then parametrized as follows:

$$I_{\text{app}}(x, y, z, t) = I_0(x, y, z)\chi_S(x, y, z)\chi_{[0,t_{\text{act}}]}(t)\psi(x, z, t),$$

where

$$I_0(x, y, z) \stackrel{\text{def}}{=} i_{\text{app}} \left[\frac{c_2}{c_2 - c_1} - \frac{1}{c_2 - c_1}(ax^2 + by^2 + cz^2) \right],$$

with i_{app} the amplitude of the external applied stimulus,

$$\chi_S(x,y,z) \stackrel{\text{def}}{=} \begin{cases} 1 & \text{if} \quad (x,y,z) \in S, \\ 0 & \text{if} \quad (x,y,z) \notin S, \end{cases}$$

$$\chi_{[0,t_{\text{act}}]}(t) \stackrel{\text{def}}{=} \begin{cases} 1 & \text{if} \quad t \in [0,t_{\text{act}}], \\ 0 & \text{if} \quad t \notin [0,t_{\text{act}}], \end{cases}$$

$$\psi(x,z,t) \stackrel{\text{def}}{=} \begin{cases} 1 & \text{if} \quad \text{atan}\left(\dfrac{x-x_0}{z-z_0}\right) \leq \alpha(t), \\ 0 & \text{if} \quad \text{atan}\left(\dfrac{x-x_0}{z-z_0}\right) > \alpha(t), \end{cases}$$

the activated angle $\alpha(t) \stackrel{\text{def}}{=} \frac{t\pi}{2t_{\text{act}}}$ and $t_{\text{act}} = 10$ ms. The activation current in the right ventricle is built in a similar fashion.

Cell heterogeneity

Action potential duration (APD) heterogeneity may be found at different myocardium locations, for instance: between base and apex, between septal and posterior sides, and transmurally (see *e.g.* [FBR$^+$87] or [MP95]). Figure 5.5 shows the action potential duration heterogeneity in different locations in the heart.

Although not yet fully explained (see *e.g.* [CO06], for a review), experimental evidence [HN84, FBR$^+$87, YA98, Ant06] suggests that transmural APD heterogeneity is likely to be the most important factor in the genesis of the normal ECG T-wave shape and polarity. A number of simulation studies [dBM02, PDG03, PBLV07, KSW$^+$07, BFGZ07] confirm also this (still debated) postulate. Interestingly, the numerical investigations recently reported in [CFPST09] (using a highly idealized geometry) indicate that the polarity of the T-wave (for unipolar ECG leads) may be mainly driven by the cardiac tissue anisotropy.

In the present work, cell heterogeneity is only considered as transmural variation of APD in the left ventricle. Hence, we assume that epicardial cells have the shortest APD and that endocardial cells have an intermediate APD between mid-myocardial cells (M-cells) and epicardial cells (see *e.g.* [YA98]). From the analysis reported in [MS03, Section 3.1], the leading order of the maximum APD provided by the Mitchell-Schaeffer ionic model (5.2.6) is proportional to the parameter τ_{close}. Thus, the APD heterogeneity is modeled with a parameter τ_{close} varying across the left ventricle transmural direction: $\tau_{\text{close}}^{\text{endo}}$ near the endocardium, $\tau_{\text{close}}^{\text{mcell}}$ in the mid-myocardium (M-cells) and $\tau_{\text{close}}^{\text{epi}}$ near the epicardium (see Figure 5.6). For simplicity, we take a constant value of $\tau_{\text{close}}^{\text{RV}}$ in the whole right ventricle. The values of the parameters are given in Table 5.3.

$A_{\text{m}}(\text{cm}^{-1})$	$C_{\text{m}}(\text{mF})$	τ_{in}	τ_{out}	τ_{open}	$\tau_{\text{close}}^{\text{RV}}$	$\tau_{\text{close}}^{\text{endo}}$	$\tau_{\text{close}}^{\text{mcell}}$	$\tau_{\text{close}}^{\text{epi}}$	V_{gate}	V_{min}	V_{max}
200	10^{-3}	4.5	90	100	120	130	140	90	-67	-80	20

Table 5.3: Cell membrane parameters.

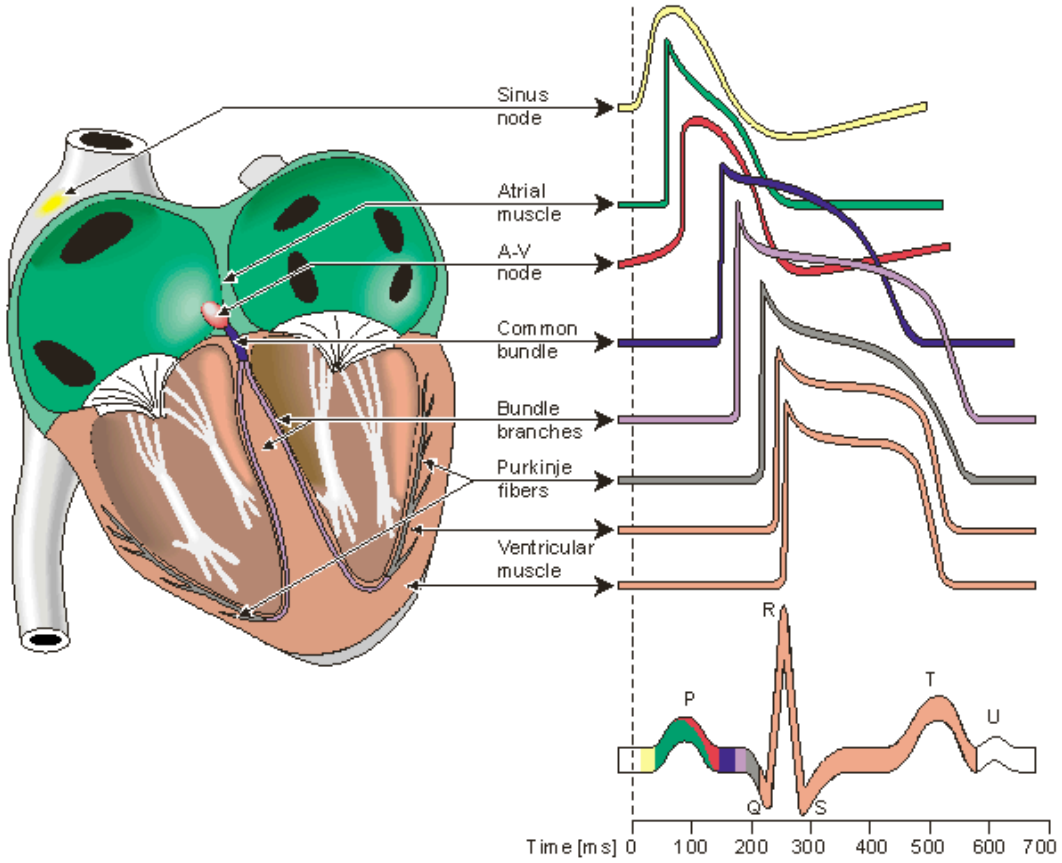

Figure 5.5: Electrophysiology of the heart.The different waveforms for each of the specialized cells found in the heart are shown. The latency shown approximates that normally found in the healthy heart. *Source:* [MP95].

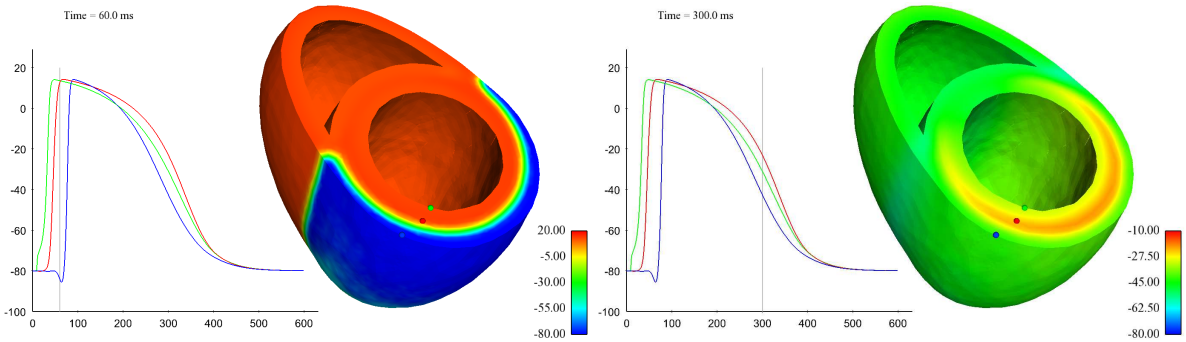

Figure 5.6: Transmural APD heterogeneity: comparison of the simulated transmembrane potentials for endocardial cells (green), M-cells (red) and epicardial cells (blue). Snapshots of the transmembrane potential at times $t = 60$ and 300 ms.

Results

The ECGs are computed according to the standard 12-lead ECG definition (see [MP95], for instance):

$$\begin{aligned} \mathrm{I} &\stackrel{\text{def}}{=} u_{\mathrm{T}}(L) - u_{\mathrm{T}}(R), \quad \mathrm{II} \stackrel{\text{def}}{=} u_{\mathrm{T}}(F) - u_{\mathrm{T}}(R), \quad \mathrm{III} \stackrel{\text{def}}{=} u_{\mathrm{T}}(F) - u_{\mathrm{T}}(L), \\ \mathrm{aVR} &\stackrel{\text{def}}{=} \frac{3}{2}(u_{\mathrm{T}}(R) - u_{\mathrm{W}}), \quad \mathrm{aVL} \stackrel{\text{def}}{=} \frac{3}{2}(u_{\mathrm{T}}(L) - u_{\mathrm{W}}), \quad \mathrm{aVF} \stackrel{\text{def}}{=} \frac{3}{2}(u_{\mathrm{T}}(F) - u_{\mathrm{W}}), \\ \mathrm{V}i &\stackrel{\text{def}}{=} u_{\mathrm{T}}(V_i) - u_{\mathrm{W}} \quad i = 1, .., 6, \end{aligned} \tag{5.4.17}$$

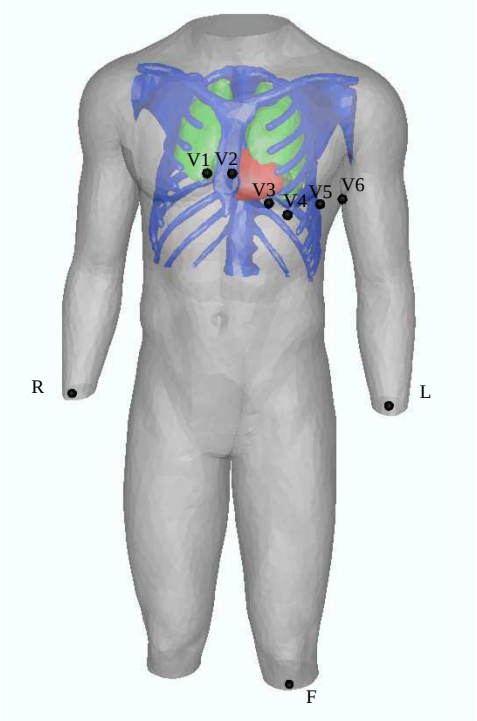

Figure 5.7: Torso domain: ECG electrodes locations.

where $u_{\mathrm{W}} \stackrel{\mathrm{def}}{=} (u_{\mathrm{T}}(L) + u_{\mathrm{T}}(R) + u_{\mathrm{T}}(F))/3$ and the body surface electrode locations L, R, F, $\{V_i\}_{i=1,\ldots,6}$ are indicated in Figure 5.7.

The simulated ECG obtained from **RS** is reported in Figure 5.8. The time and space discretization parameters used to perform this simulation are respectively $h = 0.15$ cm and $\delta t = 0.25$ ms. Some snapshots of the corresponding body surface potential are depicted in Figure 5.9. Compared to a physiological ECG, the computed ECG has some minor flaws. First, the T-wave amplitude is slightly lower than expected. Second, the electrical heart axis (*i.e.* the mean frontal plane direction of the depolarization wave traveling through the ventricles during ventricular activation) is about -40 degrees whereas it should be between 0 and 90 degrees (see *e.g.* [Aeh06]). This is probably due to a too horizontal position of the heart in the thoracic cavity. Third, in the precordial leads, the R-wave presents abnormal (low) amplitudes in V1 and V2 and the QRS complex shows transition from negative to positive polarity in V4 whereas this could be expected in V3.

Despite that, the main features of a physiological ECG can be observed. For example, the QRS-complex has a correct orientation and a realistic amplitude in each of the 12 leads. In particular, it is negative in lead V1 and becomes positive in lead V6. Moreover, its duration is between 80 ms and 120 ms, which is the case of a healthy subject. The orientation and the duration of the T-wave are also satisfactory. To the best of our knowledge, this 12-lead ECG is the most realistic ever published from a fully based PDE/ODE 3D computational model.

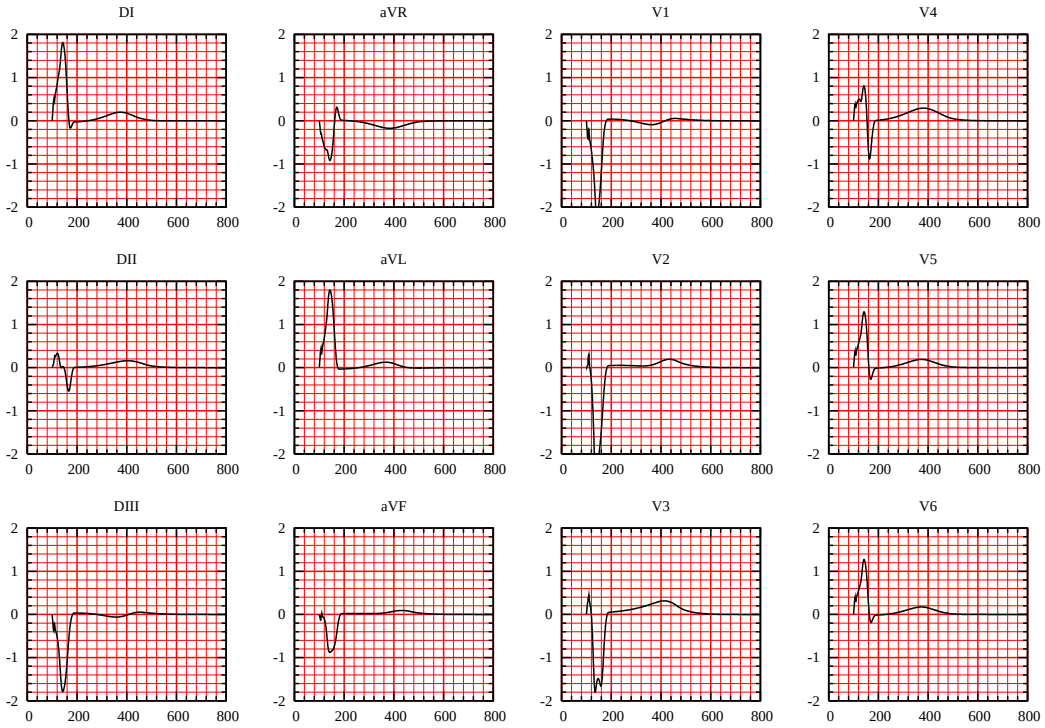

Figure 5.8: Reference simulation: 12-lead ECG signals obtained by a strong coupling with the torso, including anisotropy and APD heterogeneity. As usual, the units in the x- and y-axis are ms and mV, respectively.

5.4.2 Bundle brunch blocks simulations

In this paragraph, we modify the reference simulation that provided the "healthy" ECG (Figure 5.8) in order to simulate a right or a left bundle branch block (RBBB or LBBB). The purpose is to test whether the ECG produced by our model possesses the main characteristics that allow a medical doctor to detect these pathologies.

In the **RS**, the right and the left ventricle are activated simultaneously. Now, in order to simulate a LBBB (resp. a RBBB) the initial activation is blocked in the left (resp. right) ventricle. There are two ways to model the bundle brunch blocks. The first is to consider a dyssynchrony of activation between right and left ventricles. This is performed by introducing a time delay of the activation wave in the left ventricle (respectively, the right ventricle) for a LBBB simulation (respectively RBBB simulation). This fashion of modeling a RBBB for instance considers that the hole right brunch is activated after the left brunch. We denote by RBBB-50, for example, the simulation of an ECG where the delay between the right and the left ventricle is 50 ms. In other word the activation current in the right ventricle $I_{\text{app}}(x, y, z, t)$ is replaced by

$$I_{\text{app}}(x, y, z, t - 50)$$

An ECG simulation of a RBBB-700 is reported in Figure 5.10. Numerical simulations of a RBBB with different degrees of severity are reported in the annex 9.6.2.

The second way of modeling a bundle brunch blocks is to consider a spacial blocks, this assumes that a part of the brunches is damaged. Using the analytical geometry and

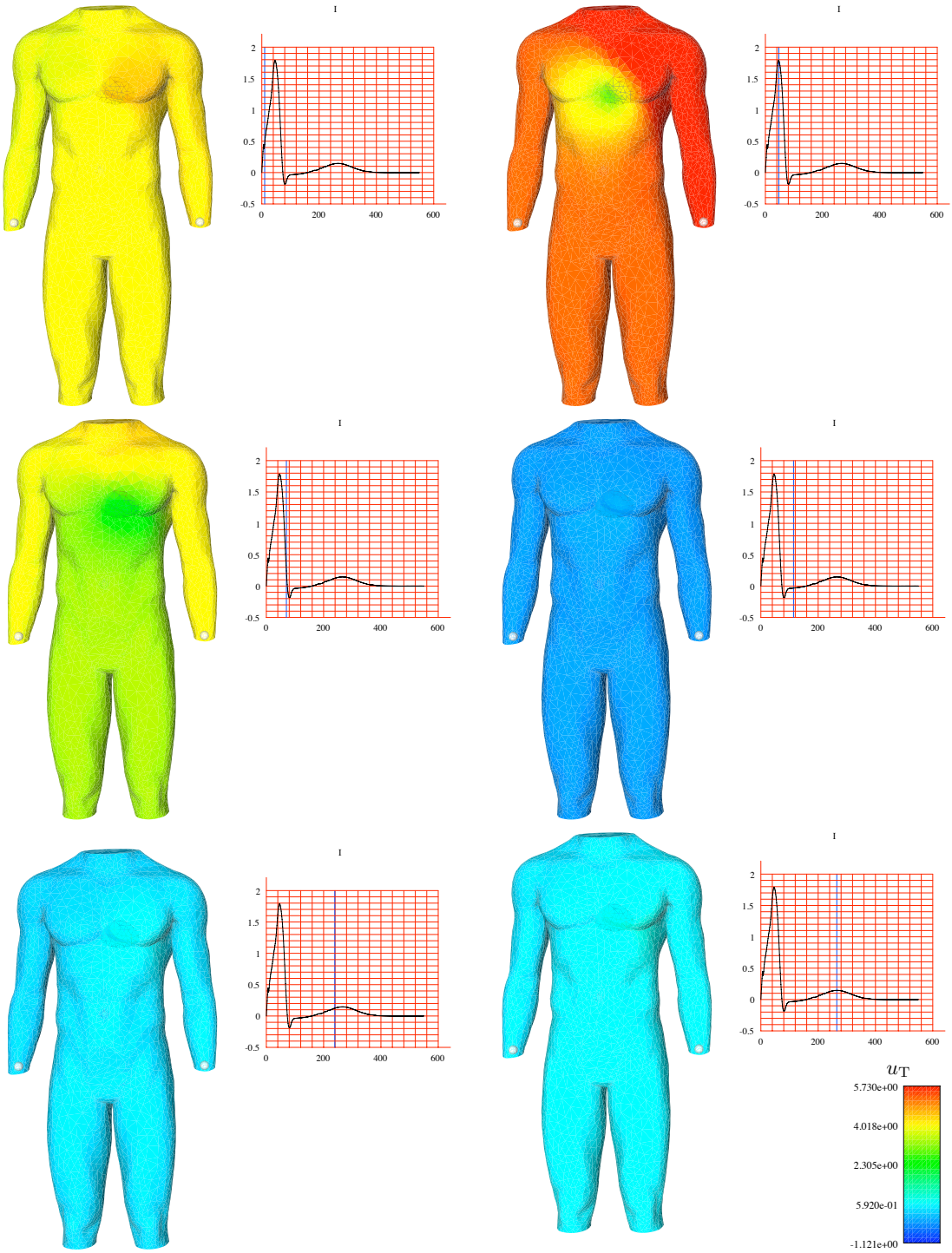

Figure 5.9: Reference simulation: some snapshots of the body surface potentials at times $t = 10$, 47, 70, 114, 239 and 265 ms (from left to right and top to bottom).

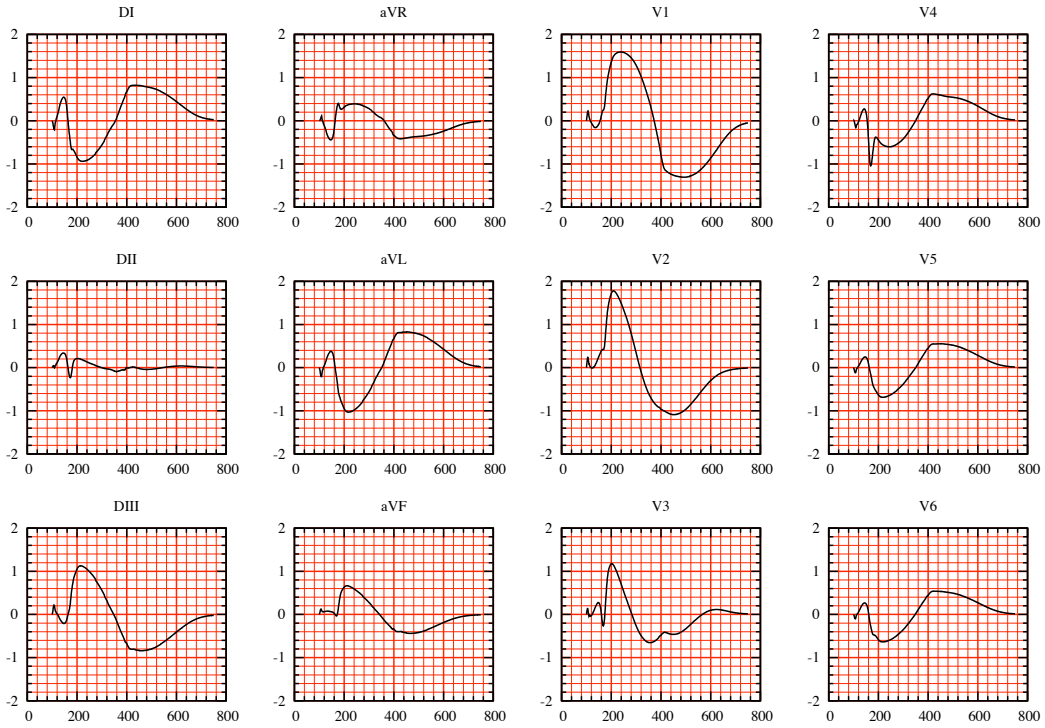

Figure 5.10: Simulated ECG signals for a RBBB-700

the way of defining I_{app}, the activation current is blocked at a certain bundle block angle α_{bb}. To be clearer, this could be modeled by modifying the expression of $\psi(x, y, z, t)$ in the definition of I_{app} by

$$\psi(x, z, t) \stackrel{\text{def}}{=} \begin{cases} 1 & \text{if} \quad \text{atan}\left(\dfrac{x - x_0}{z - z_0}\right) \leq \min(\alpha(t), \alpha_{\text{bb}}) \\ 0 & \text{if} \quad \text{atan}\left(\dfrac{x - x_0}{z - z_0}\right) > \min(\alpha(t), \alpha_{\text{bb}}), \end{cases}$$

The results are reported in Figure 5.11 (RBBB) and 5.12 (LBBB). As in the healthy case, an expert would detect some flaws in these ECGs. For example, he would expect a larger QRS and a lead V1 without Q-wave. Nevertheless, he would also recognize the main features that indicate the bundle branch blocks (see *e.g.* [MP95]). First, the QRS-complex exceeds 120 ms in both cases. Second, it can be seen in Figure 5.11 that the duration between the beginning of the QRS complex and its last positive wave in V1 exceeds 40 ms which is a sign of RBBB. Third, it can be seen in Figure 5.12 that the duration between the beginning of the QRS complex and its last positive wave in V6 exceeds 40 ms which is a sign of LBBB. These ECG signals compared to clinical ECGs of the same pathology show the predictive aspect of the model. In fact, one can see significant similarities between the generated LBBB ECG (Figure 5.12) and the clinical one (Figure 5.13). Specially for the QRS duration and the shape of different leads. It is noticeable that these results have been obtained without any recalibration of the **RS**, besides the above mentioned (natural) modifications needed to model the disease.

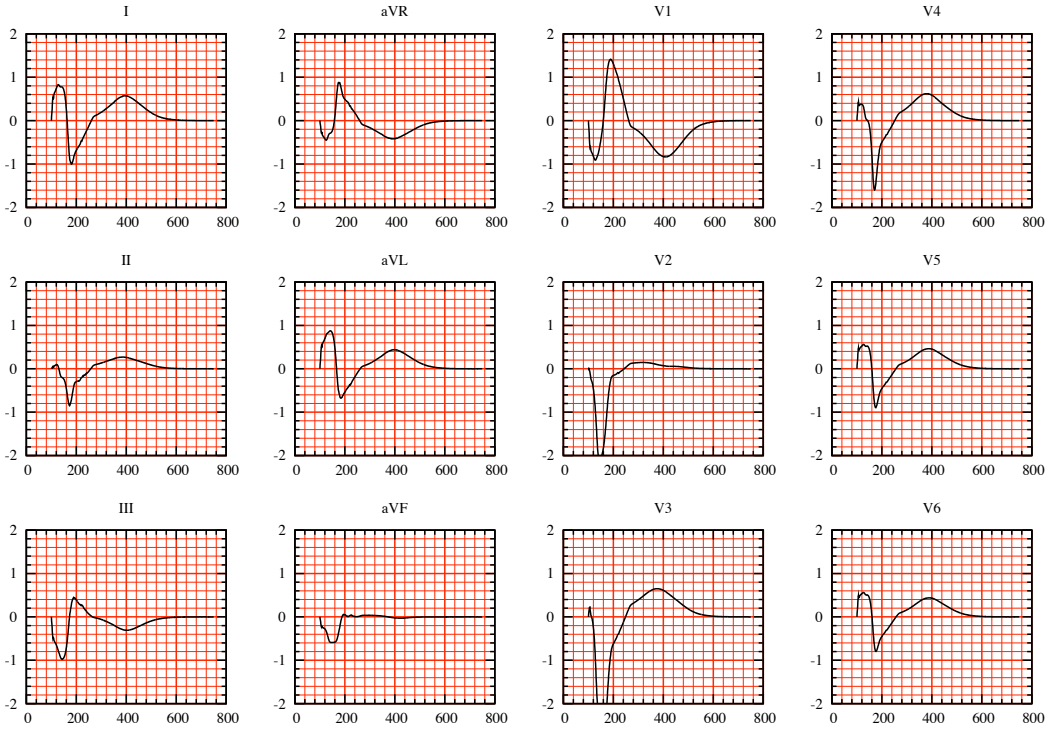

Figure 5.11: Simulated 12-lead ECG signals for a RBBB ($\alpha_{\text{bb}} = \pi/10$).

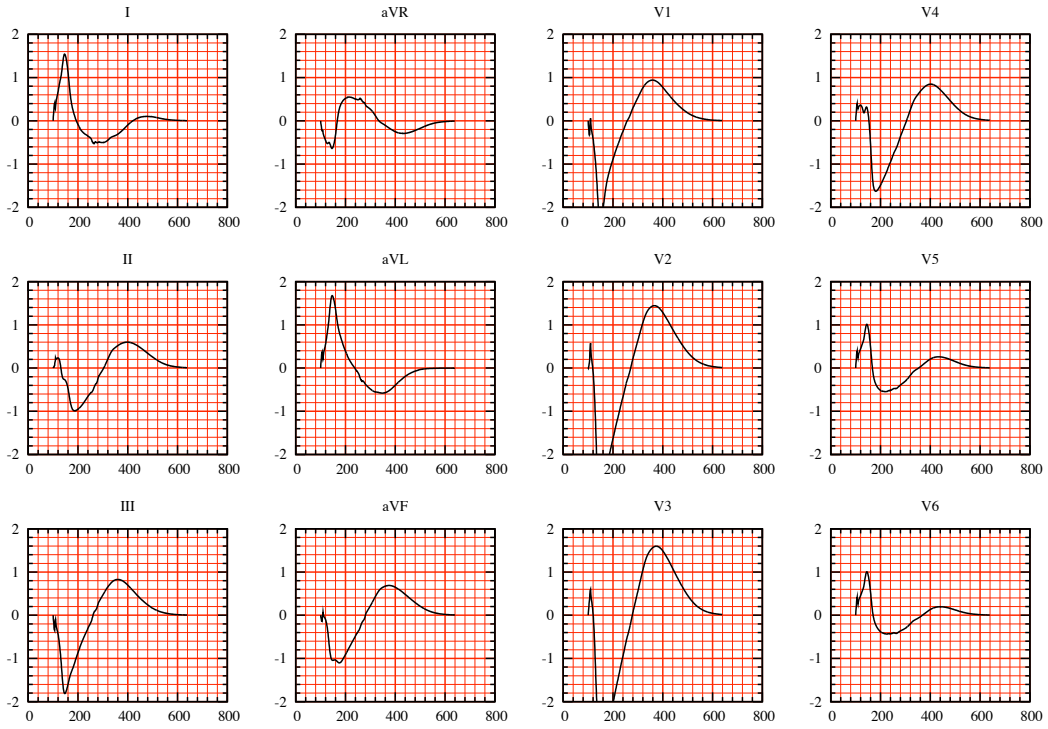

Figure 5.12: Simulated 12-lead ECG signals for a LBBB ($\alpha_{\text{bb}} = \pi/10$).

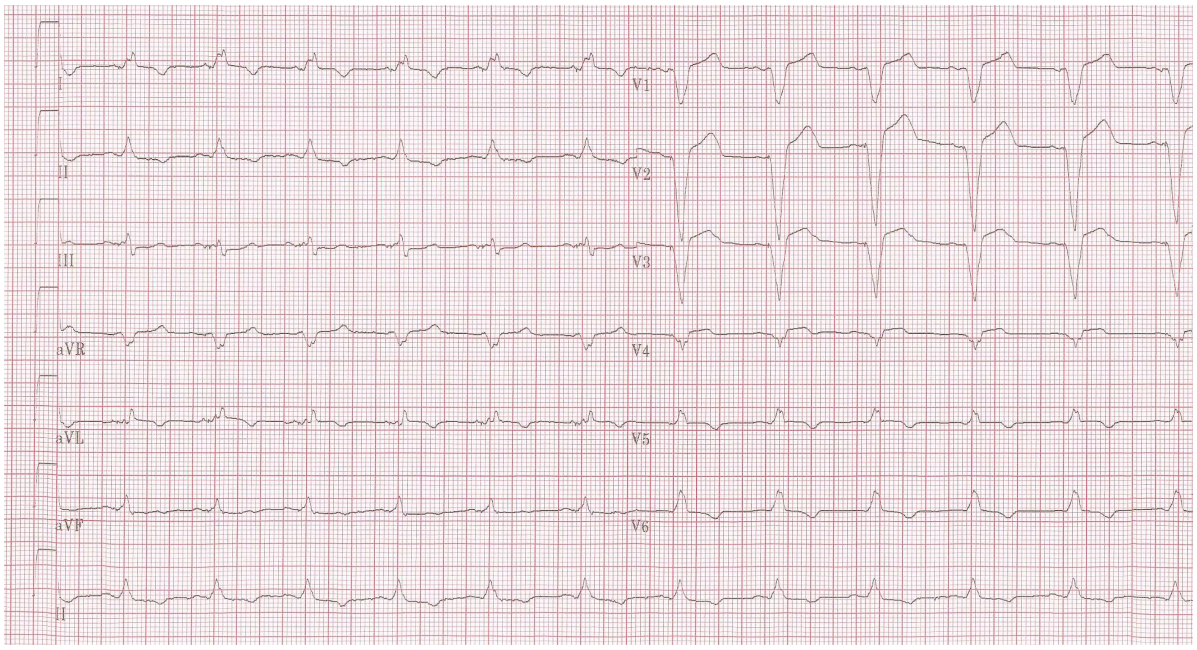

Figure 5.13: Clinical 12-lead ECG signals for a LBBB. Source: `www.ecgpedia.org` (reproduced with permission).

5.4.3 Simulations of arrhythmia

In this paragraph, we provide simulations of ventricular arrhythmia pathologies. Many of these diseases are du to an abnormal activation of the heart muscle. In [Dub89] this strange activation of the myocardium is considered as a result of the presence of some ectopic sources activating the heart with a very high frequency. To explore the effect of this kind of pathology, we introduce ectopic sources in the heart ventricles. These sources activate the heart in an abnormal way with a frequency between 350 and 450 stimulations per minute. The resulting simulations using this approach are reported in Figure 5.14. Since the simulated ECGs show a kind of periodicity the simulation are more similar to ventricular *tachycardia* or *flutter* than to ventricular *fibrillation* (*see* [Dub89]).

This pathology (flutter) could responsible of an abnormal behavior to some myocardial cells. Physiologically, a ventricular flutter could easily evolute in ventricular fibrillation: The hight frequency of contration caused by the flutter (about 3 contraction per second, see Figure 5.14) did not allow the ventricles relaxation, so that the ventricles do not fill with blood. Consequently a very small quantity of blood is ejected to the body. In particular, the irrigation of the heart is not well accomplished by the coronary arteries. This induce a nutrition lack of the myocardial cells which begin to behave abnormally. That is one of the origins of a fibrillation (*see* [Dub89]).

Using a phenomenological ionic model, one can imagine, for instance, that the abnormal behavior is fomulated by an increase of the action potential duration in some region. By simply increasing the value of $\tau_{\text{close}}^{\text{endo}}$, which is equivalent increasing the APD in the endocardium in the left ventricle, a *reentry wave* appears and causes a ventricular fibrillation. That is explained as follows: After the heart is depolarized, the epicardium begin to repolarize ($\tau_{\text{close}}^{\text{epi}}$ is small) while the endocardium is in the plateau phase. Once

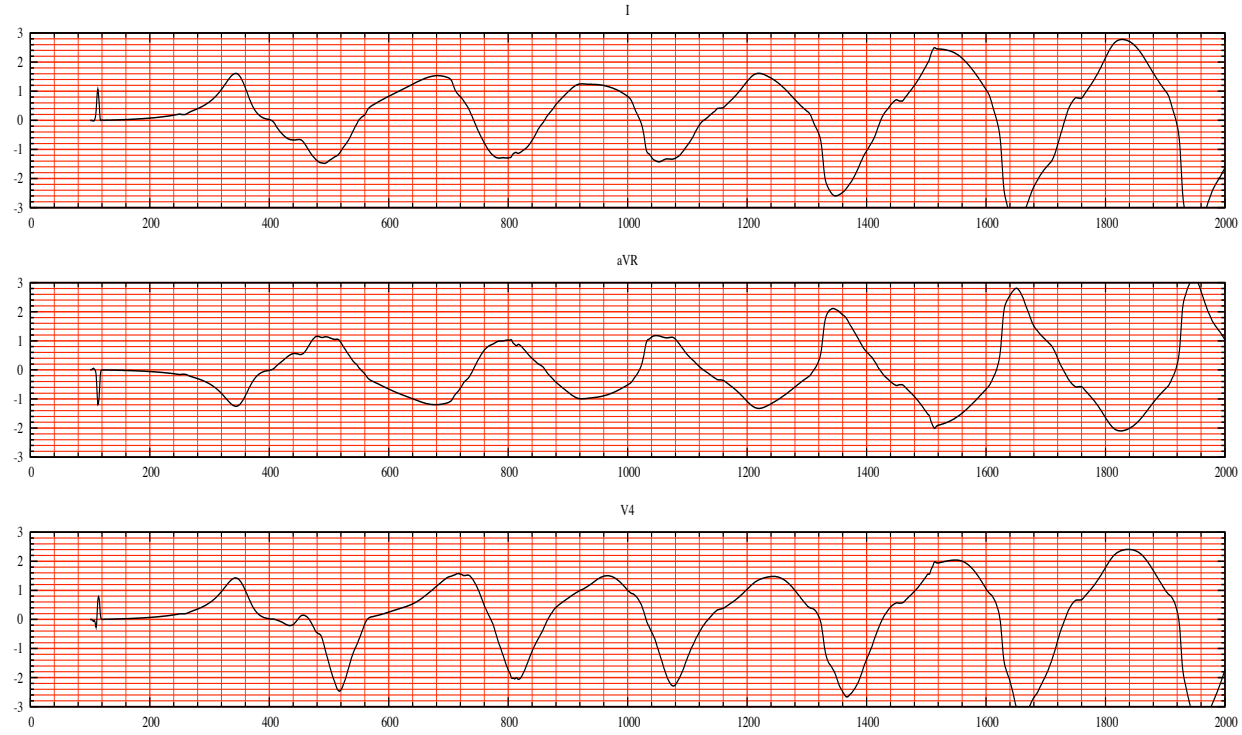

Figure 5.14: Simulated ECG signals for an abnormal activation of the heart: The abnormality comes from ectopic sources stimulating the heart with frequencies between 350 and 450 activation per minute. First lead, aVR and V4 (from top to bottom).

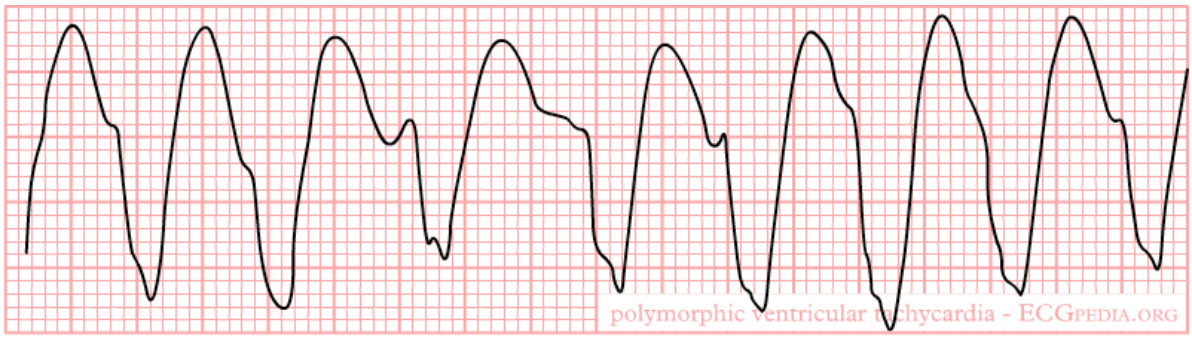

Figure 5.15: Clinical polymorphic ventricular tachycardia rhythm. Source: `www.ecgpedia.org` (reproduced with permission).

the epicardium is totally repolarized and the endocardium is still depolarized, a hight potential gradient between the two regions is created. This gradient is responsible of the generation of a current density. The epicardium totally repolarized is then activated by the generated current, then the right ventricle is activated. At the same time, the endocardium is repolarizing. At a certain time it is activated by the electrical waves coming from the other regions of the heart: A reentry wave is then initialized. We report the corresponding ECGs to this simulation in Figure 5.16. First, we remark a hight frequent activation of the myocardium, about 5 heart beats per second. Second, the ECG signal shows different forms and different amplitudes without any periodicity. Finally, we don't see any feature of the ECG waves (QRS-complex and T-wave) in the ECG shape. These are clear characteristics of a fibrillation disease. The comparison

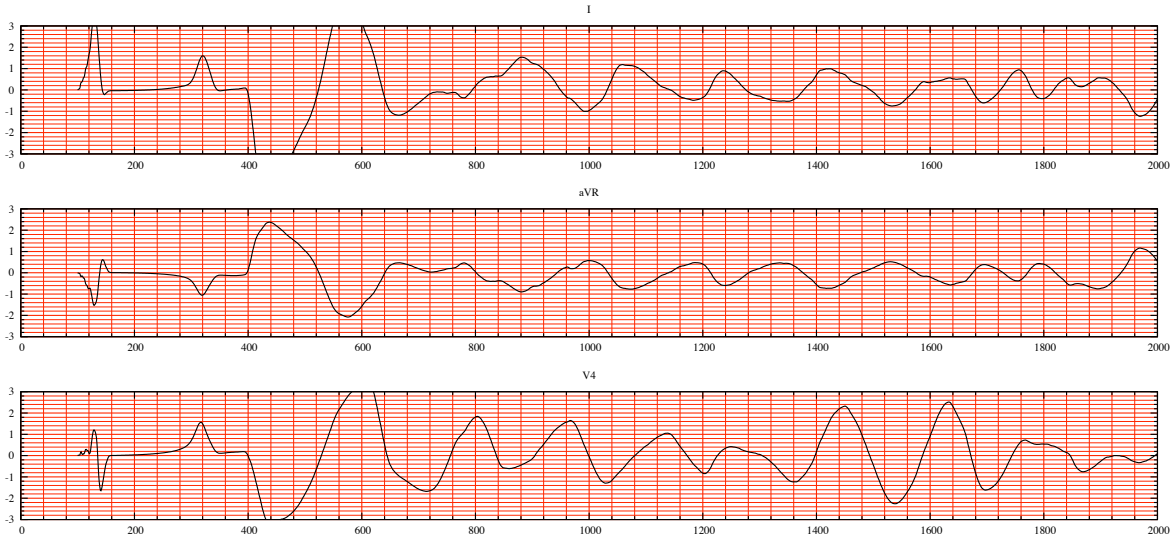

Figure 5.16: Simulated reentry ECG signals: First lead, aVR and V4.

between the simulated ECG signals (Figure 5.16) and a typical clinical ECG of a fibrillation disease (Figure 5.17) shows similarities both in frequencies and shapes of the two signals.

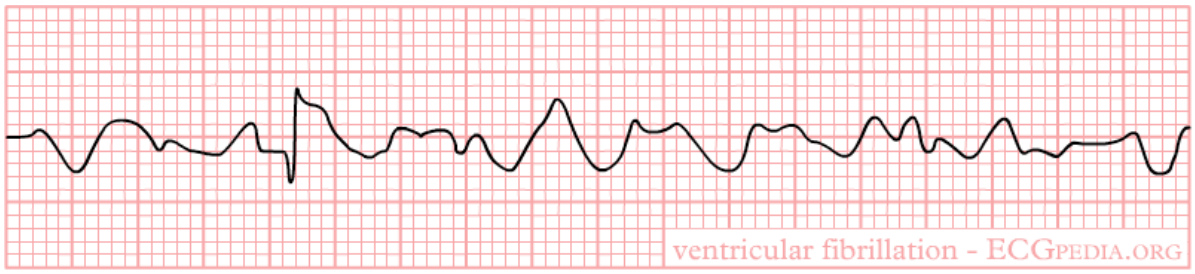

Figure 5.17: Clinical ventricular fibrillation rhythm. Source:`www.ecgpedia.org` (Reproduced with permission).

5.5 Impact of some modeling assumptions

In this section, the impact of some alternative modeling assumptions on the simulated ECG is investigated. This allows to assess to what extent the modeling assumptions involved in the **RS** are necessary to obtain a meaningful ECG.

5.5.1 Heart-torso uncoupling

A common approach to reduce the computational complexity of the **RM** consists in uncoupling the computation of $(V_{\mathrm{m}}, u_{\mathrm{e}})$ and u_{T}. This can be achieved by neglecting, in (5.2.10), the electrical torso feedback on the cardiac region. That is, by replacing the coupling condition $(5.2.10)_2$ by

$$\boldsymbol{\sigma}_{\mathrm{e}} \boldsymbol{\nabla} u_{\mathrm{e}} \cdot \boldsymbol{n} = 0, \quad \text{on} \quad \Sigma, \tag{5.5.18}$$

which amounts to work with an isolated heart domain (see *e.g.* [CNLH04b, PDR$^+$06]).

As a result, the intracardiac quantities $(V_{\rm m}, u_{\rm e})$ can be obtained, independently of $u_{\rm T}$, by solving (5.2.7) with initial condition (5.2.8) and insulating conditions

$$\begin{cases} \boldsymbol{\sigma}_{\rm i}\boldsymbol{\nabla}V_{\rm m}\cdot\boldsymbol{n}+\boldsymbol{\sigma}_{\rm i}\boldsymbol{\nabla}u_{\rm e}\cdot\boldsymbol{n}=0, & \text{on} \quad \Sigma, \\ \boldsymbol{\sigma}_{\rm e}\boldsymbol{\nabla}u_{\rm e}\cdot\boldsymbol{n}=0, & \text{on} \quad \Sigma. \end{cases} \tag{5.5.19}$$

Thereafter, the torso potential $u_{\rm T}$ is recovered by solving (5.2.11) with

$$\begin{cases} u_{\rm T}=u_{\rm e}, & \text{on} \quad \Sigma, \\ \boldsymbol{\sigma}_{\rm T}\boldsymbol{\nabla}u_{\rm T}\cdot\boldsymbol{n}_{\rm T}=0, & \text{on} \quad \Gamma_{\rm ext}, \end{cases} \tag{5.5.20}$$

as boundary conditions. In other words, the uncoupled heart potential $u_{\rm e}$ is transferred, from $\Omega_{\rm H}$ to $\Omega_{\rm T}$, through the interface Σ (see [BRS77, SSN94]).

Remark 5.5.1.1. *Rather than interface based, as* (5.5.20)*, most of the uncoupled approaches reported in the literature are volume based (see [LBG$^+$03, Section 4.2.4] for a review). Thus, the torso potentials are generated by assuming a (multi-)dipole representation of the cardiac source, typically based on the transmembrane potential gradient* $\boldsymbol{\nabla}V_{\rm m}$ *(see e.g. [Gul88, PBC05]).*

From the numerical point of view, the heart-torso uncoupling amounts to replace step 4, in section 5.3.1, by:

- Solving for $(V_{\rm m}^{n+1}, u_{\rm e}^{n+1}) \in V_h \times V_h$, with $\displaystyle\int_{\Omega_{\rm H}} u_{\rm e}^{n+1}=0$:

$$\begin{cases} A_{\rm m}\displaystyle\int_{\Omega_{\rm H}}\frac{C_{\rm m}}{\delta t}\left(\frac{3}{2}V_{\rm m}^{n+1}-2V_{\rm m}^{n}+\frac{1}{2}V_{\rm m}^{n-1}\right)\phi+\int_{\Omega_{\rm H}}\boldsymbol{\sigma}_{\rm i}\boldsymbol{\nabla}(V_{\rm m}^{n+1}+u^{n+1})\cdot\boldsymbol{\nabla}\phi \\ \qquad\qquad = A_{\rm m}\displaystyle\int_{\Omega_{\rm H}}\left(I_{\rm app}(t_{n+1})-I_{\rm ion}(\widetilde{V}_{\rm m}^{n+1},w^{n+1})\right)\phi, \\ \displaystyle\int_{\Omega_{\rm H}}(\boldsymbol{\sigma}_{\rm i}+\boldsymbol{\sigma}_{\rm e})\boldsymbol{\nabla}u_{\rm e}^{n+1}\cdot\boldsymbol{\nabla}\psi_{\rm e}+\int_{\Omega_{\rm H}}\boldsymbol{\sigma}_{\rm i}\boldsymbol{\nabla}V_{\rm m}^{n+1}\cdot\boldsymbol{\nabla}\psi_{\rm e}=0, \end{cases}$$

  for all $(\phi, \psi_{\rm e}) \in V_h \times V_h$, with $\displaystyle\int_{\Omega_{\rm H}}\psi_{\rm e}=0$.

Then, once $\{u_{\rm e}^{n+1}\}_{0\le n\le N-1}$ are available, the torso potential is obtained by solving, for $u_{\rm T}^{n+1} \in Z_h$,

$$\begin{aligned} u_{\rm T}^{n+1}&=u_{\rm e}^{n+1}, \quad \text{on} \quad \Sigma, \\ \int_{\Omega_{\rm T}}\boldsymbol{\sigma}_{\rm T}\boldsymbol{\nabla}u_{\rm T}^{n+1}\cdot\boldsymbol{\nabla}\psi_{\rm T}&=0, \quad \forall\psi_{\rm T}\in Z_{h,0}. \end{aligned} \tag{5.5.21}$$

The remainder of this section discusses the impact of the uncoupled approach on ECG accuracy and computational cost.

Numerical results

Figure 5.18 presents the ECGs obtained with the fully coupled (*i.e.* the **RS**) and the uncoupled approaches in a healthy condition. For the sake of conciseness, we have only reported the I, aVR, V1 and V4 leads of the ECG. Figure 5.19 reports the comparison in the case of a pathological RBBB situation.

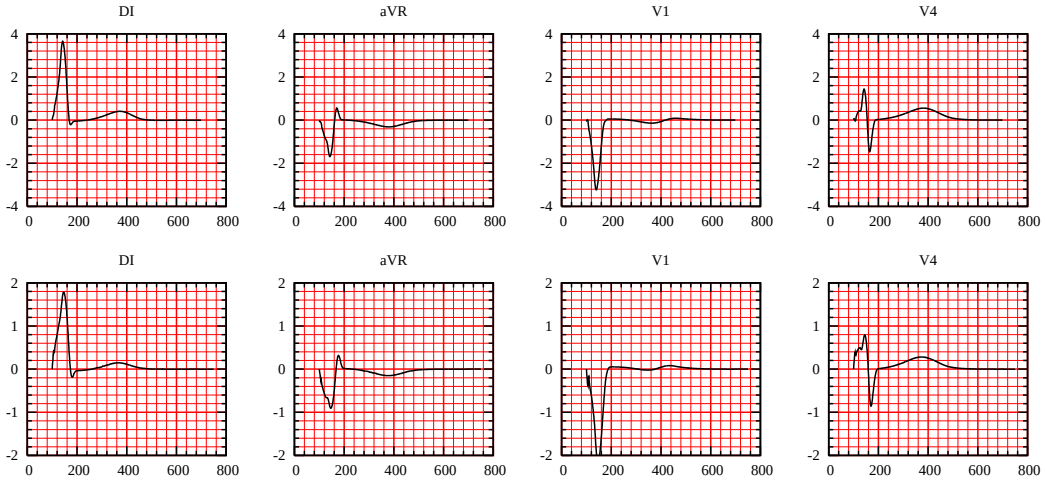

Figure 5.18: Comparison of the simulated healthy ECGs obtained using heart-torso uncoupling (top) and fully heart-torso coupling (bottom).

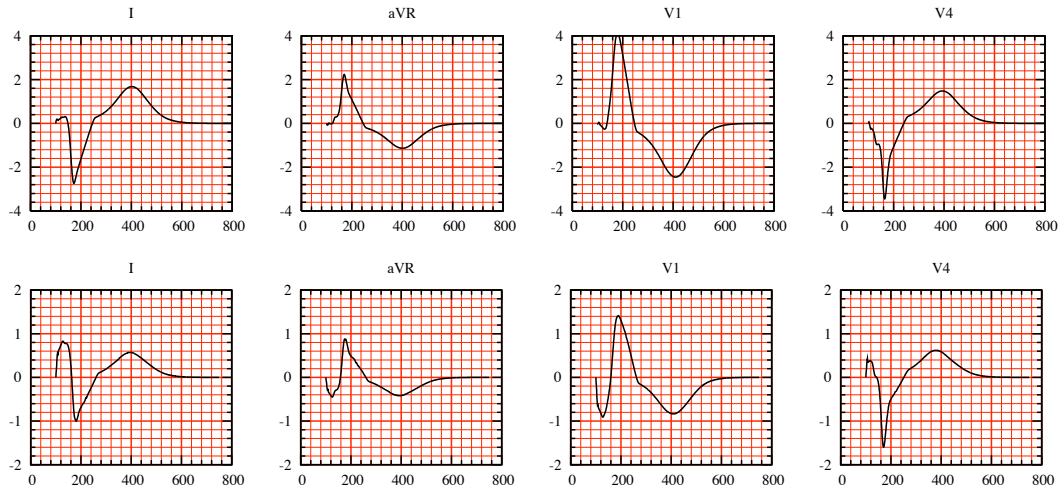

Figure 5.19: Comparison of the simulated RBBB ECGs obtained using heart-torso uncoupling (top) and fully heart-torso coupling (bottom).

In both cases, the amplitude of the waves of the uncoupled formulation is much larger than in the fully coupled formulation. In the healthy case (Figure 5.18), it can nevertheless be noted that the shape of the ECG is almost unaffected. These results are consistent with the experimental findings reported in [GTEL91]: no significant changes in epicardial activation but substantial increasing in epicardial potentials magnitude were observed when the heart surface was exposed to insulating air. Thus, considering an uncoupled formulation can be reasonable to get a qualitatively correct ECGs, in the

sense that some important features of the ECGs – for example, the QRS or the QT intervals – are the same as in the fully coupled case. This observation is the basis of the numerical study reported in section 5.6 using heart-torso uncoupling. Nevertheless, Figure 5.19 shows that both amplitude and shape can differ in some cases. The uncoupling assumption has therefore to be considered with caution. Similar conclusions are given in [PBC05, Page 315] (see also [LBG+03, Section 4.3]), by comparing the surface potentials, on a 2D torso slice, obtained with a multi-dipole representation of the cardiac source (see remark 5.5.1.1).

Torso transfer matrix computation

Under a heart-torso uncoupling assumption, the torso potential u_{T} is computed by solving the generalized Laplace equation (5.2.11) with boundary conditions (5.5.20). Therefore, u_{T} depends linearly on the heart extracellular potential at the heart-torso interface $u_{\mathrm{e}|\Sigma}$. At the discrete level, we will see that this leads to a matrix-vector product representation of the ECG computation in terms of the discrete extracellular potential at the heart-torso interface Σ.

To this aim, we introduce some additional notation and assume that the heart and torso finite element discretizations match at the interface. For the sake of simplicity, the degrees of freedom (DOF) of torso potential are partitioned as $\boldsymbol{x}_{\mathrm{T}} \overset{\text{def}}{=} [\boldsymbol{x}_{\mathrm{T,I}}, \boldsymbol{x}_{\mathrm{T},\Sigma}] \in \mathbb{R}^{n_{\mathrm{I}}+n_{\Sigma}}$, where $\boldsymbol{x}_{\mathrm{T},\Sigma}$ denotes the heart-torso interface DOF and $\boldsymbol{x}_{\mathrm{T,I}}$ the remaining DOF. We denote by $\boldsymbol{x}_{\mathrm{e}|\Sigma} \in \mathbb{R}^{n_{\Sigma}}$ the extracellular potential DOF at the heart-torso interface Σ. Finally, we assume that the 9 potential values generating the ECG (see section 5.4.1), say $\boldsymbol{x}_{\mathrm{ECG}} \in \mathbb{R}^9$, are obtained from the discrete torso potential $\boldsymbol{x}_{\mathrm{T}}$ in terms of an interpolation operator $\boldsymbol{P} \in \mathbb{R}^{9\times n_{\mathrm{I}}}$, so that

$$\boldsymbol{x}_{\mathrm{ECG}} = \boldsymbol{P}\boldsymbol{x}_{\mathrm{T,I}}, \tag{5.5.22}$$

for instance, $\boldsymbol{P}$ can be a nodal value extraction of $\boldsymbol{x}_{\mathrm{T,I}}$. On the other hand, from (5.5.21), the discrete torso potential $\boldsymbol{x}_{\mathrm{T}}$ is solution to the following finite element linear system:

$$\begin{bmatrix} \boldsymbol{A}_{\mathrm{II}} & \boldsymbol{A}_{\mathrm{I}\Sigma} \\ \boldsymbol{0} & \boldsymbol{I}_{\Sigma\Sigma} \end{bmatrix} \quad \begin{bmatrix} \boldsymbol{x}_{\mathrm{T,I}} \\ \boldsymbol{x}_{\mathrm{T},\Sigma} \end{bmatrix} = \begin{bmatrix} \boldsymbol{0} \\ \boldsymbol{x}_{\mathrm{e}|\Sigma} \end{bmatrix}. \tag{5.5.23}$$

Hence, by Gaussian elimination, we have that $\boldsymbol{x}_{\mathrm{T,I}} = -\boldsymbol{A}_{\mathrm{II}}^{-1}\boldsymbol{A}_{\mathrm{I}\Sigma}\boldsymbol{x}_{\mathrm{e}|\Sigma}$, and by inserting this expression in (5.5.22), we obtain

$$\boldsymbol{x}_{\mathrm{ECG}} = \underbrace{-\boldsymbol{P}\boldsymbol{A}_{\mathrm{II}}^{-1}\boldsymbol{A}_{\mathrm{I}\Sigma}}_{\boldsymbol{T}}\boldsymbol{x}_{\mathrm{e}|\Sigma}.$$

Therefore, the ECG can be computed from the discrete extracellular potential at the heart torso interface, $\boldsymbol{x}_{\mathrm{e}|\Sigma}$, by a simple matrix-vector operation $\boldsymbol{x}_{\mathrm{ECG}} = \boldsymbol{T}\boldsymbol{x}_{\mathrm{e}|\Sigma}$, with $\boldsymbol{T} \overset{\text{def}}{=} -\boldsymbol{P}\boldsymbol{A}_{\mathrm{II}}^{-1}\boldsymbol{A}_{\mathrm{I}\Sigma}$.

There are different solutions to compute $\boldsymbol{T}$. The naive idea consisting of computing the matrix $\boldsymbol{A}_{\mathrm{II}}^{-1}$ is of course ruled out. A reasonable and natural option is to compute matrix $\boldsymbol{T}$ by column (see [SSN94]), *i.e.* by evaluating $\boldsymbol{T}\boldsymbol{e}_i$ for $i = 1, \ldots, n_{\Sigma}$, where $\boldsymbol{e}_i$ denotes the i-th canonical vector of $\mathbb{R}^{n_{\Sigma}}$. But each of these evaluations involve the solution of system (5.5.23) with $\boldsymbol{x}_{\mathrm{e}|\Sigma} = \boldsymbol{e}_i$, and therefore the overall computational cost

is proportional to n_Σ, which can be rather expensive (remember that n_Σ is the number of nodes on the heart-torso interface, and is therefore of the order of several thousands). In contrast, a computation by row is much more efficient since it is only needeed to evaluate $\boldsymbol{T}^T\boldsymbol{e}_i$ for $i = 1, \ldots, 9$, where $\boldsymbol{e}_i$ stands for the i-th canonical vector of $\mathbb{R}^9$. From the symmetry of the finite element matrix,

$$\boldsymbol{T}^T = -\boldsymbol{A}_{\mathrm{I}\Sigma}^T \boldsymbol{A}_{\mathrm{II}}^{-T} \boldsymbol{P}^T = -\boldsymbol{A}_{\Sigma\mathrm{I}} \boldsymbol{A}_{\mathrm{II}}^{-1} \boldsymbol{P}^T.$$

Therefore, the matrix-vector product evaluation

$$\boldsymbol{T}^T\boldsymbol{e}_i = -\boldsymbol{A}_{\Sigma\mathrm{I}} \underbrace{\boldsymbol{A}_{\mathrm{II}}^{-1}\boldsymbol{P}^T\boldsymbol{e}_i}_{\boldsymbol{x}_{\mathrm{T,I}}}, \tag{5.5.24}$$

can be performed in two steps as follows. First, solve for $[\boldsymbol{x}_{\mathrm{T,I}}, \boldsymbol{x}_{\mathrm{T},\Sigma}]$ the discrete source problem (depending on the linear operator $\boldsymbol{P}$), with homogeneous Dirichlet boundary condition on Σ:

$$\begin{bmatrix} \boldsymbol{A}_{\mathrm{II}} & \boldsymbol{A}_{\mathrm{I}\Sigma} \\ \boldsymbol{0} & \boldsymbol{I}_{\Sigma\Sigma} \end{bmatrix} \begin{bmatrix} \boldsymbol{x}_{\mathrm{T,I}} \\ \boldsymbol{x}_{\mathrm{T},\Sigma} \end{bmatrix} = \begin{bmatrix} \boldsymbol{P}^t\boldsymbol{e}_i \\ \boldsymbol{0} \end{bmatrix}, \tag{5.5.25}$$

Second, from (5.5.24), evaluate the interface residual

$$\boldsymbol{T}^T\boldsymbol{e}_i = -\boldsymbol{A}_{\Sigma\mathrm{I}}\boldsymbol{x}_{\mathrm{T,I}} = -\begin{bmatrix} \boldsymbol{A}_{\Sigma\mathrm{I}} & \boldsymbol{A}_{\Sigma\Sigma} \end{bmatrix} \begin{bmatrix} \boldsymbol{x}_{\mathrm{T,I}} \\ \boldsymbol{x}_{\mathrm{T},\Sigma} \end{bmatrix}.$$

Note that, $\boldsymbol{T}^T\boldsymbol{e}_i$ is nothing but the discrete current flux through the heart-torso interface Σ, associated to the homogeneous Dirichlet condition in (5.5.25).

In this chapter, all the numerical ECGs based on the uncoupling conditions (5.5.19)-(5.5.20) have been obtained using the matrix $\boldsymbol{T}$ presented in this paragraph (and this matrix has been computed by row).

Remark 5.5.1.2. *If the operator $\boldsymbol{P}$ is a simple extraction of nodal values from the torso potential DOF, $\boldsymbol{x}_{\mathrm{T}}$, each evaluation $\boldsymbol{T}^T\boldsymbol{e}_i$, for $i = 1, \ldots, 9$, can be (formally) interpreted at the continuous level as a current flux evaluation at Σ of the problem*

$$\begin{cases} \operatorname{div}(\boldsymbol{\sigma}_{\mathrm{T}}\boldsymbol{\nabla} v) = \delta_{\boldsymbol{x}_i}, & \text{in} \quad \Omega_{\mathrm{T}}, \\ v = 0, & \text{on} \quad \Sigma, \\ \boldsymbol{\sigma}_{\mathrm{T}}\boldsymbol{\nabla} v \cdot \boldsymbol{n}_{\mathrm{T}} = 0, & \text{on} \quad \Gamma_{\mathrm{ext}}, \end{cases}$$

with $\delta_{\boldsymbol{x}_i}$ the Dirac's delta function at the i-th point, $\boldsymbol{x}_i$, of torso potential recording on Γ_{ext}.

Remark 5.5.1.3. *Note that the transfer matrix $\boldsymbol{T}$ can be computed "off-line", since it depends neither on time nor on solution in the heart. Nevertheless, this matrix has to be recomputed when the torso conductivities are modified or when dealing with dynamic torso meshes.*

Table 5.4 reports the elapsed CPU time needed to simulate an ECG with three different approaches. As expected, the uncoupling assumption significantly reduces the computational cost of the ECG simulation, especially if the transfer matrix method is used to recover the torso potentials. Let us emphasize that, the last two columns of Table 5.4 refer to the same problem (uncoupled formulation) solved with two different algorithms, whereas the problem corresponding to the first column (fully coupled formulation) is different and *a priori* more accurate.

Full coupling	Uncoupling Laplace equation	Uncoupling Transfer matrix
60	4	1

Table 5.4: Comparison of the elapsed CPU time (dimensionless) for the computation of the ECG.

5.5.2 Study of the monodomain model

In the previous section we have investigated a simplifying modeling assumption that allows an uncoupled computation of the heart and torso potentials $(V_{\mathrm{m}}, u_{\mathrm{e}})$ and u_{T}. We now discuss another simplification known as monodomain approximation (see *e.g.* [CNLH04b, CFPT05]). Combined with a heart-torso uncoupling assumption, this approach leads to a fully decoupled computation of V_{m}, u_{e} and u_{T}.

The next subsection investigates the implications, on ECG modeling, of the general monodomain derivation proposed in [CNLH04b, CFPT05], without any assumptions on the anisotropy ratio of the intra- and extracellular conductivities. The impact of this approximation on the simulated ECG is then illustrated in subsection 5.5.2, using the heart-torso uncoupling simplification.

The monodomain approximation

We assume that the intra- and extracellular local conductivities $\sigma_{\mathrm{i}}^{\mathrm{l,t}}$ and $\sigma_{\mathrm{e}}^{\mathrm{l,t}}$ are homogeneous (constant in space). Let $\boldsymbol{j} \stackrel{\mathrm{def}}{=} \boldsymbol{j}_{\mathrm{i}} + \boldsymbol{j}_{\mathrm{e}}$ be the total current, flowing into Ω_{H}, and $\sigma_{\mathrm{b}} \stackrel{\mathrm{def}}{=} \boldsymbol{\sigma}_{\mathrm{i}} + \boldsymbol{\sigma}_{\mathrm{e}}$ be the bulk conductivity tensor of the medium.

From (5.2.3) and (5.2.4), $\boldsymbol{j} = -\boldsymbol{\sigma}_{\mathrm{i}}\boldsymbol{\nabla} u_{\mathrm{i}} - \boldsymbol{\sigma}_{\mathrm{e}}\boldsymbol{\nabla} u_{\mathrm{e}} = -\boldsymbol{\sigma}_{\mathrm{i}}\boldsymbol{\nabla} V_{\mathrm{m}} - \sigma_{\mathrm{b}}\boldsymbol{\nabla} u_{\mathrm{e}}$, or, equivalently,

$$\boldsymbol{\nabla} u_{\mathrm{e}} = -\sigma_{\mathrm{b}}^{-1}\boldsymbol{\sigma}_{\mathrm{i}}\boldsymbol{\nabla} V_{\mathrm{m}} - \sigma_{\mathrm{b}}^{-1}\boldsymbol{j}. \tag{5.5.26}$$

By inserting this expression in $(5.2.7)_1$ and (5.2.9), we obtain

$$\left\{\begin{array}{l} A_{\mathrm{m}}\left(C_{\mathrm{m}}\dfrac{\partial V_{\mathrm{m}}}{\partial t} + I_{\mathrm{ion}}(V_{\mathrm{m}}, w)\right) - \operatorname{div}\left(\boldsymbol{\sigma}_{\mathrm{i}}(\boldsymbol{I} - \sigma_{\mathrm{b}}^{-1}\boldsymbol{\sigma}_{\mathrm{i}})\boldsymbol{\nabla} V_{\mathrm{m}}\right) \\ \qquad\qquad = -\operatorname{div}(\boldsymbol{\sigma}_{\mathrm{i}}\sigma_{\mathrm{b}}^{-1}\boldsymbol{j}) + A_{\mathrm{m}} I_{\mathrm{app}}, \quad \text{in} \quad \Omega_{\mathrm{H}}, \\ \boldsymbol{\sigma}_{\mathrm{i}}(\boldsymbol{I} - \sigma_{\mathrm{b}}^{-1}\boldsymbol{\sigma}_{\mathrm{i}})\boldsymbol{\nabla} V_{\mathrm{m}} \cdot \boldsymbol{n} = \boldsymbol{\sigma}_{\mathrm{i}}\sigma_{\mathrm{b}}^{-1}\boldsymbol{j} \cdot \boldsymbol{n}, \quad \text{on} \quad \Sigma. \end{array}\right. \tag{5.5.27}$$

On the other hand, $\boldsymbol{\sigma}_{\mathrm{i}}(\boldsymbol{I} - \sigma_{\mathrm{b}}^{-1}\boldsymbol{\sigma}_{\mathrm{i}}) = \boldsymbol{\sigma}_{\mathrm{i}}\sigma_{\mathrm{b}}^{-1}(\sigma_{\mathrm{b}} - \boldsymbol{\sigma}_{\mathrm{i}}) = \boldsymbol{\sigma}_{\mathrm{i}}\sigma_{\mathrm{b}}^{-1}\boldsymbol{\sigma}_{\mathrm{e}}$. Therefore, by defining

$$\boldsymbol{\sigma}_{\mathrm{m}} \stackrel{\mathrm{def}}{=} \boldsymbol{\sigma}_{\mathrm{i}}\sigma_{\mathrm{b}}^{-1}\boldsymbol{\sigma}_{\mathrm{e}}, \tag{5.5.28}$$

the expression (5.5.27) reduces to

$$\left\{\begin{array}{l} A_{\mathrm{m}}\left(C_{\mathrm{m}}\dfrac{\partial V_{\mathrm{m}}}{\partial t} + I_{\mathrm{ion}}(V_{\mathrm{m}}, w)\right) - \operatorname{div}\left(\boldsymbol{\sigma}_{\mathrm{m}}\boldsymbol{\nabla} V_{\mathrm{m}}\right) \\ \qquad\qquad = -\operatorname{div}(\boldsymbol{\sigma}_{\mathrm{i}}\sigma_{\mathrm{b}}^{-1}\boldsymbol{j}) + A_{\mathrm{m}} I_{\mathrm{app}}, \quad \text{in} \quad \Omega_{\mathrm{H}}, \\ \boldsymbol{\sigma}_{\mathrm{m}}\boldsymbol{\nabla} V_{\mathrm{m}} \cdot \boldsymbol{n} = \boldsymbol{\sigma}_{\mathrm{i}}\sigma_{\mathrm{b}}^{-1}\boldsymbol{j} \cdot \boldsymbol{n}, \quad \text{on} \quad \Sigma. \end{array}\right. \tag{5.5.29}$$

Following [CNLH04b, CFPT05], we deduce from (5.4.16)

$$\boldsymbol{\sigma}_{\mathrm{i}}\sigma_{\mathrm{b}}^{-1} = \mu_{\mathrm{t}}\boldsymbol{I} + (\mu_{\mathrm{l}} - \mu_{\mathrm{t}})\boldsymbol{a}\otimes\boldsymbol{a}, \tag{5.5.30}$$

with

$$\mu_{\mathrm{l}} \stackrel{\mathrm{def}}{=} \frac{\sigma_{\mathrm{l}}^{\mathrm{i}}}{\sigma_{\mathrm{l}}^{\mathrm{i}} + \sigma_{\mathrm{l}}^{\mathrm{e}}}, \quad \mu_{\mathrm{t}} \stackrel{\mathrm{def}}{=} \frac{\sigma_{\mathrm{t}}^{\mathrm{i}}}{\sigma_{\mathrm{t}}^{\mathrm{i}} + \sigma_{\mathrm{t}}^{\mathrm{e}}},$$

By setting $\epsilon \stackrel{\mathrm{def}}{=} |\mu_{\mathrm{t}} - \mu_{\mathrm{l}}|$, we deduce from (5.5.30)

$$\boldsymbol{\sigma}_{\mathrm{i}}\sigma_{\mathrm{b}}^{-1} = \mu_{\mathrm{t}}\boldsymbol{I} + O(\epsilon). \tag{5.5.31}$$

As noticed in [CNLH04b], ϵ is a parameter that measures the gap between the anisotropy ratios of the intra- and extracellular media. In general $0 \leq \epsilon < 1$, and for equal anisotropy ratios $\epsilon = 0$ so that $\boldsymbol{\sigma}_{\mathrm{i}}\sigma_{\mathrm{b}}^{-1} = \mu_{\mathrm{t}}\boldsymbol{I}$.

Assuming $\epsilon \ll 1$, the expansion (5.5.31) can be inserted into (5.5.29) by keeping the terms up to the zero order. Thus, since μ_{t} is assumed to be constant, and using (5.2.1) and (5.2.9), up to the zero order in ϵ, the so-called *monodomain approximation* is obtained:

$$\begin{cases} A_{\mathrm{m}}\left(C_{\mathrm{m}}\dfrac{\partial V_{\mathrm{m}}}{\partial t} + I_{\mathrm{ion}}(V_{\mathrm{m}}, w)\right) - \operatorname{div}\left(\boldsymbol{\sigma}_{\mathrm{m}}\boldsymbol{\nabla}V_{\mathrm{m}}\right) = A_{\mathrm{m}}I_{\mathrm{app}}, & \text{in} \quad \Omega_{\mathrm{H}}, \\ \boldsymbol{\sigma}_{\mathrm{m}}\boldsymbol{\nabla}V_{\mathrm{m}}\cdot\boldsymbol{n} = -\mu_{\mathrm{t}}\boldsymbol{\sigma}_{\mathrm{e}}\boldsymbol{\nabla}u_{\mathrm{e}}\cdot\boldsymbol{n}, & \text{on} \quad \Sigma. \end{cases} \tag{5.5.32}$$

Heart-torso full coupling.

Under the full coupling conditions (5.2.10), V_{m} and u_{e} cannot be determined independently from each other. Note that, in (5.5.32) the coupling between V_{m} and u_{e} is fully concentrated on Σ, whereas in **RM** this coupling is also distributed in Ω_{H}, through $(5.2.7)_1$. Therefore, as soon as the heart and the torso are strongly coupled, the monodomain approximation does not substantially reduce the computational complexity with respect to **RM**. Owing to this observation, we will not pursue the investigations on this approach.

Heart-torso uncoupling.

Within the framework of section 5.5.1, the insulating condition (5.5.18) combined with (5.5.32) yields

$$\begin{cases} A_{\mathrm{m}}\left(C_{\mathrm{m}}\dfrac{\partial V_{\mathrm{m}}}{\partial t} + I_{\mathrm{ion}}(V_{\mathrm{m}}, w)\right) - \operatorname{div}\left(\boldsymbol{\sigma}_{\mathrm{m}}\boldsymbol{\nabla}V_{\mathrm{m}}\right) = A_{\mathrm{m}}I_{\mathrm{app}}, & \text{in} \quad \Omega_{\mathrm{H}}, \\ \boldsymbol{\sigma}_{\mathrm{m}}\boldsymbol{\nabla}V_{\mathrm{m}}\cdot\boldsymbol{n} = 0, & \text{on} \quad \Sigma, \end{cases} \tag{5.5.33}$$

which, along with (5.2.5), allows to compute V_{m} independently of u_{e}. The extra-cellular potential can then be recovered, *a posteriori*, by solving

$$\begin{cases} -\operatorname{div}((\boldsymbol{\sigma}_{\mathrm{i}} + \boldsymbol{\sigma}_{\mathrm{e}})\boldsymbol{\nabla}u_{\mathrm{e}}) = \operatorname{div}(\boldsymbol{\sigma}_{\mathrm{i}}\boldsymbol{\nabla}V_{\mathrm{m}}), & \text{in} \quad \Omega_{\mathrm{H}}, \\ (\boldsymbol{\sigma}_{\mathrm{i}} + \boldsymbol{\sigma}_{\mathrm{e}})\boldsymbol{\nabla}u_{\mathrm{e}}\cdot\boldsymbol{n} = -\boldsymbol{\sigma}_{\mathrm{i}}\boldsymbol{\nabla}V_{\mathrm{m}}\cdot\boldsymbol{n}, & \text{on} \quad \Sigma. \end{cases}$$

At last, the heart potentials are transferred to the torso by solving (5.2.11) with (5.5.20), as in section 5.5.1.

Therefore, the monodomain approximation (5.5.32) combined with a heart-torso uncoupling assumption leads to a fully decoupled computation of $V_{\rm m}$, $u_{\rm e}$ and $u_{\rm T}$. The three systems of equations which have to be solved successively read:

1. Monodomain problem, decoupled $V_{\rm m}$:

$$\left\{\begin{array}{rl} A_{\rm m}\left(C_{\rm m}\dfrac{\partial V_{\rm m}}{\partial t}+I_{\rm ion}(V_{\rm m},w)\right)-\operatorname{div}(\boldsymbol{\sigma}_{\rm m}\boldsymbol{\nabla}V_{\rm m})=A_{\rm m}I_{\rm app}, & \text{in}\quad \Omega_{\rm H},\\ \dfrac{\partial w}{\partial t}+g(V_{\rm m},w)=0, & \text{in}\quad \Omega_{\rm H},\\ \boldsymbol{\sigma}_{\rm m}\boldsymbol{\nabla}V_{\rm m}\cdot\boldsymbol{n}=0, & \text{on}\quad \Sigma. \end{array}\right. \tag{5.5.34}$$

2. Heart extracellular potential $u_{\rm e}$:

$$\left\{\begin{array}{rl} \operatorname{div}\left((\boldsymbol{\sigma}_{\rm i}+\boldsymbol{\sigma}_{\rm e})\boldsymbol{\nabla}u_{\rm e}\right)=-\operatorname{div}(\boldsymbol{\sigma}_{\rm i}\boldsymbol{\nabla}V_{\rm m}), & \text{in}\quad \Omega_{\rm H},\\ (\boldsymbol{\sigma}_{\rm i}+\boldsymbol{\sigma}_{\rm e})\boldsymbol{\nabla}u_{\rm e}\cdot\boldsymbol{n}=-\boldsymbol{\sigma}_{\rm i}\boldsymbol{\nabla}V_{\rm m}\cdot\boldsymbol{n}, & \text{on}\quad \Sigma. \end{array}\right. \tag{5.5.35}$$

3. Torso potential $u_{\rm T}$:

$$\left\{\begin{array}{rl} \operatorname{div}(\boldsymbol{\sigma}_{\rm T}\boldsymbol{\nabla}u_{\rm T})=0, & \text{in}\quad \Omega_{\rm T},\\ u_{\rm T}=u_{\rm e}, & \text{on}\quad \Sigma,\\ \boldsymbol{\sigma}_{\rm T}\boldsymbol{\nabla}u_{\rm T}\cdot\boldsymbol{n}_{\rm T}=0, & \text{on}\quad \Gamma_{\rm ext}. \end{array}\right. \tag{5.5.36}$$

To sum up the discussion of this subsection on can say that two levels of simplification can be considered with respect to **RM**: first, replacing the bidomain equations by the monodomain equations; second, replacing the full heart-torso coupling by an uncoupled formulation. The first simplification significantly reduces the computational effort only if the second one is also assumed.

Numerical results with heart-torso uncoupling

Figure 5.20 shows the ECG signals obtained with the bidomain model (bottom) and the monodomain approximation (top) in a healthy case, using the heart-torso uncoupling simplification. The simulated ECGs for a RBBB pathological condition are given in Figure 5.21. These figures clearly show that the most important clinical characteristics (*e.g.* QRS or QT durations) are essentially the same in both approaches.

The first lead, in a healthy case, of both approaches are presented together in Figure 5.22, for better comparison. The relative difference on the first lead is only 4% in l^2-norm. Thus, as far as the ECG is concerned, bidomain equations can be safely replaced by the monodomain approximation.

These observations are consistent with the conclusions of other studies based on isolated whole heart models [CNLH04b, PDR$^+$06]. For instance, the numerical results reported in [PDR$^+$06] show that the propagation of the activation wave is only 2% faster in the bidomain model and that the electrograms (point-wise values of the extra-cellular potential) are almost indistinguishable.

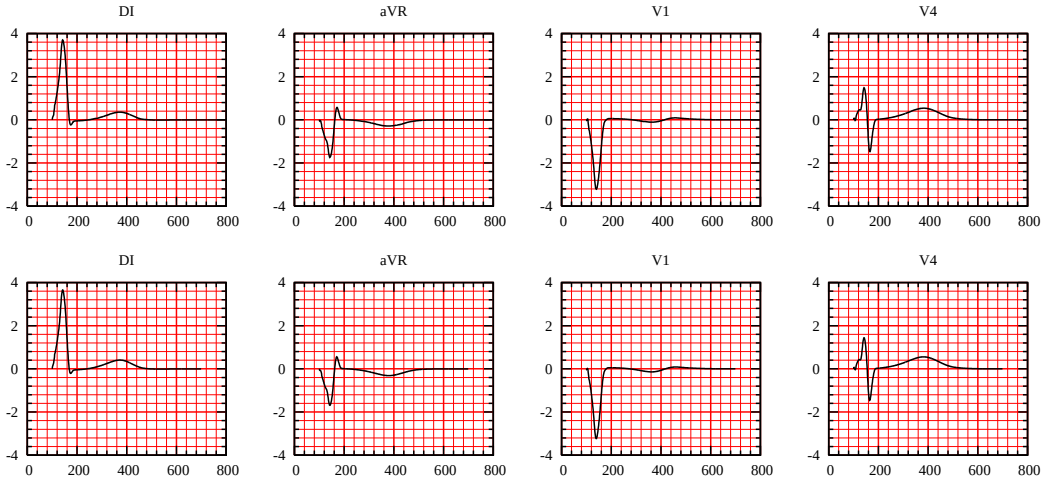

Figure 5.20: Simulated normal ECG with heart-torso uncoupling: monodomain (top) and bidomain (bottom) models.

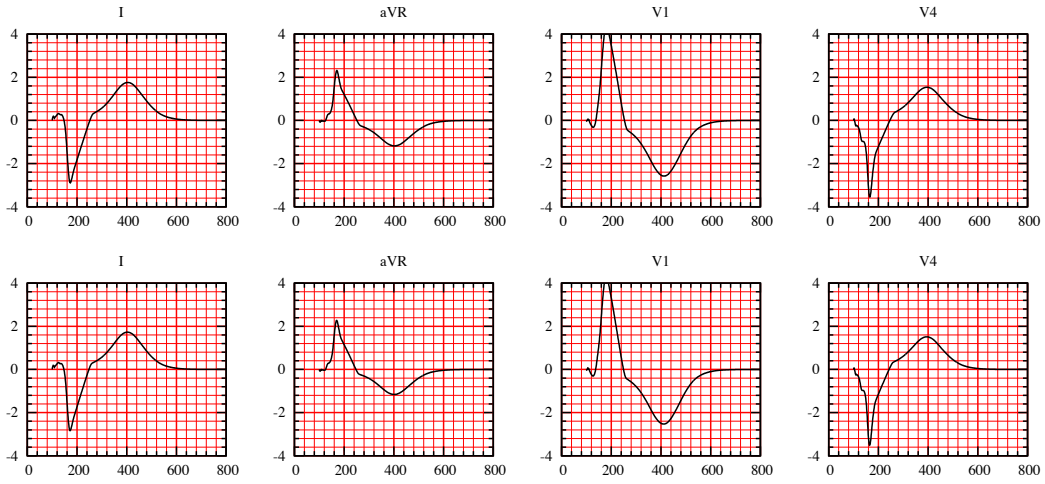

Figure 5.21: Simulated ECG for a RBBB pathology with heart-torso uncoupling: monodomain (top) and bidomain (bottom) models.

5.5.3 Isotropy

The impact of the conductivity anisotropy on the ECG signals is now investigated. To this aim, the numerical simulations of section 5.4.1 are reconsidered with isotropic conductivities, by setting

$$\boldsymbol{\sigma}_{\mathrm{e}}^{\mathrm{t}} = \boldsymbol{\sigma}_{\mathrm{e}}^{\mathrm{l}} = 3.0 \times 10^{-3} \text{ S cm}^{-1}, \quad \boldsymbol{\sigma}_{\mathrm{i}}^{\mathrm{t}} = \boldsymbol{\sigma}_{\mathrm{i}}^{\mathrm{l}} = 3.0 \times 10^{-3} \text{ S cm}^{-1}.$$

Figure 5.23 (top) shows the corresponding ECG signals. The QRS and T waves have the same polarity than in the anisotropic case, Figure 5.23 (bottom). However, we can clearly observe that the QRS-complex has a smaller duration and that the S-wave amplitude, in leads I and V4, is larger. The impact of anisotropy is much more striking when dealing with pathological activations. In Figure 5.24, for instance, the simulated ECG signals for a RBBB pathology have been reported with anisotropic and isotropic conductivities. Notice that the electrical signal is significantly distorted. In particular,

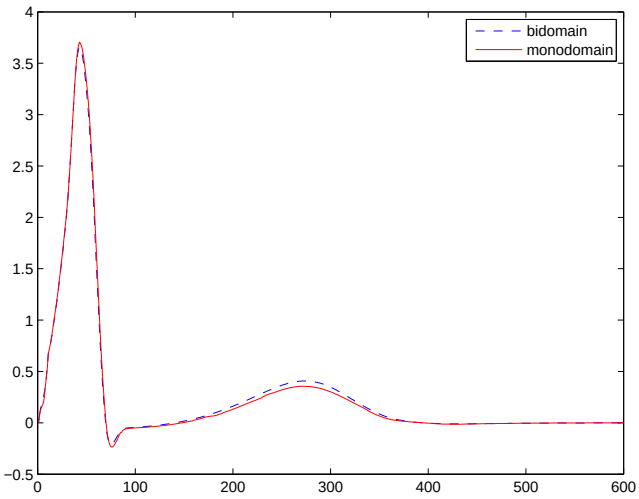

Figure 5.22: First ECG lead: bidomain and monodomain models with heart-torso uncoupling

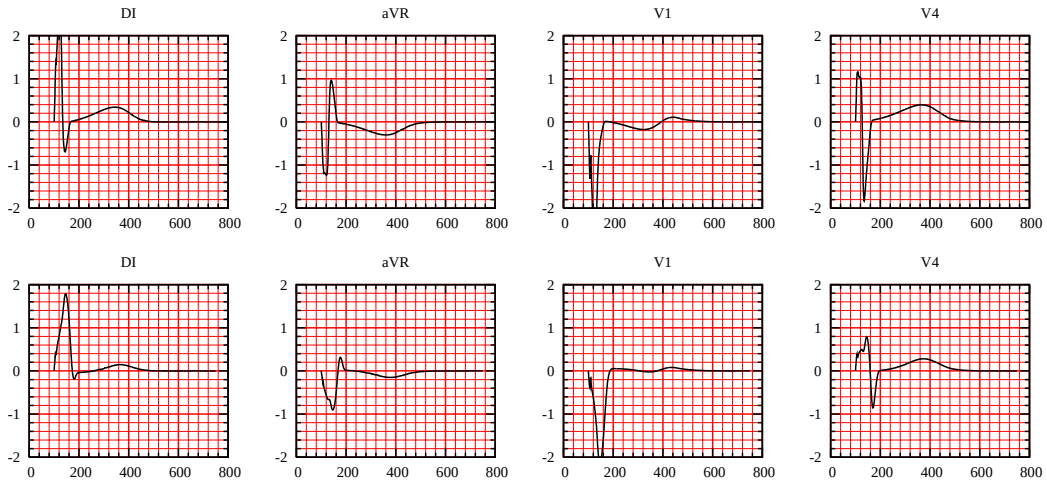

Figure 5.23: ECG signals: isotropic conductivities (top), anisotropic conductivities (bottom).

the amplitude of the QRS complex is larger in the isotropic case (this observation also holds in the healthy case).

These numerical simulations show that anisotropy has a major impact on the accuracy of ECG signals. Meaningful ECG simulations have therefore to incorporate this modeling feature (see also [CFPST09]).

5.5.4 Cell homogeneity

As mentioned in subsection 5.4.1, an heterogeneous coefficient τ_{close} has been considered in **RS** to incorporate an APD gradient across the left ventricle transmural direction. In this paragraph, the myocardium is assumed to have homogeneous cells. The ECG signals

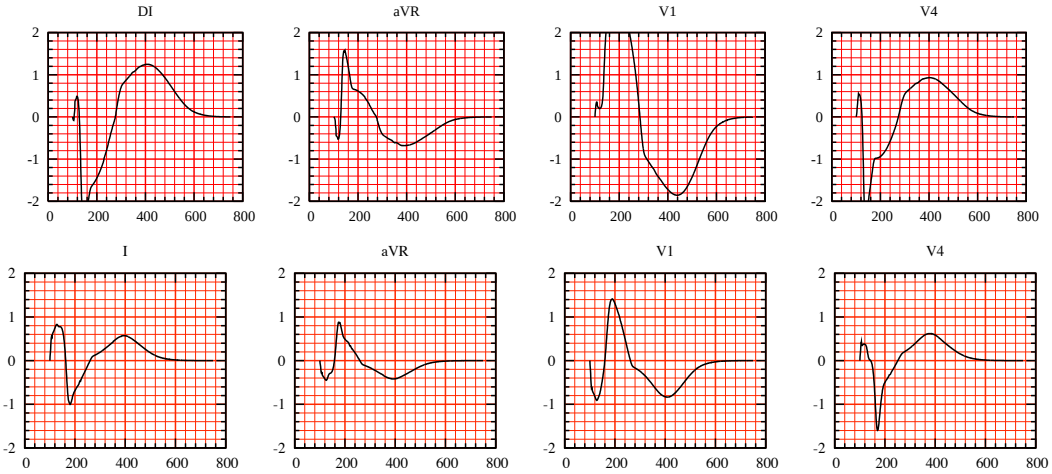

Figure 5.24: Isotropic (top) and anisotropic (bottom) conductivities in a pathological case (RBBB).

corresponding to a constant APD in the whole heart, obtained with $\tau_{\text{close}} = 140$ ms, are reported in Figure 5.25.

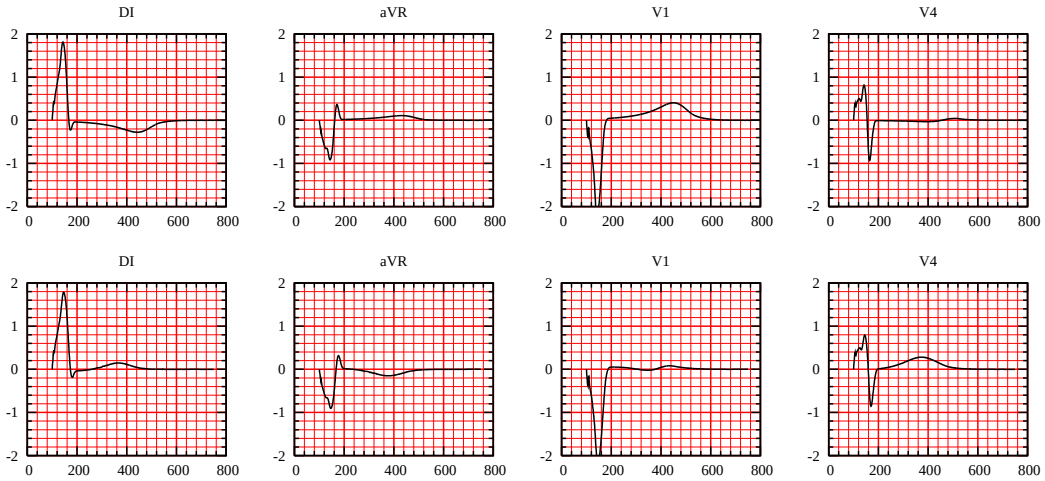

Figure 5.25: ECG signals: homogeneous action potential duration (top), heterogeneous action potential duration (bottom).

Note that now, in the bipolar lead (I), the T-wave has an opposite polarity with respect to the **RS** and to what is usually observed in normal ECGs. Indeed, without transmural APD heterogeneity, the repolarization and the depolarization waves travel in the same direction, which leads to the discordant polarity, between the QRS and the T waves, observed in lead I. On the contrary, the unipolar leads (aVR, V1 and V4) present a similar polarity, irrespectively of the ADP heterogeneity (see also [CFPST09]).

As a result, as also noticed in [PDG03, PBLV07, KSW+07, BFGZ07], transmural APD heterogeneity is a major ingredient in the simulation of a complete 12-lead ECG with physiological T-wave polarities.

5.5.5 Capacitive and resistive effect of the pericardium

The coupling conditions (5.2.10) are formally obtained in [KN94] using an homogenization procedure. In that reference, a perfect electrical coupling is assumed between the heart and the surrounding tissues.

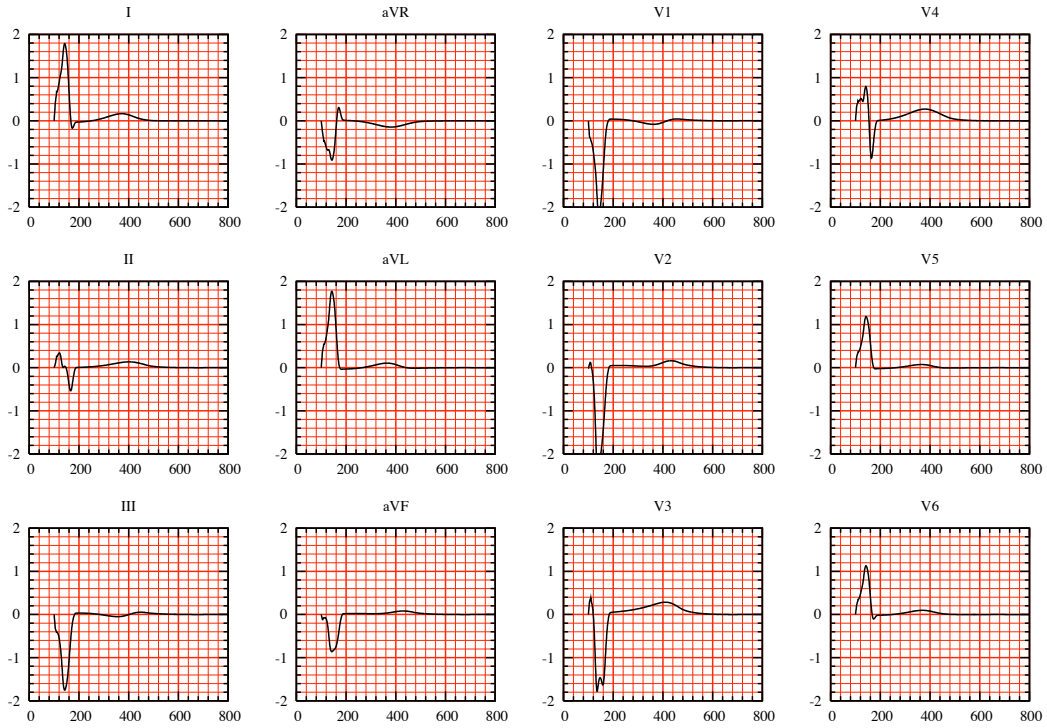

Figure 5.26: Simulated 12-lead ECG signals: R-C heart-torso coupling conditions with $R_{\mathrm{p}} = 10^2\ \Omega\ \mathrm{cm}^2$, $C_{\mathrm{p}} = 0\ \mathrm{mF\ cm}^{-2}$.

It might be interesting to consider more general coupling conditions. For instance, by assuming that the pericardium (the double-walled sac containing the heart) might induce a resistor-capacitor effect. This can be a way to model pathological conditions — *e.g.* pericarditis, when the pericardium becomes inflamed — or to take into account the fact that, even in a healthy situation, the heart-torso coupling can be more complex. Thus, we propose to generalize (5.2.10), by introducing the following resistor-capacitor (R-C) coupling conditions:

$$\begin{cases} R_{\mathrm{p}}\boldsymbol{\sigma}_{\mathrm{T}}\boldsymbol{\nabla} u_{\mathrm{T}} \cdot \boldsymbol{n} = R_{\mathrm{p}} C_{\mathrm{p}} \dfrac{\partial (u_{\mathrm{e}} - u_{\mathrm{T}})}{\partial t} + (u_{\mathrm{e}} - u_{\mathrm{T}}), & \text{on } \Sigma, \\ \boldsymbol{\sigma}_{\mathrm{e}}\boldsymbol{\nabla} u_{\mathrm{e}} \cdot \boldsymbol{n} = \boldsymbol{\sigma}_{\mathrm{T}}\boldsymbol{\nabla} u_{\mathrm{T}} \cdot \boldsymbol{n}, & \text{on } \Sigma, \end{cases} \tag{5.5.37}$$

where C_{p} and R_{p} stand for the capacitance and resistance of the pericardium, respectively. Note that, the classical relations (5.2.10) can be recovered from (5.5.37) by setting $R_{\mathrm{p}} = 0$. To the best of our knowledge, the resistor-capacitor behavior (5.5.37) of the pericardium is not documented in the literature, so we propose to study its effect on ECGs through numerical simulations.

Numerical tests showed that for R_{p} small ($R_{\mathrm{p}} < 10^3\ \Omega\ \mathrm{cm}^2$ approximatively) or C_{p} large ($C_{\mathrm{p}} > 1\ \mathrm{mF\ cm}^{-2}$ approximatively) the simulated ECG is very close to the **RS**.

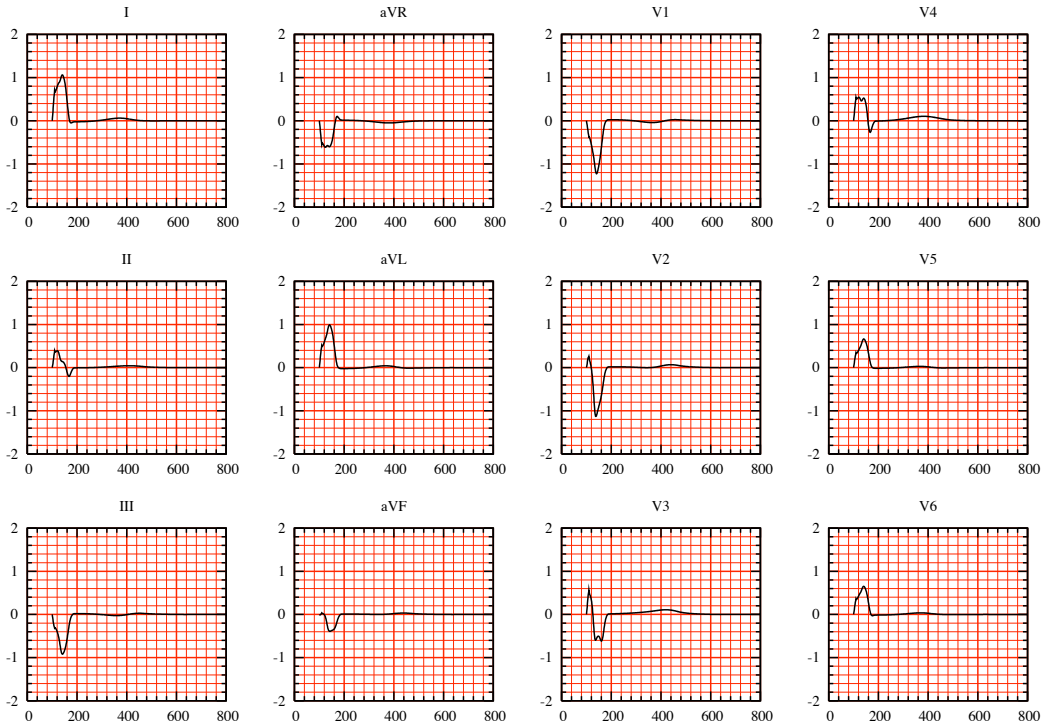

Figure 5.27: Simulated 12-lead ECG signals: R-C heart-torso coupling conditions with $R_\mathrm{p} = 10^4\,\Omega\ \mathrm{cm}^2$, $C_\mathrm{p} = 0\ \mathrm{mF\ cm}^{-2}$.

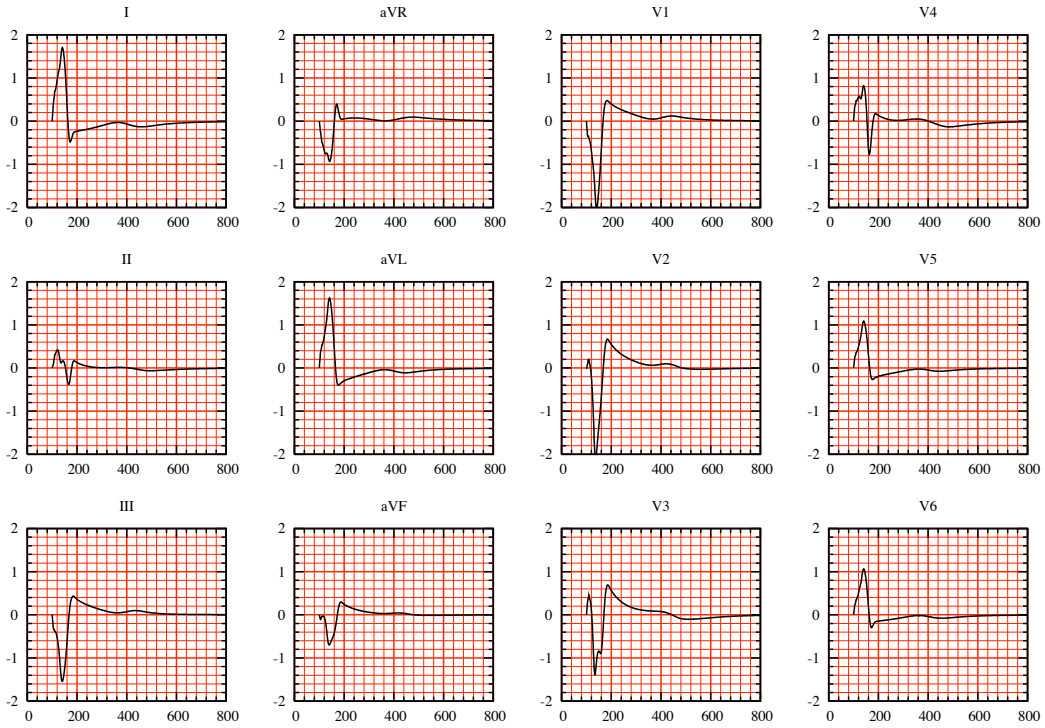

Figure 5.28: Simulated 12-lead ECG signals: R-C heart-torso coupling conditions with $R_\mathrm{p} = 10^{20}\,\Omega\ \mathrm{cm}^2$, $C_\mathrm{p} = 10^{-2}\,\mathrm{mF\,cm}^{-2}$

Figure 5.26, for instance, presents the ECG signals obtained with $R_\mathrm{p} = 10^2\,\Omega\ \mathrm{cm}^2$ and

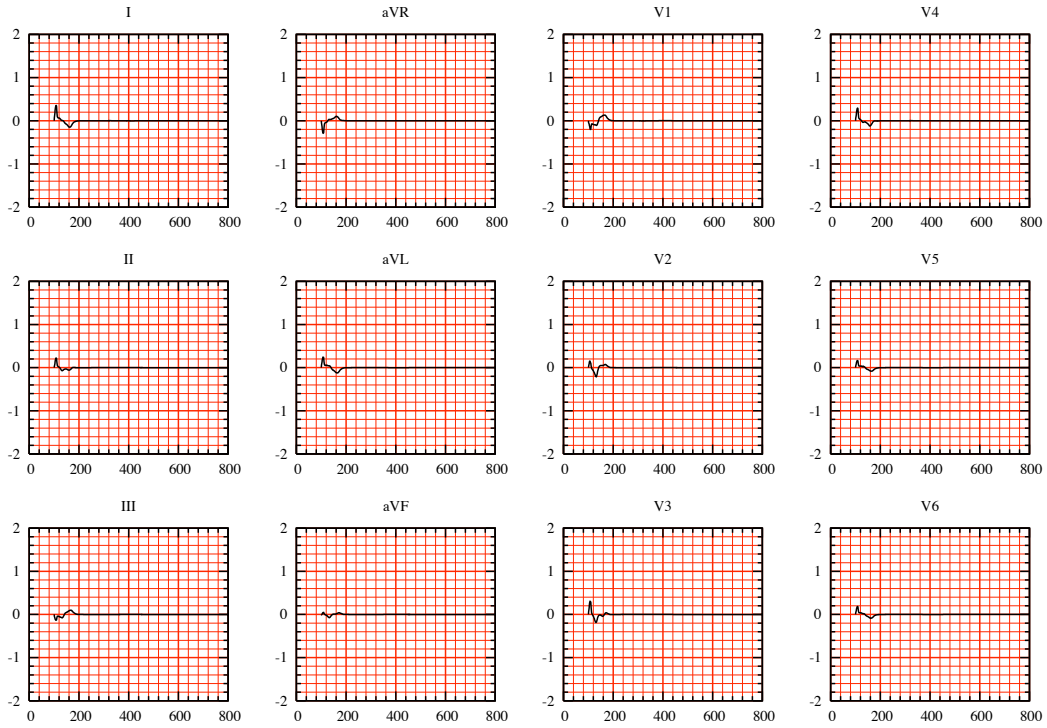

Figure 5.29: Simulated 12-lead ECG signals: R-C heart-torso coupling conditions with $R_{\rm p} = 10^{20}\,\Omega$ cm^2, $C_{\rm p} = 10^{-4}$ mF cm^{-2}.

$C_{\rm p} = 0$ mF cm^2.

In order to illustrate the resistor effect, we have reported in Figure 5.27 the ECG obtained with $C_{\rm p} = 0$ mF cm^{-2} and $R_{\rm p} = 10^4\,\Omega$.cm^2. We clearly observe that the amplitude of the signals is smaller than in the **RS**. More generally, this amplitude decreases when $R_{\rm p}$ increases, as expected.

We now focus on the capacitor effect by taking $R_{\rm p}$ very large. Figure 5.28 presents the ECG signals obtained with $R_{\rm p} = 10^{20}\,\Omega\,$cm^2 and $C_{\rm p} = 10^{-2}$ mF cm^{-2}. We observe that the capacitive term induces a relaxation effect and distorts the signal. In particular, the T-wave is inverted in all the ECG leads and the S-wave duration is larger than for the **RS**. At last, Figure 5.29 shows that for very small values of $C_{\rm p}$ the amplitude of the ECG is also very small. This can be formally explained by the fact that, in this case, condition $(5.5.37)_1$ approximately becomes $\boldsymbol{\sigma}_{\rm T}\boldsymbol{\nabla} u_{\rm T}\cdot\boldsymbol{n} = 0$ on Σ: no heart information is transferred to the torso, leading to very low ECG signals.

5.6 Numerical investigations with weak heart-torso coupling

In this section, we investigate the ECG sensitivity to the time and space discretizations and to the heart and torso model parameters. To carry out these studies at a reasonable computational cost, we consider the heart-torso uncoupling. Although we have noticed (in section 5.5.1) that uncoupling may affect the ECG accuracy in some cases,

we can expect that the conclusions of the sensitivity analysis remain still valid under this simplification.

5.6.1 Time and space convergence

In this section, we are not interested in the convergence of the whole solution of the **RM** with respect to the space and time discretization parameters, but rather in the convergence of the ECG which is here considered as the quantity of interest.

5.6.1.a) Time convergence

In Figure 5.30, we present the first ECG lead (lead I) obtained for three different time-step sizes $\delta t = 0.25$, 0.5 and 2 ms. The l^2-norm of the relative difference with the result obtained with $\delta t = 0.25$ ms is 10 % when $\delta t = 2$ ms and 2.0% when $\delta t = 0.5$ ms.

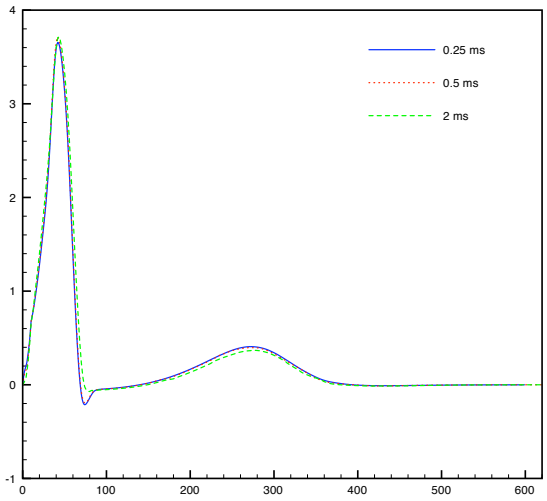

Figure 5.30: Comparison of three simulations of ECG (lead I) with three different time steps: 2, 0.5 and 0.25 ms. The computation is performed using the **RS** parameters only the time step is changed.

5.6.1.b) Space convergence

Three different levels of refinements are considered for the heart and the torso meshes, as shown in Table 5.5. The finite element meshes used in the **RS** are the R2. In Figure 5.31, we report the first lead of the ECGs obtained for these simulations using a time step $\delta t = 0.25$ ms.

Although the whole solution might not be fully converged within the heart, we can observe that the quantity of interest – namely the ECG – is almost unaffected by the last refinement. Therefore, in a goal-oriented refinement framework, the solution may indeed be considered as converged.

Meshes	Heart nodes	h (cm)	Torso nodes	Total number of tetrahedra
R1	13 000	0.30	56 000	370 000
R2	80 000	0.15	120 000	1 080 000
R3	236 000	0.11	232 000	2 524 000

Table 5.5: Three different levels of refinement for the computational heart and torso meshes (rounded off values), h denotes the discretization parameter.

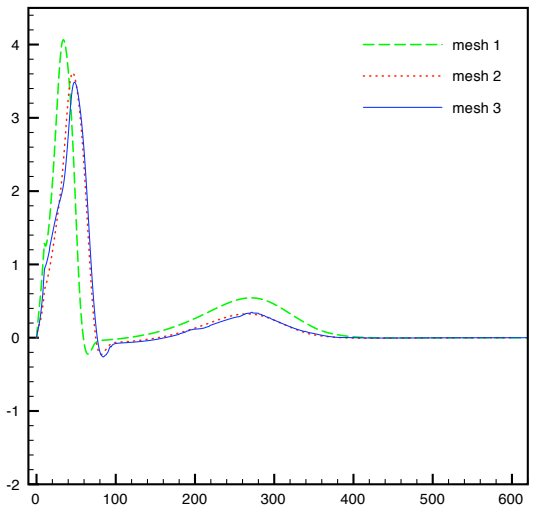

Figure 5.31: Comparison of three simulations of ECG (lead I), using three different levels of mesh refinement (see Table 5.5). The computation is performed using the **RS** parameters only the space discretization parameter is changed.

5.6.2 Sensitivity to model parameters

In this section, we study the sensitivity of ECG to some model parameters. This is fundamental step prior to addressing its estimation (see *e.g.* [BFGZ08a]) using data assimilation techniques.

Suppose that $\alpha_1, \alpha_2, ..., \alpha_\mathrm{p}$ are parameters the ECG depends upon, *i.e.*

$$ECG = ECG(\alpha_1, \alpha_2, ..., \alpha_\mathrm{p}).$$

The ECG sensitivity to parameter α_i can then be approximated as

$$\partial_{\alpha_i} ECG(\alpha_1, \alpha_2, ..., \alpha_\mathrm{p}) \approx \frac{ECG(\alpha_1, \alpha_2, ..., (1+\epsilon)\alpha_i, ..., \alpha_\mathrm{p}) - ECG(\alpha_1, \alpha_2, ..., \alpha_\mathrm{p})}{\epsilon \alpha_i},$$

where ϵ is a small parameter, in our case $10^{-6} \leq \epsilon \leq 10^{-4}$ gives a good approximation. Instead of $\partial_{\alpha_i} ECG(\alpha_1, \alpha_2, ..., \alpha_\mathrm{p})$ we consider the normalized value $\alpha_i \partial_{\alpha_i} ECG(\alpha_1, \alpha_2, ..., \alpha_\mathrm{p})$, which allows to compare the sensitivity irrespectively of the parameter scales. In the next paragraphs, we provide time evolution of this scaled derivative, evaluated around the parameters used in the **RS**. Once more, for the sake of conciseness, we focus on the first ECG lead.

Ionic model parameters

In this paragraph, we investigate the sensitivity of the ECG to the Mitchell-Schaeffer parameters. In Figure 5.32, we have reported the normalized derivatives with respect to τ_{in}, τ_{out}, τ_{open} or τ_{close}. The high ECG sensitivity to τ_{in} is clearly visible, particularly during the QRS-complex. The sensitivity to τ_{out} is moderate both during the depolarization and depolarization phases. As expected, the sensitivity to τ_{close} is only relevant during repolarization. Interestingly, the sensitivity to τ_{open} is relatively small. Therefore, this parameter may be removed (*i.e.* keep fixed) within an inverse estimation procedure.

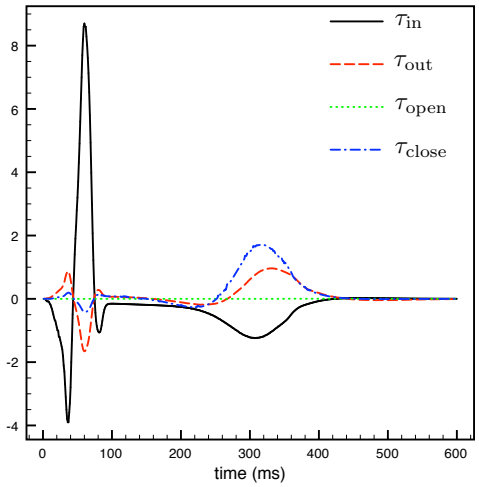

Figure 5.32: Normalized ECG sensitivity to τ_{in}, τ_{out}, τ_{open} and τ_{close}.

Bidomain model parameters

We first focus on the ECG sensitivity to the local myocardium conductivities: $\sigma_{\text{e}}^{\text{t}}$, $\sigma_{\text{e}}^{\text{l}}$, $\sigma_{\text{i}}^{\text{t}}$ and $\sigma_{\text{i}}^{\text{l}}$. The corresponding normalized derivatives are given in Figure 5.33. During

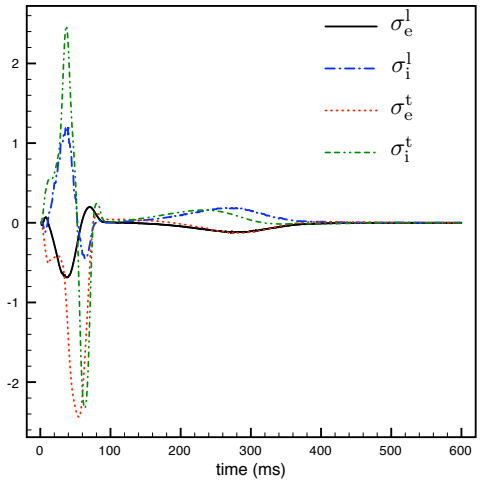

Figure 5.33: Normalized ECG sensitivity to the local myocardium conductivities: $\sigma_{\text{e}}^{\text{t}}$, $\sigma_{\text{e}}^{\text{l}}$, $\sigma_{\text{i}}^{\text{t}}$ and $\sigma_{\text{i}}^{\text{l}}$.

depolarization (QRS-complex), the ECG is mainly sensitive to transverse conductivity (σ_e^t, σ_i^t). This can be due to the dominating transmural propagation of the depolarization wave in the left ventricle (see Figure 5.6 (left)). During repolarization (T-wave), on the contrary, the ECG shows approximately the same sensitivity to all the local conductivities. We now pursue our sensitivity analysis, by considering the parameters A_m and

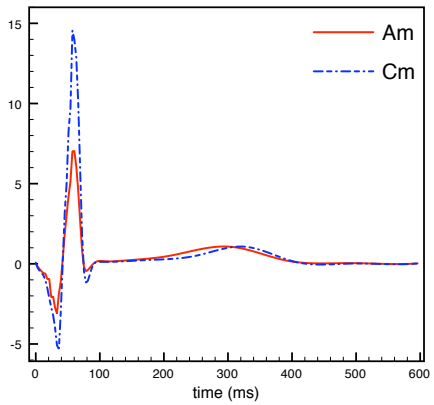

Figure 5.34: Normalized ECG sensitivity to A_m and C_m.

C_m. The corresponding normalized derivatives are given in Figure 5.34. We observe a strong sensitivity to both parameters during depolarization. Whereas, during the repolarization phase, the sensitivity is reduced. At last, we investigate the sensitivity of the

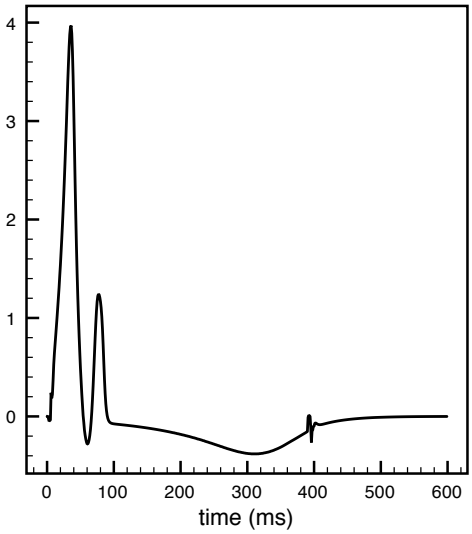

Figure 5.35: Normalized ECG sensitivity to the activation angular velocity.

ECG to the initial activation in the heart (see Appendix 5.4.1). More precisely, we focus on the sensitivity to the activation angular velocity $\frac{\pi}{2t_{act}}$. The corresponding normalized derivative is reported Figure 5.35. As expected, the ECG is strongly sensitive to this parameter, particularly during the depolarization phase.

Torso parameters

We finally consider the sensitivity of the ECG to the torso conductivities $\sigma_{\mathrm{T}}^{\mathrm{l}}$, $\sigma_{\mathrm{T}}^{\mathrm{b}}$ and $\sigma_{\mathrm{T}}^{\mathrm{t}}$. Note that, in a heart-torso uncoupling framework, the corresponding three normalized derivatives are linked by a linear relation. Indeed, from (5.2.11) and (5.5.20), we have that, for all $\lambda \in \mathbb{R}$, u_{T} solves

$$\begin{cases} \operatorname{div}(\lambda \boldsymbol{\sigma}_{\mathrm{T}} \boldsymbol{\nabla} u_{\mathrm{T}}) = 0, & \text{in} \quad \Omega_{\mathrm{T}}, \\ u_{\mathrm{T}} = u_{\mathrm{e}}, & \text{on} \quad \Sigma, \\ \lambda \boldsymbol{\sigma}_{\mathrm{T}} \boldsymbol{\nabla} u_{\mathrm{T}} \cdot \boldsymbol{n}_{\mathrm{T}} = 0, & \text{on} \quad \Gamma_{\mathrm{ext}}. \end{cases}$$

In other words,

$$u_{\mathrm{T}}(\lambda \sigma_{\mathrm{T}}^{\mathrm{l}}, \lambda \sigma_{\mathrm{T}}^{\mathrm{b}}, \lambda \sigma_{\mathrm{T}}^{\mathrm{t}}) = u_{\mathrm{T}}(\sigma_{\mathrm{T}}^{\mathrm{l}}, \sigma_{\mathrm{T}}^{\mathrm{b}}, \sigma_{\mathrm{T}}^{\mathrm{t}}). \tag{5.6.38}$$

Differentiating this relation with respect to λ (and evaluating the resulting expression at $\lambda = 1$) yields

$$\sigma_{\mathrm{T}}^{\mathrm{l}} \partial_{\sigma_{\mathrm{T}}^{\mathrm{l}}} u_{\mathrm{T}} + \sigma_{\mathrm{T}}^{\mathrm{b}} \partial_{\sigma_{\mathrm{T}}^{\mathrm{b}}} u_{\mathrm{T}} + \sigma_{\mathrm{T}}^{\mathrm{t}} \partial_{\sigma_{\mathrm{T}}^{\mathrm{t}}} u_{\mathrm{T}} = 0.$$

Thus, from (5.4.17), we obtain a similar relation for the normalized ECG derivatives:

$$\sigma_{\mathrm{T}}^{\mathrm{l}} \partial_{\sigma_{\mathrm{T}}^{\mathrm{l}}} ECG + \sigma_{\mathrm{T}}^{\mathrm{b}} \partial_{\sigma_{\mathrm{T}}^{\mathrm{b}}} ECG + \sigma_{\mathrm{T}}^{\mathrm{t}} \partial_{\sigma_{\mathrm{T}}^{\mathrm{t}}} ECG = 0.$$

Figure 5.36 presents the normalized derivatives of the ECG with respect to the tissue, lung and bone conductivities. This figure clearly shows that the ECG sensitivity

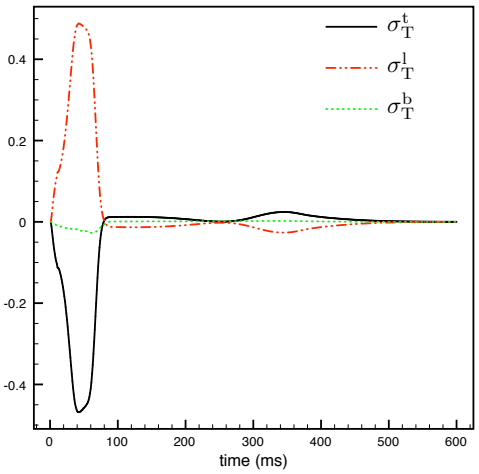

Figure 5.36: Normalized ECG sensitivity to $\sigma_{\mathrm{T}}^{\mathrm{l}}$, $\sigma_{\mathrm{T}}^{\mathrm{b}}$ and $\sigma_{\mathrm{T}}^{\mathrm{t}}$.

to the bone parameter $\sigma_{\mathrm{T}}^{\mathrm{b}}$ is negligible compared to its sensitivity to the tissue and lung parameters. Thus, if we have in mind to limit the number of parameters to be estimated, $\sigma_{\mathrm{T}}^{\mathrm{b}}$ can safely be fixed to the value used in the **RS**.

5.7 Conclusion

A fully PDE/ODE based mathematical model for the numerical simulation of ECGs has been described. The electrical activity of the heart is based on the coupling of the

bidomain equations with the Mitchell-Schaeffer phenomenological ionic model, including anisotropic conductivities and transmural APD heterogeneity. This system of equations has been coupled to a generalized Laplace equation in the torso, with inhomogeneous conductivity (bone, lungs and remaining tissue). A detailed description of the different algorithms used for the numerical solution of the resulting ECG model has been also provided.

Our approach has several limitations: we did not consider the atria, which prevents us from computing the P wave of the ECG; the cell model being phenomenological, it cannot handle complex ionic interactions; the effect of the blood flow on the ECG was neglected; the geometry of the ventricles were simplified.

Despite the above mentioned limitations, we were able to compute a satisfactory healthy 12-lead ECG, with a limited number a parameters. To the best of our knowledge, this constitutes a breakthrough in the modeling of ECGs with partial differential equations. Moreover, for pathological situations corresponding to a bundle branch block and arrhythmia, our simulations have provided ECGs which satisfy typical criteria used by medical doctors to detect these pathologies. This shows, in particular, that our numerical model have some predictive features.

In a second part, we have studied the impact of some modeling assumptions on the ECGs. The main conclusions of this investigation are the following:

1. As far as the general shape of the ECGs is concerned, heart-torso uncoupling can be considered. The level of accuracy obtained with uncoupling is probably sufficient in several applications, which may explain why this simplification is so widespread in the literature. Nevertheless, our numerical results have clearly pointed out that the amplitudes of the ECG signals obtained via uncoupling and full coupling can significantly differ. We therefore recommend to carefully check in each specific situations whether the uncoupling approximation is acceptable or not.

2. In agreement with other studies, we noticed that cell heterogeneity and fiber anisotropy have an important impact on the ECG and, therefore, cannot be neglected.

3. The bidomain equations can apparently be safely replaced by the monodomain equations without significantly affecting the ECG. Nevertheless, even with this simplification, we point out that the transmembrane potential V_{m} and the extracellular potential u_{e} still have to be solved simultaneously when the heart and the torso are fully coupled. To be really attractive, the monodomain simplification has therefore to come with the uncoupling approximation, which can affect the ECG, as mentioned above.

4. We have proposed a new heart-torso coupling condition which takes into account possible capacitive and resistive effects of the pericardium. We did not find in the literature any evidence of these effects and our results show that it does not seem necessary to include them in order to get realistic healthy ECGs. Nevertheless, these coupling conditions might be relevant in some pathologies affecting the pericardial sac and the simulations we provided to illustrate these effects might be useful for future works.

5. At last, a sensitivity analysis has shown that the most critical parameters of the bidomain model are C_{m}, A_{m}, the angular velocity of the activation wave and the transverse conductivities $\sigma_{\mathrm{i}}^{\mathrm{t}}$ and $\sigma_{\mathrm{e}}^{\mathrm{t}}$. As regards the ECG sensitivity to the ionic model parameters, we have noticed a extreme sensitivity of the QRS-complex to the parameter τ_{in} and a high sensitivity of the T-wave to the parameter τ_{close}. Moreover, we have also observed that the ECG sensitivity to the torso conductivity parameters is less significant than to the heart model parameters.

To conclude, our main concern during this study was to build a model rich enough to provide realistic ECGs and simple enough to be easily parametrized. In spite of its shortcomings, the proposed approach essentially fulfills these requirements and is therefore a good candidate to address inverse problems. This will be investigated in future works.

Chapter 6

Decoupled time-marching schemes in computational cardiac electrophysiology and ECG numerical simulation

In order to decouple the computation of the unknown fields (ionic state, transmembrane potential, extracellular and torso potentials) in both isolated heart problem (3.2.18) and heart-torso problem (3.4.24)-(3.4.26), we propose in this chapter first order semi-implicit time-marching schemes and a Robin-Robin treatment of the heart-torso coupling conditions. For the isolated bidomain system, we show that the Gauss-Seidel and Jacobi like splittings do not compromise energy stability; they simply alter the energy norm. Time-step constraints are only due to the semi-implicit treatment of the non-linear reaction terms. Within the framework of the numerical simulation of electrocardiograms (ECG), these bidomain splittings are combined with an explicit Robin-Robin treatment of the heart-torso coupling conditions. We show that the resulting schemes allow a fully decoupled (energy) stable computation of the heart and torso fields, under an additional mild CFL like condition. Numerical simulations, based on anatomical heart and torso geometries, illustrate the stability and accuracy of the proposed schemes.

This chapter is part of a joint work with M.A. Fernández, it is reported in [FZ09].

6.1 Introduction

Computational models of cardiac electrophysiology typically incorporate the cell membrane activity and the intra- and extracellular components of cardiac tissue by means of the *bidomain model* (see e.g. [SLC$^+$06, PBC05]). This mathematical model can be formulated as a *three-field* system (ionic state, transmembrane and extracellular potentials) coupling a non-linear reaction-diffusion equation, an elliptic equation and a non-linear system of ODE (alternative formulations are discussed in [HHLR94, PS02]).

The rapid dynamics of the ODE system, acting on the reaction terms, lead to the presence of a sharp propagating wavefront, which often requires fine resolutions

in space and in time. As a result, fully implicit time-marching is extremely difficult to perform since it involves the resolution of a large system of non-linear equations at each time step (see *e.g.* [HHLR94, BEL03, MC04, MP09]). Attempts to reduce this computational complexity (without compromising too much numerical stability) consist in introducing some sort of explicit treatment within the time-marching procedure. For instance, by considering semi-implicit described in chapter 5 (see *e.g.* [SLT01, LGT03, CFP04, ATP06, BFGZ07, EB08]) or operator splitting (see *e.g.* [KB98, SLT05, VWdSP$^+$08]) schemes. All these approaches uncouple the ODE system (ionic state and non-linear reaction terms) from the electrodiffusive components (transmembrane and extracellular potentials). Other works [SLT01, LGT03, ATP06, VWdSP$^+$08, PDR$^+$06] propose a decoupled (*Gauss-Seidel* like) time-marching of the three fields.

In this chapter we go further in the investigation of this kind of decoupling techniques, by providing a general energy based stability analysis that covers both the Gauss-Seidel and the Jacobi like approaches. In particular, we show that these electrodiffusive splittings do not compromise the stability of the resulting scheme. They simply alter the energy norm and time step restrictions are uniquely dictated by the semi-implicit treatment of the ODE system and the non-linear reaction terms.

In the second part, we propose to extend these time-marching techniques to the numerical simulation of the ECG, namely, the *forward problem* of cardiac electrophysiolgy (see *e.g.* [LBG$^+$03]). The bidomain equations have then to be coupled to a generalized Laplace equation, describing the electrical potential within the surrounding torso tissue. The heart-torso coupling is enforced through standard interface conditions, ensuring a perfect electrical balance (see *e.g.* [KN94, PBC05, SLC$^+$06]). This results in a coupled *four-field* problem (ionic state, transmembrane, extracellular and torso potentials) coupling a non-linear system of ODEs, a non-linear reaction-diffusion equation and two elliptic equations (see *e.g.* [LBG$^+$03, SLC$^+$06]).

Traditionally, the heart-torso coupling has been treated using two different approaches (see *e.g.* [LBG$^+$03]). The so called *heart-torso uncoupling* approximation (see Chapter 5 section 5.5.1 or [PDG03, LBG$^+$03, BCF$^+$09]) uncouples the heart and torso problems by neglecting the torso-to-heart electrical feedback (*i.e.* the heart is isolated). Although this approach is very appealing in terms of computational cost, it can compromise the accuracy of the corresponding ECG signals (see *e.g.* [LBG$^+$03, PBC05, BCF$^+$09]). The second approach, the so called *heart-torso full coupling*, treats the heart-torso interface conditions in a fully implicit fashion and, therefore, requires the resolution of a large heart-torso system at each time step (see *e.g.* [SLT01, LGT03, PBC05, BCF$^+$09]). To the best of our knowledge, none of the current approaches is able to provide accurate ECG signals (*i.e.* close to heart-torso full coupling) with a decoupled computation of the extracellular and torso potentials.

In this chapter, we introduce a series of time-marching schemes for ECG numerical simulation involving a fully decoupled computation of the ionic state, the transmembrane potential, the extracellular potential and the torso potential. The main idea consists in combining the above mentioned Gauss-Seidel or Jacobi like bidomain splittings, with an explicit Robin-Robin treatment (derived from [ACF09]) of the heart-torso coupling. An energy based stability analysis shows that the proposed schemes are stable under and additional mild CFL like condition. Note that, since the time discretization of the two

(quasi-static) elliptic equations does not produce numerical dissipation, conventional explicit Dirichlet-Neumann heart-torso coupling might lead to numerical instability.

The remainder of this chapter is organized as follows. In the next section we briefly recall the coupled system of equations describing the electrical activity of the heart and its interaction with the surrounding torso tissue. The time discretization of the bidomain equations is addressed in section §6.3, using Gauss-Seidel and Jacobi like eletrodiffusive splittings. The stability of the resulting schemes is analyzed by means of energy arguments. Section §6.4 is devoted to the discretization of the heart-torso system. The schemes analyzed in section §6.3 are then combined with a specific explicit Robin-Robin treatment of the heart-torso coupling. The energy based stability of the resulting schemes is investigated. Numerical evidence is provided in section §6.5, using realistic heart and torso geometries. A summary of the results and some concluding remarks are given in section §6.6.

6.2 Mathematical models

This section contains standard material (see *e.g.* [SLC+06, Chapter 2]). We introduce the notation and the coupled system of equations commonly used to model the electrical activity of the heart and its interaction with surrounding tissue (extramyocardial regions).

6.2.1 Isolated heart

The bidomain equations, originally derived in [Tun78], are the most widely accepted mathematical model of the macroscopic electrical activity of the heart (see *e.g.* the monographs [SLC+06, PBC05]). This model is usually formulated in terms of three variables: the transmembrane potential V_{m}, the extracellular potential u_{e} and the ionic state w (possibly vector valued). These space and time dependent variables are defined in $\Omega_{\mathrm{H}} \times (0,T)$, where Ω_{H} and $(0,T)$ denote, respectively, the heart domain and the time interval of interest.

The governing equations consist of a coupled system of ODE, a nonlinear reaction-diffusion equation and an elliptic equation, with appropriate boundary and initial conditions (see *e.g.* [SLC+06, PBC05]):

$$\partial_t w + g(V_{\mathrm{m}}, w) = 0, \quad \text{in} \quad \Omega_{\mathrm{H}} \times (0,T), \tag{6.2.1}$$

$$\chi_{\mathrm{m}} \partial_t V_{\mathrm{m}} + I_{\mathrm{ion}}(V_{\mathrm{m}}, w) - \operatorname{div}(\boldsymbol{\sigma}_{\mathrm{i}} \boldsymbol{\nabla} V_{\mathrm{m}}) - \operatorname{div}(\boldsymbol{\sigma}_{\mathrm{i}} \boldsymbol{\nabla} u_{\mathrm{e}}) = I_{\mathrm{app}}, \quad \text{in} \quad \Omega_{\mathrm{H}} \times (0,T), \tag{6.2.2}$$

$$-\operatorname{div}((\boldsymbol{\sigma}_{\mathrm{i}} + \boldsymbol{\sigma}_{\mathrm{e}}) \boldsymbol{\nabla} u_{\mathrm{e}}) - \operatorname{div}(\boldsymbol{\sigma}_{\mathrm{i}} \boldsymbol{\nabla} V_{\mathrm{m}}) = 0, \quad \text{in} \quad \Omega_{\mathrm{H}} \times (0,T), \tag{6.2.3}$$

$$\boldsymbol{\sigma}_{\mathrm{i}} \boldsymbol{\nabla} V_{\mathrm{m}} \cdot \boldsymbol{n} + \boldsymbol{\sigma}_{\mathrm{i}} \boldsymbol{\nabla} u_{\mathrm{e}} \cdot \boldsymbol{n} = 0, \quad \text{on} \quad \Sigma \times (0,T), \tag{6.2.4}$$

$$\boldsymbol{\sigma}_{\mathrm{e}} \boldsymbol{\nabla} u_{\mathrm{e}} \cdot \boldsymbol{n} = 0, \quad \text{on} \quad \Sigma \times (0,T), \tag{6.2.5}$$

$$V_{\mathrm{m}}(\boldsymbol{x}, 0) = V_{\mathrm{m}}^0(\boldsymbol{x}), \quad w(\boldsymbol{x}, 0) = w^0(\boldsymbol{x}), \quad \forall \boldsymbol{x} \in \Omega_{\mathrm{H}}. \tag{6.2.6}$$

Here, $\chi_{\mathrm{m}} \overset{\mathrm{def}}{=} A_{\mathrm{m}} C_{\mathrm{m}}$ where A_{m} is a geometrical quantity, C_{m} denotes the membrane capacitance and tensors $\boldsymbol{\sigma}_{\mathrm{i}}$ and $\boldsymbol{\sigma}_{\mathrm{e}}$ represent, respectively, the intra- and extracellular

conductivities. The term $I_{\rm ion}(V_{\rm m},w) \stackrel{\rm def}{=} A_{\rm m} i_{\rm ion}(V_{\rm m},w)$ denotes the ionic current across the membrane and $I_{\rm app}$ a given external current stimulus. The explicit expression of functions g and $i_{\rm ion}$ depends on the considered cell ionic model (see e.g. [SLC$^+$06, PBC05] and the references therein). At last, $\boldsymbol{n}$ stands for the outward unit normal to $\Sigma \stackrel{\rm def}{=} \partial\Omega_{\rm H}$ (see Figure 6.1), and $V_{\rm m}^0$, w^0 are given initial data.

The boundary conditions (6.2.4)-(6.2.5) state that the intra- and extracellular currents do not propagate outside the heart. While (6.2.4) is a widely accepted condition (see *e.g.* [Tun78, KN94, PBC05, SLC$^+$06]), the enforcement of (6.2.5) is only justified under an isolated heart assumption (see [SLC$^+$06, PBC05]). The coupled system of equations (6.2.1)-(6.2.6) is often known in the literature as *isolated bidomain* model (see *e.g.* [CFP04, CFP04, SLC$^+$06]). The interested reader is referred to [CFS02, BK06, BCP09, Ven09] for the mathematical analysis of problem (6.2.1)-(6.2.6).

The choice of the formulation (6.2.1)-(6.2.6) is motivated by the decoupling time-marching schemes introduced in section §6.3. Other formulations of the bidomain equations and their impact on the performance of the algebraic solvers have been discussed in [HHLR94, PS02]. A recent review of numerical methods for the bidomain equations can be found in [LSH$^+$09].

Remark 6.2.1.1. *The complexity of* (6.2.1)-(6.2.6) *can be reduced by using, instead of* (6.2.2) *and* (6.2.4)*, the so-called monodomain approximation:*

$$\begin{aligned} \chi_{\rm m}\partial_t V_{\rm m} + I_{\rm ion}(V_{\rm m},w) - \operatorname{div}\left(\boldsymbol{\sigma}\boldsymbol{\nabla} V_{\rm m}\right) = I_{\rm app}, \quad & \textit{in} \quad \Omega_{\rm H}, \\ \boldsymbol{\sigma}\boldsymbol{\nabla} V_{\rm m}\cdot\boldsymbol{n} = 0, \quad & \textit{on} \quad \Sigma, \end{aligned} \tag{6.2.7}$$

where $\boldsymbol{\sigma} \stackrel{\rm def}{=} \boldsymbol{\sigma}_{\rm i}(\boldsymbol{\sigma}_{\rm i}+\boldsymbol{\sigma}_{\rm e})^{-1}\boldsymbol{\sigma}_{\rm e}$ *is the bulk conductivity tensor (see e.g. [LH91, CNLH04b, CFP04, PDR$^+$06]). Note that* (6.2.7) *decouples de computation of* $V_{\rm m}$ *from that of* $u_{\rm e}$*. Under the isolating condition* (6.2.5)*,* (6.2.7) *can be interpreted as the zeroth-order approximation of* (6.2.2) *and* (6.2.4) *with respect to a parameter,* $0 \le \epsilon < 1$*, which measures the gap between the anisotropy ratios of the intra- and extracellular domains (see [CNLH04b, CFP04] for details). Although several simulation analysis (see e.g. [CNLH04b, PDR$^+$06]) suggest that the monodomain approximation may be adequate for some propagation studies in isolated hearts, it cannot be applied in all situations since it neglects the extracellular feedback into* $V_{\rm m}$ *(see e.g. [EGR00, CNLH04b, PDR$^+$06] and Remark 6.2.2.2 below).*

6.2.2 Coupling with torso: ECG modeling

The myocardium is surrounded by a volume conductor, $\Omega_{\rm T}$, which contains all the extramyocardial regions (see Figure 6.1). As a matter of fact, ECG signals monitor the electrical activity of the heart from potential measurements at the torso skin surface $\Gamma_{\rm ext}$. The torso volume is commonly modeled as a passive conductor (generalized Laplace equation), electrically coupled to the heart across the heart-torso interface Σ. The resulting coupled system can be formulated in terms of $V_{\rm m}$, $u_{\rm e}$, w and the torso potential

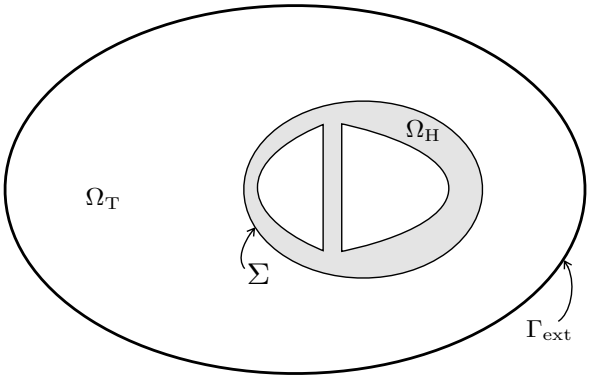

Figure 6.1: Two-dimensional geometrical description: heart domain Ω_{H}, torso domain Ω_{T} (extramyocardial regions), heart-torso interface Σ and torso external boundary Γ_{ext}.

u_{T}, as follows (see *e.g.* [SLC$^+$06, PBC05]):

$$\partial_t w + g(V_{\mathrm{m}}, w) = 0, \quad \text{in} \quad \Omega_{\mathrm{H}} \times (0,T), \tag{6.2.8}$$

$$\chi_{\mathrm{m}} \partial_t V_{\mathrm{m}} + I_{\mathrm{ion}}(V_{\mathrm{m}}, w) - \mathrm{div}(\boldsymbol{\sigma}_{\mathrm{i}} \boldsymbol{\nabla} V_{\mathrm{m}}) - \mathrm{div}(\boldsymbol{\sigma}_{\mathrm{i}} \boldsymbol{\nabla} u_{\mathrm{e}}) = I_{\mathrm{app}}, \quad \text{in} \quad \Omega_{\mathrm{H}} \times (0,T), \tag{6.2.9}$$

$$-\mathrm{div}((\boldsymbol{\sigma}_{\mathrm{i}} + \boldsymbol{\sigma}_{\mathrm{e}}) \boldsymbol{\nabla} u_{\mathrm{e}}) - \mathrm{div}(\boldsymbol{\sigma}_{\mathrm{i}} \boldsymbol{\nabla} V_{\mathrm{m}}) = 0, \quad \text{in} \quad \Omega_{\mathrm{H}} \times (0,T), \tag{6.2.10}$$

$$-\mathrm{div}(\boldsymbol{\sigma}_{\mathrm{T}} \boldsymbol{\nabla} u_{\mathrm{T}}) = 0, \quad \text{in} \quad \Omega_{\mathrm{T}} \times (0,T), \tag{6.2.11}$$

$$\boldsymbol{\sigma}_{\mathrm{T}} \boldsymbol{\nabla} u_{\mathrm{T}} \cdot \boldsymbol{n}_{\mathrm{T}} = 0, \quad \text{on} \quad \Gamma_{\mathrm{ext}} \times (0,T), \tag{6.2.12}$$

$$\boldsymbol{\sigma}_{\mathrm{i}} \boldsymbol{\nabla} V_{\mathrm{m}} \cdot \boldsymbol{n} + \boldsymbol{\sigma}_{\mathrm{i}} \boldsymbol{\nabla} u_{\mathrm{e}} \cdot \boldsymbol{n} = 0, \quad \text{on} \quad \Sigma \times (0,T), \tag{6.2.13}$$

$$u_{\mathrm{T}} = u_{\mathrm{e}}, \quad \text{on} \quad \Sigma \times (0,T), \tag{6.2.14}$$

$$\boldsymbol{\sigma}_{\mathrm{e}} \boldsymbol{\nabla} u_{\mathrm{e}} \cdot \boldsymbol{n} = -\boldsymbol{\sigma}_{\mathrm{T}} \boldsymbol{\nabla} u_{\mathrm{T}} \cdot \boldsymbol{n}_{\mathrm{T}}, \quad \text{on} \quad \Sigma \times (0,T), \tag{6.2.15}$$

$$V_{\mathrm{m}}(\boldsymbol{x}, 0) = V_{\mathrm{m}}^0(\boldsymbol{x}), \quad w(\boldsymbol{x}, 0) = w^0(\boldsymbol{x}), \quad \forall \boldsymbol{x} \in \Omega_{\mathrm{H}}. \tag{6.2.16}$$

Here, $\boldsymbol{\sigma}_{\mathrm{T}}$ stands for the conductivity tensor of the torso tissue and $\boldsymbol{n}_{\mathrm{T}}$ for the outward unit normal to the external boundary $\Gamma_{\mathrm{ext}} \stackrel{\mathrm{def}}{=} \partial\Omega_{\mathrm{T}} \setminus \Sigma$ (see Figure 6.1).

The boundary condition (6.2.12) states that no current can flow from the external torso surface Γ_{ext}, whereas (6.2.14)-(6.2.15) enforce a perfect electric balance between the heart and torso domains (see *e.g.* [Tun78, KN94, PBC05, SLC$^+$06]).

The coupled system of equations (6.2.8)-(6.2.16) is often known in the literature as *full bidomain* or *coupled bidomain* model (see *e.g.* [CNLH04b, SLC$^+$06]). It can be considered as the state-of-the-art in the modeling of the ECG or, equivalently, the forward problem of cardiac electrophysiology (see *e.g.* [LBG$^+$03, PBC05, SLC$^+$06]). The interested reader is referred to chapter 4 or [BFGZ08b] for the mathematical analysis of problem (6.2.8)-(6.2.16), and to [LBG$^+$03] (see also Chapter 5 section 5.3) for a review of the numerical methods.

Remark 6.2.2.1. *A common approach to reduce the computational complexity of* (6.2.8)-(6.2.16) *consists in* uncoupling *the computation of* $(w, V_{\mathrm{m}}, u_{\mathrm{e}})$ *and* u_{T}*, by neglecting the electrical torso-to-heart feedback (see* e.g. *[CNLH04b, PDG03, LBG$^+$03]). Thus, the coupling condition* (6.2.15) *is replaced by*

$$\boldsymbol{\sigma}_{\mathrm{e}} \boldsymbol{\nabla} u_{\mathrm{e}} \cdot \boldsymbol{n} = 0, \quad \textit{on} \quad \Sigma, \tag{6.2.17}$$

which amounts to work with an isolated bidomain model, as described in the previous subsection. Thereafter, the torso potential u_T is recovered by solving (6.2.11) *with boundary conditions* (6.2.12)-(6.2.14)*. Although this approach is very appealing in terms of computational cost, numerical evidence has shown that it can compromise the accuracy of the ECG signals (see e.g. [LBG+03, PBC05, BCF+09] and the numerical study of subsection §6.5.3). The heart-torso uncoupling approximation is often further simplified by replacing the interface condition* (6.2.14) *by a (multi-) dipole representation of the cardiac source (see e.g. [Gul88, Hui98]).*

Remark 6.2.2.2. *The monodomain approximation* (6.2.7) *can be combined with the heart-torso uncoupling framework of Remark 6.2.2.1 (see e.g. [Hui98, PDG03, BCF+09]). This yields a simplified mathematical model which allows a fully decoupled computation of V_m, u_e and u_T. However, as noticed in Chapter 5 section 5.5.2 (see also [CNLH04b]), without the uncoupling assumption* (6.2.17) *the monodomain approximation becomes*

$$\begin{aligned} \chi_m \partial_t V_m + I_{ion}(V_m, w) - \operatorname{div}\left(\boldsymbol{\sigma}\boldsymbol{\nabla} V_m\right) = I_{app}, \quad &in \quad \Omega_H, \\ \boldsymbol{\sigma}\boldsymbol{\nabla} V_m \cdot \boldsymbol{n} = -\mu \boldsymbol{\sigma}_e \boldsymbol{\nabla} u_e \cdot \boldsymbol{n}, \quad &on \quad \Sigma, \end{aligned} \tag{6.2.18}$$

where $0 < \mu < 1$ is a dimensionless parameter related to the local conductivities. Note that in (6.2.18) *V_m and u_e are still coupled. Therefore, under the full heart-torso coupling* (6.2.14)-(6.2.15)*, the monodomain approximation does not reduce the computational complexity with respect to* (6.2.8)-(6.2.16)*.*

6.3 Decoupled time-marching for the bidomain equation

In this section we analyze some time-discretization schemes for the isolated bidomain system (6.2.1)-(6.2.6). The main feature of the analyzed schemes is that they all allow a decoupled (Gauss-Seidel or Jacobi like) computation of V_m and u_e, without compromising stability.

6.3.1 Preliminaries

In what follows, we will consider the usual Lebesgue and Sobolev spaces, $L^m(\Omega)$ and $H^m(\Omega)$ respectively ($m > 0$), for a domain $\Omega \subset \mathbb{R}^3$. Then, for a given $X \subset \partial\Omega$ (with $\text{meas}(X) > 0$), we define $H^1_X(\Omega)$ as the subspace of $H^1(\Omega)$ with vanishing trace on X. The $L^2(\Omega)$-norm is denoted by $\|\cdot\|_{0,\Omega}$ and the vanishing mean value subspace of $L^2(\Omega)$ by $L^2_0(\Omega)$.

Problem (6.2.1)-(6.2.6) can be cast into weak form as in chapter 4 (see *e.g.* [BFGZ08b]): for $t > 0$, find $w(\cdot,t) \in L^\infty(\Omega_H)$, $V_m(\cdot,t) \in H^1(\Omega_H)$ and $u_e(\cdot,t) \in$

$H^1(\Omega_{\rm H}) \cap L^2_0(\Omega_{\rm H})$, such that

$$\begin{gathered}\int_{\Omega_{\rm H}} \big(\partial_t w + g(V_{\rm m}, w)\big)\xi = 0,\\ \chi_{\rm m}\int_{\Omega_{\rm H}} \big(\partial_t V_{\rm m} + I_{\rm ion}(V_{\rm m}, w)\big)\phi + \int_{\Omega_{\rm H}} \boldsymbol{\sigma}_{\rm i}\boldsymbol{\nabla}(V_{\rm m}+u_{\rm e})\cdot\boldsymbol{\nabla}\phi = \int_{\Omega_{\rm H}} I_{\rm app}\phi,\\ \int_{\Omega_{\rm H}} (\boldsymbol{\sigma}_{\rm i}+\boldsymbol{\sigma}_{\rm e})\boldsymbol{\nabla}u_{\rm e}\cdot\boldsymbol{\nabla}\psi + \int_{\Omega_{\rm H}} \boldsymbol{\sigma}_{\rm i}\boldsymbol{\nabla}V_{\rm m}\cdot\boldsymbol{\nabla}\psi = 0,\end{gathered} \tag{6.3.19}$$

for all $(\xi,\phi,\psi) \in L^2(\Omega_{\rm H}) \times H^1(\Omega_{\rm H}) \times \big(H^1(\Omega_{\rm H}) \cap L^2_0(\Omega_{\rm H})\big)$.

6.3.2 Time semi-discrete formulations: decoupled time-marching schemes

Let $N \in \mathbb{N}^*$ be a given integer and consider a uniform partition $\{[t_n, t_{n+1}]\}_{0\le n\le N-1}$, with $t_n \stackrel{\rm def}{=} n\tau$, of the time interval of interest $(0,T)$, with time-step $\tau \stackrel{\rm def}{=} T/N$. For a given time dependent function X, the quantity X^n denotes an approximation of $X(t_n)$ and $D_\tau X^n \stackrel{\rm def}{=} (X^n - X^{n-1})/\tau$ the first order backward difference. Moreover, we set $I^n_{\rm app} \stackrel{\rm def}{=} I_{\rm app}(t_n,\cdot)$.

We propose to time semi-discretize (6.3.19) by combining a first order semi-implicit treatment of the ionic current evaluation with an explicit (Gauss-Seidel or Jacobi like) treatment of the coupling between $V_{\rm m}$ and $u_{\rm e}$. The resulting schemes can be cast into a common frame as follows: For $0 \le n \le N-1$, we solve

1. Ionic state: find $w^{n+1} \in L^\infty(\Omega_{\rm H})$ such that

$$\int_{\Omega_{\rm H}} \big(D_\tau w^{n+1} + g(V^n_{\rm m}, w^{n+1})\big)\xi = 0 \tag{6.3.20}$$

   for all $\xi \in L^2(\Omega_{\rm H})$.

2. Transmembrane potential: find $V^{n+1}_{\rm m} \in H^1(\Omega_{\rm H})$ such that

$$\begin{aligned}\chi_{\rm m}\int_{\Omega_{\rm H}} D_\tau V^{n+1}_{\rm m}\phi + \int_{\Omega_{\rm H}} \boldsymbol{\sigma}_{\rm i}\boldsymbol{\nabla}V^{n+1}_{\rm m}\cdot\boldsymbol{\nabla}\phi\\ + \int_{\Omega_{\rm H}} \boldsymbol{\sigma}_{\rm i}\boldsymbol{\nabla}u^\star_{\rm e}\cdot\boldsymbol{\nabla}\phi = \int_{\Omega_{\rm H}} \big(I^{n+1}_{\rm app} - I_{\rm ion}(V^n_{\rm m}, w^{n+1})\big)\,\phi\end{aligned} \tag{6.3.21}$$

   for all $\phi \in H^1(\Omega_{\rm H})$.

3. Extracellular potential: find $u^{n+1}_{\rm e} \in H^1(\Omega_{\rm H}) \cap L^2_0(\Omega_{\rm H})$,

$$\int_{\Omega_{\rm H}} (\boldsymbol{\sigma}_{\rm i}+\boldsymbol{\sigma}_{\rm e})\boldsymbol{\nabla}u^{n+1}_{\rm e}\cdot\boldsymbol{\nabla}\psi + \int_{\Omega_{\rm H}} \boldsymbol{\sigma}_{\rm i}\boldsymbol{\nabla}V^\star_{\rm m}\cdot\boldsymbol{\nabla}\psi = 0 \tag{6.3.22}$$

   for all $\psi \in H^1(\Omega_{\rm H}) \cap L^2_0(\Omega_{\rm H})$.

Note that the non-linear system (6.3.20) and the ionic current evaluation $I_{\rm ion}(V_{\rm m}^n, w^{n+1})$ in (6.3.21) are decoupled from (6.3.21)-(6.3.22). This semi-implicit treatment is quite popular in the literature (see *e.g.* [SLT01, LGT03, CFP04, ATP06, BFGZ07, EB08]). For $(u_{\rm e}^\star, V_{\rm m}^\star) = (u_{\rm e}^{n+1}, V_{\rm m}^{n+1})$, the unknown potentials $V_{\rm m}^{n+1}$ and $u_{\rm e}^{n+1}$ are implicit coupled and, therefore, equations (6.3.21) and (6.3.22) have to be solved simultaneously (see *e.g.* [KB98, SLT05, EB08, EB08, BCF$^+$09]). The energy based stability analysis of this semi-implicit scheme, using first and second order time discretizations, has been recently reported in [EB08].

On the contrary, for $(u_{\rm e}^\star, V_{\rm m}^\star) = (u_{\rm e}^n, V_{\rm m}^{n+1})$ or $(u_{\rm e}^\star, V_{\rm m}^\star) = (u_{\rm e}^n, V_{\rm m}^n)$, the electrodiffusive coupling becomes explicit and therefore (6.3.21) and (6.3.22) can be solved separately: either sequentially (Gauss-Seidel) or in parallel (Jacobi). Similar Gauss-Seidel like splittings have been proposed and successfully applied in [SLT01, LGT03, ATP06, VWdSP$^+$08]. The theoretical stability of the schemes is, however, not established therein. To the best of our knowledge, the Jacobi like splitting has not yet been considered in the literature.

The energy based stability analysis of these time splitting schemes is performed in the next subsection.

Remark 6.3.2.1. *The Gauss-Seidel and Jacobi like electrodiffusive splittings allow a decoupled computation of $V_{\rm m}$ and $u_{\rm e}$ without the need to resort to monodomain approximations (see Remark 6.2.1.1).*

6.3.3 Stability analysis

For the stability analysis below, we shall make use of the following simplifying assumption (see [EB08, Section 3.2.2] and Remark 3.1 therein) on the structure of the ionic functions g and $I_{\rm ion}$:

$$\begin{aligned} I_{\rm ion}(V_{\rm m}, w) &\leq C_I\big(|V_{\rm m}| + |w|\big), \\ g(V_{\rm m}, w) &\leq C_g\big(|V_{\rm m}| + |w|\big) \end{aligned} \tag{6.3.23}$$

for all $V_{\rm m}, w$, and we set $\alpha \stackrel{\rm def}{=} 1 + 3C_I + C_g$ and $\beta \stackrel{\rm def}{=} C_I + 3C_g$.

The next theorem states the energy based stability of the time-marching schemes (6.3.20)-(6.3.22), in terms of $u_{\rm e}^\star$ and $V_{\rm m}^\star$.

Theorem 6.3.3.1. *Assume that* (6.3.23) *holds and that the conductivity tensors $\boldsymbol{\sigma}_{\rm i}, \boldsymbol{\sigma}_{\rm e}$ are symmetric and positive-definite. Let $\{(w^n, V_{\rm m}^n, u_{\rm e}^n)\}_{n=0}^N$ be solution of* (6.3.20)-(6.3.22) *and $C(T, \alpha, \beta) \stackrel{\rm def}{=} \exp\big(T/(1 - \tau\max\{\alpha, \beta\})\big)$. Then, under the condition*

$$\tau < \frac{1}{\max\{\alpha, \beta\}}, \tag{6.3.24}$$

there follows:

- *For* $(u_{\mathrm{e}}^{\star}, V_{\mathrm{m}}^{\star}) = (u_{\mathrm{e}}^{n+1}, V_{\mathrm{m}}^{n+1})$*:*

$$\left\|w^{n}\right\|_{0,\Omega_{\mathrm{H}}}^{2}+\chi_{\mathrm{m}}\left\|V_{\mathrm{m}}^{n}\right\|_{0,\Omega_{\mathrm{H}}}^{2}+2\sum_{m=0}^{n-1}\tau\left\|\boldsymbol{\sigma}_{\mathrm{e}}^{\frac{1}{2}}\boldsymbol{\nabla}u_{\mathrm{e}}^{m+1}\right\|_{0,\Omega_{\mathrm{H}}}^{2}+2\sum_{m=0}^{n-1}\tau\left\|\boldsymbol{\sigma}_{\mathrm{i}}^{\frac{1}{2}}\boldsymbol{\nabla}(V_{\mathrm{m}}^{m+1}+u_{\mathrm{e}}^{m+1})\right\|_{0,\Omega_{\mathrm{H}}}^{2}$$
$$\leq C(T,\alpha,\beta)\left(\left\|w^{0}\right\|_{0,\Omega_{\mathrm{H}}}^{2}+\chi_{\mathrm{m}}\left\|V_{\mathrm{m}}^{0}\right\|_{0,\Omega_{\mathrm{H}}}^{2}+\sum_{m=0}^{n-1}\tau\left\|I_{\mathrm{app}}^{m+1}\right\|_{0,\Omega_{\mathrm{H}}}^{2}\right), \quad (6.3.25)$$

with $1 \leq n \leq N$*.*

- *For* $(u_{\mathrm{e}}^{\star}, V_{\mathrm{m}}^{\star}) = (u_{\mathrm{e}}^{n}, V_{\mathrm{m}}^{n+1})$*:*

$$\left\|w^{n}\right\|_{0,\Omega_{\mathrm{H}}}^{2}+\chi_{\mathrm{m}}\left\|V_{\mathrm{m}}^{n}\right\|_{0,\Omega_{\mathrm{H}}}^{2}+\tau\left\|\boldsymbol{\sigma}_{\mathrm{i}}^{\frac{1}{2}}\boldsymbol{\nabla}u_{\mathrm{e}}^{n}\right\|_{0,\Omega_{\mathrm{H}}}^{2}$$
$$+2\sum_{m=0}^{n-1}\tau\left\|\boldsymbol{\sigma}_{\mathrm{e}}^{\frac{1}{2}}\boldsymbol{\nabla}u_{\mathrm{e}}^{m+1}\right\|_{0,\Omega_{\mathrm{H}}}^{2}+\sum_{m=0}^{n-1}\tau\left\|\boldsymbol{\sigma}_{\mathrm{i}}^{\frac{1}{2}}\boldsymbol{\nabla}(V_{\mathrm{m}}^{m+1}+u_{\mathrm{e}}^{m+1})\right\|_{0,\Omega_{\mathrm{H}}}^{2}$$
$$\leq C(T,\alpha,\beta)\left(\left\|w^{0}\right\|_{0,\Omega_{\mathrm{H}}}^{2}+\chi_{\mathrm{m}}\left\|V_{\mathrm{m}}^{0}\right\|_{0,\Omega_{\mathrm{H}}}^{2}+\tau\left\|\boldsymbol{\sigma}_{\mathrm{i}}^{\frac{1}{2}}\boldsymbol{\nabla}u_{\mathrm{e}}^{0}\right\|_{0,\Omega_{\mathrm{H}}}^{2}+\sum_{m=0}^{n-1}\tau\left\|I_{\mathrm{app}}^{m+1}\right\|_{0,\Omega_{\mathrm{H}}}^{2}\right), \quad (6.3.26)$$

with $1 \leq n \leq N$*.*

- *For* $(u_{\mathrm{e}}^{\star}, V_{\mathrm{m}}^{\star}) = (u_{\mathrm{e}}^{n}, V_{\mathrm{m}}^{n})$*:*

$$\left\|w^{n}\right\|_{0,\Omega_{\mathrm{H}}}^{2}+\chi_{\mathrm{m}}\left\|V_{\mathrm{m}}^{n}\right\|_{0,\Omega_{\mathrm{H}}}^{2}+\tau\left\|\boldsymbol{\sigma}_{\mathrm{i}}^{\frac{1}{2}}\boldsymbol{\nabla}u_{\mathrm{e}}^{n}\right\|_{0,\Omega_{\mathrm{H}}}^{2}+\tau\left\|\boldsymbol{\sigma}_{\mathrm{i}}^{\frac{1}{2}}\boldsymbol{\nabla}V_{\mathrm{m}}^{n}\right\|_{0,\Omega_{\mathrm{H}}}^{2}$$
$$+2\sum_{m=0}^{n-1}\tau\left\|\boldsymbol{\sigma}_{\mathrm{e}}^{\frac{1}{2}}\boldsymbol{\nabla}u_{\mathrm{e}}^{m+1}\right\|_{0,\Omega_{\mathrm{H}}}^{2} \leq C(T,\alpha,\beta)\left(\left\|w^{0}\right\|_{0,\Omega_{\mathrm{H}}}^{2}+\chi_{\mathrm{m}}\left\|V_{\mathrm{m}}^{0}\right\|_{0,\Omega_{\mathrm{H}}}^{2}+\tau\left\|\boldsymbol{\sigma}_{\mathrm{i}}^{\frac{1}{2}}\boldsymbol{\nabla}V_{\mathrm{m}}^{0}\right\|_{0,\Omega_{\mathrm{H}}}^{2}\right.$$
$$\left.+\tau\left\|\boldsymbol{\sigma}_{\mathrm{i}}^{\frac{1}{2}}\boldsymbol{\nabla}u_{\mathrm{e}}^{0}\right\|_{0,\Omega_{\mathrm{H}}}^{2}+\sum_{m=0}^{n-1}\tau\left\|I_{\mathrm{app}}^{m+1}\right\|_{0,\Omega_{\mathrm{H}}}^{2}\right), \quad (6.3.27)$$

with $1 \leq n \leq N$*.*

Proof. Under assumptions (6.3.23) and (6.3.24), the stability estimate (6.3.25), for the monolithic case $(u_{\mathrm{e}}^{\star}, V_{\mathrm{m}}^{\star}) = (u_{\mathrm{e}}^{n+1}, V_{\mathrm{m}}^{n+1})$, can be straightforwardly derived from the analysis reported in [EB08] (see also [Tho06]). Therefore, we only detail here the proofs of (6.3.26) and (6.3.27).

Let first consider the Gauss-Seidel like decoupling $(u_{\mathrm{e}}^{\star}, V_{\mathrm{m}}^{\star}) = (u_{\mathrm{e}}^{n}, V_{\mathrm{m}}^{n+1})$. By testing (6.3.20)-(6.3.22) with $\tau(w^{n+1}, V_{\mathrm{m}}^{n+1}, u_{\mathrm{e}}^{n+1})$ and after summation of the resulting expressions we have:

$$\frac{1}{2}\left(\left\|w^{n+1}\right\|_{0,\Omega_{\mathrm{H}}}^{2}-\left\|w^{n}\right\|_{0,\Omega_{\mathrm{H}}}^{2}\right)+\frac{\chi_{\mathrm{m}}}{2}\left(\left\|V_{\mathrm{m}}^{n+1}\right\|_{0,\Omega_{\mathrm{H}}}^{2}-\left\|V_{\mathrm{m}}^{n}\right\|_{0,\Omega_{\mathrm{H}}}^{2}\right)+\tau\left\|\boldsymbol{\sigma}_{\mathrm{e}}^{\frac{1}{2}}\boldsymbol{\nabla}u_{\mathrm{e}}^{n+1}\right\|_{0,\Omega_{\mathrm{H}}}^{2}$$
$$+\tau\left\|\boldsymbol{\sigma}_{\mathrm{i}}^{\frac{1}{2}}\boldsymbol{\nabla}(V_{\mathrm{m}}^{n+1}+u_{\mathrm{e}}^{n+1})\right\|_{0,\Omega_{\mathrm{H}}}^{2}+\underbrace{\tau\int_{\Omega_{\mathrm{H}}}\boldsymbol{\sigma}_{\mathrm{i}}\boldsymbol{\nabla}(u_{\mathrm{e}}^{n}-u_{\mathrm{e}}^{n+1})\cdot\boldsymbol{\nabla}V_{\mathrm{m}}^{n+1}}_{I_1}$$
$$\leq\underbrace{\tau\int_{\Omega_{\mathrm{H}}}\left(I_{\mathrm{app}}^{n+1}-I_{\mathrm{ion}}(V_{\mathrm{m}}^{n},w^{n+1})\right)V_{\mathrm{m}}^{n+1}-\tau\int_{\Omega_{\mathrm{H}}}g(V_{\mathrm{m}}^{n},w^{n+1})\big)w^{n+1}}_{I_2}, \quad (6.3.28)$$

where the square roots $\boldsymbol{\sigma}_{\mathrm{e}}^{\frac{1}{2}}, \boldsymbol{\sigma}_{\mathrm{i}}^{\frac{1}{2}}$ are well defined since $\boldsymbol{\sigma}_{\mathrm{i}}, \boldsymbol{\sigma}_{\mathrm{e}}$ are symmetric and positive-definite tensors (see *e.g.* [Ste80]). We now provide appropriate bounds for terms I_1 and I_2.

As regards the first term, we have

$$\begin{aligned} I_1 =& \tau \int_{\Omega_{\mathrm{H}}} \boldsymbol{\sigma}_{\mathrm{i}} \boldsymbol{\nabla}(u_{\mathrm{e}}^n - u_{\mathrm{e}}^{n+1}) \cdot \boldsymbol{\nabla}(V_{\mathrm{m}}^{n+1} + u_{\mathrm{e}}^{n+1}) + \int_{\Omega_{\mathrm{H}}} \boldsymbol{\sigma}_{\mathrm{i}} \boldsymbol{\nabla}(u_{\mathrm{e}}^{n+1} - u_{\mathrm{e}}^n) \cdot \boldsymbol{\nabla} u_{\mathrm{e}}^{n+1} \\ \geq & -\frac{\tau}{2} \big\| \boldsymbol{\sigma}_{\mathrm{i}}^{\frac{1}{2}} \boldsymbol{\nabla}(u_{\mathrm{e}}^n - u_{\mathrm{e}}^{n+1}) \big\|_{0,\Omega_{\mathrm{H}}}^2 - \frac{\tau}{2} \big\| \boldsymbol{\sigma}_{\mathrm{i}}^{\frac{1}{2}} \boldsymbol{\nabla}(V_{\mathrm{m}}^{n+1} + u_{\mathrm{e}}^{n+1}) \big\|_{0,\Omega_{\mathrm{H}}}^2 \\ & + \frac{\tau}{2} \left(\big\| \boldsymbol{\sigma}_{\mathrm{i}}^{\frac{1}{2}} \boldsymbol{\nabla} u_{\mathrm{e}}^{n+1} \big\|_{0,\Omega_{\mathrm{H}}}^2 - \big\| \boldsymbol{\sigma}_{\mathrm{i}}^{\frac{1}{2}} \boldsymbol{\nabla} u_{\mathrm{e}}^n \big\|_{0,\Omega_{\mathrm{H}}}^2 \right) + \frac{\tau}{2} \big\| \boldsymbol{\sigma}_{\mathrm{i}}^{\frac{1}{2}} \boldsymbol{\nabla}(u_{\mathrm{e}}^{n+1} - u_{\mathrm{e}}^n) \big\|_{0,\Omega_{\mathrm{H}}}^2 \\ =& \frac{\tau}{2} \left(\big\| \boldsymbol{\sigma}_{\mathrm{i}}^{\frac{1}{2}} \boldsymbol{\nabla} u_{\mathrm{e}}^{n+1} \big\|_{0,\Omega_{\mathrm{H}}}^2 - \big\| \boldsymbol{\sigma}_{\mathrm{i}}^{\frac{1}{2}} \boldsymbol{\nabla} u_{\mathrm{e}}^n \big\|_{0,\Omega_{\mathrm{H}}}^2 \right) - \frac{\tau}{2} \big\| \boldsymbol{\sigma}_{\mathrm{i}}^{\frac{1}{2}} \boldsymbol{\nabla}(V_{\mathrm{m}}^{n+1} + u_{\mathrm{e}}^{n+1}) \big\|_{0,\Omega_{\mathrm{H}}}^2. \end{aligned} \tag{6.3.29}$$

On the other hand, from (6.3.23), for the second term can be bounded as follows

$$\begin{aligned} I_2 =& \frac{\tau}{2} \big\| I_{\mathrm{app}}^{n+1} \big\|_{0,\Omega_{\mathrm{H}}^2}^2 + \frac{\tau}{2} \big\| V_{\mathrm{m}}^{n+1} \big\|_{0,\Omega_{\mathrm{H}}}^2 + \frac{\tau C_I}{2} \left(3 \big\| V_{\mathrm{m}}^{n+1} \big\|_{0,\Omega_{\mathrm{H}}}^2 + \big\| w^{n+1} \big\|_{0,\Omega_{\mathrm{H}}}^2 \right) \\ & + \frac{\tau C_g}{2} \left(\big\| V_{\mathrm{m}}^{n+1} \big\|_{0,\Omega_{\mathrm{H}}}^2 + 3 \big\| w^{n+1} \big\|_{0,\Omega_{\mathrm{H}}}^2 \right) \\ =& \frac{\tau}{2} \big\| I_{\mathrm{app}}^{n+1} \big\|_{0,\Omega_{\mathrm{H}}}^2 + \frac{\tau}{2} \underbrace{(1 + 3C_I + C_g)}_{\alpha} \big\| V_{\mathrm{m}}^{n+1} \big\|_{0,\Omega_{\mathrm{H}}}^2 + \frac{\tau}{2} \underbrace{(C_I + 3C_g)}_{\beta} \big\| w^{n+1} \big\|_{0,\Omega_{\mathrm{H}}}^2. \end{aligned} \tag{6.3.30}$$

As a result, inserting (6.3.29) and (6.3.30) into (6.3.28), yields

$$\begin{aligned} \frac{1}{2} \left(\big\| w^{n+1} \big\|_{0,\Omega_{\mathrm{H}}}^2 - \big\| w^n \big\|_{0,\Omega_{\mathrm{H}}}^2 \right) + \frac{\chi_{\mathrm{m}}}{2} \left(\big\| V_{\mathrm{m}}^{n+1} \big\|_{0,\Omega_{\mathrm{H}}}^2 - \big\| V_{\mathrm{m}}^n \big\|_{0,\Omega_{\mathrm{H}}}^2 \right) + \tau \big\| \boldsymbol{\sigma}_{\mathrm{e}}^{\frac{1}{2}} \boldsymbol{\nabla} u_{\mathrm{e}}^{n+1} \big\|_{0,\Omega_{\mathrm{H}}}^2 \\ + \frac{\tau}{2} \big\| \boldsymbol{\sigma}_{\mathrm{i}}^{\frac{1}{2}} \boldsymbol{\nabla}(V_{\mathrm{m}}^{n+1} + u_{\mathrm{e}}^{n+1}) \big\|_{0,\Omega_{\mathrm{H}}}^2 + \frac{\tau}{2} \left(\big\| \boldsymbol{\sigma}_{\mathrm{i}}^{\frac{1}{2}} \boldsymbol{\nabla} u_{\mathrm{e}}^{n+1} \big\|_{0,\Omega_{\mathrm{H}}}^2 - \big\| \boldsymbol{\sigma}_{\mathrm{i}}^{\frac{1}{2}} \boldsymbol{\nabla} u_{\mathrm{e}}^n \big\|_{0,\Omega_{\mathrm{H}}}^2 \right) \\ \leq \frac{\tau}{2} \big\| I_{\mathrm{app}}^{n+1} \big\|_{0,\Omega_{\mathrm{H}}}^2 + \frac{\tau \alpha}{2} \big\| V_{\mathrm{m}}^{n+1} \big\|_{0,\Omega_{\mathrm{H}}}^2 + \frac{\tau \beta}{2} \big\| w^{n+1} \big\|_{0,\Omega_{\mathrm{H}}}^2, \end{aligned}$$

so that, replacing index n by m and summing over $0 \leq m \leq n-1$, we have

$$\begin{aligned} & \big\| w^n \big\|_{0,\Omega_{\mathrm{H}}}^2 + \chi_{\mathrm{m}} \big\| V_{\mathrm{m}}^n \big\|_{0,\Omega_{\mathrm{H}}}^2 + \tau \big\| \boldsymbol{\sigma}_{\mathrm{i}}^{\frac{1}{2}} \boldsymbol{\nabla} u_{\mathrm{e}}^n \big\|_{0,\Omega_{\mathrm{H}}}^2 + 2 \sum_{m=0}^{n-1} \tau \big\| \boldsymbol{\sigma}_{\mathrm{e}}^{\frac{1}{2}} \boldsymbol{\nabla} u_{\mathrm{e}}^{m+1} \big\|_{0,\Omega_{\mathrm{H}}}^2 \\ & + \sum_{m=0}^{n-1} \tau \big\| \boldsymbol{\sigma}_{\mathrm{i}}^{\frac{1}{2}} \boldsymbol{\nabla}(V_{\mathrm{m}}^{m+1} + u_{\mathrm{e}}^{m+1}) \big\|_{0,\Omega_{\mathrm{H}}}^2 \leq \big\| w^0 \big\|_{0,\Omega_{\mathrm{H}}}^2 + \chi_{\mathrm{m}} \big\| V_{\mathrm{m}}^0 \big\|_{0,\Omega_{\mathrm{H}}}^2 + \tau \big\| \boldsymbol{\sigma}_{\mathrm{i}}^{\frac{1}{2}} \boldsymbol{\nabla} u_{\mathrm{e}}^0 \big\|_{0,\Omega_{\mathrm{H}}}^2 \\ & \qquad + \sum_{m=0}^{n-1} \tau \big\| I_{\mathrm{app}}^{m+1} \big\|_{0,\Omega_{\mathrm{H}}}^2 + \alpha \sum_{m=0}^{n-1} \tau \big\| V_{\mathrm{m}}^{m+1} \big\|_{0,\Omega_{\mathrm{H}}}^2 + \beta \sum_{m=0}^{n-1} \tau \big\| w^{m+1} \big\|_{0,\Omega_{\mathrm{H}}}^2. \end{aligned}$$

Estimate (6.3.26) then follows by applying Gronwall's lemma (see *e.g.* [HR90, Lemma 5.1]) under condition (6.3.24).

Finally, let consider the Jacobi like decoupling $(u_{\mathrm{e}}^\star, V_{\mathrm{m}}^\star) = (u_{\mathrm{e}}^n, V_{\mathrm{m}}^n)$. In this case,

estimate (6.3.28) becomes

$$\frac{1}{2}\left(\left\|w^{n+1}\right\|_{0,\Omega_{\mathrm{H}}}^2-\left\|w^{n}\right\|_{0,\Omega_{\mathrm{H}}}^2\right)+\frac{\chi_{\mathrm{m}}}{2}\left(\left\|V_{\mathrm{m}}^{n+1}\right\|_{0,\Omega_{\mathrm{H}}}^2-\left\|V_{\mathrm{m}}^{n}\right\|_{0,\Omega_{\mathrm{H}}}^2\right)+\tau\left\|\boldsymbol{\sigma}_{\mathrm{e}}^{\frac{1}{2}}\boldsymbol{\nabla}u_{\mathrm{e}}^{n+1}\right\|_{0,\Omega_{\mathrm{H}}}^2 + \tau\left\|\boldsymbol{\sigma}_{\mathrm{i}}^{\frac{1}{2}}\boldsymbol{\nabla}(V_{\mathrm{m}}^{n+1}+u_{\mathrm{e}}^{n+1})\right\|_{0,\Omega_{\mathrm{H}}}^2+I_1+\underbrace{\tau\int_{\Omega_{\mathrm{H}}}\boldsymbol{\sigma}_{\mathrm{i}}\boldsymbol{\nabla}(V_{\mathrm{m}}^{n}-V_{\mathrm{m}}^{n+1})\cdot\boldsymbol{\nabla}u_{\mathrm{e}}^{n+1}}_{I_3}\leq I_2. \quad (6.3.31)$$

The new term I_3 can be bounded similarly to I_1, that is,

$$\begin{aligned}I_3=&\tau\int_{\Omega_{\mathrm{H}}}\boldsymbol{\sigma}_{\mathrm{i}}\boldsymbol{\nabla}(V_{\mathrm{m}}^{n}-V_{\mathrm{m}}^{n+1})\cdot\boldsymbol{\nabla}(V_{\mathrm{m}}^{n+1}+u_{\mathrm{e}}^{n+1})+\int_{\Omega_{\mathrm{H}}}\boldsymbol{\sigma}_{\mathrm{i}}\boldsymbol{\nabla}(V_{\mathrm{m}}^{n+1}-V_{\mathrm{m}}^{n})\cdot\boldsymbol{\nabla}V_{\mathrm{m}}^{n+1}\\ \geq&-\frac{\tau}{2}\left\|\boldsymbol{\sigma}_{\mathrm{i}}^{\frac{1}{2}}\boldsymbol{\nabla}(V_{\mathrm{m}}^{n}-V_{\mathrm{m}}^{n+1})\right\|_{0,\Omega_{\mathrm{H}}}^2-\frac{\tau}{2}\left\|\boldsymbol{\sigma}_{\mathrm{i}}^{\frac{1}{2}}\boldsymbol{\nabla}(V_{\mathrm{m}}^{n+1}+u_{\mathrm{e}}^{n+1})\right\|_{0,\Omega_{\mathrm{H}}}^2\\ &+\frac{\tau}{2}\left(\left\|\boldsymbol{\sigma}_{\mathrm{i}}^{\frac{1}{2}}\boldsymbol{\nabla}V_{\mathrm{m}}^{n+1}\right\|_{0,\Omega_{\mathrm{H}}}^2-\left\|\boldsymbol{\sigma}_{\mathrm{i}}^{\frac{1}{2}}\boldsymbol{\nabla}V_{\mathrm{m}}^{n}\right\|_{0,\Omega_{\mathrm{H}}}^2\right)+\frac{\tau}{2}\left\|\boldsymbol{\sigma}_{\mathrm{i}}^{\frac{1}{2}}\boldsymbol{\nabla}(V_{\mathrm{m}}^{n+1}-V_{\mathrm{m}}^{n})\right\|_{0,\Omega_{\mathrm{H}}}^2\\ =&\frac{\tau}{2}\left(\left\|\boldsymbol{\sigma}_{\mathrm{i}}^{\frac{1}{2}}\boldsymbol{\nabla}V_{\mathrm{m}}^{n+1}\right\|_{0,\Omega_{\mathrm{H}}}^2-\left\|\boldsymbol{\sigma}_{\mathrm{i}}^{\frac{1}{2}}\boldsymbol{\nabla}V_{\mathrm{m}}^{n}\right\|_{0,\Omega_{\mathrm{H}}}^2\right)-\frac{\tau}{2}\left\|\boldsymbol{\sigma}_{\mathrm{i}}^{\frac{1}{2}}\boldsymbol{\nabla}(V_{\mathrm{m}}^{n+1}+u_{\mathrm{e}}^{n+1})\right\|_{0,\Omega_{\mathrm{H}}}^2.\end{aligned} \quad (6.3.32)$$

Therefore, by inserting (6.3.29), (6.3.30) and (6.3.32) into (6.3.31), there follows that

$$\begin{aligned}&\frac{1}{2}\left(\left\|w^{n+1}\right\|_{0,\Omega_{\mathrm{H}}}^2-\left\|w^{n}\right\|_{0,\Omega_{\mathrm{H}}}^2\right)+\frac{\chi_{\mathrm{m}}}{2}\left(\left\|V_{\mathrm{m}}^{n+1}\right\|_{0,\Omega_{\mathrm{H}}}^2-\left\|V_{\mathrm{m}}^{n}\right\|_{0,\Omega_{\mathrm{H}}}^2\right)+\tau\left\|\boldsymbol{\sigma}_{\mathrm{e}}^{\frac{1}{2}}\boldsymbol{\nabla}u_{\mathrm{e}}^{n+1}\right\|_{0,\Omega_{\mathrm{H}}}^2\\ &\frac{\tau}{2}\left(\left\|\boldsymbol{\sigma}_{\mathrm{i}}^{\frac{1}{2}}\boldsymbol{\nabla}V_{\mathrm{m}}^{n+1}\right\|_{0,\Omega_{\mathrm{H}}}^2-\left\|\boldsymbol{\sigma}_{\mathrm{i}}^{\frac{1}{2}}\boldsymbol{\nabla}V_{\mathrm{m}}^{n}\right\|_{0,\Omega_{\mathrm{H}}}^2\right)+\frac{\tau}{2}\left(\left\|\boldsymbol{\sigma}_{\mathrm{i}}^{\frac{1}{2}}\boldsymbol{\nabla}u_{\mathrm{e}}^{n+1}\right\|_{0,\Omega_{\mathrm{H}}}^2-\left\|\boldsymbol{\sigma}_{\mathrm{i}}^{\frac{1}{2}}\boldsymbol{\nabla}u_{\mathrm{e}}^{n}\right\|_{0,\Omega_{\mathrm{H}}}^2\right)\\ &\qquad\leq\frac{\tau}{2}\left\|I_{\mathrm{app}}^{n+1}\right\|_{0,\Omega_{\mathrm{H}}}^2+\frac{\tau\alpha}{2}\left\|V_{\mathrm{m}}^{n+1}\right\|_{0,\Omega_{\mathrm{H}}}^2+\frac{\tau\beta}{2}\left\|w^{n+1}\right\|_{0,\Omega_{\mathrm{H}}}^2.\end{aligned}$$

Estimate (6.3.27) then holds, under condition (6.3.24), by replacing index n by m, summing over $0\leq m\leq n-1$ and applying Gronwall's lemma. This completes the proof. □

We conclude this section with a series of remarks.

Remark 6.3.3.2. *Theorem 6.3.3.1 shows that electrodiffusive Gauss-Seidel and Jacobi splittings are energy stable under condition* (6.3.24)*, as for the unsplit case* $(u_{\mathrm{e}}^{\star},V_{\mathrm{m}}^{\star})=(u_{\mathrm{e}}^{n+1},V_{\mathrm{m}}^{n+1})$ *(analyzed in [EB08]), but with slightly altered energy norms. As a result, stability is not compromised.*

Remark 6.3.3.3. *The proof of Theorem 6.3.3.1 does not depend on the time discretizations considered in* (6.3.20) *and* (6.3.21)*. Indeed, we do not make use of any numerical dissipation produced by the scheme, apart from that is directly provided by the splitting. Therefore, the backward Euler quotients,* $D_\tau w^{n+1}$ *and* $D_\tau V_{\mathrm{m}}^{n+1}$*, can be safely replaced by a second order backward difference formula, and perform one correction (see e.g. [Ste78, SM00]) to recover overall second order accuracy.*

Remark 6.3.3.4. *The above stability result can be adapted, with minor modifications, to the case* $(u_{\mathrm{e}}^{\star},V_{\mathrm{m}}^{\star})=(u_{\mathrm{e}}^{n+1},V_{\mathrm{m}}^{n})$*. The full Jacobi splitting, obtained after replacing* $I_{\mathrm{ion}}(V_{\mathrm{m}}^{n},w^{n+1})$ *by* $I_{\mathrm{ion}}(V_{\mathrm{m}}^{n},w^{n})$ *in* (6.3.21) *could also be considered.*

Remark 6.3.3.5. *Theorem 6.3.3.1 holds also for the fully discrete counterpart of* (6.3.20)-(6.3.22) *obtained by discretizing in space using finite elements (see subsection §6.4.1).*

6.4 Decoupled time-marching for ECG numerical simulation

In this section, we introduce fully discrete schemes for the heart-torso system (6.2.8)-(6.2.16), allowing a decoupled computation of the transmembrane, extracellular and torso potentials. The main idea consists in combining the bidomain splittings of the previous section, with a specific explicit Robin-Robin treatment of the heart-torso coupling conditions (6.2.14)-(6.2.15).

6.4.1 Preliminaries

Problem (6.2.8)-(6.2.16) can be cast into weak form as follows (see *e.g.* [BFGZ08b]): for $t > 0$, find $w(\cdot,t) \in L^\infty(\Omega_{\rm H})$, $V_{\rm m}(\cdot,t) \in H^1(\Omega_{\rm H})$, $u_{\rm e}(\cdot,t) \in H^1(\Omega_{\rm H}) \cap L^2_0(\Omega_{\rm H})$ and $u_{\rm T}(\cdot,t) \in H^1(\Omega_{\rm T})$ with $u_{\rm e}(\cdot,t) = u_{\rm T}(\cdot,t)$ on Σ, such that

$$\begin{aligned}
\int_{\Omega_{\rm H}} \big(\partial_t w + g(V_{\rm m},w)\big)\xi = 0,\\
\chi_{\rm m}\int_{\Omega_{\rm H}} \big(\partial_t V_{\rm m} + I_{\rm ion}(V_{\rm m},w)\big)\phi + \int_{\Omega_{\rm H}} \boldsymbol{\sigma}_{\rm i}\boldsymbol{\nabla}(V_{\rm m}+u_{\rm e})\cdot\boldsymbol{\nabla}\phi = \int_{\Omega_{\rm H}} I_{\rm app}\phi,\\
\int_{\Omega_{\rm H}} (\boldsymbol{\sigma}_{\rm i}+\boldsymbol{\sigma}_{\rm e})\boldsymbol{\nabla}u_{\rm e}\cdot\boldsymbol{\nabla}\psi + \int_{\Omega_{\rm H}} \boldsymbol{\sigma}_{\rm i}\boldsymbol{\nabla}V_{\rm m}\cdot\boldsymbol{\nabla}\psi + \int_{\Omega_{\rm T}} \boldsymbol{\sigma}_{\rm T}\boldsymbol{\nabla}u_{\rm T}\cdot\boldsymbol{\nabla}\zeta = 0,
\end{aligned} \tag{6.4.33}$$

for all $(\xi,\phi,\psi,\zeta) \in L^2(\Omega_{\rm H}) \times H^1(\Omega_{\rm H}) \times \big(H^1(\Omega_{\rm H}) \cap L^2_0(\Omega_{\rm H})\big) \times H^1(\Omega_{\rm T})$ with $\psi = \zeta$ on Σ.

Assume that $\Omega_{\rm H}$ and $\Omega_{\rm T}$ are polygonal domains and let $\{\mathcal{T}_{{\rm H},h}\}_{0<h\leq 1}$ ($\{\mathcal{T}_{{\rm T},h}\}_{0<h\leq 1}$) be a family of triangulations of $\Omega_{\rm H}$ (resp. $\Omega_{\rm T}$) satisfying the usual requirements of finite element approximations (see *e.g.* [EG04]). The subscript $h \in (0,1]$ refer to the level of refinement of the triangulations. For the sake of simplicity and without loss of generality, we assume that both families of triangulations are quasi-uniform and that they match at the heart-torso interface Σ. We define $X_{{\rm H},h}$ (resp. $X_{{\rm T},h}$) as an internal continuous Lagrange finite element approximation of $H^1(\Omega_{\rm H})$ (resp. $H^1(\Omega_{\rm T})$). We also introduce the standard finite element (heart-to-torso) lifting operator $\mathcal{L}_h : X_{{\rm H},h} \to X_{{\rm T},h} \cap H^1_{\Gamma_{\rm ext}}(\Omega_{\rm T})$, such that $\mathcal{L}_h\psi = \psi$ on Σ and $\mathcal{L}_h\psi = 0$ on $\Gamma_{\rm ext}$, for all $\psi \in X_{{\rm H},h}$. Note that we have the direct sum decomposition

$$\big\{(\psi,\zeta) \in X_{{\rm H},h}\times X_{{\rm T},h} \,:\, \psi_{|\Sigma} = \zeta_{|\Sigma}\big\} = \big\{\big(\psi,\mathcal{L}_h\psi\big) \,:\, \psi \in X_{{\rm H},h}\big\} \oplus \big\{(0,\zeta) \,:\, \zeta \in X_{{\rm T},h}\cap H^1_\Sigma(\Omega_{\rm T})\big\}. \tag{6.4.34}$$

In the stability analysis below, we shall make use of the following standard discrete trace-inverse inequality (see *e.g.* [Tho06]):

$$||v||^2_{0,\partial K} \leq \frac{C_{\rm ti}}{h}||v||^2_{0,K} \quad \forall v \in X_{{\rm T},h}, \tag{6.4.35}$$

for all $K \in \mathcal{T}_{{\rm T},h}$, and with $C_{\rm ti} > 0$ a constant independent of the discretization parameter h (but that might depend on the polynomial order).

By combining the semi-implicit time-marching schemes of section §6.3 with a finite element discretization in space, we can derive from (6.4.33) the following fully discrete

heart-torso scheme: for $0 \leq n \leq N-1$, find $w^{n+1} \in X_{\mathrm{H},h}$, $V_{\mathrm{m}}^{n+1} \in X_{\mathrm{H},h}$, $u_{\mathrm{e}}^{n+1} \in X_{\mathrm{H},h} \cap L_0^2(\Omega_{\mathrm{H}})$ and $u_{\mathrm{T}}^{n+1} \in X_{\mathrm{T},h}$ with $u_{\mathrm{T}}^{n+1} = u_{\mathrm{e}}^{n+1}$ on Σ, such that

$$\int_{\Omega_{\mathrm{H}}} \big(D_\tau w^{n+1} + g(V_{\mathrm{m}}^n, w^{n+1})\big)\xi = 0, \tag{6.4.36}$$

$$\chi_{\mathrm{m}} \int_{\Omega_{\mathrm{H}}} D_\tau V_{\mathrm{m}}^{n+1}\phi + \int_{\Omega_{\mathrm{H}}} \boldsymbol{\sigma}_{\mathrm{i}} \boldsymbol{\nabla}(V_{\mathrm{m}}^{n+1} + u_{\mathrm{e}}^\star) \cdot \boldsymbol{\nabla}\phi = \int_{\Omega_{\mathrm{H}}} \big(I_{\mathrm{app}}^{n+1} - I_{\mathrm{ion}}(V_{\mathrm{m}}^n, w^{n+1})\big)\phi, \tag{6.4.37}$$

$$\int_{\Omega_{\mathrm{H}}} (\boldsymbol{\sigma}_{\mathrm{i}} + \boldsymbol{\sigma}_{\mathrm{e}}) \boldsymbol{\nabla} u_{\mathrm{e}}^{n+1} \cdot \boldsymbol{\nabla}\psi + \int_{\Omega_{\mathrm{H}}} \boldsymbol{\sigma}_{\mathrm{i}} \boldsymbol{\nabla} V_{\mathrm{m}}^\star \cdot \boldsymbol{\nabla}\psi + \int_{\Omega_{\mathrm{T}}} \boldsymbol{\sigma}_{\mathrm{T}} \boldsymbol{\nabla} u_{\mathrm{T}}^{n+1} \cdot \boldsymbol{\nabla}\zeta = 0, \tag{6.4.38}$$

for all $(\xi, \phi, \psi, \zeta) \in X_{\mathrm{H},h} \times X_{\mathrm{H},h} \times \big(X_{\mathrm{H},h} \cap L_0^2(\Omega_{\mathrm{H}})\big) \times X_{\mathrm{T},h}$ with $\zeta = \psi$ on Σ. Equivalently, using (6.4.34), the heart-torso subproblem (6.4.38) can be split into two coupled, torso (Dirichlet) and heart (Neumann), subproblems as follows:

- Find $u_{\mathrm{T}}^{n+1} \in X_{\mathrm{T},h}$, with $u_{\mathrm{T}}^{n+1} = u_{\mathrm{e}}^{n+1}$ on Σ, such that

$$\int_{\Omega_{\mathrm{T}}} \boldsymbol{\sigma}_{\mathrm{T}} \boldsymbol{\nabla} u_{\mathrm{T}}^{n+1} \cdot \boldsymbol{\nabla}\zeta = 0 \tag{6.4.39}$$

  for all $\zeta \in X_{\mathrm{T},h}$, with $\zeta = 0$ on Σ.

- Find $u_{\mathrm{e}}^{n+1} \in X_{\mathrm{H},h} \cap L_0^2(\Omega_{\mathrm{H}})$ such that

$$\int_{\Omega_{\mathrm{H}}} (\boldsymbol{\sigma}_{\mathrm{i}} + \boldsymbol{\sigma}_{\mathrm{e}}) \boldsymbol{\nabla} u_{\mathrm{e}}^{n+1} \cdot \boldsymbol{\nabla}\psi + \int_{\Omega_{\mathrm{H}}} \boldsymbol{\sigma}_{\mathrm{i}} \boldsymbol{\nabla} V_{\mathrm{m}}^\star \cdot \boldsymbol{\nabla}\psi = -\int_{\Omega_{\mathrm{T}}} \boldsymbol{\sigma}_{\mathrm{T}} \boldsymbol{\nabla} u_{\mathrm{T}}^{n+1} \cdot \boldsymbol{\nabla}\mathcal{L}_h\psi \tag{6.4.40}$$

  for all $\psi \in X_{\mathrm{H},h} \cap L_0^2(\Omega_{\mathrm{H}})$.

Remark 6.4.1.1. *The residual term in the right hand side of* (6.4.40) *amounts to enforce the Neumann condition* (6.2.15) *in a variational consistent fashion.*

Despite the Gauss-Seidel and Jacobi splittings allow a decoupled solution of (6.4.36) and (6.4.37), the heart and torso potentials u_{e}^{n+1} and u_{T}^{n+1} are still implicitly coupled. Therefore, problems (6.4.39) and (6.4.40) must be solved simultaneously: either *monolithically*, after assembling of (6.4.38) (see *e.g.* [SLT01, LGT03, SLT05, VWdSP$^+$08]) or, in a *partitioned* fashion, by sub-iterating between them as in Chapter 5 section 5.3 (see also [BP02, BCF$^+$09]). Note that, since the (quasi-static) time discretizations (6.4.39) and (6.4.40) do not generate numerical dissipation in time, the naive Dirichlet-Neumann explicit coupling, obtained by enforcing

$$u_{\mathrm{T}}^{n+1} = u_{\mathrm{e}}^n \quad \text{on} \quad \Sigma,$$

in the torso subproblem (6.4.39), might lead to numerical instability.

In the next subsection, we introduce an alternative heart-torso splitting, based on Robin-Robin transmission conditions, which remains stable under a mild CFL like condition.

6.4.2 Fully discrete formulation: decoupled time-marching schemes

We propose to combine the decoupling techniques introduced in section §6.3 with the following explicit Robin-Robin splitting, derived from [ACF09] (see also [BF09]), of the heart-torso coupling:

$$\begin{aligned} \boldsymbol{\sigma}_{\mathrm{e}}\boldsymbol{\nabla}u_{\mathrm{e}}^{n+1}\cdot\boldsymbol{n}+\frac{\gamma\sigma_{\mathrm{t}}}{h}u_{\mathrm{e}}^{n+1} &= -\boldsymbol{\sigma}_{\mathrm{T}}\boldsymbol{\nabla}u_{\mathrm{T}}^{n}\cdot\boldsymbol{n}_{\mathrm{T}}+\frac{\gamma\sigma_{\mathrm{t}}}{h}u_{\mathrm{T}}^{n}, \quad \text{on} \quad \Sigma, \\ \boldsymbol{\sigma}_{\mathrm{T}}\boldsymbol{\nabla}u_{\mathrm{T}}^{n+1}\cdot\boldsymbol{n}_{\mathrm{T}}+\frac{\gamma\sigma_{\mathrm{t}}}{h}u_{\mathrm{T}}^{n+1} &= \boldsymbol{\sigma}_{\mathrm{T}}\boldsymbol{\nabla}u_{\mathrm{T}}^{n}\cdot\boldsymbol{n}_{\mathrm{T}}+\frac{\gamma\sigma_{\mathrm{t}}}{h}u_{\mathrm{e}}^{n+1}, \quad \text{on} \quad \Sigma, \end{aligned} \tag{6.4.41}$$

where $\gamma > 0$ is a free Robin parameter, to be specified later on, and σ_{t} is such that $\boldsymbol{\sigma}_{\mathrm{T}|\Sigma} = \sigma_{\mathrm{t}}\boldsymbol{I}$.

Remark 6.4.2.1. *We have assumed, without loss of generality, that the torso conductivity tensor is isotropic on the boundary, $\boldsymbol{\sigma}_{\mathrm{T}|\Sigma} = \sigma_{\mathrm{t}}\boldsymbol{I}$, and that σ_{t} is constant.*

Thus, the resulting schemes read as follows: for $0 \leq n \leq N-1$, we solve:

1. Ionic state: find $w^{n+1} \in X_h$ such that

$$\int_{\Omega_{\mathrm{H}}} \left(D_\tau w^{n+1} + g(V_{\mathrm{m}}^{n}, w^{n+1})\right)\xi = 0 \tag{6.4.42}$$

   for all $\xi \in X_h$.

2. Transmembrane potential: find $V_{\mathrm{m}}^{n+1} \in X_h$ such that

$$\begin{aligned} \chi_{\mathrm{m}}\int_{\Omega_{\mathrm{H}}} D_\tau V_{\mathrm{m}}^{n+1}\phi + \int_{\Omega_{\mathrm{H}}} \boldsymbol{\sigma}_{\mathrm{i}}\boldsymbol{\nabla}V_{\mathrm{m}}^{n+1}\cdot\boldsymbol{\nabla}\phi + \int_{\Omega_{\mathrm{H}}} \boldsymbol{\sigma}_{\mathrm{i}}\boldsymbol{\nabla}u_{\mathrm{e}}^{\star}\cdot\boldsymbol{\nabla}\phi \\ = \int_{\Omega_{\mathrm{H}}} \left(I_{\mathrm{app}}^{n+1} - I_{\mathrm{ion}}(V_{\mathrm{m}}^{n}, w^{n+1})\right)\phi \end{aligned} \tag{6.4.43}$$

   for all $\phi \in X_h$.

3. Extracellular potential: find $u_{\mathrm{e}}^{n+1} \in X_h$ such that

$$\begin{aligned} \int_{\Omega_{\mathrm{H}}} (\boldsymbol{\sigma}_{\mathrm{i}}+\boldsymbol{\sigma}_{\mathrm{e}})\boldsymbol{\nabla}u_{\mathrm{e}}^{n+1}\cdot\boldsymbol{\nabla}\psi + \int_{\Omega_{\mathrm{H}}} \boldsymbol{\sigma}_{\mathrm{i}}\boldsymbol{\nabla}V_{\mathrm{m}}^{\star}\cdot\boldsymbol{\nabla}\psi + \frac{\gamma\sigma_{\mathrm{t}}}{h}\int_{\Sigma} u_{\mathrm{e}}^{n+1}\psi \\ = -\int_{\Sigma} \boldsymbol{\sigma}_{\mathrm{T}}\boldsymbol{\nabla}u_{\mathrm{T}}^{n}\cdot\boldsymbol{n}_{\mathrm{T}}\psi + \frac{\gamma\sigma_{\mathrm{t}}}{h}\int_{\Sigma} u_{\mathrm{T}}^{n}\psi \end{aligned} \tag{6.4.44}$$

   for all $\psi \in X_h$.

4. Torso potential: find $u_{\mathrm{T}}^{n+1} \in X_h$

$$\int_{\Omega_{\mathrm{T}}} \boldsymbol{\sigma}_{\mathrm{T}}\boldsymbol{\nabla}u_{\mathrm{T}}^{n+1}\cdot\boldsymbol{\nabla}\zeta + \frac{\gamma\sigma_{\mathrm{t}}}{h}\int_{\Sigma} u_{\mathrm{T}}^{n+1}\zeta = \int_{\Sigma} \boldsymbol{\sigma}_{\mathrm{T}}\boldsymbol{\nabla}u_{\mathrm{T}}^{n}\cdot\boldsymbol{n}_{\mathrm{T}}\zeta + \frac{\gamma\sigma_{\mathrm{t}}}{h}\int_{\Sigma} u_{\mathrm{e}}^{n+1}\zeta \tag{6.4.45}$$

   for all $\zeta \in X_h$.

In contrast to (6.4.36)-(6.4.38), the cardiac subproblem (6.4.42)-(6.4.44) can be solved independently of the torso subproblem (6.4.45). In particular, the choices $(u_{\mathrm{e}}^{\star}, V_{\mathrm{m}}^{\star}) = (u_{\mathrm{e}}^{n}, V_{\mathrm{m}}^{n+1})$ or $(u_{\mathrm{e}}^{\star}, V_{\mathrm{m}}^{\star}) = (u_{\mathrm{e}}^{n}, V_{\mathrm{m}}^{n})$ lead to a fully decoupled computation of w^{n+1}, V_{m}^{n+1}, u_{e}^{n+1} and u_{T}^{n+1}. In other words, the four subproblems (6.4.42)-(6.4.45) are decoupled and can be solved sequentially.

The energy based numerical stability of these schemes is addressed in the next subsection.

Remark 6.4.2.2. *The choices* $(u_{\mathrm{e}}^{\star}, V_{\mathrm{m}}^{\star}) = (u_{\mathrm{e}}^{n}, V_{\mathrm{m}}^{n+1})$ *or* $(u_{\mathrm{e}}^{\star}, V_{\mathrm{m}}^{\star}) = (u_{\mathrm{e}}^{n}, V_{\mathrm{m}}^{n})$ *in* (6.4.42)-(6.4.45) *allow a fully decoupled computation of* w^{n+1}, V_{m}^{n+1}, u_{e}^{n+1} *and* u_{T}^{n+1} *without the need to resort to monodomain and uncoupling approximations (see Remark 6.2.2.2).*

6.4.3 Stability analysis

We address here the energy based stability of the heart-torso coupling schemes (6.4.42)-(6.4.45). Hence, in order to alleviate the exposition, we denote by $E_{\mathrm{H}}^{0}\big(u_{\mathrm{e}}^{\star}, V_{\mathrm{m}}^{\star}\big)$ (resp. $E_{\mathrm{H}}^{n}\big(u_{\mathrm{e}}^{\star}, V_{\mathrm{m}}^{\star}\big)$) the discrete bidomain energy at steps 0 (resp. n), arising in the stability estimates provided by Theorem 6.3.3.1. For instance, in the case $(u_{\mathrm{e}}^{\star}, V_{\mathrm{m}}^{\star}) = (u_{\mathrm{e}}^{n}, V_{\mathrm{m}}^{n})$, we have

$$
\begin{aligned}
E_{\mathrm{H}}^{0}\big(u_{\mathrm{e}}^{\star}, V_{\mathrm{m}}^{\star}\big) &\stackrel{\mathrm{def}}{=} \big\|w^{0}\big\|_{0,\Omega_{\mathrm{H}}}^{2} + \chi_{\mathrm{m}}\big\|V_{\mathrm{m}}^{0}\big\|_{0,\Omega_{\mathrm{H}}}^{2} + \tau\big\|\boldsymbol{\sigma}_{\mathrm{i}}^{\frac{1}{2}}\boldsymbol{\nabla} V_{\mathrm{m}}^{0}\big\|_{0,\Omega_{\mathrm{H}}}^{2} + \tau\big\|\boldsymbol{\sigma}_{\mathrm{i}}^{\frac{1}{2}}\boldsymbol{\nabla} u_{\mathrm{e}}^{0}\big\|_{0,\Omega_{\mathrm{H}}}^{2},\\
E_{\mathrm{H}}^{n}\big(u_{\mathrm{e}}^{\star}, V_{\mathrm{m}}^{\star}\big) &\stackrel{\mathrm{def}}{=} \big\|w^{n}\big\|_{0,\Omega_{\mathrm{H}}}^{2} + \chi_{\mathrm{m}}\big\|V_{\mathrm{m}}^{n}\big\|_{0,\Omega_{\mathrm{H}}}^{2} + \tau\big\|\boldsymbol{\sigma}_{\mathrm{i}}^{\frac{1}{2}}\boldsymbol{\nabla} u_{\mathrm{e}}^{n}\big\|_{0,\Omega_{\mathrm{H}}}^{2} + \tau\big\|\boldsymbol{\sigma}_{\mathrm{i}}^{\frac{1}{2}}\boldsymbol{\nabla} V_{\mathrm{m}}^{n}\big\|_{0,\Omega_{\mathrm{H}}}^{2}\\
&\qquad + 2\sum_{m=0}^{n-1}\tau\big\|\boldsymbol{\sigma}_{\mathrm{e}}^{\frac{1}{2}}\boldsymbol{\nabla} u_{\mathrm{e}}^{m+1}\big\|_{0,\Omega_{\mathrm{H}}}^{2},
\end{aligned}
$$

and similarly for the rest.

The next theorem states the main result of this section.

Theorem 6.4.3.1. *Assume that the hypothesis of Theorem 6.3.3.1 hold and that the torso conductivity tensor* $\boldsymbol{\sigma}_{\mathrm{T}}$ *is symmetric and positive-definite. Let* $\big\{\big(w^{n}, V_{\mathrm{m}}^{n}, u_{\mathrm{e}}^{n}, u_{\mathrm{T}}^{n}\big)\big\}_{n=0}^{N}$ *be solution of* (6.4.42)-(6.4.45). *Then for*

$$
\gamma > 2C_{\mathrm{ti}}, \tag{6.4.46}
$$

the following estimate holds

$$
\begin{aligned}
&E_{\mathrm{H}}^{n}\big(u_{\mathrm{e}}^{\star}, V_{\mathrm{m}}^{\star}\big) + \tau\frac{\gamma\sigma_{\mathrm{t}}}{h}\big\|u_{\mathrm{T}}^{n}\big\|_{0,\Sigma}^{2} + \sum_{m=0}^{n-1}\tau\big\|\boldsymbol{\sigma}_{\mathrm{T}}^{\frac{1}{2}}\boldsymbol{\nabla} u_{\mathrm{T}}^{m+1}\big\|_{0,\Omega_{\mathrm{T}}}^{2} + \sum_{m=0}^{n-1}\tau\frac{\gamma\sigma_{\mathrm{t}}}{2h}\big\|u_{\mathrm{T}}^{m+1} - u_{\mathrm{e}}^{m+1}\big\|_{0,\Sigma}^{2}\\
&\leq C(T,\alpha,\beta)\left(E_{\mathrm{H}}^{0}\big(u_{\mathrm{e}}^{\star}, V_{\mathrm{m}}^{\star}\big) + \tau\frac{\gamma\sigma_{\mathrm{t}}}{h}\big\|u_{\mathrm{T}}^{0}\big\|_{0,\Sigma}^{2} + \tau\big\|\boldsymbol{\sigma}_{\mathrm{T}}^{\frac{1}{2}}\boldsymbol{\nabla} u_{\mathrm{T}}^{0}\big\|_{0,\Omega_{\mathrm{T}}}^{2} + \sum_{m=0}^{n-1}\tau\|I_{\mathrm{app}}^{m+1}\|_{0,\Omega_{\mathrm{H}}}^{2}\right),
\end{aligned}
\tag{6.4.47}
$$

with $1 \leq n \leq N$. *In particular,* (6.4.47) *ensures the energy based stability of the explicit heart-torso coupling* (6.4.42)-(6.4.45) *under the condition* $\tau = O(h)$.

Proof. Since the stability of the heart-torso coupling (6.4.44)-(6.4.45) does not depend on the choice of $u_{\rm e}^\star$ and $V_{\rm m}^\star$, we restrict ourselves to the case $(u_{\rm e}^\star, V_{\rm m}^\star) = (u_{\rm e}^n, V_{\rm m}^n)$. The rest of estimates can be derived in a similar fashion.

By testing (6.3.20)-(6.3.22) with $(\xi, \phi, \psi, \zeta) = \tau(w^{n+1}, V_{\rm m}^{n+1}, u_{\rm e}^{n+1}, u_{\rm T}^{n+1})$ and after summation of the resulting expressions we have:

$$\begin{aligned}
&\frac{1}{2}\left(\left\|w^{n+1}\right\|_{0,\Omega_{\rm H}}^2 - \left\|w^n\right\|_{0,\Omega_{\rm H}}^2\right) + \frac{\chi_{\rm m}}{2}\left(\left\|V_{\rm m}^{n+1}\right\|_{0,\Omega_{\rm H}}^2 - \left\|V_{\rm m}^n\right\|_{0,\Omega_{\rm H}}^2\right) + \tau\left\|\boldsymbol{\sigma}_{\rm e}^{\frac{1}{2}}\boldsymbol{\nabla} u_{\rm e}^{n+1}\right\|_{0,\Omega_{\rm H}}^2 \\
&\quad + \tau\left\|\boldsymbol{\sigma}_{\rm i}^{\frac{1}{2}}\boldsymbol{\nabla}\left(V_{\rm m}^{n+1} + u_{\rm e}^{n+1}\right)\right\|_{0,\Omega_{\rm H}}^2 + \tau\left\|\boldsymbol{\sigma}_{\rm T}^{\frac{1}{2}}\boldsymbol{\nabla} u_{\rm T}^{n+1}\right\|_{0,\Omega_{\rm T}}^2 + \frac{\tau\gamma\sigma_{\rm t}}{h}\left\|u_{\rm T}^{n+1} - u_{\rm e}^{n+1}\right\|_{0,\Sigma}^2 \\
&+ \underbrace{\frac{\tau\gamma\sigma_{\rm t}}{h}\int_\Sigma \left(u_{\rm T}^{n+1} - u_{\rm T}^n\right)u_{\rm e}^{n+1}}_{I_4} \underbrace{- \tau\int_\Sigma \boldsymbol{\sigma}_{\rm T}\boldsymbol{\nabla} u_{\rm T}^n\cdot\boldsymbol{n}_{\rm T}\left(u_{\rm T}^{n+1} - u_{\rm e}^{n+1}\right)}_{I_5} + I_1 + I_3 \le I_2. \quad (6.4.48)
\end{aligned}$$

Terms I_1, I_2 and I_3 have already been estimated in the proof of Theorem 6.3.3.1, so we only need to provide bounds for I_4 and I_5.

Term I_4 is treated as follows (see [ACF09, BF09]),

$$\begin{aligned}
I_4 =& \frac{\tau\gamma\sigma_{\rm t}}{h}\int_\Sigma \left(u_{\rm T}^{n+1} - u_{\rm T}^n\right)\left(u_{\rm e}^{n+1} - u_{\rm T}^{n+1}\right) + \frac{\tau\gamma\sigma_{\rm t}}{h}\int_\Sigma \left(u_{\rm T}^{n+1} - u_{\rm T}^n\right)u_{\rm T}^{n+1} \\
\ge& -\frac{\tau\gamma\sigma_{\rm t}}{2h}\left\|u_{\rm T}^{n+1} - u_{\rm T}^n\right\|_{0,\Sigma}^2 - \frac{\tau\gamma\sigma_{\rm t}}{2h}\left\|u_{\rm e}^{n+1} - u_{\rm T}^{n+1}\right\|_{0,\Sigma}^2 \\
&+ \frac{\tau\gamma\sigma_{\rm t}}{2h}\left(\left\|u_{\rm T}^{n+1}\right\|_{0,\Sigma}^2 - \left\|u_{\rm T}^n\right\|_{0,\Sigma}^2\right) + \frac{\tau\gamma\sigma_{\rm t}}{2h}\left\|u_{\rm T}^{n+1} - u_{\rm T}^n\right\|_{0,\Sigma}^2 \\
=& \frac{\tau\gamma\sigma_{\rm t}}{2h}\left(\left\|u_{\rm T}^{n+1}\right\|_{0,\Sigma}^2 - \left\|u_{\rm T}^n\right\|_{0,\Sigma}^2\right) - \frac{\tau\gamma\sigma_{\rm t}}{2h}\left\|u_{\rm e}^{n+1} - u_{\rm T}^{n+1}\right\|_{0,\Sigma}^2.
\end{aligned} \quad (6.4.49)$$

On the other hand, using (6.4.35), for the last term we have

$$\begin{aligned}
I_5 \ge& -\frac{\tau h}{\gamma}\left\|(\sigma_{\rm t})^{\frac{1}{2}}\boldsymbol{\nabla} u_{\rm T}^n\right\|_{0,\Sigma}^2 - \frac{\tau\gamma\sigma_{\rm t}}{4h}\left\|u_{\rm e}^{n+1} - u_{\rm T}^{n+1}\right\|_{0,\Sigma}^2 \\
\ge& -\frac{\tau C_{\rm ti}}{\gamma}\left\|\boldsymbol{\sigma}_{\rm T}^{\frac{1}{2}}\boldsymbol{\nabla} u_{\rm T}^n\right\|_{0,\Omega_{\rm T}}^2 - \frac{\tau\gamma\sigma_{\rm t}}{4h}\left\|u_{\rm e}^{n+1} - u_{\rm T}^{n+1}\right\|_{0,\Sigma}^2.
\end{aligned} \quad (6.4.50)$$

Therefore, by inserting (6.3.29), (6.3.30), (6.3.32), (6.4.49) and (6.4.50) into (6.4.48) we get the estimate

$$\begin{aligned}
&\frac{1}{2}\left(\|w^{n+1}\|_{0,\Omega_{\rm H}}^2 - \|w^n\|_{0,\Omega_{\rm H}}^2\right) + \frac{\chi_{\rm m}}{2}\left(\|V_{\rm m}^{n+1}\|_{0,\Omega_{\rm H}}^2 - \|V_{\rm m}^n\|_{0,\Omega_{\rm H}}^2\right) + \tau\|\boldsymbol{\sigma}_{\rm e}^{\frac{1}{2}}\boldsymbol{\nabla} u_{\rm e}^{n+1}\|_{0,\Omega_{\rm H}}^2 \\
&\quad + \tau\left(\left\|\boldsymbol{\sigma}_{\rm T}^{\frac{1}{2}}\boldsymbol{\nabla} u_{\rm T}^{n+1}\right\|_{0,\Omega_{\rm T}}^2 - \frac{C_{\rm ti}}{\gamma}\left\|\boldsymbol{\sigma}_{\rm T}^{\frac{1}{2}}\boldsymbol{\nabla} u_{\rm T}^n\right\|_{0,\Omega_{\rm T}}^2\right) + \frac{\tau\gamma\sigma_{\rm t}}{4h}\left\|u_{\rm T}^{n+1} - u_{\rm e}^{n+1}\right\|_{0,\Sigma}^2 \\
&\quad + \frac{\tau\gamma\sigma_{\rm t}}{2h}\left(\left\|u_{\rm T}^{n+1}\right\|_{0,\Sigma}^2 - \left\|u_{\rm T}^n\right\|_{0,\Sigma}^2\right) + \frac{\tau}{2}\left(\|\boldsymbol{\sigma}_{\rm i}^{\frac{1}{2}}\boldsymbol{\nabla} V_{\rm m}^{n+1}\|_{0,\Omega_{\rm H}}^2 - \|\boldsymbol{\sigma}_{\rm i}^{\frac{1}{2}}\boldsymbol{\nabla} V_{\rm m}^n\|_{0,\Omega_{\rm H}}^2\right) \\
&+ \frac{\tau}{2}\left(\|\boldsymbol{\sigma}_{\rm i}^{\frac{1}{2}}\boldsymbol{\nabla} u_{\rm e}^{n+1}\|_{0,\Omega_{\rm H}}^2 - \|\boldsymbol{\sigma}_{\rm i}^{\frac{1}{2}}\boldsymbol{\nabla} u_{\rm e}^n\|_{0,\Omega_{\rm H}}^2\right) \le \frac{\tau}{2}\|I_{\rm app}^{n+1}\|_{0,\Omega_{\rm H}}^2 + \frac{\tau\alpha}{2}\|V_{\rm m}^{n+1}\|_{0,\Omega_{\rm H}}^2 + \frac{\tau\beta}{2}\|w^{n+1}\|_{0,\Omega_{\rm H}}^2.
\end{aligned}$$

Estimate (6.4.47) then follows, under conditions (6.4.46) and (6.3.24), by replacing index n by m, summing over $0 \le m \le n-1$ and applying Gronwall's lemma, which completes the proof. □

Remark 6.4.3.2. *The above proof does not make use of any numerical dissipation apart from that directly provided by the explicit Robin-Robin splitting* (6.4.41)*. Note that this is particularly well adapted to the heart-torso coupling* (6.2.8)-(6.2.16)*, since the quasi-static elliptic equations* (6.2.9) *and* (6.2.10) *do not generate numerical dissipation in time.*

Remark 6.4.3.3. *The flux terms in* (6.4.44) *and* (6.4.45) *can be evaluated face-wise, i.e. as broken integrals, or using a discrete variational expression, as in* (6.4.40)*. Hence,* $\int_\Sigma \boldsymbol{\sigma}_{\mathrm{T}} \boldsymbol{\nabla} u_{\mathrm{T}}^n \cdot \boldsymbol{n}_{\mathrm{T}} \psi$ *and* $\int_\Sigma \boldsymbol{\sigma}_{\mathrm{T}} \boldsymbol{\nabla} u_{\mathrm{T}}^n \cdot \boldsymbol{n}_{\mathrm{T}} \zeta$*, can be safely replaced by* $\int_{\Omega_{\mathrm{T}}} \boldsymbol{\sigma}_{\mathrm{T}} \boldsymbol{\nabla} u_{\mathrm{T}}^n \cdot \boldsymbol{\nabla} \mathcal{L}_h \psi$ *and* $\int_{\Omega_{\mathrm{T}}} \boldsymbol{\sigma}_{\mathrm{T}} \boldsymbol{\nabla} u_{\mathrm{T}}^n \cdot \boldsymbol{\nabla} \mathcal{L}_h \zeta$*, respectively.*

6.5 Numerical results

In this section we illustrate, via numerical simulations based on anatomical heart and torso geometries, the stability and accuracy of the explicit splitting schemes analyzed in the previous sections. Numerical results for an isolated bidomain model using the time-marching procedures of section §6.3 are presented in subsection §6.5.2. Subsection §6.5.3 demonstrates the capabilities of the splitting schemes introduced in section §6.4 to provide accurate 12-lead ECG signals.

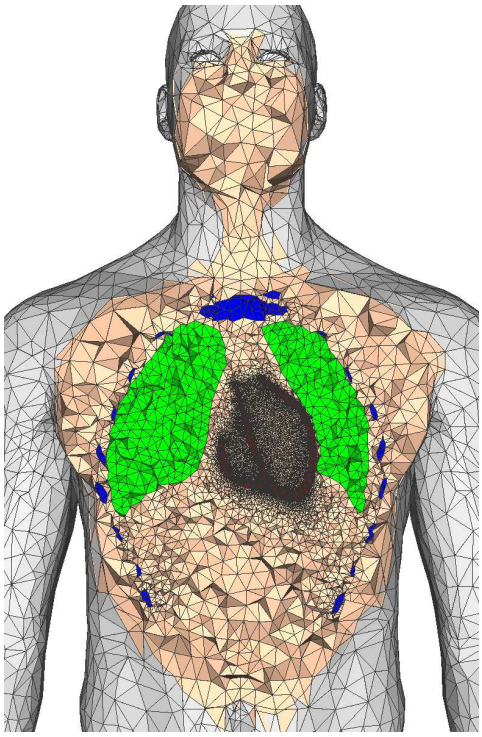

Figure 6.2: Cut view of the heart-torso computational mesh: heart (red) lungs (green), bone (blue) and remaining tissue (apricot).

6.5.1 Simulation data

The simulations are performed with the anatomical data and the model parameters used in [CFG$^+$09a, CFG$^+$09b]. For the sake of conciseness we only report here the main

ingredients (full details are given in [CFG+09a, CFG+09b]).

The computational heart and torso meshes were obtained starting from the Zygote (`www.3dscience.com`) anatomical model, using the `3-matic` software (`www.materialise.com`) to obtain computationally-correct surface meshes. The mesh, displayed in Figure 6.2, contains the heart, lung, bones and remaining extramyocardial tissue. They have been obtained by processing the surface meshes with `Yams` [Fre01] and `GHS3D` [GHS90]. The volume heart and torso meshes are made of 542 000 and 1 242 000 tetrahedra, respetively.

The bidomain model parameters are given in Table 6.1, where $\sigma_{i,e}^{l}$ (resp. $\sigma_{i,e}^{t}$) denotes the scalar intra- and extracelluar longitudinal (resp. transverse) conductivities. Table 6.2 provides the conductivity parameters for the torso (supposed isotropic).

A_m (cm^{-1})	C_m (mF)	σ_i^l (S cm^{-1})	σ_e^l (S cm^{-1})	σ_i^t (S cm^{-1})	σ_e^t (S cm^{-1})
500	10^{-3}	3.0×10^{-3}	3.0×10^{-3}	3.0×10^{-4}	1.2×10^{-3}

Table 6.1: Bidomain model parameters.

σ_t (S cm^{-1})	σ_T^l (S cm^{-1})	σ_T^b (S cm^{-1})
6.0×10^{-4}	2.4×10^{-4}	4.0×10^{-5}

Table 6.2: Torso conductivity parameters: tissue (t), lungs (l) and bone (b).

As in Chapter 5 section 5.2, a rescaled version of the two-variable model proposed by Mitchell and Schaeffer in [MS03] is considered as ionic model. Functions g and I_{ion} are then given by

$$I_{ion}(V_m, w) = -w\frac{(V_m - V_{min})^2(V_{max} - V_m)}{\tau_{in}(V_{max} - V_{min})} + \frac{V_m - V_{min}}{\tau_{out}(V_{max} - V_{min})},$$

$$g(V_m, w) = \begin{cases} \dfrac{w}{\tau_{open}} - \dfrac{1}{\tau_{open}(V_{max} - V_{min})^2} & \text{if} \quad V_m < V_{gate}, \\ \dfrac{w}{\tau_{close}} & \text{if} \quad V_m \geq V_{gate}, \end{cases}$$

where the values of the free parameters τ_{in}, τ_{out}, τ_{open}, τ_{close}, V_{gate} are reported in Table 6.3, and V_{min}, V_{max} are scaling constants (-80 and 20 mV, respectively).

τ_{in}	τ_{out}	τ_{open}	τ_{close}^{RV}	$\tau_{close}^{LV-endo}$	τ_{close}^{LV-epi}	V_{gate}
4.5	90	100	120	140	105	-67

Table 6.3: Mitchell-Schaeffer ionic model parameters.

Continuous $\mathbb{P}_1$ Lagrange finite elements are used forthe space discretization of both the heart and the torso equations. The time step size was fixed to $\tau = 0.25$ ms and the Robin parameter, for the heart-torso coupling scheme (6.4.42)-(6.4.45), to $\gamma = 0.1$.

6.5.2 Isolated heart

The isolated bidomain equations (6.3.20)-(6.3.22) are approximated using the time-marching schemes (6.3.21)-(6.3.22). In what follows, we shall refer to each of these schemes using the following terminology:

- *Coupled*: $(u_{\mathrm{e}}^{\star}, V_{\mathrm{m}}^{\star}) = (u_{\mathrm{e}}^{n+1}, V_{\mathrm{m}}^{n+1})$;
- *Gauss-Seidel*: $(u_{\mathrm{e}}^{\star}, V_{\mathrm{m}}^{\star}) = (u_{\mathrm{e}}^{n}, V_{\mathrm{m}}^{n+1})$;
- *Jacobi*: $(u_{\mathrm{e}}^{\star}, V_{\mathrm{m}}^{\star}) = (u_{\mathrm{e}}^{n}, V_{\mathrm{m}}^{n})$.

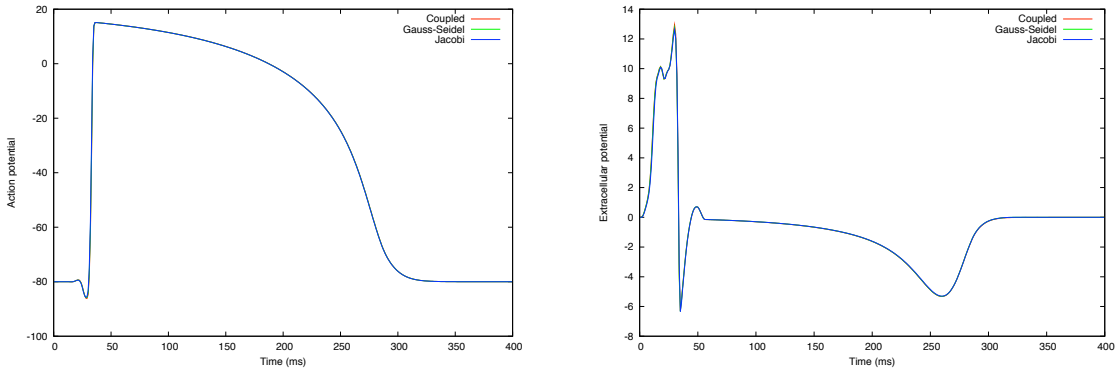

Figure 6.3: Time course of the transmembrane potential (left) and extracellular potential (right) at a given location in the epicardium.

The time course of the transmembrane and extracellular potentials at a given epicardial location are displayed in Figure 6.3. We can observe that the simulations are numerically stable and the curves are practically indistinguishable. Somehow, this is not surprising since the electrodiffusive Gauss-Seidel and Jacobi splittings are expected to still provide optimal first order accuracy. A slight difference can be seen after axis rescaling, as shown in Figure 6.4.

τ (ms) \ scheme	Coupled	Gauss-Seidel	Jacobi
0.25	OK	OK	OK
0.50	OK	OK	OK
1.00	OK	OK	OK
1.25	NO	NO	NO
1.50	NO	NO	NO

Table 6.4: Stability sensitivity to the time step size τ. OK indicates numerical stability and NO indicates numerical instability.

The results reported in Table 6.4 confirm that the electrodiffusive Gauss-Seidel and Jacobi splittings do not introduce additional constraints on the time step size τ, as predicted by Theorem 6.3.3.1.

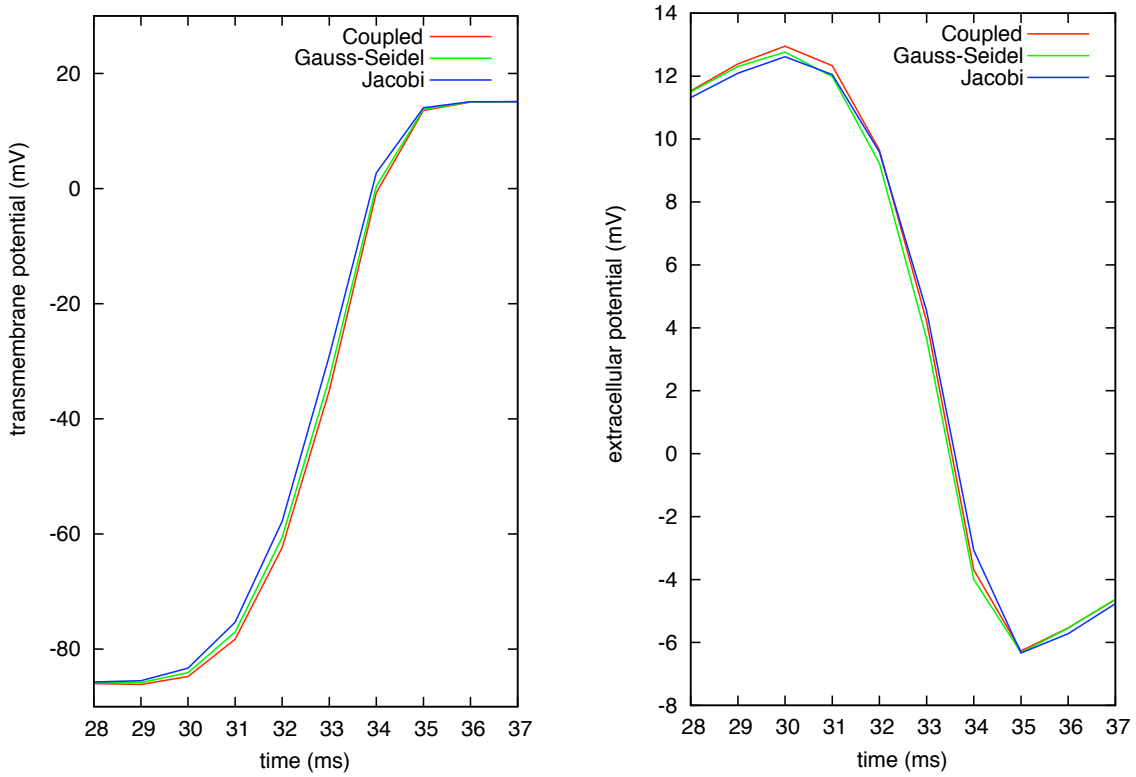

Figure 6.4: Time course, after axis rescaling, of the transmembrane potential (left) and extracellular potential (right) at a given location in the epicardium.

6.5.3 12-lead ECG

For comparison purposes, the simulated 12-lead ECG signals obtained with the explicit coupling procedures (6.3.21)-(6.3.22) will be compared with those obtained using heart-torso coupling (section 5.4)(see also [LBG+03, BCF+09]) and heart-torso uncoupling (section 5.5.1). We shall refer to each of the considered schemes according to the following terminology:

- *Full coupling*: $(u_e^\star, V_m^\star) = (u_e^{n+1}, V_m^{n+1})$ in (6.4.36)-(6.4.38);
- *Uncoupling*: $(u_e^\star, V_m^\star) = (u_e^{n+1}, V_m^{n+1})$ and heart-torso uncoupling (see Remark 6.2.2.1 and *e.g.* [BCF+09]).
- *Robin*: $(u_e^\star, V_m^\star, u_T^\star) = (u_e^{n+1}, V_m^{n+1}, u_T^n)$ in (6.4.42)-(6.4.45);
- *Gauss-Seidel-Robin*: $(u_e^\star, V_m^\star, u_T^\star) = (u_e^n, V_m^{n+1}, u_T^n)$ in (6.4.42)-(6.4.45);
- *Jacobi-Robin*: $(u_e^\star, V_m^\star, u_T^\star) = (u_e^n, V_m^n, u_T^n)$ in (6.4.42)-(6.4.45);

In Figures 6.5 and 6.6 we provide the complete 12-lead ECG signals obtained using the full coupling (black) and uncoupling (red) approaches. We can observe that the uncoupling approach is unable to reproduce the correct signal amplitude, which is indeed magnified by a factor close to 2 in practically all the ECG leads. Moreover, the shape mismatch in some of the leads is clearly visible: the QRS complex in V3 and the T-wave in V2, for instance. Similar observations have been reported in chapter 5 (see also [LBG+03, BCF+09]), for both healthy and pathological conditions.

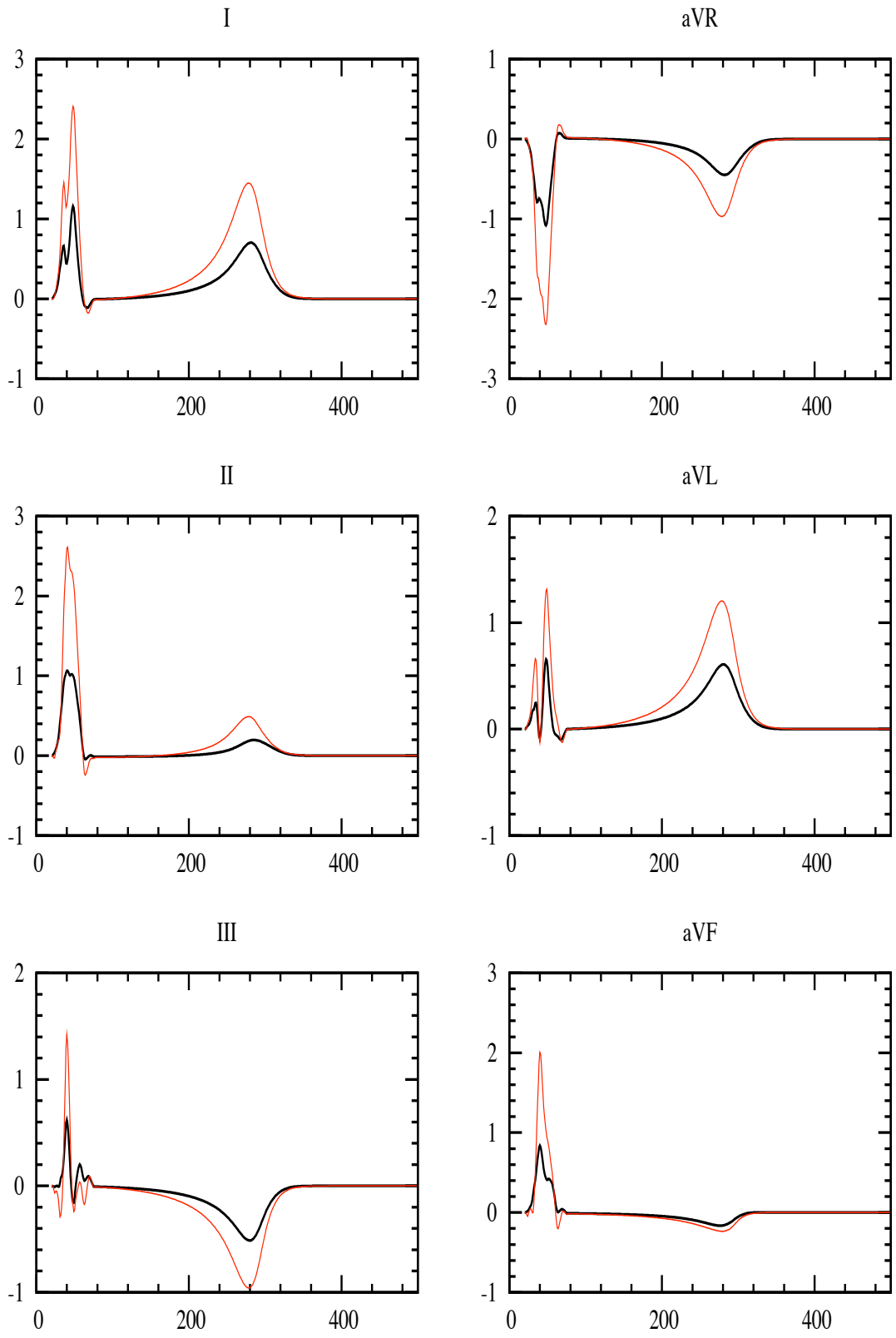

Figure 6.5: Simulated ECG signals (standard and augmented leads) obtained using heart-torso full coupling (black) and uncoupling (red).

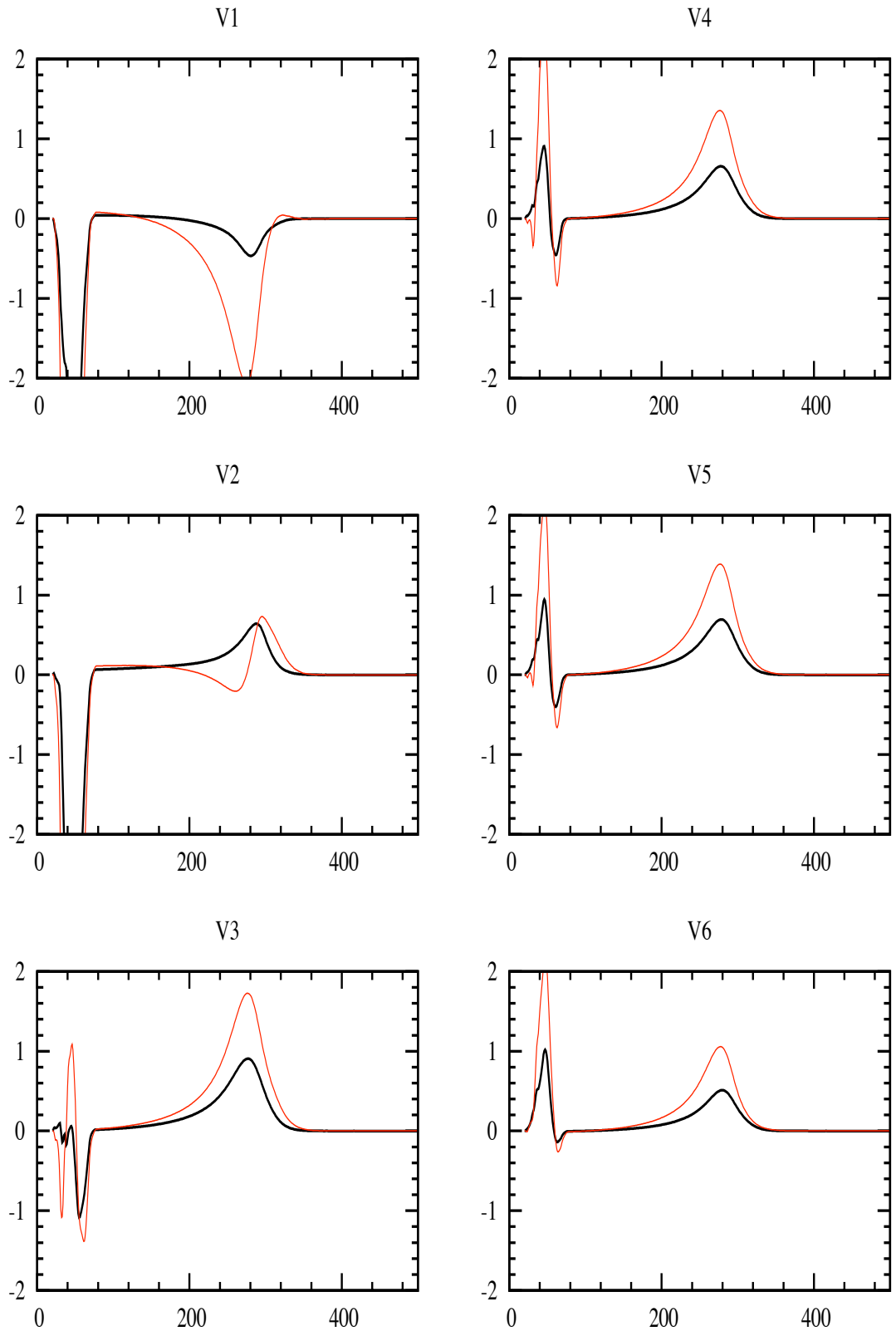

Figure 6.6: Simulated ECG signals (chest leads) obtained using heart-torso full coupling (black) and uncoupling (red).

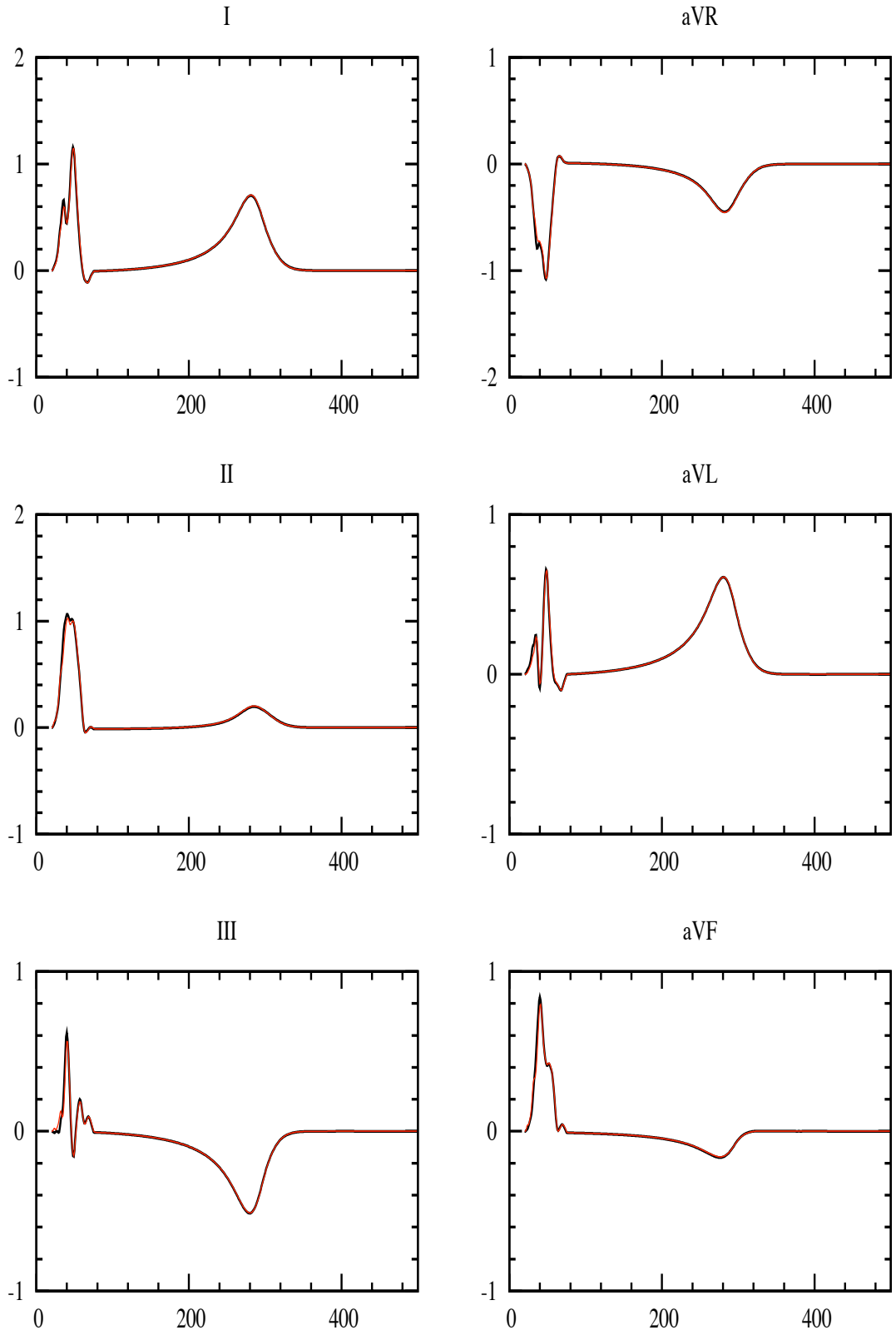

Figure 6.7: Simulated ECG signals (standard and augmented leads) obtained using heart-torso full coupling (black) and Jacobi-Robin scheme (red).

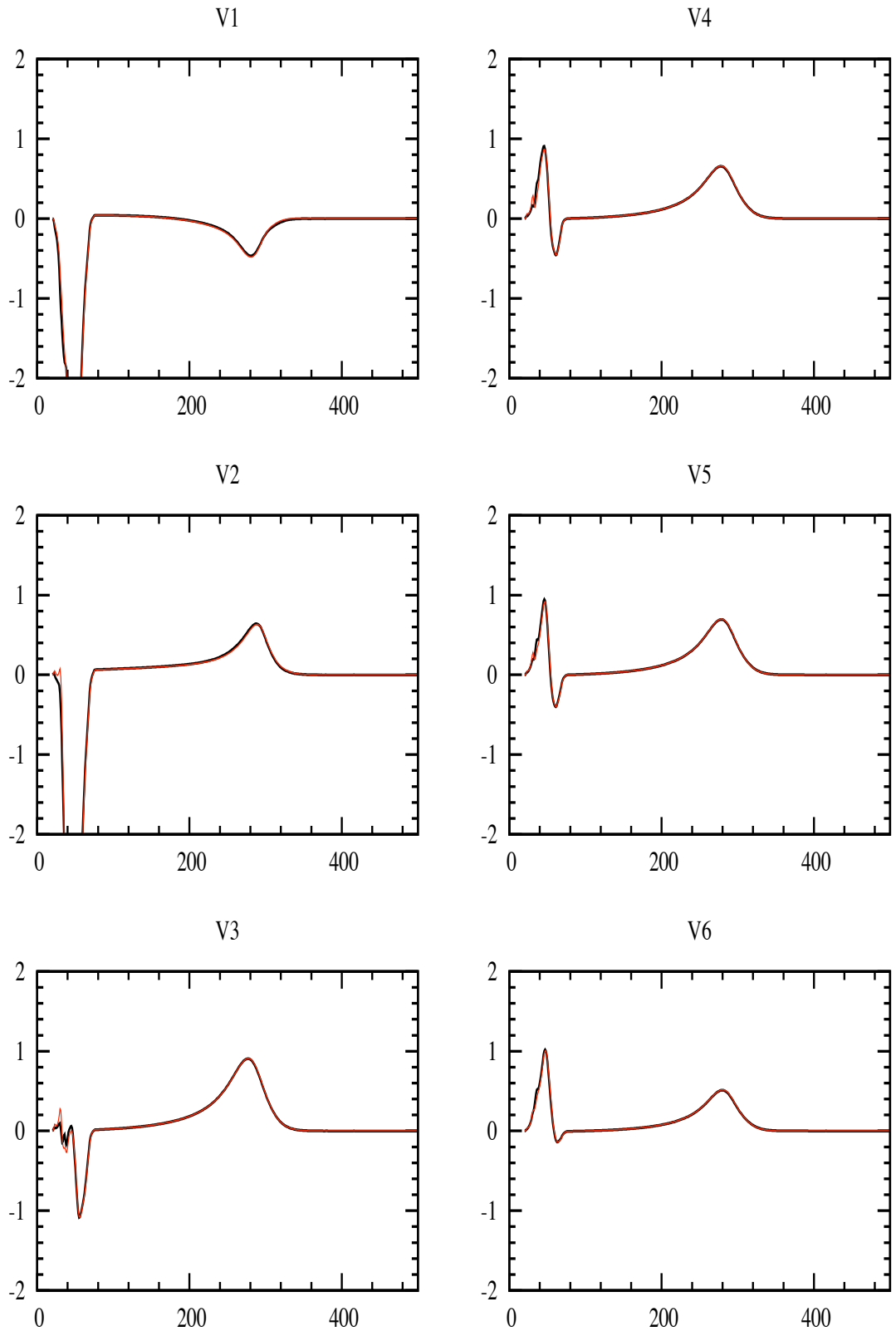

Figure 6.8: Simulated ECG signals (chest leads) obtained using heart-torso full coupling (black) and Jacobi-Robin scheme (red).

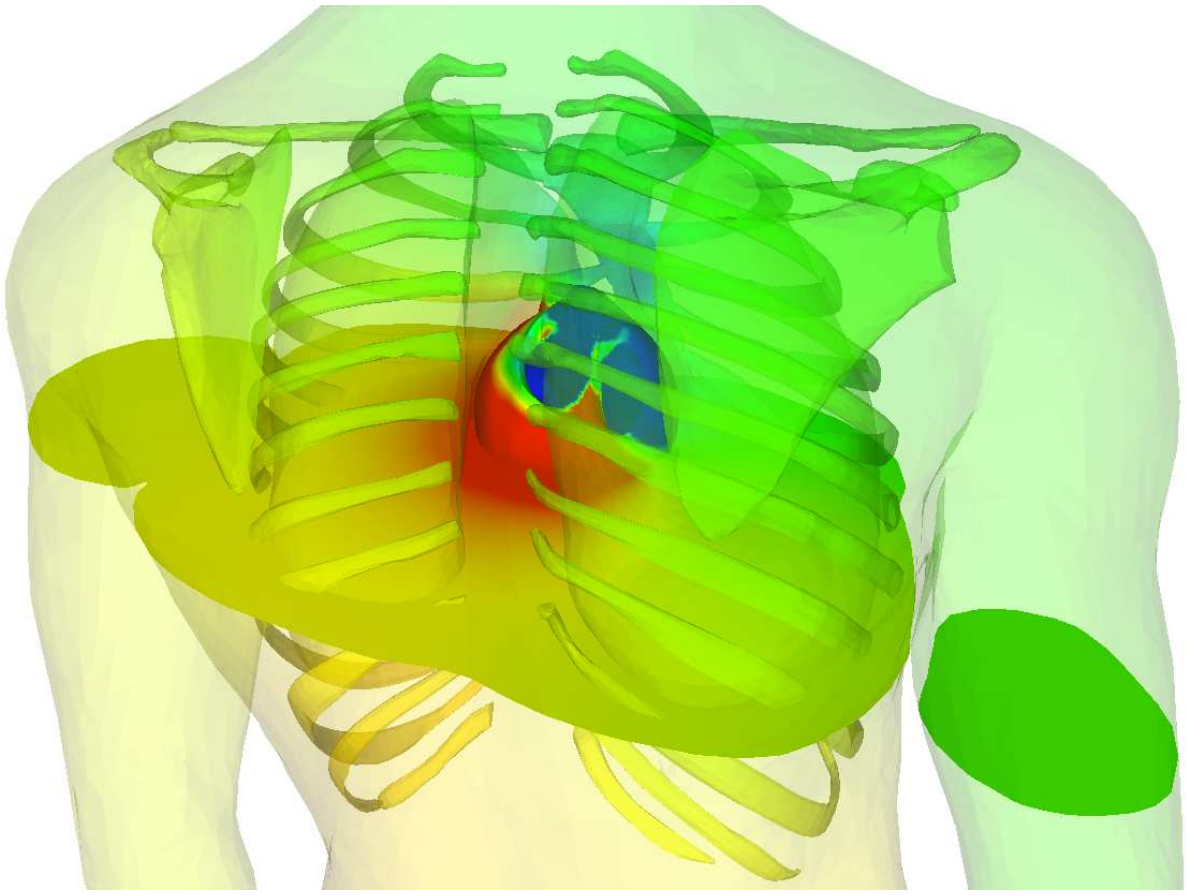

Figure 6.9: Posterior view and cut plane of the torso potential at time $t = 10$ ms.

In the next paragraphs, we shall see that (for an equivalent computational cost) the Robin based explicit coupling introduced in section §6.4 provides much more accurate ECG signals. For illustration purposes, in Figure 6.10, we have reported some snapshots of the body surface potentials obtained with the Jacobi-Robin scheme. Figure 6.9 shows a posterior view of the potential within the torso and the heart. The potential matching at the heart-torso interface is clearly visible.

In Figures 6.7 and 6.8 we compare the simulated 12-lead ECG signals obtained with full coupling (black) to those obtained with fully decoupled Jacobi-Robin scheme (red). The improved accuracy with respect to the uncoupling approach is striking. Indeed, the signals are practically indistinguishable in all the 12 leads. Some minor differences are visible in the QRS complex of V2 and V3. Similar results are obtained with the Robin and Gauss-Seidel-Robin schemes, that we omit for the sake of conciseness. Nevertheless, in order to illustrate the impact of the level of decoupling in the accuracy of the ECG, we have reported in Figure 6.11 a rescaled comparison of the QRS complex (left) and T-wave (right) of the first ECG lead, obtained with the full coupling, Robin, Gauss-Seidel-Robin and Jacobin-Robin approaches. No significant differences are observed in the T-wave, whereas slightly better results are obtained with the Robin approach in the QRS-complex.

The 12-lead ECG signals of a pathological situation, a left bundle branch block (LBBB), have been also computed to illustrate the robustness of the proposed splitting schemes. Figures 6.12 and 6.13 presents the corresponding signals obtained with the

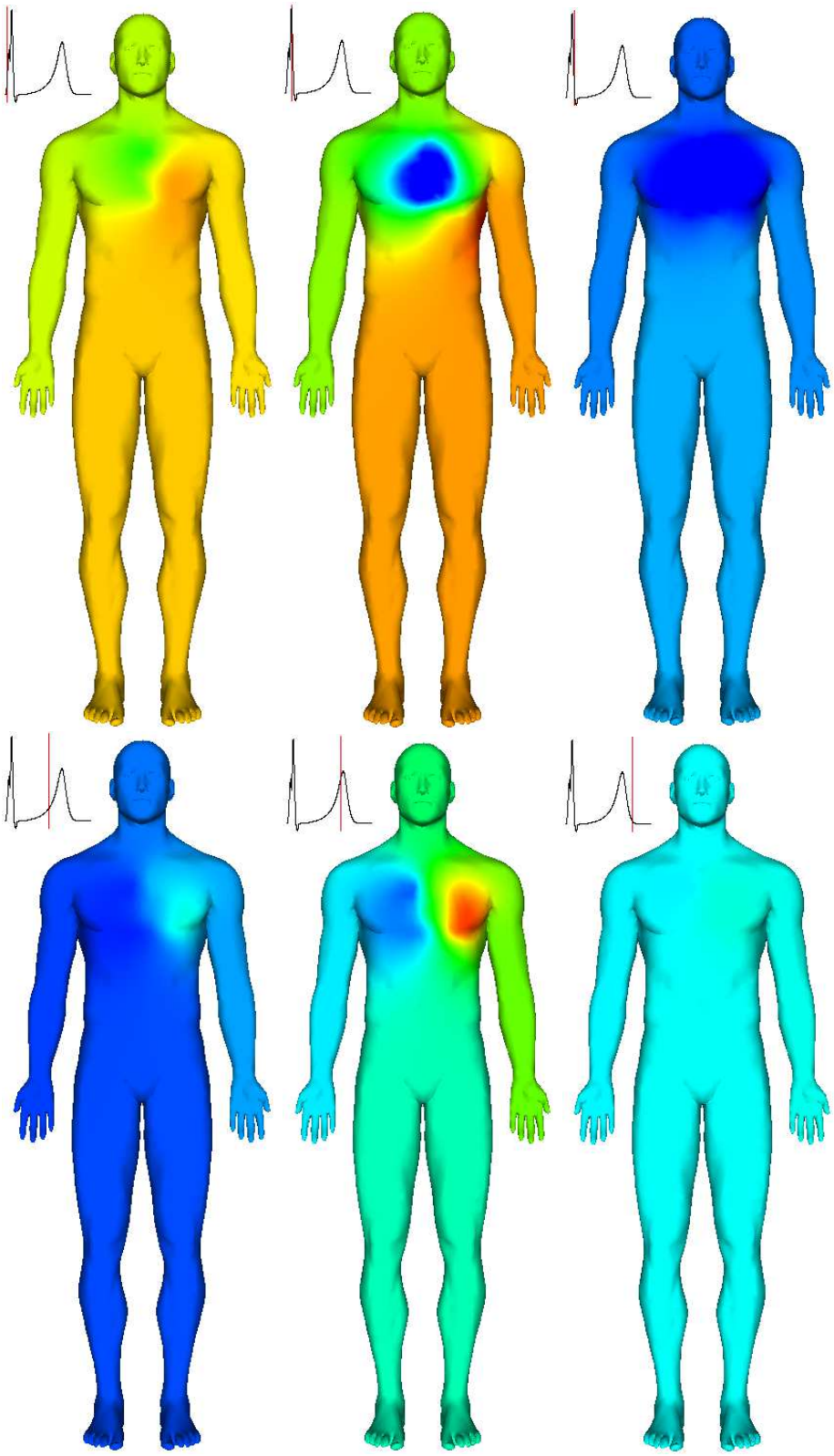

Figure 6.10: Snapshots of the body surface potentials at times $t = 10$, 32, 40, 200, 250 and 310 ms (from left to right and top to bottom).

full coupling (black) and Jacobi-Robin (red) schemes. Once more, the decoupled scheme shows very good accuracy and stability.

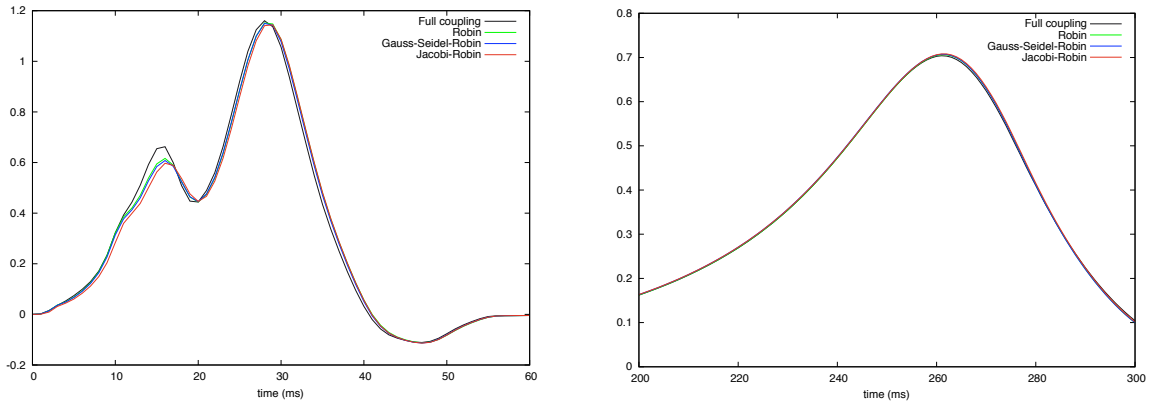

Figure 6.11: Comparison of the QRS complex (left) and T-wave (right) of the first ECG lead: Full coupling (black), Robin (green), Gauss-Seidel-Robin (blue), Jacobin-Robin (red).

Finally, we go further in the investigation of the robustness of the schemes, by considering different heart and torso geometries and model parameters. In particular, we keep $\gamma = 0.1$ as in the previous cases. To this aim, we revisit the ECG numerical simulations recently reported in [BCF$^+$09]. Figures 6.12 and 6.13 the corresponding signals obtained with the full coupling (black) and Jacobi-Robin (red) schemes. Once more, both signals are in excellent agreement. Similar results have been obtained for a LBBB pathology, that we omit here for the sake of conciseness.

6.6 Conclusion

We have introduced and analyzed a series of first order semi-implicit time-marching schemes for the cardiac bidomain equations, either isolated or coupled with generalized Laplace equation for the torso. The main feature of the analyzed schemes is that they all allow a fully decoupled computation of the ionic state, the transmembrane potential, the extracellular potential and the torso potential.

For the isolated bidomain model, Theorem 6.3.3.1 shows that the Gauss-Seidel and Jacobi splittings do not compromise the stability of the resulting schemes; they simply alter the energy norm. Moreover, the time step restrictions are only dictated by the semi-implicit treatment of then non-linear reaction terms. The numerical results reported in section 6.5.2 confirmed these theoretical findings.

We extended these time-marching techniques to the numerical simulation of the ECG, by combining the Gauss-Seidel and the Jacobi like bidomain splittings with an explicit Robin-Robin heart-torso coupling. This specific treatment of the heat-torso coupling is well-suited, particularly, since the time discretization of the two (quasi-static) elliptic equations does not produce numerical dissipation and, therefore, conventional Dirichlet-Neumann explicit coupling might lead to numerical instability. Theorem 6.4.3.1 shows that the proposed splitting schemes are stable under an additional mild CFL like condition $\tau = O(h)$. The numerical study reported in section 6.5.3, using anatomical heart and torso geometries, demonstrated that the Gauss-Seidel-Robin and the Jacobi-Robin splittings are able to provide accurate 12-lead ECG signals, both

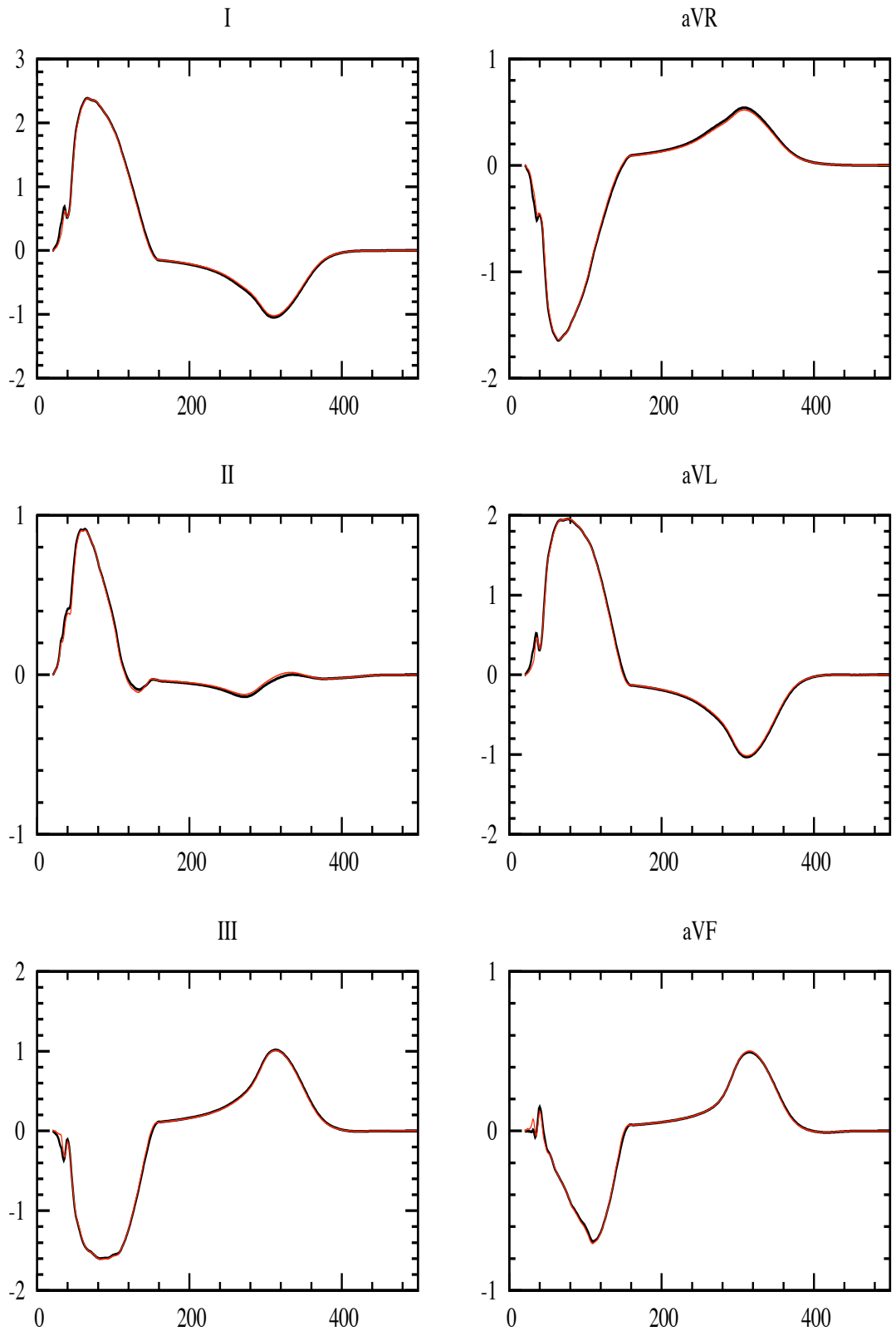

Figure 6.12: Simulated ECG signals (standard and augmented leads) for a LBBB pathology, obtained using heart-torso full coupling (black) and Jacobi-Robin scheme (red).

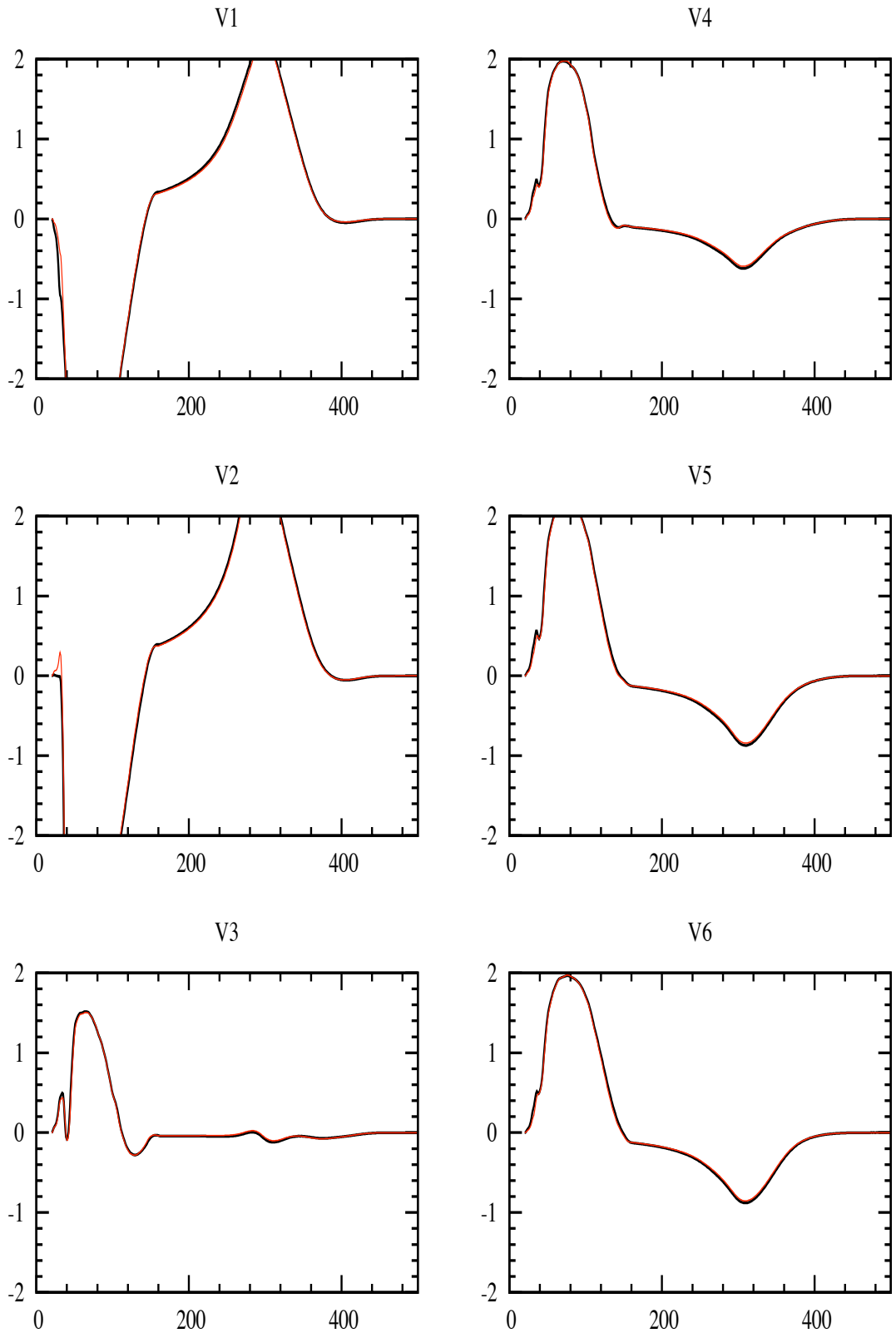

Figure 6.13: Simulated ECG signals (chest leads) for a LBBB pathology, obtained using heart-torso full coupling (black) and Jacobi-Robin scheme (red).

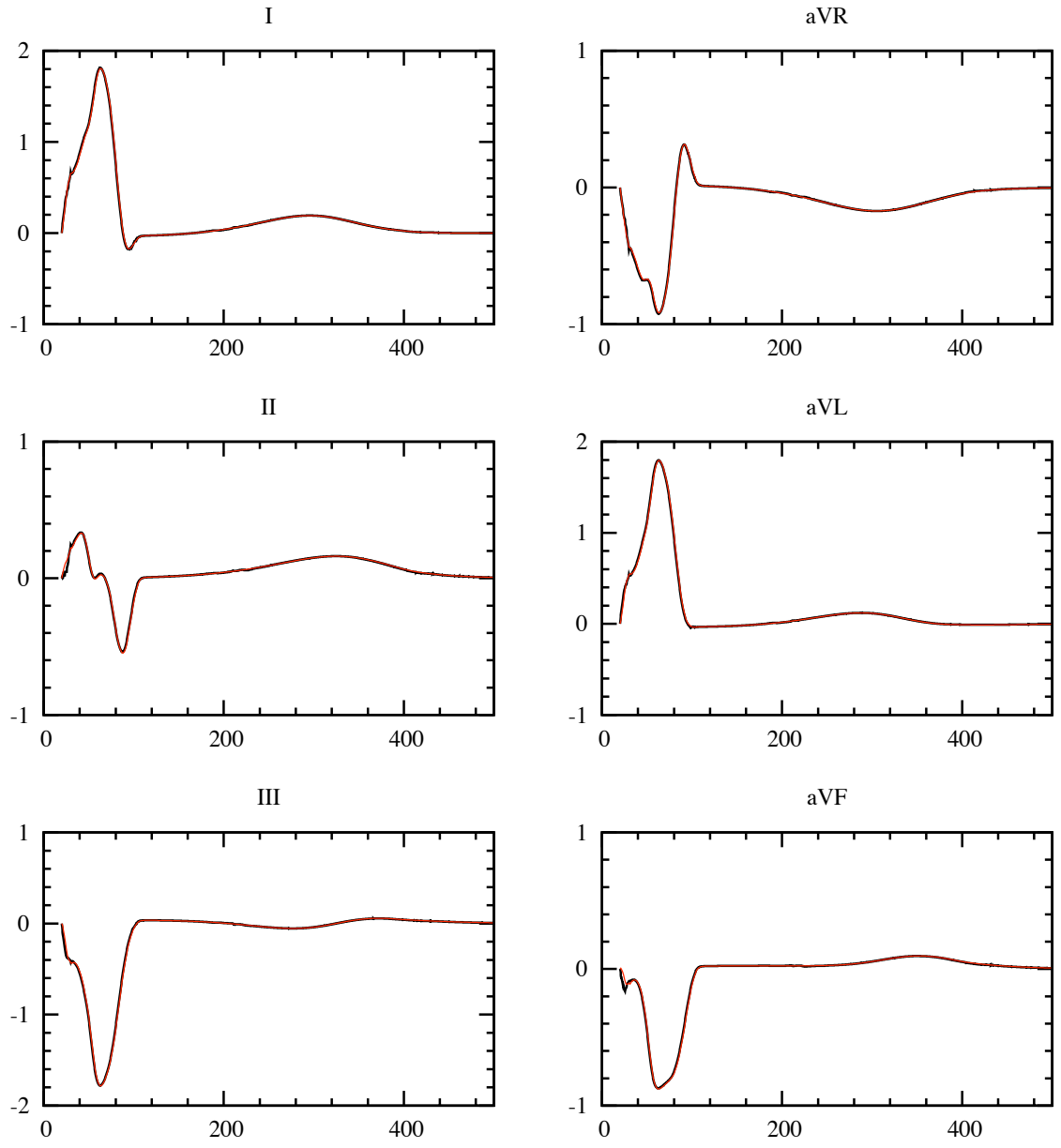

Figure 6.14: Simulated ECG signals (standard and augmented leads) with the geometry data and model parameters of Chapter 5, obtained using heart-torso full coupling (black) and Jacobi-Robin scheme (red).

for a healthy and a pathological condition. Note that this is a major advantage with respect to the conventional heart-torso uncoupling approximations, which (for a similar computational cost) are known to provide inaccurate ECG signals (see *e.g.* [LBG$^+$03, PBC05, BCF$^+$09]). The robustness of the proposed splitting schemes has been also illustrated with numerical experiments based on different model parameters and heart/torso geometries.

The theoretical and numerical study in this chapter is limited to discretizations yielding first order accuracy in time. Some insights into feasible extensions to higher order are commented in Remark 6.3.3.3. Although the present stability analysis holds irrespectively of the original time discretization scheme, it does depend on the (first order)

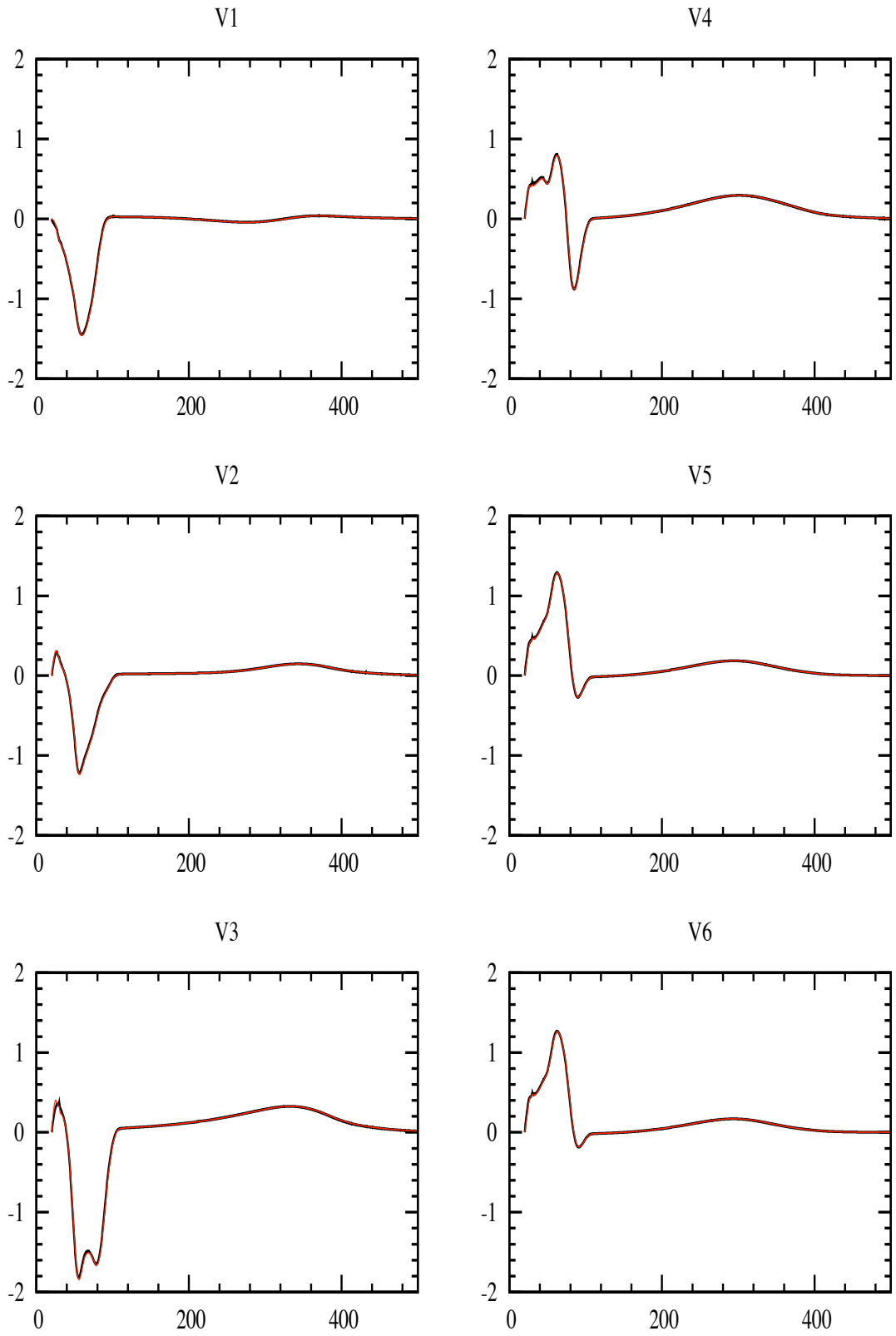

Figure 6.15: Simulated ECG signals (chest leads) with the geometry data and model parameters of Chapter 5, obtained using heart-torso full coupling (black) and Jacobi-Robin scheme (red).

extrapolation involved in the splittings. As a result, the generalization of the present analysis to hight order extrapolations seems not straightforward. Further numerical investigations would certainly help to clarify this issue and could be the topic of future work.

Part IV

Applications

Summary

Chapter 7

Inverse problems in Electrocardiography

We present in this chapter preliminary results of parameters estimation problem. We provide a strategy allowing to estimate the torso conductivity parameters. We present also numerical results concerning the identification of two ionic model parameters.

The estimation of the torso conductivity parameters is part of a joint work with M. Boulakia, M.A. Fernández and J.-F. Gerbeau, reported in [BFGZ08a].

7.1 Introduction

In the literature, (*see e.g.* [NLT+06, SSN94]) the aim of the inverse problem is generally to identify the epicardial potential. Our approach is to identify the parameters of the model. As a first step we only consider the torso conductivity parameters. We consider the heart-torso uncoupled problem introduced in chapter 5 (section5.5.1). In section 7.2, we study the sensitivity of the ECG to the torso coductivity parameters. In section 7.3, we present a for the estimation of the torso conductivity ratios. Finally, we provide in section 7.4 preliminary results for the identification of the ionic model parameters.

We remark that if the torso potential is computed using the weak coupling condition in the heart-torso interface, we can reduce the number of the conductivity parameters to estimate. In fact, suppose that we have the bidomain solution in the heart ($V_{\rm m}$ and $u_{\rm e}$) and $u_{\rm T}(\gamma)$ is the solution of the following problem:

$$(\mathrm{P}_\gamma)\begin{cases} \mathrm{div}(\gamma\boldsymbol{\sigma}_{\rm T}\boldsymbol{\nabla}u_{\rm T}) = 0, \text{ in } \Omega_{\rm T}, \\ u_{\rm T} = u_{\rm e}, \quad \text{on} \quad \Sigma, \\ \gamma\boldsymbol{\sigma}_{\rm T}\boldsymbol{\nabla}u_{\rm T}\cdot\boldsymbol{n}_{\rm T} = 0, \text{ on } \Gamma_{\rm ext}, \end{cases} \tag{7.1.1}$$

$$\text{where } \gamma \in \mathbb{R} \text{ and } \boldsymbol{\sigma}_{\rm T} = \begin{cases} \sigma_l, & \text{in } \Omega_{\rm l}, \\ \sigma_b, & \text{in } \Omega_{\rm b}, \\ \sigma_t, & \text{in } \Omega_{\rm t}, \end{cases} \tag{7.1.2}$$

and $\Omega_{\rm l}, \Omega_{\rm b}$ and $\Omega_{\rm t}$ are respectively the lungs, bones and tissue domains. The solution

$u_{\mathrm{T}}(\gamma)$ is independent of γ, thus, if we take $\gamma = \dfrac{1}{\sigma_i}$, where $\sigma_i \in \{\sigma_{\mathrm{t}}, \sigma_{\mathrm{l}}, \sigma_{\mathrm{b}}\}$, the parameters to estimate are now the ratios of the two remaining parameters by σ_i: $(\dfrac{\boldsymbol{\sigma}_{\mathrm{j}}}{\sigma_i})_{\sigma_j \neq \sigma_i}$. The choice of γ is postponed to the next section.

7.2 Sensitivity

In this paragraph, we study the sensitivity of the electrocardiograms to the torso conductivity parameters, in order to choose the parameter γ described before. Suppose that $ECG = ECG(\sigma_{\mathrm{t}}, \sigma_{\mathrm{l}}, \sigma_{\mathrm{b}})$, then the ECG derivative to the parameter σ_{t} is approximated by $\partial_{\sigma_{\mathrm{t}}} ECG(\sigma_{\mathrm{t}}, \sigma_{\mathrm{l}}, \sigma_{\mathrm{b}}) \approx \dfrac{ECG((1+\epsilon)\sigma_{\mathrm{t}}, \sigma_{\mathrm{l}}, \sigma_{\mathrm{b}}) - ECG(\sigma_{\mathrm{t}}, \sigma_{\mathrm{l}}, \sigma_{\mathrm{b}})}{\epsilon \sigma_{\mathrm{t}}}$, where ϵ is a small real. We define by the same way the quantities $\partial_{\sigma_{\mathrm{l}}} ECG$ and $\partial_{\sigma_{\mathrm{b}}} ECG$. For $\sigma_i \in \{\sigma_{\mathrm{t}}, \sigma_{\mathrm{l}}, \sigma_{\mathrm{b}}\}$, the normalized σ_i-derivative of the ECG is defined by $\sigma_i \partial_{\sigma_i} ECG(\sigma_{\mathrm{t}}, \sigma_{\mathrm{l}}, \sigma_{\mathrm{b}})$. This quantity allows to compare the sensitivity of the ECG to different parameters whatever their magnitude. In Figure 7.1 we plot the normalized conductivity parameters derivatives of the first lead of the ECG, $\sigma_i \partial_{\sigma_i} ECG(\sigma_{\mathrm{t}}, \sigma_{\mathrm{l}}, \sigma_{\mathrm{b}})$, where σ_i denotes the conductivity σ_{l} of the lungs, σ_{b} of the bones (skeleton) and σ_{t} of the remaining tissue (torso tissue). We remark that the sensitivity of the ECG to the skeleton parameter is negligible compared to its sensitivity to other parameters. Thus, we choose $\gamma = \dfrac{1}{\sigma_{\mathrm{b}}}$ and the parameters to estimate are now, $\dfrac{\sigma_{\mathrm{t}}}{\sigma_{\mathrm{b}}}$ and $\dfrac{\sigma_{\mathrm{l}}}{\sigma_{\mathrm{b}}}$.

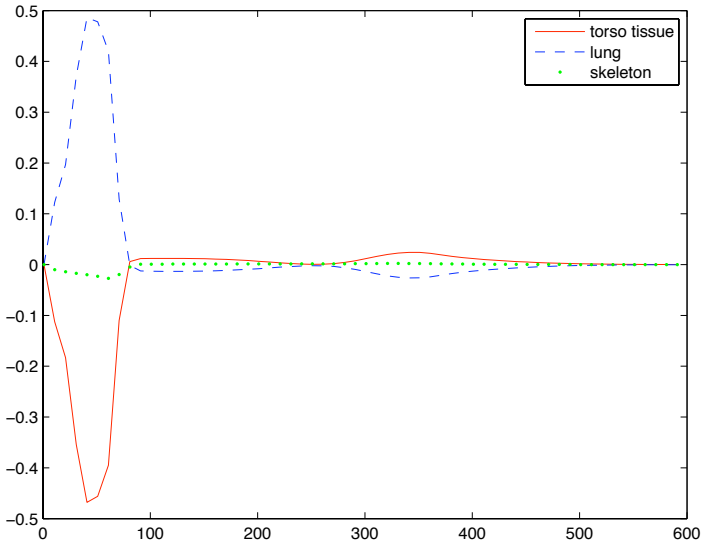

Figure 7.1: The normalized parameter derivatives of the electrocardiogram: $\sigma_{\mathrm{t}} \partial_{\sigma_t} ECG$ (red, continuous line) for the tissue derivative, $\sigma_{\mathrm{l}} \partial_{\sigma_{\mathrm{l}}} ECG$ (blue dashed line) for the lung derivative and $\sigma_{\mathrm{l}} \partial_{\sigma_{\mathrm{l}}} ECG$ (green, doted line) for bones (skeleton)

Remark 7.2.0.1. *The number of torso conductivity parameters to estimate in the inverse problem is reduced when we use the weak coupling. This simplification could not*

be done if we use a full heart-torso coupling, since the solution $u_{\mathrm{T}}(\gamma)$ of the problem P_γ depends on γ due to the coupling condition $(5.2.10)_2$.

7.3 Estimation of the torso conductivity parameters

Let $\omega \subset \Gamma_{\mathrm{ext}}$ be the domain of measurement in the torso that will be made precise later. The inverse problem could be formulated as follows: For a given measurment u_{meas} on ω, find $\sigma = \begin{cases} \sigma_t/\sigma_b, & \text{in } \Omega_{\mathrm{t}}, \\ \sigma_l/\sigma_b, & \text{in } \Omega_{\mathrm{l}}, \\ 1, & \text{in } \Omega_{\mathrm{t}}, \end{cases}$ such that the solution of the following problem satisfies $u_{\mathrm{T}/\omega} \approx u_{\mathrm{meas}}$ on ω.

$$\begin{cases} \mathrm{div}(\sigma \boldsymbol{\nabla} u_{\mathrm{T}}) = 0, \text{ in } \Omega_{\mathrm{T}}, \\ \qquad u_{\mathrm{T}} = u_{\mathrm{e}}, \quad \text{on} \quad \Sigma, \\ \sigma \boldsymbol{\nabla} u_{\mathrm{T}} \cdot \boldsymbol{n}_{\mathrm{T}} = 0, \text{ on } \Gamma_{\mathrm{ext}} \backslash \omega, \\ \sigma \boldsymbol{\nabla} u_{\mathrm{T}} \cdot \boldsymbol{n}_{\mathrm{T}} = 0, \text{ on } \omega, \end{cases}$$

We have to deal with two difficulties to solve this problem. The first obstacle is a practical difficulty: the heart potential on the heart-torso interface $u_{\mathrm{e}/\Sigma}$ is considered as a data, whereas, in practice, it is very difficult to access. The second problem is the ill-posedeness of the problem. In fact, we impose two boundary conditions on the domain of measurements ω ($\sigma \boldsymbol{\nabla} u_{\mathrm{T}} \cdot \boldsymbol{n}_{\mathrm{T}} = 0$, and $u_{\mathrm{T}/\omega} \approx u_{\mathrm{meas}}$ on ω).

In the following paragraph we present an experimental method allowing the elimination of the practical difficulty and a mathematical regularization allowing the well-posedeness of the optimization algorithm

7.3.1 Numerical experiment

The estimation of the conductivity ratios $\dfrac{\sigma_{\mathrm{t}}}{\sigma_{\mathrm{b}}}$ and $\dfrac{\sigma_{\mathrm{l}}}{\sigma_{\mathrm{b}}}$ from equation (7.1.1) is difficult in practice since the potential on the epicardium is an unknown of the problem. Nevertheless, in the framework of our simplified model, it is easy to eliminate this missing information using a superposition principle. Let u_{S} be the solution to the torso equation with a Dirichlet boundary condition ϕ_S applied on a part S of the torso skin. We denote by ξ the quantity $u_{\mathrm{S}} - u_{\mathrm{T}}$. Note that ξ satisfies the following equation:

$$\begin{cases} \mathrm{div}(\boldsymbol{\sigma}_{\mathrm{T}} \boldsymbol{\nabla} \xi) = 0, \text{ in } \Omega_{\mathrm{T}}, \\ \qquad \xi = 0, \text{ on } \Sigma, \\ \quad \xi = \phi_S - u_{\mathrm{T}}, \text{ on } S, \\ \boldsymbol{\sigma}_{\mathrm{T}} \boldsymbol{\nabla} \xi \cdot \boldsymbol{n}_{\mathrm{T}} = 0, \text{ in } \Gamma_{\mathrm{ext}} \backslash S. \end{cases} \tag{7.3.3}$$

We now propose to estimate the conductivity ratios from this equation using the following procedure:

- **E1:** We first measure $\bar{u_{\mathrm{T}}}$ on S and on ω.
- **E2:** Next, we impose a potential ϕ_S on S and we measure the resulting potential $\bar{u_{\mathrm{S}}}$ on ω.

- **E3:** We then denote by $\bar{\xi}$ the quantity $\bar{u_{\mathrm{S}}} - \bar{u_{\mathrm{T}}}$ on ω

We propose to solve the following optimization problem:

$$\min_{\sigma} I(\sigma),$$

with

$$I(\sigma) = J(\sigma, \xi(\sigma))$$

where,

for each $\sigma = \begin{cases} \alpha_1, & \text{in } \Omega_{\mathrm{t}}, \\ \alpha_2, & \text{in } \Omega_{\mathrm{l}}, \\ 1, & \text{in } \Omega_{\mathrm{b}}, \end{cases}$

the function $\xi(\sigma)$ is the solution of the following problem:

$$\begin{cases} \operatorname{div}(\boldsymbol{\sigma}_{\mathrm{T}} \boldsymbol{\nabla} \xi) = 0, \text{ in } \Omega_{\mathrm{T}}, \\ \xi = 0, \text{ on } \Sigma, \\ \xi = \bar{\xi}, \text{ on } S, \\ \boldsymbol{\sigma}_{\mathrm{T}} \boldsymbol{\nabla} \xi \cdot \boldsymbol{n}_{\mathrm{T}} = 0, \text{ in } \Gamma_{\mathrm{ext}} \backslash S. \end{cases} \tag{7.3.4}$$

The function J is given by

$$J(\sigma, \xi) = \frac{1}{2} \parallel \xi - \bar{\xi} \parallel^2_{L^2(\omega)} + \frac{\beta}{2} \big(|\alpha_1 - \bar{\alpha_1}|^2 + |\alpha_2 - \bar{\alpha_2}|^2 \big),$$

here $\beta > 0$ is a regularization parameter and $\boldsymbol{\sigma}_{\mathrm{M}} = \begin{cases} \bar{\alpha_1}, & \text{in } \Omega_{\mathrm{t}}, \\ \bar{\alpha_2}, & \text{in } \Omega_{\mathrm{l}}, \\ 1, & \text{in } \Omega_{\mathrm{b}}, \end{cases}$ is in the average of torso conductivity ratios. We use the quasi-Newton algorithm with line search method provided by the package OPT++[1] library. The used algorithm in this toolbox requires the evaluation the function I and its gradient. To compute the gradient of I we use the adjoint method. For given ξ and $\lambda \in H^1(\Omega_{\mathrm{T}})$ and $\epsilon > 0$, we define the Lagrangian as follows

$$L(\sigma, \xi, \lambda) = J(\sigma, \xi) + \int_{\Omega_{\mathrm{T}}} \sigma \boldsymbol{\nabla} \xi \boldsymbol{\nabla} \lambda + \frac{1}{\epsilon} \int_S (\xi - \bar{\xi}) \lambda + \frac{1}{\epsilon} \int_{\Sigma} \xi \lambda,$$

where ϵ is a penalization parameter which has been introduced to conveniently include the Dirichlet boundary condition in the definition of the Lagrangian. Since $\xi(\sigma)$ is solution of the problem (7.3.4), we have

$$\begin{aligned} L(\sigma, \xi(\sigma), \lambda) &= J(\sigma, \xi(\sigma)) + \int_{\Omega_{\mathrm{T}}} \sigma \boldsymbol{\nabla} \xi(\sigma) \boldsymbol{\nabla} \lambda + \frac{1}{\epsilon} \int_S (\xi(\sigma) - \bar{\xi}) \lambda + \frac{1}{\epsilon} \int_{\Sigma} \xi(\sigma) \lambda \\ &= J(\sigma, \xi(\sigma)). \end{aligned}$$

Then,

$$\frac{\mathrm{d}I}{\mathrm{d}\sigma}(\sigma) = \frac{\mathrm{d}J(\sigma, \xi(\sigma))}{\mathrm{d}\sigma} = \frac{\mathrm{d}L(\sigma, \xi(\sigma), \lambda)}{\mathrm{d}\sigma}.$$

We have

$$\frac{\mathrm{d}L(\sigma, \xi(\sigma), \lambda)}{\mathrm{d}\sigma} = \frac{\mathrm{d}L}{\mathrm{d}\sigma}(\sigma, \xi(\sigma), \lambda) + \frac{\mathrm{d}L}{\mathrm{d}\xi}(\sigma, \xi(\sigma), \lambda) \frac{\mathrm{d}\xi}{\mathrm{d}\sigma}.$$

[1] `http://csmr.ca.sandia.gov/opt++/`

In prctice it is difficult to compute $\dfrac{\mathrm{d}\xi}{\mathrm{d}\sigma}$, the dual approach allow to eliminate this term by searching λ, such that $\dfrac{\mathrm{d}L}{\mathrm{d}\xi}(\sigma, \xi(\sigma), \lambda) = 0$.

$$\begin{aligned}\frac{\mathrm{d}L}{\mathrm{d}\xi}(\sigma, \xi(\sigma), \lambda)\phi = 0 \Leftrightarrow \frac{\mathrm{d}J}{\mathrm{d}\xi}(\sigma, \xi(\sigma))\phi + \int_{\Omega_\mathrm{T}} \sigma \boldsymbol{\nabla}\lambda \boldsymbol{\nabla}\phi + \frac{1}{\epsilon}\int_S \lambda\phi + \frac{1}{\epsilon}\int_\Sigma \lambda\phi = 0 \\ \Leftrightarrow \int_\omega (\xi(\sigma) - \bar{\xi})\phi + \int_{\Omega_\mathrm{T}} \sigma \boldsymbol{\nabla}\lambda \boldsymbol{\nabla}\phi + \frac{1}{\epsilon}\int_S \lambda\phi + \frac{1}{\epsilon}\int_\Sigma \lambda\phi = 0.\end{aligned}$$

By taking λ solution of the following problem

$$\begin{cases} -\operatorname{div}(\sigma\boldsymbol{\nabla}\lambda) = -(\xi - \bar{\xi})\chi_\omega, \text{ in } \Omega_\mathrm{T}, \\ \qquad\qquad\qquad\qquad \lambda = 0, \quad \text{on} \quad \Sigma \cup S, \\ \qquad\qquad\quad \sigma\boldsymbol{\nabla}\lambda \cdot \boldsymbol{n}_\mathrm{T} = 0, \text{ on } \Gamma_{\text{ext}} \backslash S, \end{cases}$$

where χ_ω is equal to 1 in ω and 0 else. We then obtain

$$\frac{\mathrm{d}I}{\mathrm{d}\sigma}(\sigma) = \frac{\mathrm{d}L}{\mathrm{d}\sigma}(\sigma, \xi(\sigma), \lambda)$$

Consequently we have

$$\frac{\mathrm{d}I}{\mathrm{d}\sigma_\mathrm{t}}(\sigma) = \beta(\alpha_1 - \bar{\alpha_1}) + \int_{\Omega_\mathrm{t}} \boldsymbol{\nabla}\xi \cdot \boldsymbol{\nabla}\lambda,$$

$$\frac{\mathrm{d}I}{\mathrm{d}\sigma_\mathrm{l}}(\sigma) = \beta(\alpha_2 - \bar{\alpha_2}) + \int_{\Omega_\mathrm{l}} \boldsymbol{\nabla}\xi \cdot \boldsymbol{\nabla}\lambda.$$

7.3.2 Parameter estimation using synthetic data

For the numerical experiments, we will consider two cost functions corresponding to two different choices of ω. The first choice consists in taking $\omega = \Omega_\mathrm{T}$. For the second cost function, we consider the points of the ECG measurements $x_1, x_2, ...x_9$, and we define $w = \cup_{i=1}^9 B(x_i, r)$, where r is "small" (in practice 0.5 cm).

In Figure 7.2 we provide the convergence result of the parameter estimation using the quasi-Newton algorithm for the two cost functions. In (Figure 7.2, left) the cost function is computed on all the torso and in (Figure 7.2, right) the cost function uses the ECG lead position as explained previously. The data $\bar{\xi}$ is computed with the conductivity tensor $\boldsymbol{\sigma}_\mathrm{T}$ given by $\sigma_\mathrm{t} = 6 \times 10^{-4}$ Scm^{-1}, $\sigma_\mathrm{l} = 2.4 \times 10^{-4}$ Scm^{-1} and $\sigma_\mathrm{b} = 0.4 \times 10^{-4}$ Scm^{-1}. For the regularization parameter we take $\beta = 10^{-6}$ and $\boldsymbol{\sigma}_\mathrm{M}$ is given by $\bar{\alpha_1} = 8.0$, $\bar{\alpha_2} = 3.0$.

With the first cost function, we obtain $\alpha_1 = \dfrac{\sigma_\mathrm{t}}{\sigma_\mathrm{b}} = 15$ and $\alpha_2 = \dfrac{\sigma_\mathrm{l}}{\sigma_\mathrm{b}} = 6.0$ which are exactly the values used to generate $\bar{\xi}$. From the practical viewpoint, the second cost function is of course much more convenient. In that case, we obtain $\alpha_1 = 14.98$ and $\alpha_2 = 5.992$, which is satisfactory.

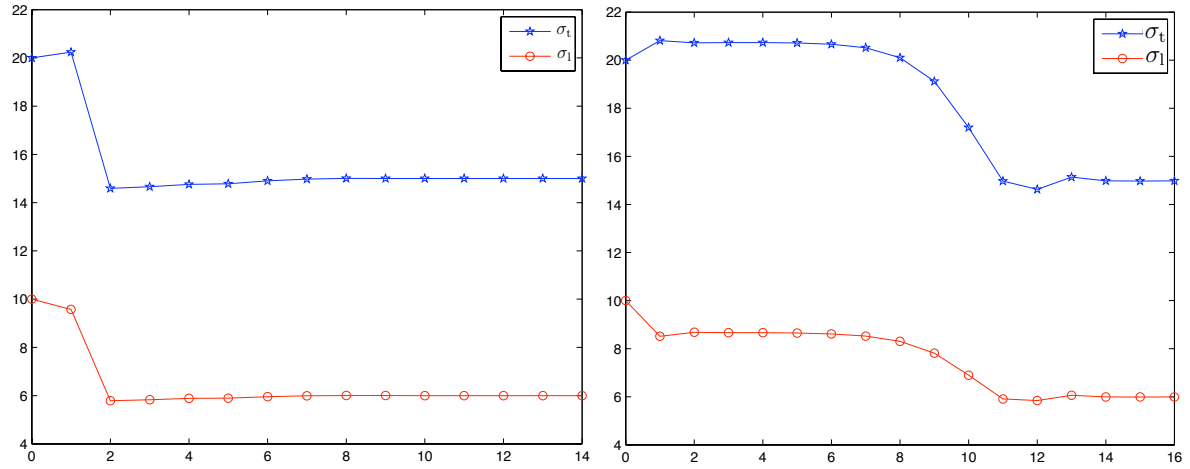

Figure 7.2: Convergence of the quasi-Newton algorithm: Left: the cost function computed in all of the torso domain. Right: the cost function is computed using ECG lead position. (x-axis) iterations, (y-axis) value of conductivity ratios .

7.4 Ionic parameter estimation

In this paragraph we provide some results of the ionic parameters estimation. We begin our work by estimating the parameter τ_{close} in different regions. This parameter is responsible of the generation of the T-wave in the ECG. We estimate the parameter τ_{close} in two different regions, in the right ventricle τ_{close}^{RV} and in the epicardium $\tau_{\text{close}}^{Epi}$. We simplify the problem by generating a synthetic ECG that we denote ECG_{ref}. To estimate the parameters, we propose a cost function based on ECG. We will solve the following minimization problem

$$\min_{\tau_{\text{close}}^{RV},\tau_{\text{close}}^{Epi}} \| ECG_{ref} - ECG(\tau_{\text{close}}^{RV},\tau_{\text{close}}^{Epi}) \|_{L^p(0,T)},$$

where $ECG(\tau_{\text{close}}^{RV},\tau_{\text{close}}^{Epi})$ is the ECG depending only on τ_{close}^{RV} and $\tau_{\text{close}}^{Epi}$, all of the remaining model parameter are fixed to the values which served to compute ECG_{ref} and p is the norm order. In the case $p = 1$, the problem could be translated to a minimization of the surface between two ECG plots which could be meaningful for a medical doctor. We use the `matlab optimisation toolbox` to minimise the function cost. More precisely we can use the function `fminsearch` or `fsolve` for an unconstrained optimization or `fmincon` for a constrained optimization. In our case we do not provide the gradient to the optimization function. We only provide the evalution of the function cost when it is called by the optimizer. This last one computes the gradient using finite difference method. We refer to the matlab optimization toolbox documentation for more details about the used algorithms.

In Figure 7.3 we provide an illustration of the algorithm convergence. In fact we plot the values of of τ_{close}^{RV}, $\tau_{\text{close}}^{Epi}$ and the cost function at each algorithm iteration. The values of τ_{close}^{RV} and $\tau_{\text{close}}^{Epi}$ were initialized to the value 150 and we see that they converge to the values 121.5 and 91.7 respectively. These values are close to the values of the used to compute ECG_{ref} which are respectively 120 and 90. In Figure 7.4, we provide an illustration of the algorithm convergence, but starting from an other point. In fact , the parameters were initialized to the value 50 and they converge to the 117.5 for τ_{close}^{RV} and 87.5 for $\tau_{\text{close}}^{Epi}$. Which remains an acceptable result.

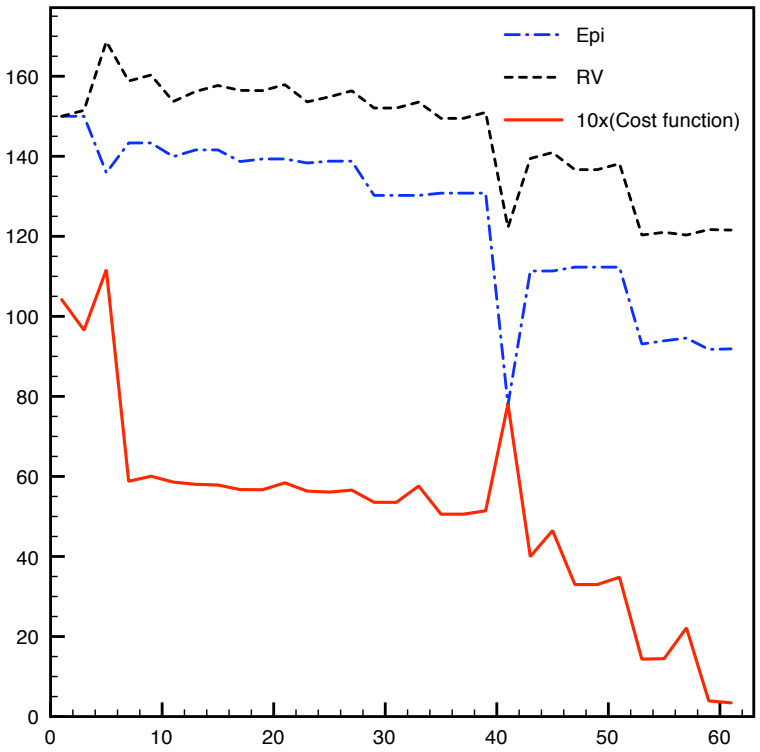

Figure 7.3: Plots of the values of τ_{close}^{RV}, $\tau_{\text{close}}^{Epi}$ and the cost function during the algorithm iteration. (x-axis) iterations. The starting point is (150 ,150).

7.5 Conclusion

We have proposed a model based on the bidomain equation to generate numerical ECG which can be compared to real ones. This model depends on 14 parameters which should be identified. In this preliminary study we focussed on the conductivity of the torso. Assuming we fix the conductivity of the bones – which has been shown to barely affect the ECG – we have proposed a strategy to estimate the conductivity of the lung and the remaining tissues. We have also proposed an example of estimation of the ionic parameters. The results show that a deterministic method could be efficient for this problem. The good results obtained with this method on synthetic data still have to be confirmed on experimental ones. The estimation of the bidomain model parameters will be the topic of a forthcoming work.

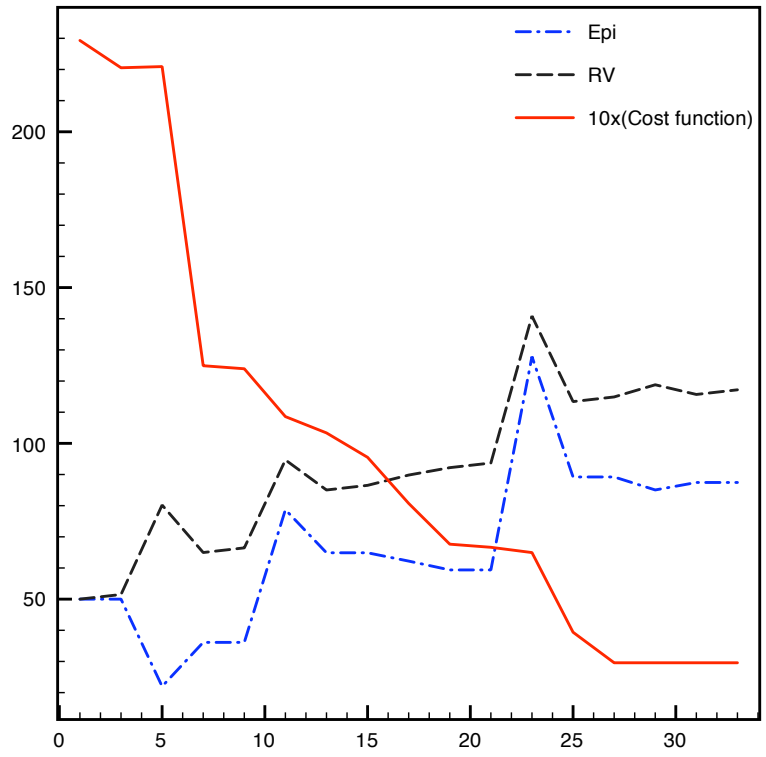

Figure 7.4: Plots of the values of τ_{close}^{RV}, $\tau_{\text{close}}^{Epi}$ and the cost function during the algorithm iteration. (x-axis) iterations. The starting point is (50 ,50).

Chapter 8

From intracardiac electrograms to electrocardiograms. Models and metamodels

This chapter concerns an industrial application of the ECGs modeling. The problem is how to reconstruct ECGs from electrograms? To deal with this problem, we propose a metamodel technique based on *kernel ridge regression* method. The 3D model of ECGs is used to train and test the metamodel. We illustrate the performance of the proposed strategy on bundle branch blocks of various severities.

A part of this chapter has been the subject of a published work coauthored with G. Ebrard, M.A. Fernández, J.-F. Gerbeau and F. Rossi reported in [EFG+09].

8.1 Introduction

In this work, we show how an ECG simulation tool can be used to address an industrial problem raised by a pacemaker manufacturer. A typical modern pacemaker with implantable defibrillator can provide the measurements of the electrical potential in several points of the heart. Instead of these raw data, the pacemaker manufacturer would like to provide the clinician with something more familiar, namely, an standard electrocardiogram. Of course, given the small number of measurements in the heart, this "pseudo-ECG" is not expected to be very accurate. The idea is rather to get a rough instantaneous ECG, just by remotely questioning the pacemaker, without setting up all the leads needed to get a real standard ECG. Of course, this cannot replace a genuine ECG but since the data are available for free, one can find it interesting to use them for a simple routine clinical examination.

To formalize a little bit the problem at hand, we denote by $x(t) \in \mathbb{R}^{m_P}$ the vector representing the intracardiac potential measured by the pacemaker in m_p points in the heart at time t. A typical value for m_P is five. Quantity $x(t)$ will be called an electrogram (EGM). We denote by $y(t)$ a lead of a standard ECG, for example the first lead, known as DI, which is the difference of potential between the left and the right arms. The data $(x(t), y(t))$ define a *training set*. With the training set, we try to build a function f such

that $y \approx f(x)$ (as a matter of fact the argument of f will be slightly more complicated, see below). After a while, say a few months later, the same patient will probably have a different EGM $\tilde{x}(t)$. Nonetheless, computing $\tilde{y} = f(\tilde{x})$, $\tilde{y}$ is expected to give a good approximation of the first lead of the ECG. The purpose of this work is to propose a possible approach to actually build function f.

The construction of a function f that satisfies $y \approx f(x)$ on the training set is a relatively easy task. The difficulty is to build f such that is able to reconstruct a good ECG $\tilde{y}$ from an EGM $\tilde{x}$ which is not in the training set. Several methods have been developed in the machine learning community to address this kind of problem. In this work, we propose to use the so-called *kernel ridge regression* and a simple treatment of the time series defined by the EGM. We present this method in Section §8.2.

Another difficulty of the problem is that the function f has to be patient specific (for the obvious reason for example that the location of the points where the EGM is measured varies from a patient to another). The training set corresponds to a certain state of the patient and it is not easy to test the reconstruction algorithm on different situations. Another contribution of this work is to show that a numerical simulation tool can be convenient to address this issue. This simulation tool has been presented in Chapter 5. Of course, many simplifications are done to model the complex electrophysiology of the heart in a tractable way. Nevertheless, in spite of these simplification, the model has been built in order to provide realistic ECGs. It is therefore a good candidate to test the reconstruction algorithm, as shown in Section §8.3.

8.2 Metamodel

As explained in the introduction, our purpose is to build a "metamodel", denoted by f which takes in input an EGM and provides in output the first lead (for example) of a standard ECG. More precisely, the EGM is made of the measurements $(x_i)_{i=1..n} \in (\mathbb{R}^p)^n$ of the potential in m_P points $(P_k)_{k=1..p}$ of the heart at time $t_1, \ldots, t_n$. The first lead of the ECG $(y_i)_{i=1..n}$ is made of the difference of potential between two points of the torso denoted by P_L and P_R. For the sake of simplificity, we first assume that $t_1, \ldots, t_n$ correspond to *one* heart beat. Thus, for $k \in \mathbb{N}$, $0 \leq k < n$, we can define by periodicity $x_{n+k} = x_k$. and $x_{-k} = x_{n-k}$.

The model presented in the previous section will be used to train and test the metamodel f. With the above notations, we have:

$$x_i = (u_{\mathrm{e}}(t_i, P_j))_{j=1..m_P} \in \mathbb{R}^{m_P},$$

and

$$y_i = u_{\mathrm{T}}(t_i, P_L) - u_{\mathrm{T}}(t_i, P_R) \in \mathbb{R}.$$

8.2.1 Temporal dynamics

Searching a function f such that $y_i \approx f(x_i)$ would assume the relationship between the torso potential and the extracellular potential in the myocardium be static, which is

obviously not the case. To take into account in a simple way the time dynamics of the problem, we define a temporal window of length m_T and we build the metamodel f such that $y_i \approx f(\mathbf{x}_i)$, with

$$\mathbf{x}_i = (x_i, \ldots, x_{i+m_T-1}) \in \mathbb{R}^{m_P \times m_T}. \tag{8.2.1}$$

In the sequel, the product $m_P \times m_T$, which is the dimension in the data space, will be denoted by m.

When several heart beats are used to train the algorithm, we first build the vectors $\mathbf{x}_i$ according to (8.2.1) for each heart beat and we put together all the $\mathbf{x}_i$ in the training set.

8.2.2 Kernel ridge regression

The proposed method is known as *kernel ridge regression* (see *e.g.* [HTF01]). It has some similarities with a *Support Vector Machine* (see *e.g.* [SS01]) except that the solution depends on all the training examples and not only on a subset (the support vectors). This typically makes the kernel ridge regression more expensive but less difficult to train than SVM.

Function f is looked for in a Hilbert space $(\mathcal{H}, \langle\cdot,\cdot\rangle_{\mathcal{H}})$, using a least square method with a regularization term ensuring that the norm $\|f\|_{\mathcal{H}} = \langle f, f\rangle_{\mathcal{H}}^{\frac{1}{2}}$ remains "small". We choose the space $\mathcal{H}$ as the *Reproducing Kernel Hilbert Space* (RKHS) based on a Gaussian kernel

$$K(\mathbf{x}, \mathbf{y}) = e^{-\dfrac{|\mathbf{x}-\mathbf{y}|^2}{2\sigma^2}}, \quad \forall \mathbf{x}, \mathbf{y} \in \mathbb{R}^m.$$

The kernel is said to be reproducing on $\mathcal{H}$ because of the following property:

$$f(\mathbf{x}) = \langle f(\cdot), K(\cdot, \mathbf{x})\rangle_{\mathcal{H}}, \quad f \in \mathcal{H}, \quad \forall \mathbf{x} \in \mathbb{R}^m, \tag{8.2.2}$$

where $\langle\cdot,\cdot\rangle_{\mathcal{H}}$ the scalar product in $\mathcal{H}$.

Consider in $\mathcal{H}$ the following regularized least square problem: given a training set $\{(\mathbf{x}_i, y_i)\}_{i=1}^n \in (\mathbb{R}^m \times \mathbb{R})^n$, solve

$$\min_{f \in \mathcal{H}} \left\{ \frac{1}{n} \sum_{i=1}^{n} (f(\mathbf{x}_i) - y_i)^2 + \lambda \|f\|_{\mathcal{H}}^2 \right\}, \tag{8.2.3}$$

where $\lambda > 0$ is a given regularization coefficient. The representer theorem ([SS01]) states that the solution to (8.2.3) can be written as:

$$\sum_{i=1}^{n} \alpha_i K(\cdot, \mathbf{x}_i),$$

where $\alpha = (\alpha_i)_{i=1\ldots n} \in \mathbb{R}^n$ is the new unknown. Defining the Gram matrix $\mathrm{K} = (K_{ij})_{i,j=1\ldots n}$ with $K_{ij} = K(\mathbf{x}_i, \mathbf{x}_j)$, the training problem (8.2.3) is equivalent to solving:

$$\min_{\alpha \in \mathbb{R}^n} \left\{ \frac{1}{n} (\mathrm{K}\alpha - y)^T (\mathrm{K}\alpha - y) + \lambda \alpha^T \mathrm{K} \alpha \right\},$$

whose solution is simply given by

$$\alpha = (\mathrm{K} + \lambda n \mathrm{I})^{-1} y. \tag{8.2.4}$$

Remark 8.2.2.1. *If the eight independent leads of the standard ECG are to be reconstructed, one should solve eight least square problems of this kind, with different right-hand sides but with the same matrix. In other words, the training phase of the algorithm consists in solving:*

$$\mathrm{A} = (\mathrm{K} + \lambda n \mathrm{I})^{-1} \mathrm{Y},$$

with $\mathrm{A} \in \mathbb{R}^{n \times 8}$ *and* $\mathrm{Y} \in \mathbb{R}^{n \times 8}$*. Each column of A and Y corresponding, respectively to the coefficient* α *and to the values of a given lead of the ECG.*$\diamondsuit$

Once the training phase is completed, the reconstruction of an ECG from a given one beat EGM $(\tilde{x}_i)_{i=1..\tilde{n}} \in (\mathbb{R}^{m_P})^{\tilde{n}}$ is obtained, according to (8.2.2), by

$$\widetilde{\mathrm{Y}} = \widetilde{\mathrm{K}}\mathrm{A},$$

with $\widetilde{\mathrm{K}}_{ij} = K(\tilde{\mathbf{x}}_i, \mathbf{x}_j)$, $i = 1 \ldots \tilde{n}$, $j = 1 \ldots n$, where the $\tilde{\mathbf{x}}_i$ are defined from the $\tilde{x}_i$ as explained in (8.2.1).

8.2.3 Parameters optimization

The proposed algorithm depends on a relatively small number of parameters: the regularization coefficient λ, the width of the Gaussian kernel σ and the size of the temporal window m_T. Assuming that m_T is fixed, we determine parameters λ and σ with a *leave-one-out* procedure: we train the metamodel with all the examples but one and we assess its performance on the example which has been removed from the training set. In other words, we use of cross validation with a singleton as testing set. We repeat the procedure with all the singletons of the training set. The brute force leave-one-out may be extremely expensive. Fortunately, there exists formulae ([OW00]) to compute the leave-one-out mean-squared error using the results of a single training on the whole training set. This is one of the interesting features of the kernel ridge regression.

8.3 Numerical results

8.3.1 Synthetic Data

We use the mathematical model presented in Section §5 to generate "synthetic" data. We consider the extracellular potential in $m_P = 5$ arbitrary points of the heart and the DI lead of the corresponding "computational ECG". The versatility of the numerical model allows to test the reconstruction algorithm in various situations more easily than with clinical data. All the examples of this section are obtained with the following parameters: $\sigma = 150$, $\lambda = 10^{-4}$, $m_T = 6$ (σ and λ are obtained by the leave-one-out procedure described in 8.2.3).

We focus on a pathological case called right bundle branch block (RBBB). Starting from the healthy situation represented in Figure 5.8, we simulate a RBBB by artificially

delaying the activation of the right ventricle. For example, a delay of 10 ms will be denoted by RBBB-10. A larger delay of course corresponds to a solution which is farther from the healthy solution.

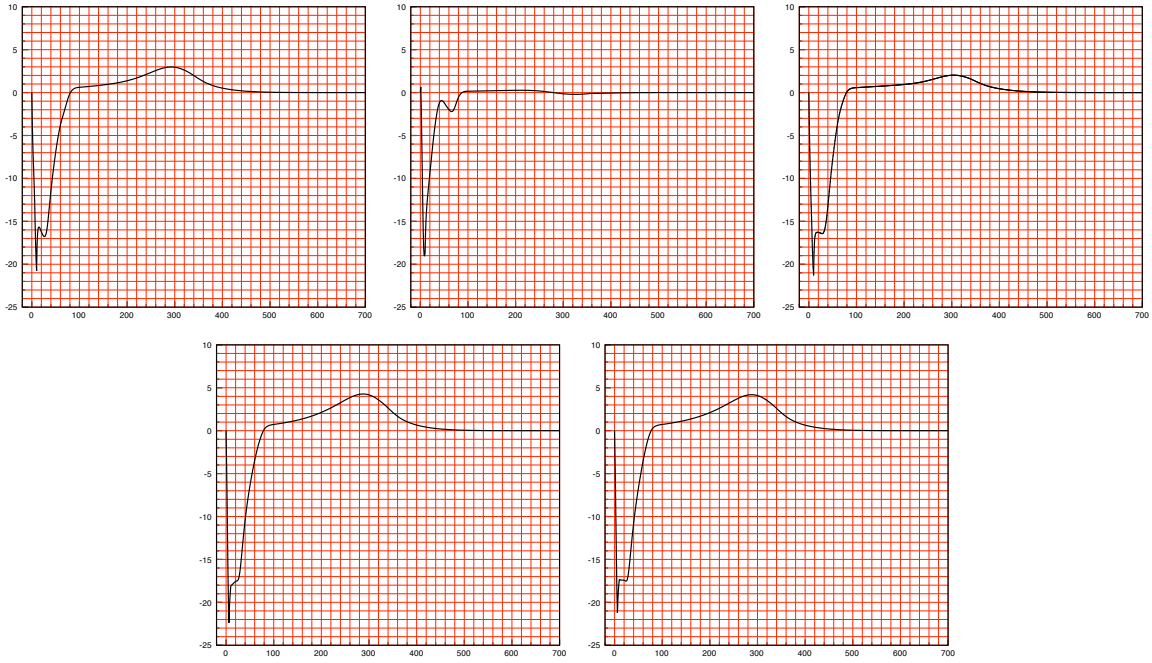

Figure 8.1: An example of a computational EGM obtained with the model of Section §5: distal RV, distal LV, proximal RV, distal coil, proximal coil (from left to right and top to bottom).

First suppose the test case is a part of the training set. In that case, the reconstruction of the ECG is, as expected, very good. In Figure 8.2, we see that increasing the size of the training set do not deteriorate significantly the result.

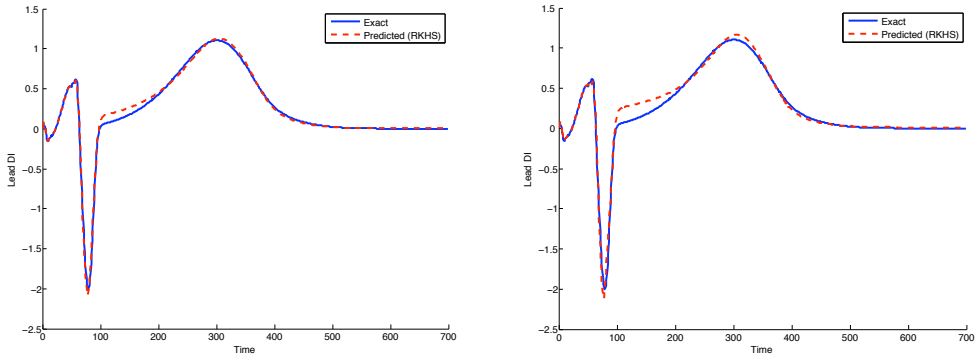

Figure 8.2: Reconstruction of a RBBB-50 when the training set is RBBB-{10, 50, 100, 200} (left) and RBBB-{10, 50, 100, 200, 400, 700} (right).

Next consider a test case which does not belong to the training set. In practice, this corresponds for example to the following situation: the patient has a slight right bundle branch block when the algorithm is trained, but when he comes back a few months later, the pathology is getting worse. Figure 8.3 (left) shows what happens if we train

the algorithm with a RBBB-10, and if we try to reconstruct the ECG corresponding to a RBBB-50. We can see that the result is poor. Since we get good results with larger

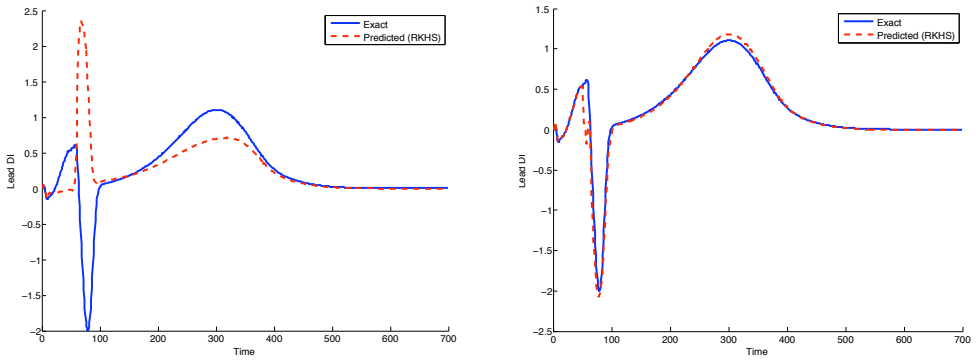

Figure 8.3: Left: Reconstruction of a RBBB-50 with training from RBBB-10. Right: Reconstruction of a RBBB-50 when the training set is RBBB-{10,40,60} (right)

training sets, a natural idea to improve the result is to enrich the training set so that the new situation be close to a training case. For the sake of illustration, suppose a patient has a RBBB-10 and suppose the numerical model can be parametrized to reproduce the patient's ECG. With the simulation tool, we can investigate possible situations the patient may encounter in the future. For example, assume we compute a RBBB-40 and a RBBB-60. Thus we build a training set made of RBBB-{10,40,60}. We show in Figure 8.3 (right) that the prediction obtained if the patient has a RBBB-50 is then much better.

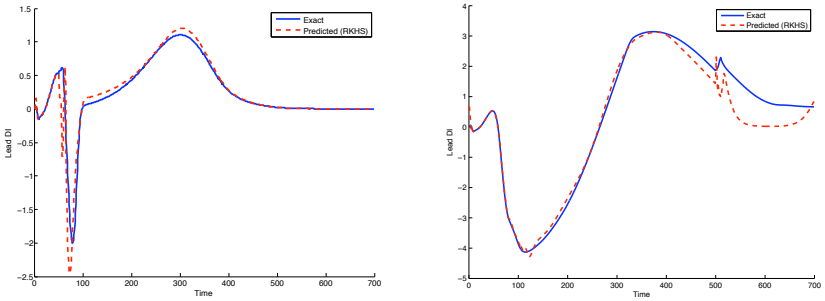

Figure 8.4: Reconstruction of a RBBB-50 (left) and a RBBB-500 (right) when the training set is RBBB-{10, 20, 40, 60, 70, 80, 100, 150, 200, 300, 400, 700}.

In Figure 8.4 (Left), we show the result obtained with a much larger training set {RBBB-10, 20, 40, 60, 70, 80, 90, 100, 120, 150, 200, 300, 400, 700}. In that case the result for a RBBB-50 is slightly less accurate than with the training set of only 3 cases, but the resulting metamodel is more robust and can be used in a wide range of situations. This is illustrated in Figure 8.4 (right), where we report the reconstruction of a RBBB-500 with the same training set.

8.3.2 Clinical Data

In this paragraph we use the RKHS tool to reconstruct ECGs for a clinical EGM data. The training is done on a clinical data base. In figure 8.5 (left) we reconstruct the ECG

of a myocardial ischemia disease patient ("patient 1") from a learning on a Tachycardia heart disease patient ("patient 2"). As expected the reconstruction is worst. Now, if add the data of "patient 1" to the training set, the reconstruction becomes very good, see figure 8.5 (right). Again, if we add more cases, for example an atrial fibrillation disease ("patient 3") and a LBBB disease ("patient 4") in the traning data set, the reconstruction of the ECG remains acceptable, see figure 8.6 (left). This confirms on a the clinical data the results obtained using numerical simulation.

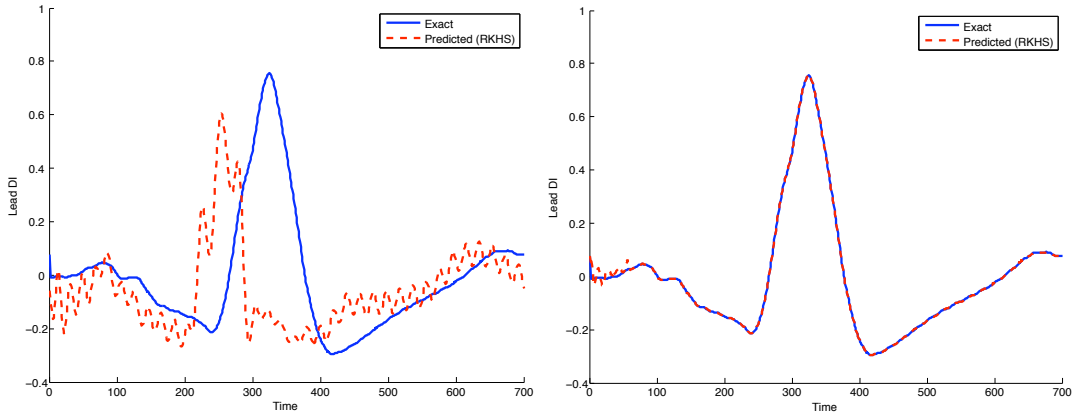

Figure 8.5: Reconstruction of "patient 1" ECG when the training set is recorded from: "patient 2" (left) and "patient 1" & "patient 2" (right).

In figure 8.6 (right), we learn on a data base recorded from "patient 1" and we try to reconstruct the ECG of the same patient but, for another EGM recordings. The reconstruction of two heart beats is acceptable. But this suppose that the disease of the patient does not deeply progress.

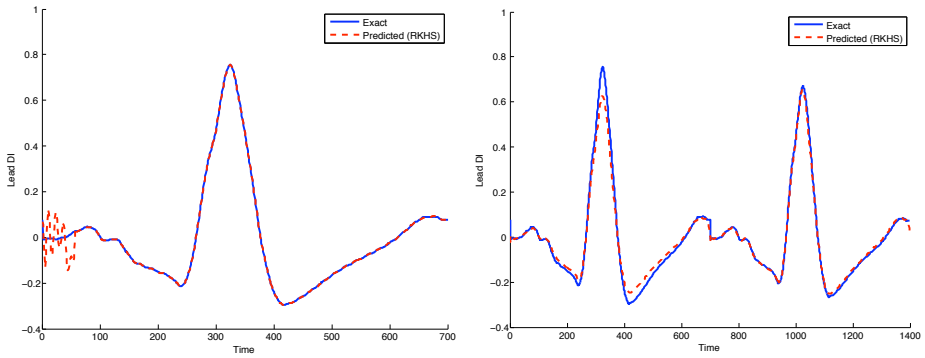

Figure 8.6: Left: Reconstruction of "patient 1" ECG when the training set is recorded from "patient 1", "patient 2", "patient 3" and "patient 4". Right: Reconstruction of "patient 1" ECG during two heart beats when the training set is recorded from the same patient during an other time period (right).

8.3.3 Limits of the method

One of the difficulties of the used approch is that we cannot do a train on data set containing more than 12 EGM and ECG measurements, using a 2 Go memory computer

machine. That is due to matrices size which is about $(700 \times 6 \times n)^2$, where n is the number of EGM and ECG measurements. An other problem when using the squential method is that we are not able to reconstruct with a very good accuracy the ECG of a data that is in the trainning set. To deal with these problems we propose, in the following section, an other approach.

8.4 RKHS Global in time

In this section we present an other approach to compute the ECG from an EGM data. The main idea is to consider all the EGM (all the leads in time) as a pattern (an element of the EGM space), not sequentially like what we have previously presented. Using the same tool -RKHS method-, the difference from the approach used in the previous paragraph is the definition the EGM and ECG spaces and the application which maps the EGM into the ECG space. In the following paragraphs we explain this method and compare the numerical results with the sequential method.

8.4.1 Data training choice

In this paragraph we present two different strategies to redefine the data training space. We recall that the first method (sequential method) considers the EGM leads values at a given time t_n as an element of the source space ($\mathbb{R}^5$) and the values of the ECG leads at time t_n as an element of the target space ($\mathbb{R}^8$). The second method that we produce called "global in time" considers all the EGM (respectively the ECG) during a heart beat cycle as an element of the EGM (respectively the ECG) training set. The third method "global in time windows" considers a time window of the EGM (respectively the ECG) as an element of the EGM (respectively the ECG) training set. Generally the time window is less than a heart beat cycle .

Second method (global in time):

Suppose that $\tilde{\mathbf{x}} \in \mathbb{R}^{700\times5}$ is the given element of the EGM data set and $\tilde{\mathbf{y}} \in \mathbb{R}^{700\times8}$ is the corresponding ECG that we want to construct. This suppose that the training data set consists of couples of EGM cycles and their corresponding ECG cycles. Therefore, we have a training set $\{(\mathbf{x}_i, \mathbf{y}_i)\}_{i=1}^n \subset (\mathbb{R}^{700\times5} \times \mathbb{R}^{700\times8})$, where n is the number of training measurements. Using the RKHS method (like for the first method) but with different source and target spaces, the algorithm we will use to reconstruct $\tilde{\mathbf{y}}$ is as follows: First we compute the Gram matrix K, we use the l^1 norm in the EGM space ($\mathbb{R}^{700\times5}$). Hence, the Gram matrix coefficients measure the surfaces between two EGM plots $K_{i,j} = K(\mathbf{x}_i, \mathbf{x}_j) = e^{-\frac{\| \mathbf{x}_i - \mathbf{x}_j \|_{l^1}}{2\sigma}}$, for $i, j = 1 \dots n$. The size of K is $n \times n$. Second, we compute the matrix $\mathrm{A} \in \mathbb{R}^{n\times(700\times8)}$, by solving the following equation $\mathrm{A} = (\mathrm{K} + \lambda n \mathrm{I})^{-1}\mathrm{Y}$, where $\mathrm{Y} \in \mathbb{R}^{\mathrm{n}\times(700\times8)}$ is the matrix containing all the eight ECG's leads in each of its rows. Third we compute $\widetilde{\mathrm{K}} \in \mathbb{R}^{1\times n}$ such that $\widetilde{\mathrm{K}}_j = K(\tilde{\mathbf{x}}, \mathbf{x}_j)$, $j = 1 \dots n$. We finally, construct the ECG $\tilde{\mathbf{y}} = \widetilde{\mathrm{K}}\mathrm{A}$.

Third method (global in time windows):

An other approach could be considered by decomposing $\tilde{\mathbf{x}} = (\tilde{\mathbf{x}}_1, \tilde{\mathbf{x}}_2, ..., \tilde{\mathbf{x}}_p, \tilde{\mathbf{x}}_{p+1})$, where $\tilde{\mathbf{x}}_i \in \mathbb{R}^{W\times 5}$ for $i = 1, ..., p$, $\tilde{\mathbf{x}}_{p+1} \in \mathbb{R}^{r\times 5}$, $W \in \mathbb{N}$ is the length of a time window where $W \times p + r = 700$ and $r \in \mathbb{N}$ is the length of the last time window and satisfies $1 \leq r \leq p$. The ECG data is decomposed by the same way: $\tilde{\mathbf{y}} = (\tilde{\mathbf{y}}_1, \tilde{\mathbf{y}}_2, ..., \tilde{\mathbf{y}}_p, , \tilde{\mathbf{y}}_{p+1})$, where $\tilde{\mathbf{y}}_i \in \mathbb{R}^{W\times 8}$ for $i = 1, ..., p$ and $\tilde{\mathbf{y}}_{p+1} \in \mathbb{R}^{r\times 8}$. The application f we construct is $f = (f_1, f_2, ..., f_p, f_{p+1})$, for each EGM $\tilde{\mathbf{x}} \in \mathbb{R}^{700\times 5}$ we have $f(\tilde{\mathbf{x}}) = (f_1(\tilde{\mathbf{x}}_1), f_2(\tilde{\mathbf{x}}_2), ..., f_p(\tilde{\mathbf{x}}_p)) = \tilde{\mathbf{y}}$. Each of the functions f_i, $i = 1, ..., p$ (respectively f_{p+1}) is constructed using the algorithm of the second method in a training set included in $(\mathbb{R}^{W\times 5} \times \mathbb{R}^{W\times 8})^n$ (respectively $(\mathbb{R}^{r\times 5} \times \mathbb{R}^{r\times 8})^n$).

Remark 8.4.1.1. *One can see that by taking $W = 700$, the third and the second method are the same. The goal of introducing the third method is to find an optimal time window W_{opt} allowing to obtain an optimal error when using leave-one-out procedure (see Section 8.2.3).*

8.4.2 Results

In this paragraph we perform some tests allowing to compare the results obtained using the RKHS Global in time approach and those obtained using the sequential method.

First test:

In figure 8.7 we plot the first lead of an RBBB-50 ECG when training on RBBB-(10, 50, 100, 200, 400, 700) using the three methods: Sequential (left), global in time (middle) and global in time windows (right). The model parameters of the second method σ and λ are performed using the leave-one-out procedure, we use a global optimisation algorithm ([IHR07]) to minimize the error, we obtain for this test $\sigma = 20$ and $\lambda = 4.36 \times 10^{-5}$. For the third method we have three parameters σ, λ and W_{opt}. Using the same procedure (leave-one-out) we obtain $\sigma = 187$ $\lambda = 4.25 \times 10^{-4}$ and $W_{\text{opt}} = 474$. In Tab. 8.1, we present the reconstruction error by computing the difference between the simulated and the reconstructed ECGs using different norms. First, we remark that we have a better accuracy when we use the second and the third methods see Tab.8.1. While, with the sequential method (Fig. 8.7 left), one can see that the S-T segment reconstruction is slightly deteriorated. Second, the computation time (C.T) when using the second and third methods is clearly smaller than it is for the sequential method (see Tab. 8.1 last column).

Second test:

In this paragraph we want to test the robustness of the global (in time) RKHS methods reconstructing an ECG which is not in the training data set. We try to reconstruct a RBBB-90 where the data training is RBBB-(10, 20, 40, 60, 70, 80, 100, 150, 200, 400, 700). In figure 8.8, we present the results (global in time left, global in time windows middle and sequential right). We remark that the reconstruction with the

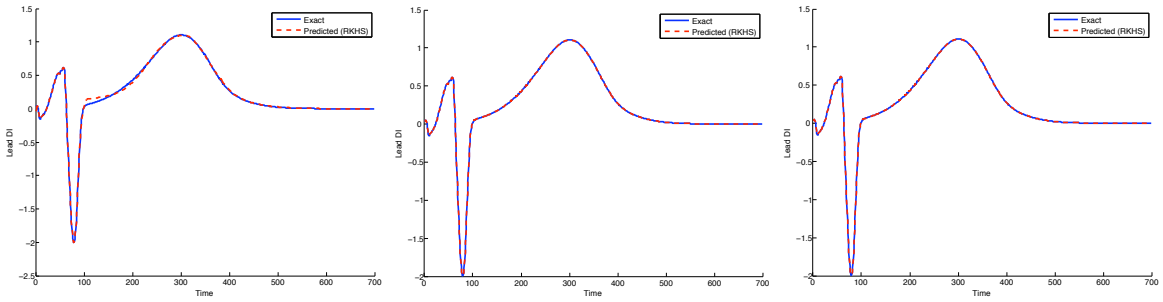

Figure 8.7: Reconstruction of a RBBB-50 when the training set is RBBB-{10, 50, 100, 200, 400, 700}. Comparison of the three methods: Sequential (left), global in time (middle) and global in time windows (right).

Method \ Norm	l^1	l^1 relative	l^2	l^2 relative	C.T
Sequential	7.16×10^{-3}	2.94×10^{-2}	5.09×10^{-4}	3.53×10^{-2}	104
Global in time	2.63×10^{-5}	1.08×10^{-7}	1.86×10^{-9}	1.29×10^{-7}	2
Global in time windows	1.31×10^{-6}	5.4×10^{-9}	6.7×10^{-11}	4.6×10^{-9}	1.1

Table 8.1: Comparison of the accuracy and the computational cost for the three methods when reconstructing a RBBB-50 and training on a data set of RBBB-{10, 50, 100, 200, 400, 700}

second method (Global in time)is worst. The best results are given by the third method (Global in time windows). In fact the accuracy of the result obtained with this method is slightly better than it is for the sequential method (see Tab.8.2). But if we compare the computational cost, one can see that we have better computing time when using the global in time windows method (see Tab.8.2). The parameter obtained after a leave-one-out optimization are ($\sigma =$ and $\lambda = \sigma = 220$, $\lambda = 1.3 \times 10^{-3}$ and $W_{\text{opt}} = 484$ for the global in time windows method) (see Tab.8.2) .

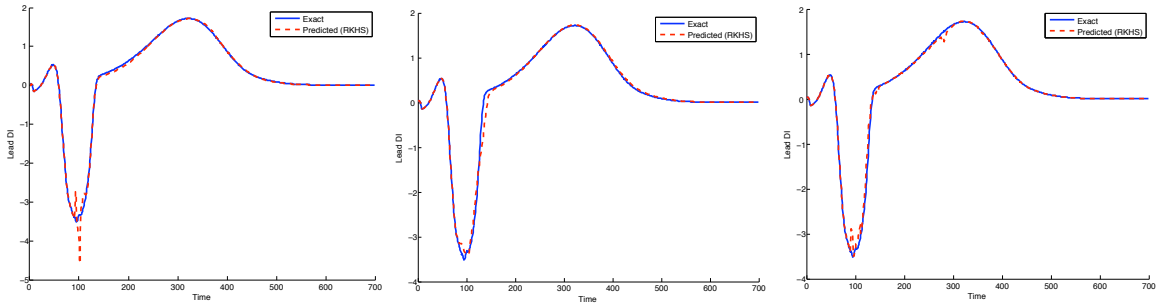

Figure 8.8: Reconstruction of a RBBB-90 when the training set is RBBB-{10, 20, 40, 60, 70, 80, 100, 150, 200, 400, 700 }. Comparison of the three methods: Sequential (left), global in time (middle) and global in time windows (right).

Method \ Norm	l^1	l^1 relative	l^2	l^2 relative	C.T
Sequential	1.87×10^{-2}	3.6×10^{-2}	2.48×10^{-3}	8.3×10^{-2}	560
Global in time	2.38×10^{-2}	4.62×10^{-2}	2.5×10^{-3}	8.4×10^{-2}	2.8
Global in time windows	1.75×10^{-2}	3.38×10^{-2}	2.08×10^{-3}	6.91×10^{-2}	2.46

Table 8.2: Comparison of the accuracy and the computational cost for the three methods when reconstructing a RBBB-90 and training on a data set of RBBB-{10, 20, 40, 60, 70, 80, 100, 150, 200, 400, 700 }

Third test:

To obtain a better comparison of the robustness of the three methods, we propose to test its predictions: Suppose that we have a data base of EGM and ECG measurements for a RBBB patient. These measurements were taken during the evolution of her pathology. Now suppose that the patient is at home and that we can access to his EGM, which is measured by a pacemaker. If his situation is stable, this means that his EGM is not so far from the training data set and we have seen we can predict his ECG with a very good accuracy. The problem is when the pathology evolves rapidly, we can imagine for example that the measurements we have are for RBBB-{10, 20, 40, 50, 60, 70, 80, 100,120, 150 } and that his situation has worsened to an RBBB-200. The question is: Are we able to predict the patient's ECG? And which method gives the better prediction?

In figure 8.9 we plot the first lead of the ECG predicted by the three models. We can remark that the reconstruction given by the third method is the better one but it is not not satisfactory, since the relative error is high (see table 8.3). This could be explained by the fact that the information that we have in the training data set is poor. If one hope to obtain better results the idea is to enrich the training data set.

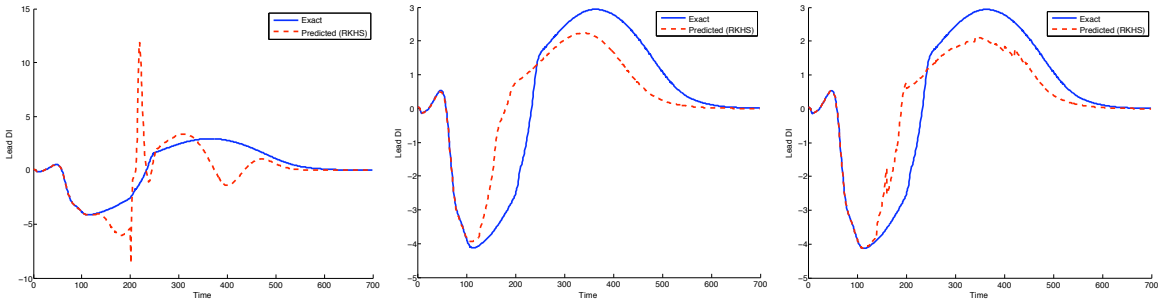

Figure 8.9: Reconstruction of a RBBB-200 when the training set is RBBB-{10, 20, 40, 50, 60, 70, 80, 100,120, 150}. Comparison of the prediction of each of the three methods: Sequential (left), global in time (middle) and global in time windows (right).

Fourth test:

In this paragraph we test the three methods on larger training sets. We remark that for a training set containing more than 12 measurements there is a memory problem when

Method \ Norm	l^1	l^1 relative	l^2	l^2 relative	C.T
Sequential	7.33×10^{-1}	4.28×10^{-1}	5.28×10^{-2}	9.34×10^{-1}	407
Global in time	5.02×10^{-1}	4.28×10^{-1}	2.93×10^{-2}	5.19×10^{-1}	2.4
Global in time windows	4.14×10^{-1}	3.4×10^{-1}	2.34×10^{-2}	4.1×10^{-1}	6.36

Table 8.3: Comparison of the accuracy and the computational cost for the three methods when reconstructing a RBBB-200 and training on a data set of RBBB-{10, 20, 40, 50, 60, 70, 80, 100,120, 150}

we use the sequential method. As explained before, that is due to the matrices size. For the two other methods, we have not this problem because for each of time window the Gram matrix is $n \times n$, where n is the number of data measurements in the training set. In figure 8.10 we try to reconstruct a RBBB-600 when training on RBBB-{ 10, 20, 30, 40, 50, 60, 70, 80, 90, 100, 120, 150, 180, 200, 250, 300, 350, 400, 450, 500}, using the global in time method and the global in time windows method. We obtain a better accuracy when using the third method (see Tab.8.4).

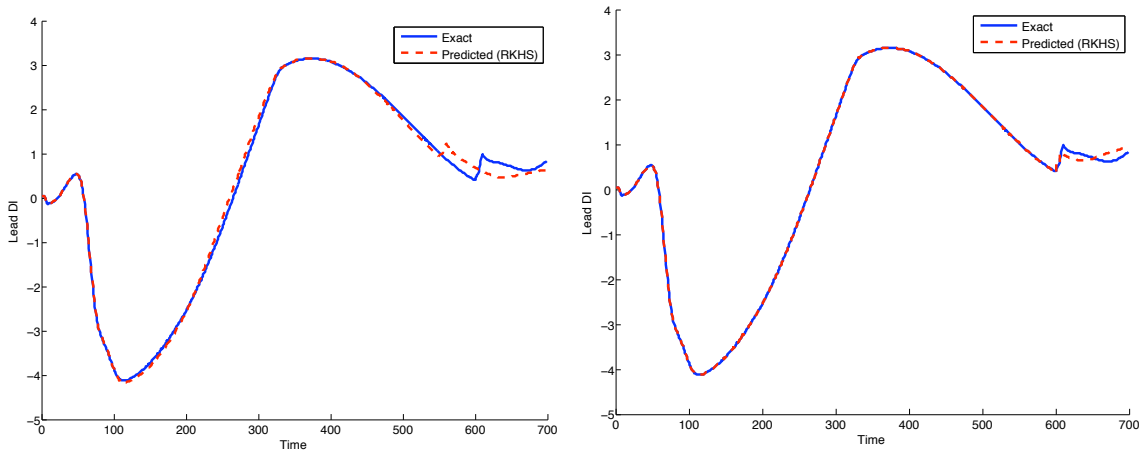

Figure 8.10: Reconstruction of a RBBB-600 when the training set is RBBB-{10, 20, 30, 40, 50, 60, 70, 80, 90, 100, 120, 150, 180, 200, 250, 300, 350, 400, 450, 500}. Comparison of the prediction of the Global in time method (left), global in time windows method (right).

Method \ Norm	l^1	l^1 relative	l^2	l^2 relative	C.T
Global in time	6.52×10^{-2}	4.97×10^{-2}	3.56×10^{-3}	6.02×10^{-2}	3.24
Global in time windows	1.37×10^{-2}	1.04×10^{-2}	1.43×10^{-3}	2.4×10^{-2}	3.72

Table 8.4: Comparison of the accuracy and the computational cost for the three methods when reconstructing a RBBB-200 and training on a data set of RBBB-{10, 20, 40, 50, 60, 70, 80, 100,120, 150, 180, 200, 250, 300, 350, 400, 450, 500}

Fifth test:

In this example we reconstruct a clinical 50 heart beats electrocardiogram of an arrhythmia patient. For this patient the arrhythmia is due to a very frequent ventricular extrasystole. The training is done on a base containing 10 heart beats of EGMs and ECGs taken from the same patient. In Fig. 8.11 we plot the first lead of the ECG during the 50 heart beats. On can see that reconstruction of the ten first heart beats is perfect. For the remaining 40 heart beats the reconstruction is barely destroyed. But it is easy to a medical doctor to recognize the pathology, specially for the arrhythmic beats. Even if the reconstruction of some beats is bad (the 37^{th} beat for example in Fig. 8.11)[1], the fact that the ECG pattern is different can give an idea about the new situation of the patient. For example, the sixth and the seventh heart beats in Fig. 8.11 (bottom) are not well reconstructed but the fact that the ECG in these two heart beats are different from the others could tell us the presence of an arrhythmia.

8.4.3 Discussion

According to the tests performed above, one could say that the third approach "global in time windows" is the best between the three proposed approaches. It is able to reconstruct ECGs with a very good accuracy, when the training data set is sufficiently rich. However, in term of computational cost the second approach is faster. The robustness of the second and the third methods is due to its ability to learn on a large training set. If the training data set does not contain the pattern of a part of the ECG that we want to reconstruct, the reconstruction could be worst (in terms of error evaluation). But, the fact the plots of the ECG are strange compared to the measurements in the data training set could be a warning to the medical doctor and tell him that the patient situation is progressing and that he needs a diagnosis.

8.5 Conclusion

In this work we have considered a machine learning approach, based on the kernel ridge regression method, in order to provide ECG information from a set of EGM measurements. The procedure has been trained using synthetic data from numerical simulations, based on a mathematical model of the ECG involving a quite complete description of the electrical activity of the heart. Several examples showed the method is able to reconstruct conveniently the ECG information included in the training data set, and is robust when reconstructing situations close to the training data set. The examples presented below show us that the use of machine learning could be a very good tool to predict ECG from EGM measurements. We have seen that the global in time windows method is efficient in term of accuracy and computational time which means that it could be implemented in a medical instrument easy to use.

[1]The heart beats are counted from left to right and from top to bottom.

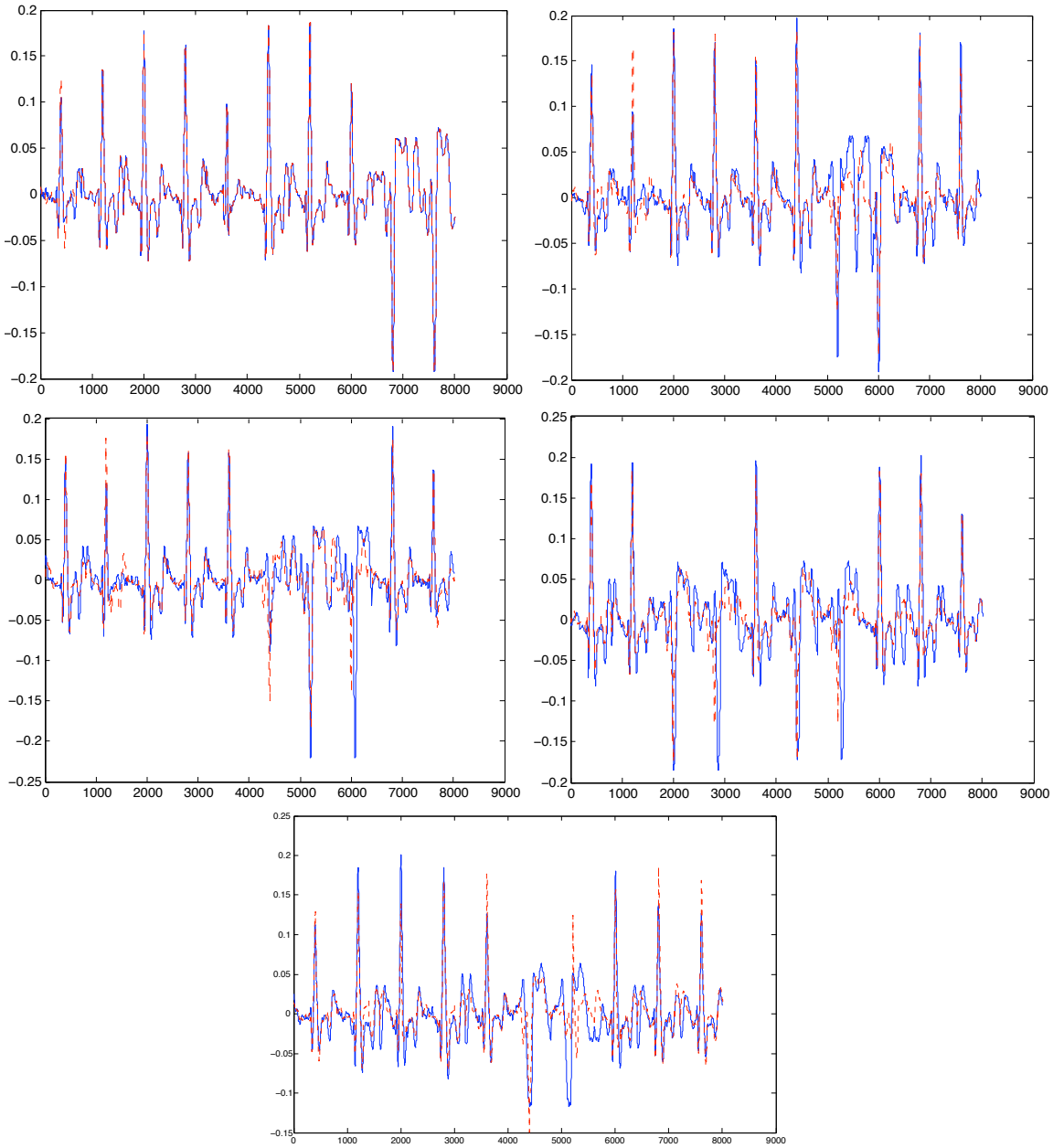

Figure 8.11: Reconstruction of 50 heart beats ECG for a "very frequent extrasystole" patient using the third method. The training was done using the ten first heart beats. From top to bottom and from left to right: The first ECG lead during the first ten heart beats, the second ten heart beats, the third ten heart beats, the fourth ten heart beats and the fifth ten heart beats. Original signal (blue continuous line) and the reconstructed signal (red dashed line)

Chapter 9

Numerical simulation of the electromechanical activity of the heart

In this chapter, we present numerical results obtained with a three-dimensional electromechanical model of the heart with a complete realistic anatomy. The mechanical model [SMCCS06, Moi08] is based on a chemically-controlled contraction law of the myofibres integrated in a 3D continuum mechanics description accounting for large displacements and strains, and the main cardiovascular blood compartments are represented by simplified lumped models. We considered a normal case and a pathological conditions, the medical indicators resulting from the simulations show physiological values, both for mechanical and electrical quantities of interest, in particular pressures, volumes and ECGs.

This chapter is part of a joint work with MACS project in INRIA Rocquencourt specialized in the cardiac mechanics. This work, coauthored with D. Chapelle, M.A. Fernández, J.-F. Gerbeau, P. Moireau and J. Sainte-Maire, is reported in [CFG$^+$09a].

9.1 Introduction

We present a complete numerical simulation of the electromechanical activity of the heart based on an integrated three-dimensional (3D) mathematical model of the cardiac electrophysiology and mechanics considered jointly. In this respect, we follow the standard approach of electromechanical modeling with "one-way coupling", namely, the electrical simulation is used as an input in the mechanical model without mechano-electrical feedback, see [KHUM06] and [LTS96] for surveys on this approach.

The major contribution of this application is to demonstrate that we are now able to obtain accurate simulations of the main electromechanical phenomena with a procedure integrating anatomical and physical models. We show that these simulations provide meaningful medical indicators, in particular pressures, volumes and ECGs, and this validation with *both mechanical and electrical indicators* is a pioneering result. This allows to investigate various pathological scenarii with predictive capabilities, namely, without any recalibration of the model parameters other than those directly affected by the pathology. Furthermore, the simulations give access to other physical quantities

which cannot be measured – such as local values of the stresses in the tissue – which can be very valuable for clinicians to better assess a pathological condition and its possible evolutions.

The chapter is organized as follows. In Section 9.2 we introduce the mathematical electromechanical model and describe the anatomical model. Section 9.3 is devoted to the numerical simulations, and we present the results obtained for both a normal and a pathological case. Some conclusions are given in Section 9.4.

9.2 An electromechanical model of the heart

In this section we summarize the electromechanical model considered in this work. We assume that the electrical activity of the heart is independent of the mechanical activity, *i.e.* we do not consider mechano-electrical feedback.

9.2.1 Mechanical model

The mechanical heart model that we consider was described in details in [SMCCS06], and here we only summarize its key ingredients for completeness. The contractile behavior relies on a chemically-controlled constitutive law of cardiac myofibre mechanics introduced in [BCS01] based on Huxley's model [Hux57]. This law dynamically relates the active stress and the strain along the sarcomere, respectively denoted by τ_c and e_c, by the following set of ordinary differential equations:

$$\begin{cases} \dot{\tau}_c = k_c \dot{e}_c - (\alpha|\dot{e}_c| + |u|)\tau_c + \sigma_0 |u|_+ & \tau_c(0) = 0 \\ \dot{k}_c = -(\alpha|\dot{e}_c| + |u|)k_c + k_0 |u|_+ & k_c(0) = 0 \end{cases} \tag{9.2.1}$$

where the parameters k_0 and σ_0 are respectively the maximum value for the active stiffness k_c and for the stress variable τ_c, while μ is a viscosity parameter. The quantity u represents the electrical input – corresponding to a normalized concentration of calcium bound on the troponin-C – with $u > 0$ during contraction and $u < 0$ during active relaxation (we use the notation $|u|_+ = \max(u, 0)$). Following [SMCCS06], we assume an affine relation between u and the transmembrane potential V_m, *i.e.* $u = \alpha V_\mathrm{m} + \beta$. This simplification is justified by the observed waveform similitudes of the transmembrane potential and the calcium concentration.

The overall tissue behavior combines this active law with passive components using a rheological model of Hill-Maxwell type [Hil38] compatible with large displacements and strains. In the parallel branch of this rheological model we considered a viscoelastic behavior, with a hyperelastic potential given by the Ciarlet-Geymonat volumic energy [Cia88, LT94]

$$W^e = \kappa_1(\tilde{I}_1 - 3) + \kappa_2(\tilde{I}_2 - 3) + K(J-1) - K \ln J,$$

where $\tilde{I}_1$, $\tilde{I}_2$ and J denote the reduced invariants of the Cauchy-Green strain tensor $\underline{\underline{C}}$. Regarding the viscous behavior of the parallel branch, we used the following dissipation pseudo-potential

$$W^v = \frac{\eta}{2} \underline{\underline{\dot{e}}} : \underline{\underline{\dot{e}}},$$

where $\underline{\underline{e}} = \frac{1}{2}(\underline{\underline{C}} - \underline{\underline{I}})$ denotes the Green-Lagrange strain tensor.

This combination of constitutive relations gives an expression of the second Piola-Kirchhoff stress tensor $\underline{\underline{S}}$. Note that the resulting behavior is *non-isotropic*, since the contraction law (9.2.1) operates in the fibre direction. We then invoke the principle of virtual work – namely the dynamical balance equation – using a total Lagrangian formulation. Denoting by Ω_{H} the reference domain corresponding to cardiac tissue, and by Γ_{endo} the left and right ventricle endocardium surfaces with outgoing unit normal vector $\underline{n}$, we have

$$\int_{\Omega_{\mathrm{H}}} \rho\, \underline{\ddot{y}} \cdot \underline{v}\, d\Omega + \int_{\Omega_{\mathrm{H}}} \underline{\underline{S}} : d_y \underline{\underline{e}}.\underline{v}\, d\Omega + \int_{\Gamma_{\mathrm{endo}}} P_{\mathrm{v}}\, \underline{n} \cdot \underline{\underline{F}}^{-1} \cdot \underline{v} J\, d\Gamma = 0, \tag{9.2.2}$$

for any test function $\underline{v}$ taken in a suitable displacement space, and with associated infinitesimal strain variation $d_y \underline{\underline{e}}.\underline{v}$. In this expression, ρ denotes volumic mass in the inertia term, and $\underline{\underline{F}}$ the deformation gradient. The quantity P_{v} represents the blood pressure inside the ventricles, itself directly related to the pressures in the arterial compartments, which we represented by adequate Windkessel models, see *e.g.* [Mac74, SMCCS06].

9.2.2 Anatomical model and computational meshes

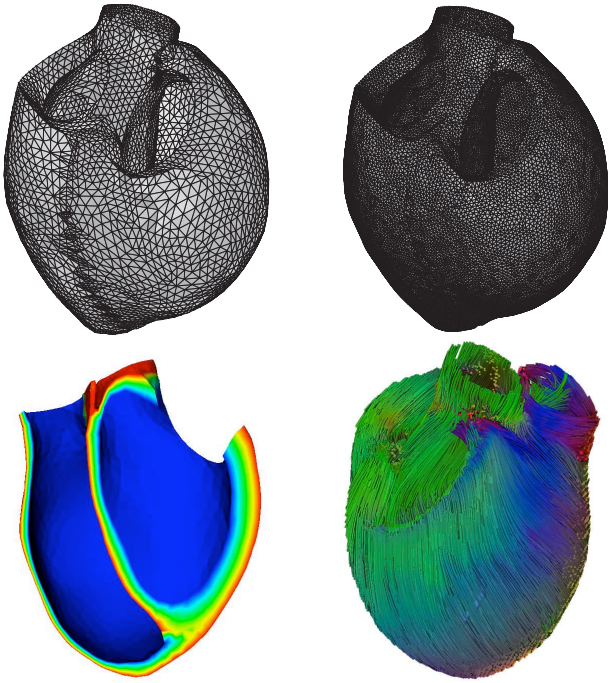

Figure 9.1: Computational heart meshes for mechanical (top left, about 20,000 nodes) and electrical (top right, about 110,000 nodes) simulations - Distance map (bottom left) - Fibre directions (bottom right)

The computational meshes were produced starting from the Zygote[1] heart model – a geometric model based on actual anatomical data – using the `3-matic`[2] software to obtain computationally-correct surface meshes, and the `Yams` [Fre01] and `GHS3D` [GHS90]

[1] `www.3dscience.com`

[2] `www.materialise.com`

meshing softwares to further process the surface meshes and generate the 3D final computational meshes, respectively. These computational meshes are displayed in Figures 9.1-9.2 and the heart meshes correspond to the diastolic stage immediately before atrial contraction, as this is assumed to provide a stress-free reference configuration. Note that the electrophysiological simulations require a finer mesh to adequately represent the propagative behavior of the depolarization and repolarization waves, hence we computed an interpolation operator to use the electrical simulations as a prescribed input at the nodes of the coarser mechanical mesh.

As regards fibre directions, since they are not provided in the original anatomical model we used an *automatic* procedure to prescribe them in the meshes. We first computed a 3D distance map [BA05] from any point in the tissue to the epicardium and endocardium, see Figure 9.1. This distance was then employed to prescribe fibres with elevation angles (with respect to the circumferential direction given by the cross product of the distance gradient and the long axis) varying linearly across the wall thickness from -65 to +65 degrees from epicardium to endocardium. We applied an additional smoothing and interpolation procedure to take into account some specific physiological direction prescriptions on the boundary resulting from tissue truncation and around the valves [SFWD99], see the final fibre directions visualized with `MedINRIA`[3] in Figure 9.1.

The distance map was also used to prescribe left-ventricle transmural action potential duration (APD) heterogeneity within the ionic model, which allows to obtain a correct T-wave orientation in the ECG, see chapter 5.

9.3 Numerical experiments

The variational formulations of the electrical and mechanical problems are both discretized in space using $\mathbb{P}_1$ Lagrangian finite elements, (see *e.g.* chapter 5 or [BFGZ07, BCF$^+$09, SMCCS06]). For the time discretization, a Newmark scheme is used for the solid part and a semi-implicit second order Backward Differentiation Formula (BDF) scheme for the electrical part.

In the next paragraphs we present the results of the electromechanical simulations performed in a normal and a pathological situation. For the meshes considered, each mechanical simulation takes about one hour on a standard PC for a complete heartbeat. As regards the electrical simulation, about four hours of computations are required on a recent workstation. In each case a convergence study with respect to the meshes was performed, see [CFG$^+$09a] for details.

9.3.1 A healthy case

In Figure 9.3 we display the simulated 12-leads ECG obtained with the electrical model in the healthy case. We can observe that the QRS-complex has a physiological orientation, duration (70 ms) and amplitude, in each of the 12 leads. We deduce that the heart axis lies around 6.5 degrees, which is also within the normal range (between 0 and 90

[3] `www-sop.inria.fr/asclepios/software/MedINRIA/`

degrees). Note that – since our anatomical model does not include the atria (Section 9.2.2) – the P-waves are missing.

This electrical simulation was used to simulate the mechanical phenomena over a complete heart beat. The resulting indicators – pressures and volumes in the various compartments – are displayed in Figure 9.4, in solid lines. The main quantitative indicators – in particular ejected fractions and maximum ventricular pressures – have physiological values.

9.3.2 Convergence analysis

Considering the healthy case, a convergence analysis was performed using sequences of increasingly refined meshes – both for electrical and mechanical simulations – in order to determine the adequate discretization for each type of simulation.

For the electrical simulations, we consider a 220,000 vertices mesh (1,150,000 tetrahedra) as reference. We compute the relative error of the electrical indicator (ECG) in L^2 norm between the reference solution and three different mesh refinement levels of the heart meshes, see Table 9.1. For the ECG computation we did not solve the toro problem for each of the heart meshes because we did not create a torso mesh for each one. A transfer matrix (see section 5.5.1, chapter 5) is computed for a reference mesh (ECG-meh) and the ECGs are computed by a matrix vector product. For each of the heart meshes the solution was interpolated on the ECG- mesh. In Figure 9.7, we plot the first lead of the ECGs obtained for these simulations. The convergence is observed for the sequence of meshes in ECG. To keep the ECG relative error under 10% we need the third mesh (see Table.9.1, last column).

Meshes	Heart nodes	Total number of heart tetrahedra	ECG L^2 relative error
mesh 1	60 000	280 000	0.2851
mesh 2	110 000	540 000	0.1808
mesh 3	170 000	860 000	0.0925

Table 9.1: Number of heart and torso nodes and tetrahedra for three different meshes (approximate values) and L^2 corresponding ECG relative error.

Even if the whole solution has not fully converged in the heart, we can see that the output of interest (namely the ECG) is almost unaffected by the last refinement. Therefore, in a goal-oriented refinement procedure, the solution could indeed be considered as converged.

Regarding the mechanical simulations, we used a mesh of about 32,000 vertices as a reference and computed displacement errors in the L^2 and L^∞ norms as a function of time, see Figure 9.8. This shows that it requires a mesh of about 20,000 vertices to keep the error below 10% in the L^2-norm (and around 15% in the L^∞-norm). Hence this is the mesh we used in the simulations presented for the various case studies. We also display in Figure 9.9 the convergence observed for the sequence of meshes in the medical indicators. We observe that the error obtained for the mesh of 20,000 vertices

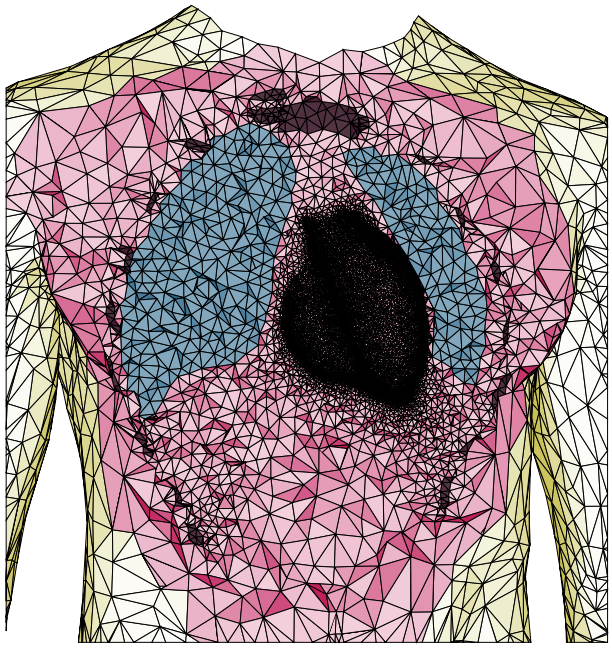

Figure 9.2: Computational heart-torso mesh (cross-section) for ECG simulations

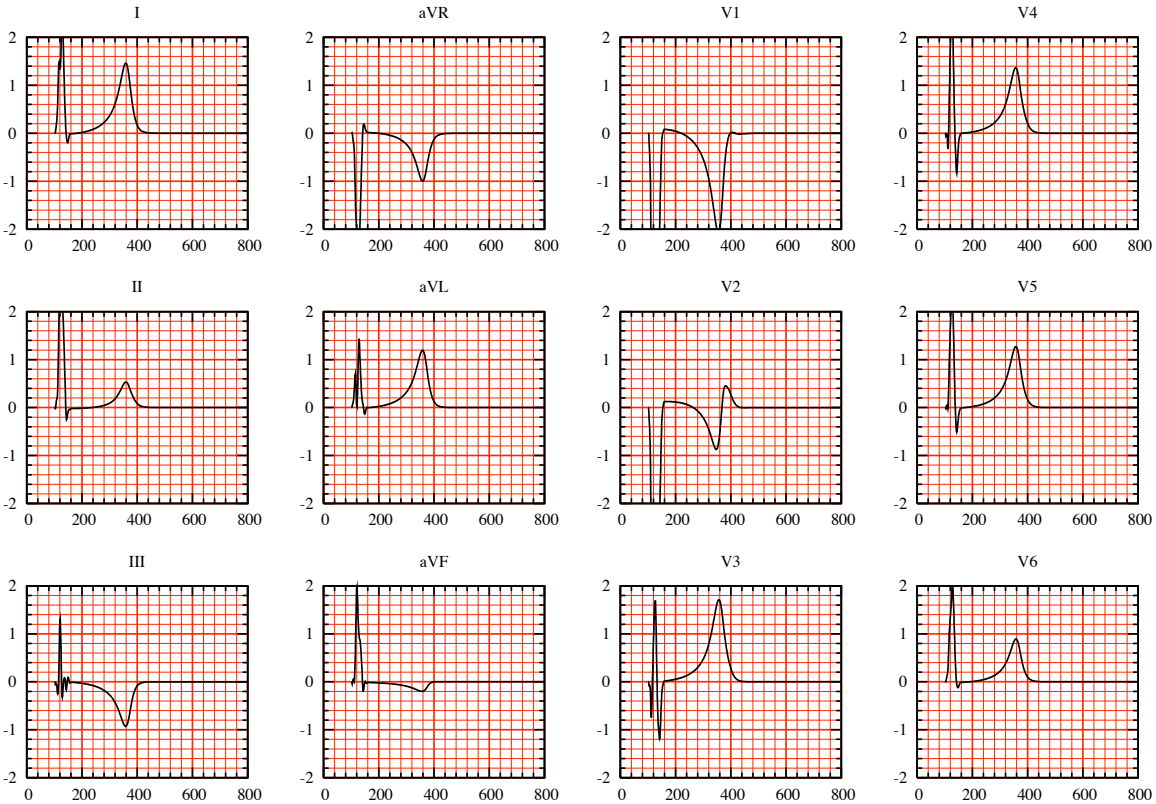

Figure 9.3: Simulated 12-leads ECGs for a healthy case

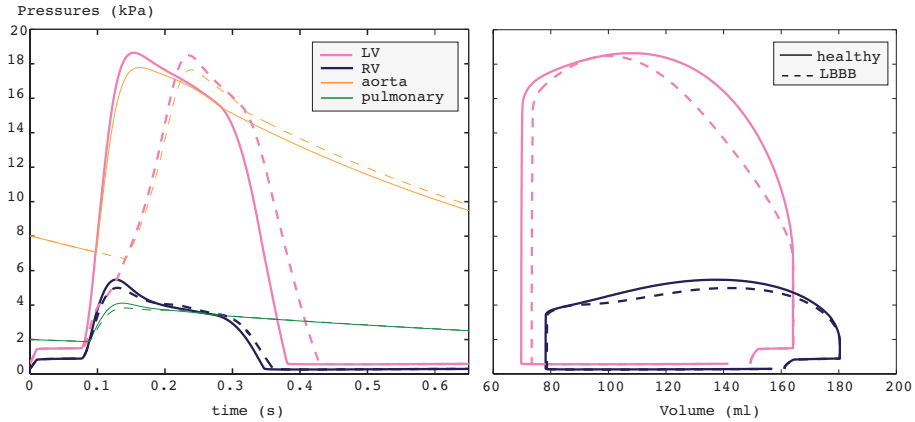

Figure 9.4: Mechanical indicators: pressures (left) and pressure-volume curves (right)

is much below 10% for these indicators, which was expected since there is an averaging effect in the computation of the volumes based on the displacements.

9.3.3 Some pathological cases

LBBB

Figure 9.11 shows the numerical ECG obtained when simulating a Left Bundle Branch Block (LBBB), *i.e.* the initial activation starts only in the right ventricle.

We emphasize that this is the only change in the model with respect to the previous healthy case. As expected, the QRS duration is larger (about 140 ms) and the time interval between the beginning of the QRS and its latest positive peak in V6 is larger than 40 ms (about 60 ms), which are recognized criteria in the diagnosis of a LBBB.

The corresponding mechanical indicators are displayed in Figure 9.4, in dashed lines. The delayed onset of the left ventricular contraction is clearly visible in the pressure curves. Compared to the healthy case, we can see that the ejection fraction is slightly reduced in the left ventricle. This is quite similar to the results of some earlier computational studies [VCMP08]. Note that this is only supposed to represent a partial and short term effect of the LBBB, as no change was introduced in the mechanical parameters (contractility, stiffness, preload, in particular), whereas of course an accompanying pathology such as a septal infarct on the one hand, and longer-term adaptation effects on the other hand, would definitely have an impact on these parameters.

In Figure 9.12 we also show some snapshots of the simulated electrical activation and mechanical deformed configurations during a cardiac cycle, and the dissynchrony of the activation and contraction is clearly visible. In addition, in these snapshots we clearly see the well-known paradoxical septal motion towards the left ventricle at the early stage of systole, quickly inverted when the left ventricular pressure starts building up, see e.g. [LRA$^+$82, GBB$^+$89] for some experimental descriptions of this phenomenon.

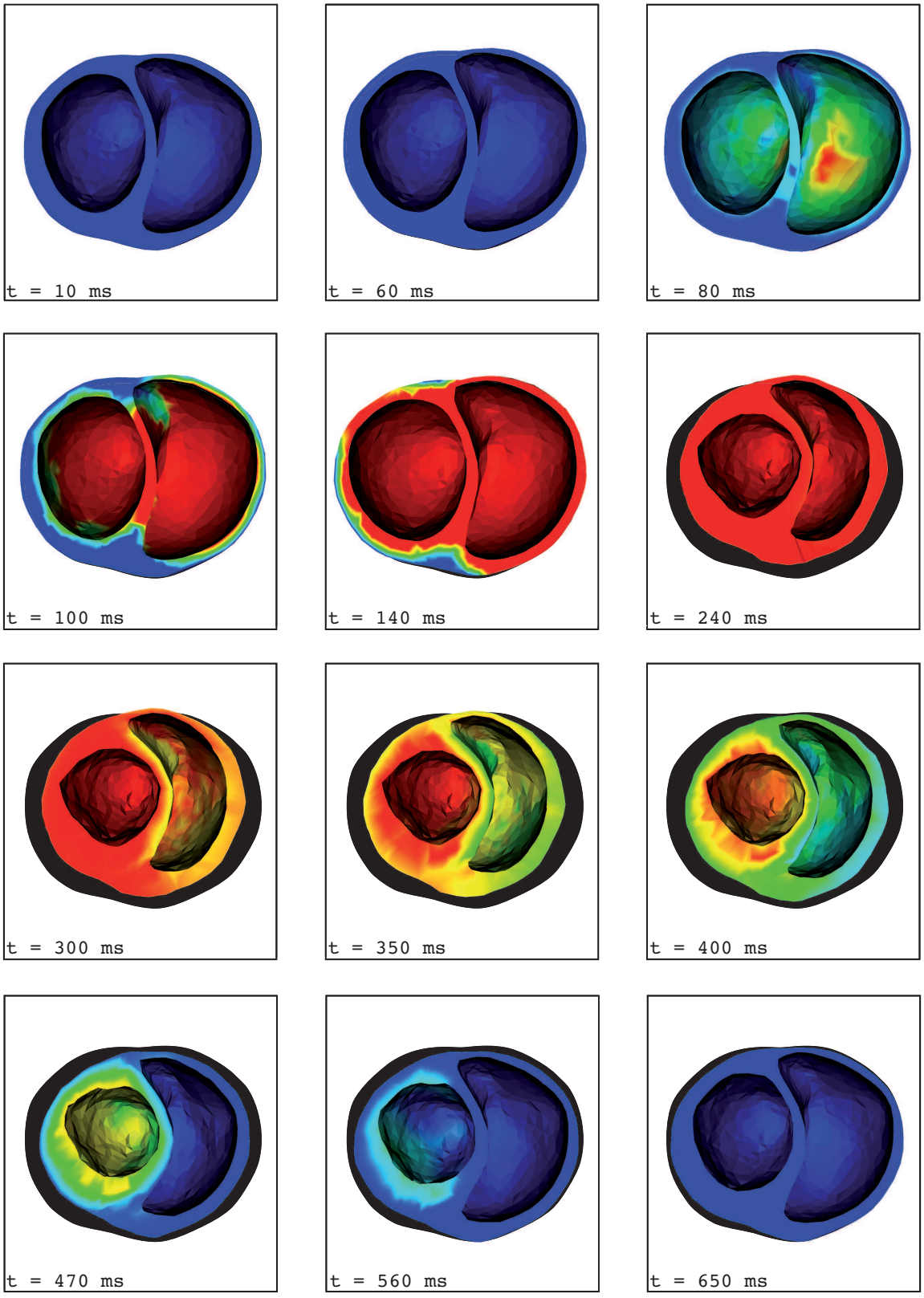

Figure 9.5: Simulation of a healthy case: Snapshots of the electrical activation V_m (in colors) and mechanical deformed configurations (black outline for reference configuration)

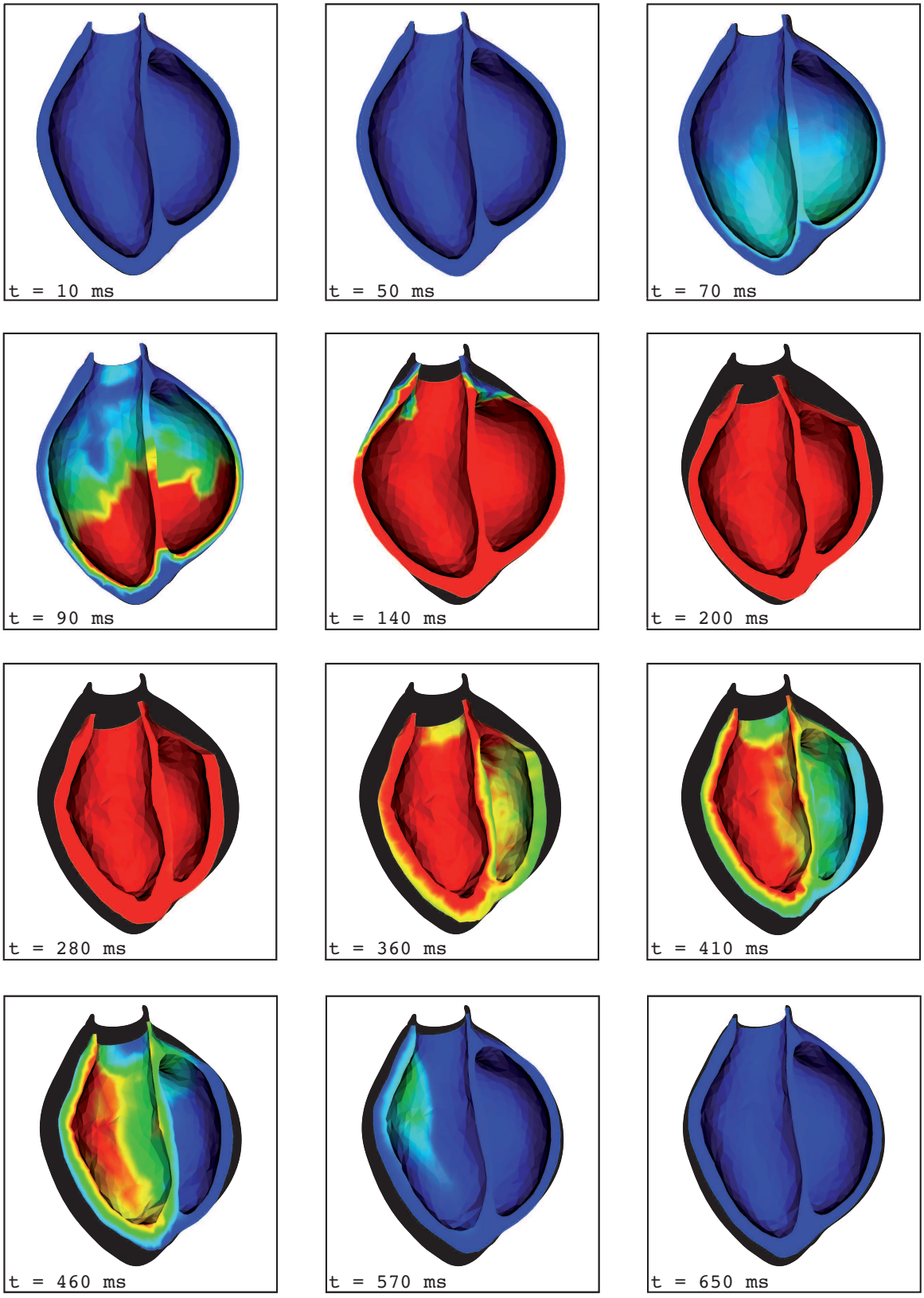

Figure 9.6: Simulation of a healthy case: Snapshots of the electrical activation V_m (in colors) and mechanical deformed configurations (black outline for reference configuration)

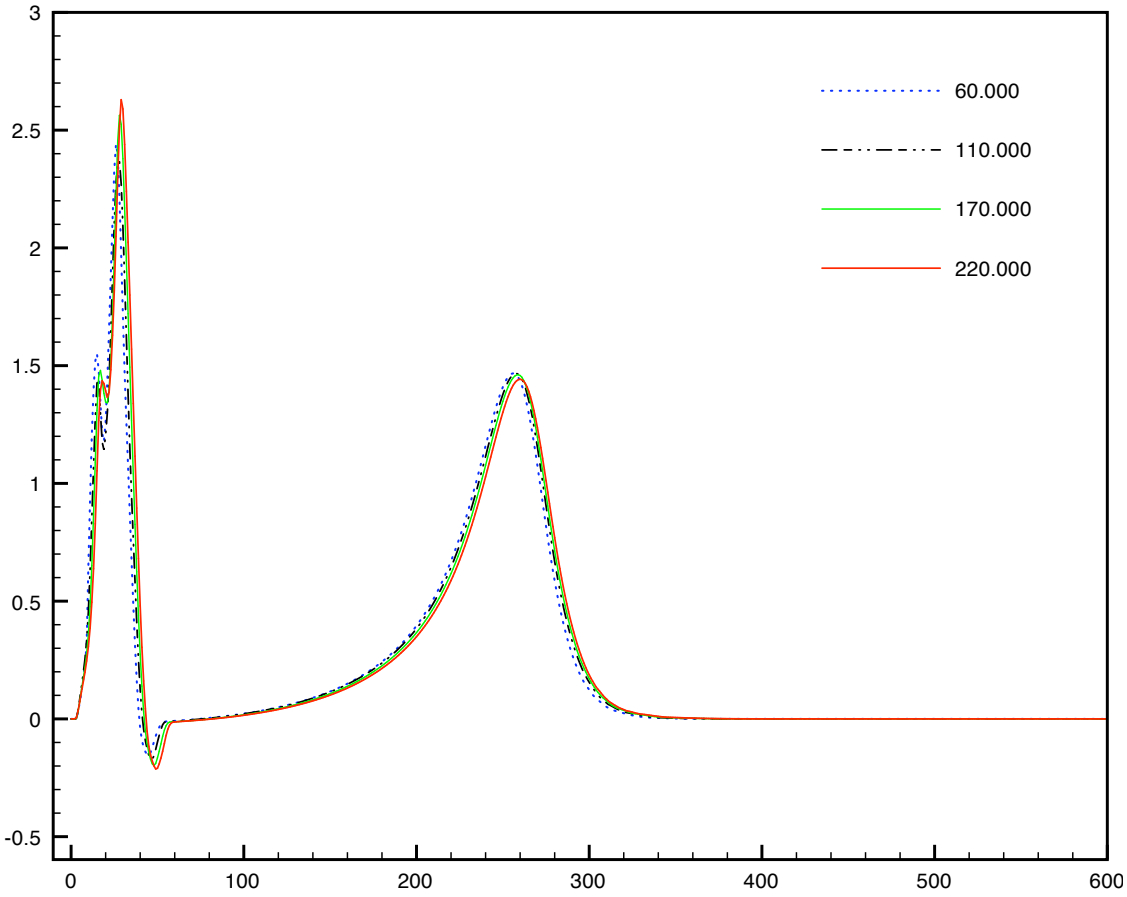

Figure 9.7: Comparison of the simulated first limb lead of the ECG , using three different levels of mesh refinement (see Table 9.1)

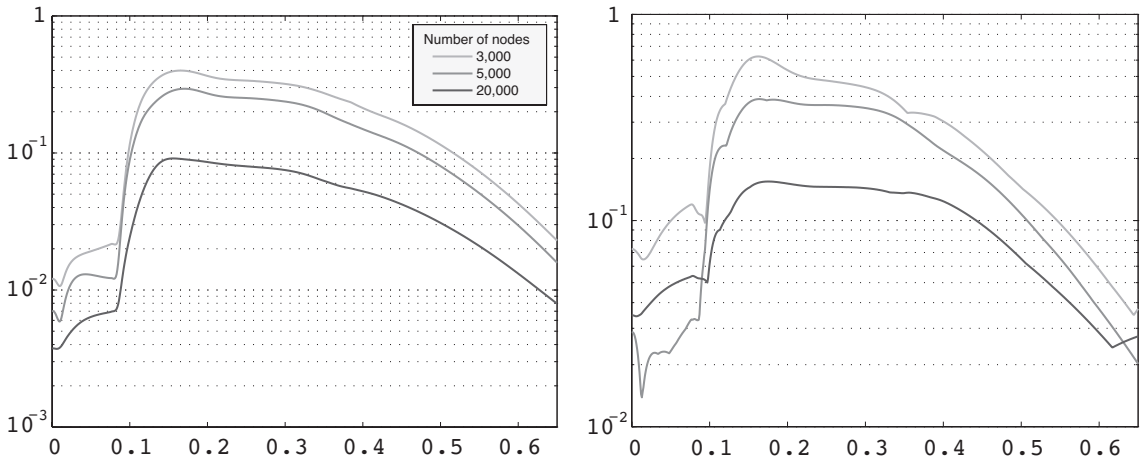

Figure 9.8: Displacement relative error w.r.t. 32,000 nodes mesh: L^2-norm (left) and L^∞-norm (right)

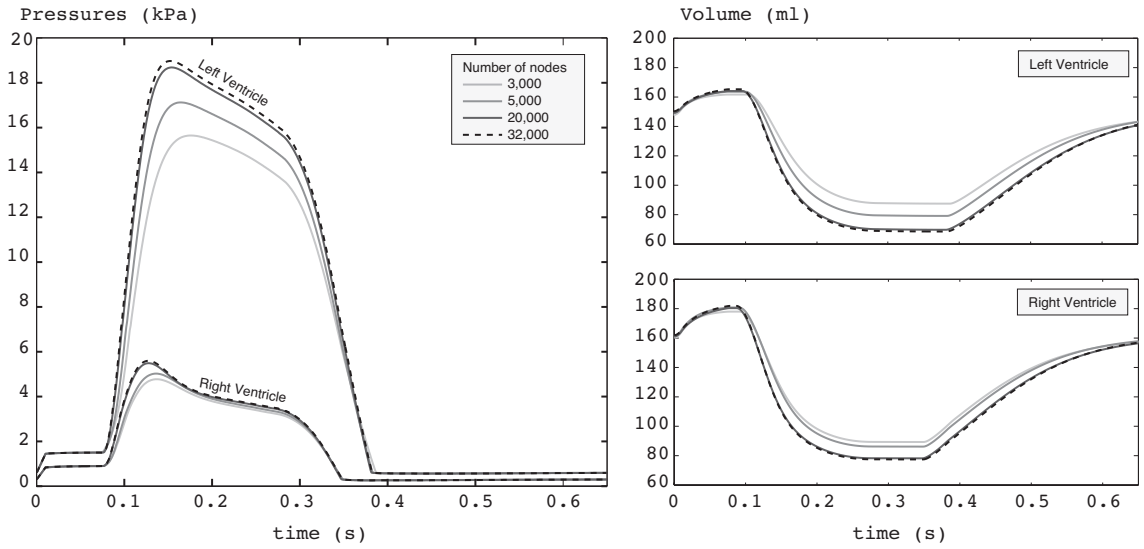

Figure 9.9: Convergence in medical indicators: pressures (left) and volumes (right)

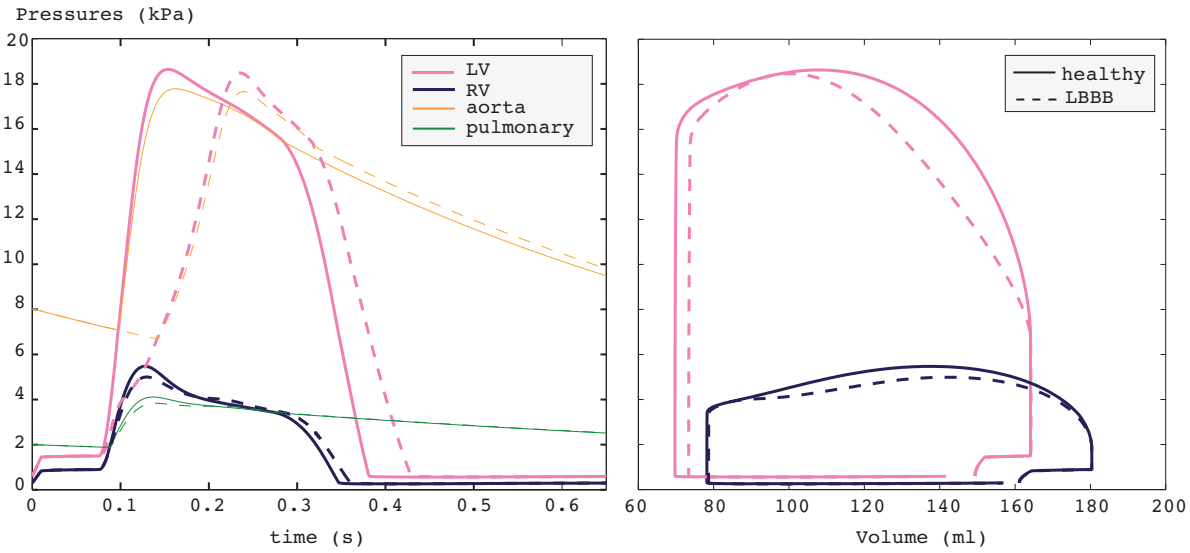

Figure 9.10: LBBB mechanical indicators: pressures (left) and pressure-volume curves (right)

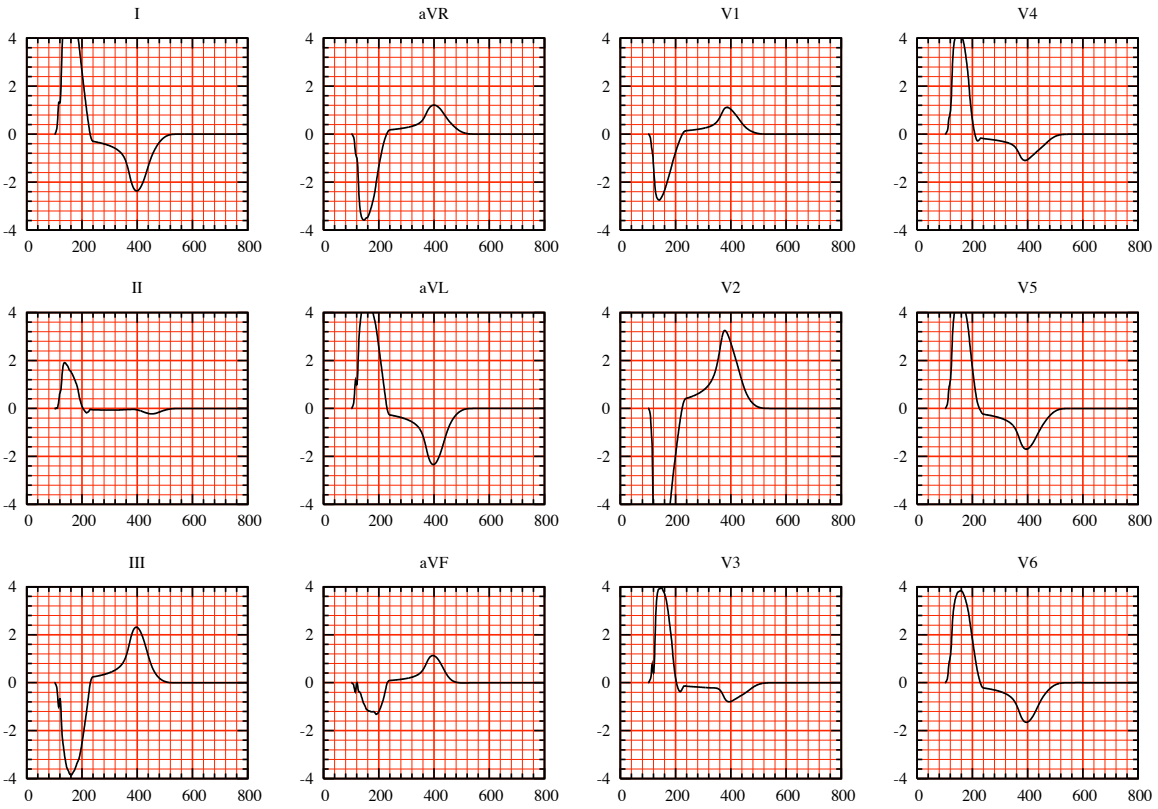

Figure 9.11: Simulated 12-leads ECGs for a LBBB case

RBBB

Figure 9.13 shows the numerical ECG obtained when simulating a Right Bundle Branch Block (RBBB) *i.e.* the initial activation starts only in the left ventricle. First, the QRS-complex exceeds 120 ms (about 140 ms). Second, one can see that the duration between the beginning of the QRS complex and its last positive wave in V1 exceeds 40 ms which are recognized criteria in the diagnosis of a RBBB

The corresponding mechanical indicators are displayed in Figure 9.14, in dashed lines. The delayed onset of the right ventricular contraction is clearly visible in the pressure curves which are recognized criteria of a RBBB pathologie. Compared to the healthy case, we can see that the ejection fraction is slightly reduced in the left ventricle.

Fibrilations

In figure 9.15 we plot the ECG simulations of a ventricular fibrillation. This pathology was modeled by introducing many ectopic sources in the heart ventricles. These sources activate the heart in an abnormal way with a very hight frequency, between 350 and 450 stimulation per minute, (see [Dub89] for more details). We plot the first lead, aVR and V4 leads of the ECG. The shape of the ECGs are similar to physiological recordings of this kind of pathology.

Mechanical indicators of the simulated fibrillation pathology are plotted in Fig-

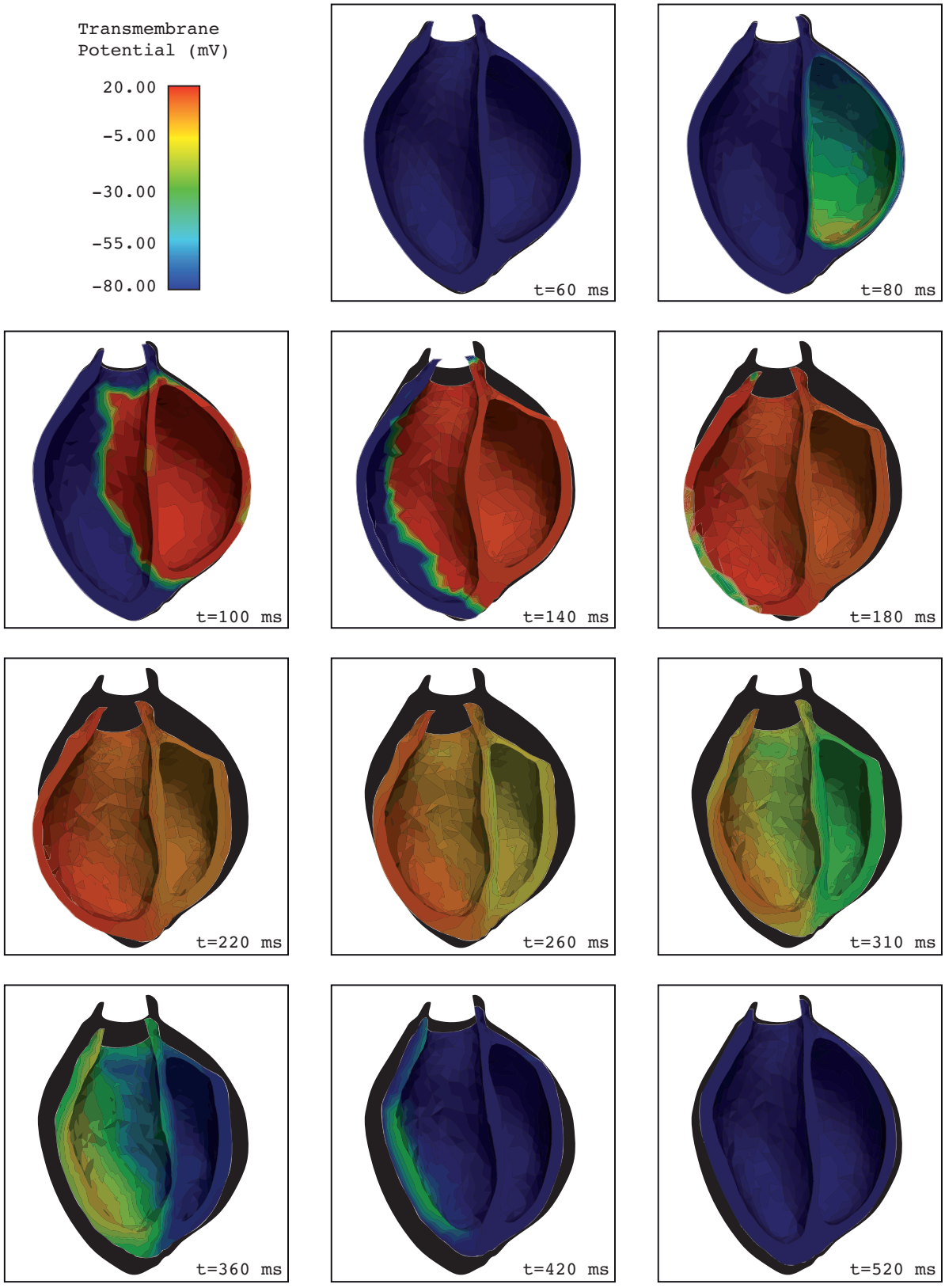

Figure 9.12: Simulation of an LBBB: Snapshots of the electrical activation V_m (in colors) and mechanical deformed configurations (black outline for reference configuration)

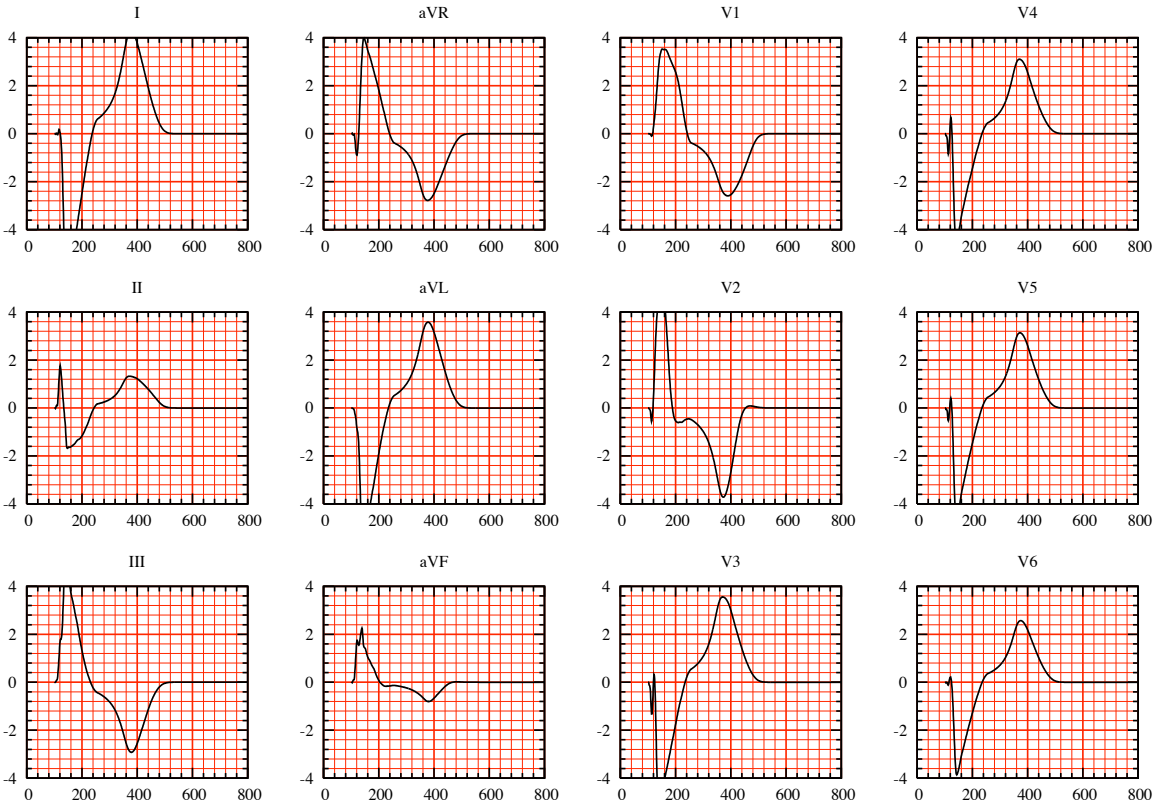

Figure 9.13: Simulated 12-leads ECGs for a RBBB case

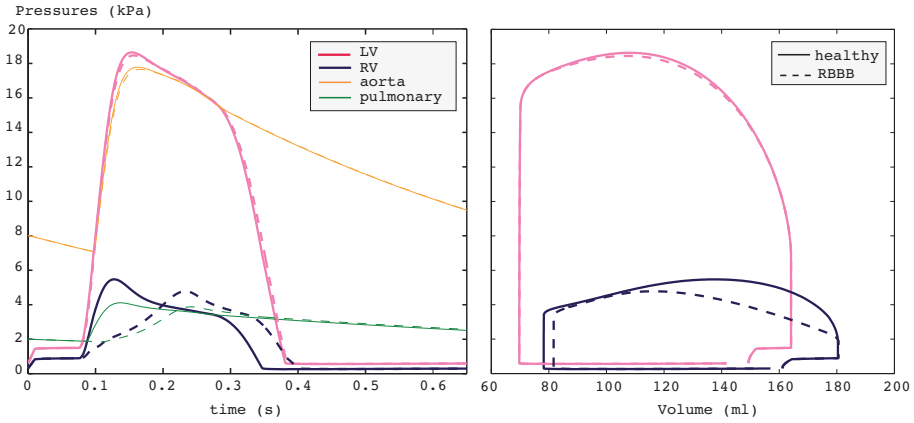

Figure 9.14: RBBB mechanical indicators: pressures (left) and pressure-volume curves (right)

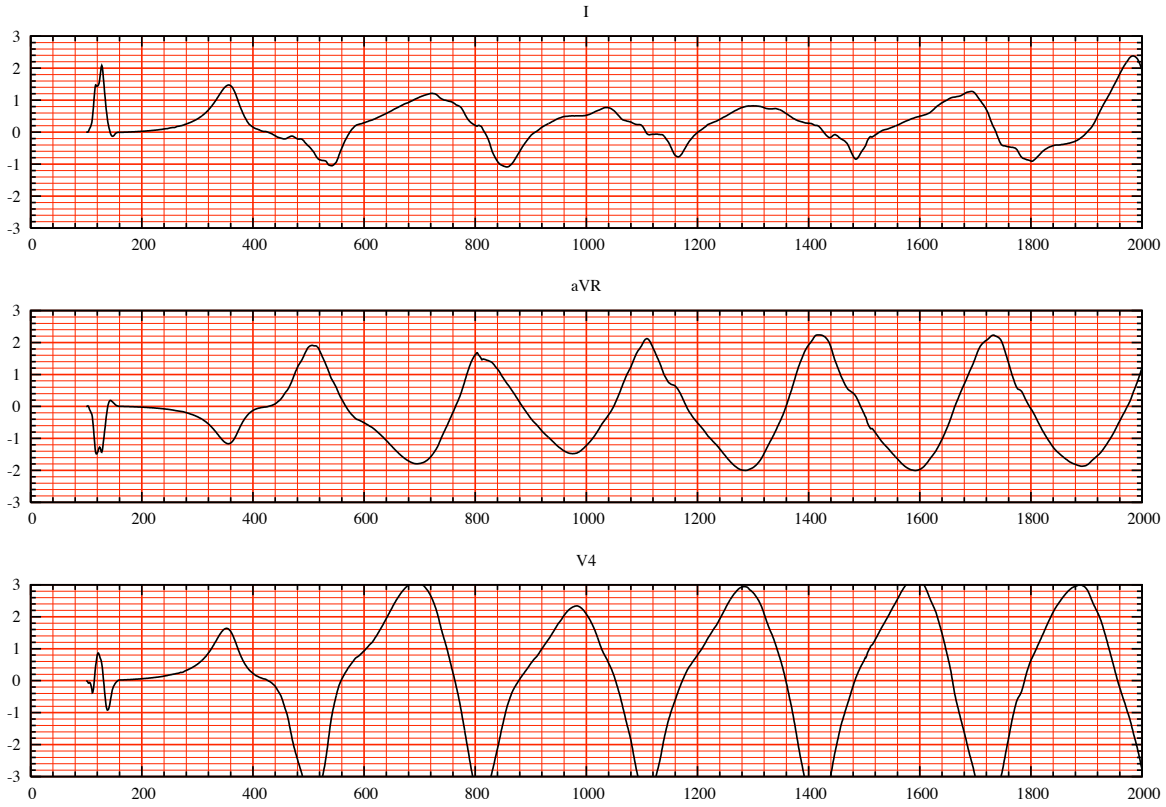

Figure 9.15: A simulated ECG for a fibrillation case.

ure 9.16. They show a decreasing of the pressure and the volume in both left and right ventricles. This could be explained by the hight frequency of the cell activation which does not allow the myocardium to repolarize normally and the ventricles to return to their initial volume.

9.4 Conclusions

We have presented numerical simulations of the electromechanical activity of the heart based on an integrated 3D mathematical model of cardiac electrophysiology and mechanics, without mechano-electrical feedback. Typical medical indicators – such as pressures, volumes and ECGs – showed physiological values in a healthy case. The predictive capabilities of the model have been illustrated with a numerical simulations of a pathological conditions (LBBB, RBBB and fibrillation). Indeed, the resulting medical indicators provided physiological values, by a simple recalibration of the model parameters directly affected by the pathology (initial activation).

Further developments will include the incorporation of mechano-electrical feedback, ventricular flows and valve mechanics, see *e.g.* [AGPT08].

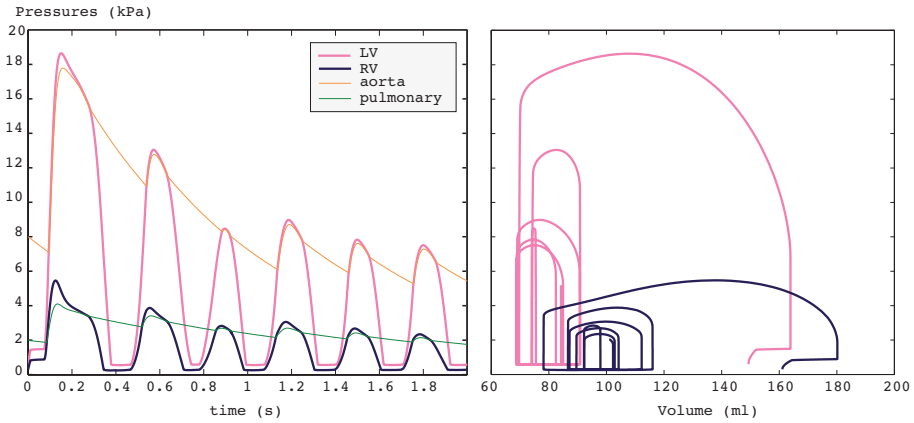

Figure 9.16: Mechanical indicators of the fibrillation pathology: Pressures (left) and pressure-volume curves (right)

Part V

Conclusions and perspectives

Meaningful computer based simulations of the ECG, linking models of the electrical activity of the heart to ECG signals, are a necessary step towards the development of personalized cardiac models from clinical ECG data. An ECG simulator is, in addition, a valuable tool for building a virtual data base of pathological conditions, to test and train medical devices but also to improve the knowledge on the clinical significance of some ECG signals.

In the present work, we have shown that meaningful ECG simulations (in normal or pathological conditions) can be obtained with a coupled heart-torso mathematical model fully based on partial differential equations (Bidomain-Laplace coupled model). These numerical simulations have then been exploited to investigate the impact of some model assumptions and the sensitivity to the model parameters. We have concluded that, in particular, cell (ADP) heterogeneity and tissue anisotropy are required modeling assumptions. For the considered cardiac conditions, the Mitchell-Schaeffer phenomenological ionic model is enough. Moreover, heart-torso full coupling is recommended and the mono-domain approximation does not significantly reduces computational cost, unless a heart-torso uncoupling approximation is considered.

On the other hand, we have shown that accurate ECG signals can be obtained with a time-marching procedure allowing a fully decoupled computation of the four unknown fields (ionic state, transmembrane potential, extracellular and torso potentials). Hence, with a computational cost equivalent to the combination of the uncoupling and the monodomain approximations. Such a decoupling is achieved via a semi-implicit treatment of the reaction term, a Gauss-Seidel (or Jacobi) like bidomain splitting and an explicit Robin-Robin treatment of the heart-torso coupling. Energy based stability is proved under mild time-step restrictions.

The above described numerical investigations are complemented with an analysis of the heart-torso system mathematical well-posedness. Existence of weak solution is obtained for a class of phenomenological ionic models (including a regularized version of the Mitchell-Schaeffer ionic model), whereas uniqueness has been only proved for the FitzHugh-Nagumo ionic model.

In the last part of this work, we have proposed examples of how the developed ECG simulator can be successfully used in different contexts and applications. The first concerns a very preliminary study (based synthetic data) of the inverse problem of electrocardiography, in which we make use of the above mentioned sensitivity analysis. A strategy to estimate the conductivity parameters of the torso has been proposed. We have also coupled our ECG simulator with a gradient-free optimization tool to estimate some ionic model parameters. The results are promising and we propose to pursue our investigations in that direction.

The second application concerns a problem raised by a pacemaker manufacturer (ELA Medical). How to exploit pacemaker measured electrograms (EGM) in order to provide the clinician with something as close as possible to a standard ECG? We have addressed this problem by combining our ECG simulator with machine learning techniques (based on the kernel ridge regression method). In this framework, the ECG simulator has been used to enrich the training set with new cardiac situations (that have not yet been undergone) and, on the other hand, to test the robustness of the reconstruction algorithms. Our numerical investigations have shown that the global-in-time-window approach was the more robust both in terms of accuracy and computational

cost.

At last, we have presented numerical simulations of the electromechanical activity of the heart (without mechano-electrical feedback) obtained with a 3D computational model, integrating our ECG simulator and a cardiac mechanics solver (developed by the MACS project-team at INRIA). We have shown that the cardiac activation patterns associated to physiological ECG signals allow to simulate also physiological medical indicators on the mechanical side, such as pressures and volumes, in healthy and pathological cases. Moreover, physiological values in the pathological conditions (LBBB, RBBB and fibrillation) have been obtained by simply recalibrating the model parameters directly affected by the pathology (initial activation). Somehow, this illustrated the predictive capabilities of the model.

Many aspects of the present work can be improved and might lead to future extensions. We discuss below some of them.

The simulated ECG signals were obtained with a mathematical model that completely neglects the mechanical feedback on the electrical model. We think it would be worth highlighting, for instance, the impact of the myocardium motion on the shape of the ECG. This might require a reformulation of the bidomain equations, using an ALE (arbitrary Lagrangian Eulerian) framework. On the other hand, the atria were not considered in our simulations and the His bundle and the Purkinje fibers were roughly modeled via a parametrized stimulation wave. Clearly, there is room for improvements on these aspects. Further investigations could also be oriented to the determination of the main factors involved in the shape and polarity of the T-wave in the 12-lead ECG, for instance, in the spirit of the recent study [CFPST09]. The incorporation of more complex ionic models will certainly allow us to enlarge the spectra of simulated normal and pathological conditions, but also to simulate the effects of drug treatment on the ECG signals.

The decoupled time-marching schemes introduced in this work (semi-implicit Gauss-Robin or Jacobi-Robin) are limited to discretizations yielding overall first order accuracy in time. The generalization of the proposed analysis to higher order extrapolations might not be straightforward. Therefore, further numerical investigations would definitely help clarify this issue and could be the topic of future work. As regards the discretization in space, mesh adaption is the topic of an ongoing work as shown in Appendix 9.9. In particular, investigations should be oriented in order to determine whether mesh adaptation is necessary in the torso or can be just confined in the heart mesh. In the latter case, the simulation of the ECG signals will require the development of appropriate interpolation/mortaring techniques in order to handle the (geometrical and approximation) mismatch at the heart-torso interface. Regarding the mathematical well-posedness of the heart-torso problem, the uniqueness issues and the consideration of more complex ionic models certainly call for further investigations. For instance, in the spirit of the results reported in [Ven09] for the insulated bidomain model.

At last, future investigations will also concern the inverse problem of electrocardiography and optimization related problems. A preliminary study on the optimal pacemaker lead positioning based on our ECG simulator has been recently reported in [DEA07]. Obviously, this type of problems is much more computational demanding than a simple forward simulation. In this way, the combination of model reduction (as

POD, see *e.g.* [KV03]) with state-of-the-art data assimilation techniques [Moi08, Section 4.5.2.c] might open a new door in the personalization of the coupled heart-torso model from clinical ECG data.

Part VI

Appendix

Summary

9.5 Simulation of a healthy case

9.5.1 Body surface potential and iso-surfaces

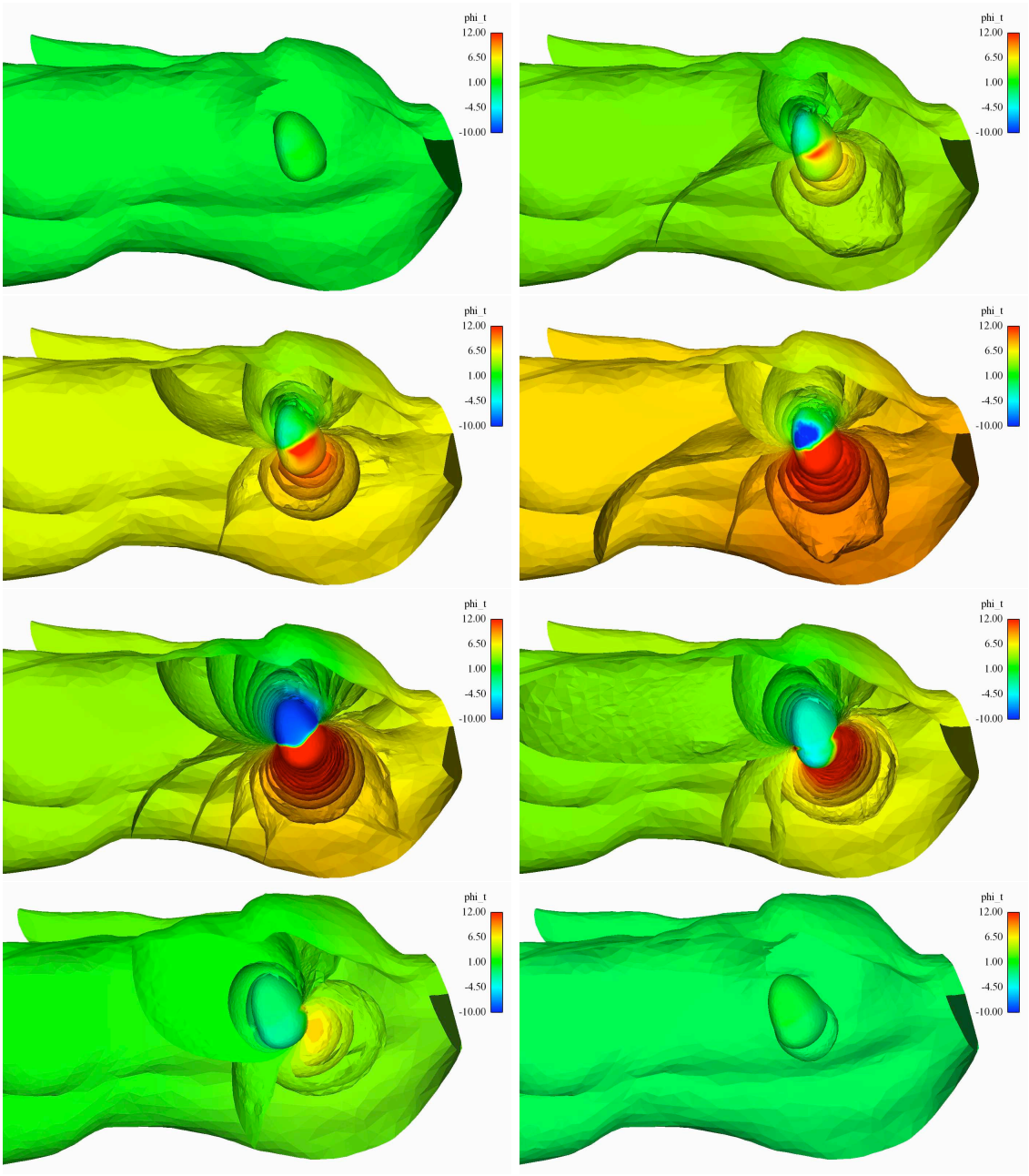

Figure 9.17: Simulation of a Healthy case: Snapshots torso potential u_{T} iso-surfaces in a cut of the torso, during the QRS-complex: Snapshot at times 1, 10, 20, 30, 50, 70, 80 and 100 ms (from left to right and from top to bottom).

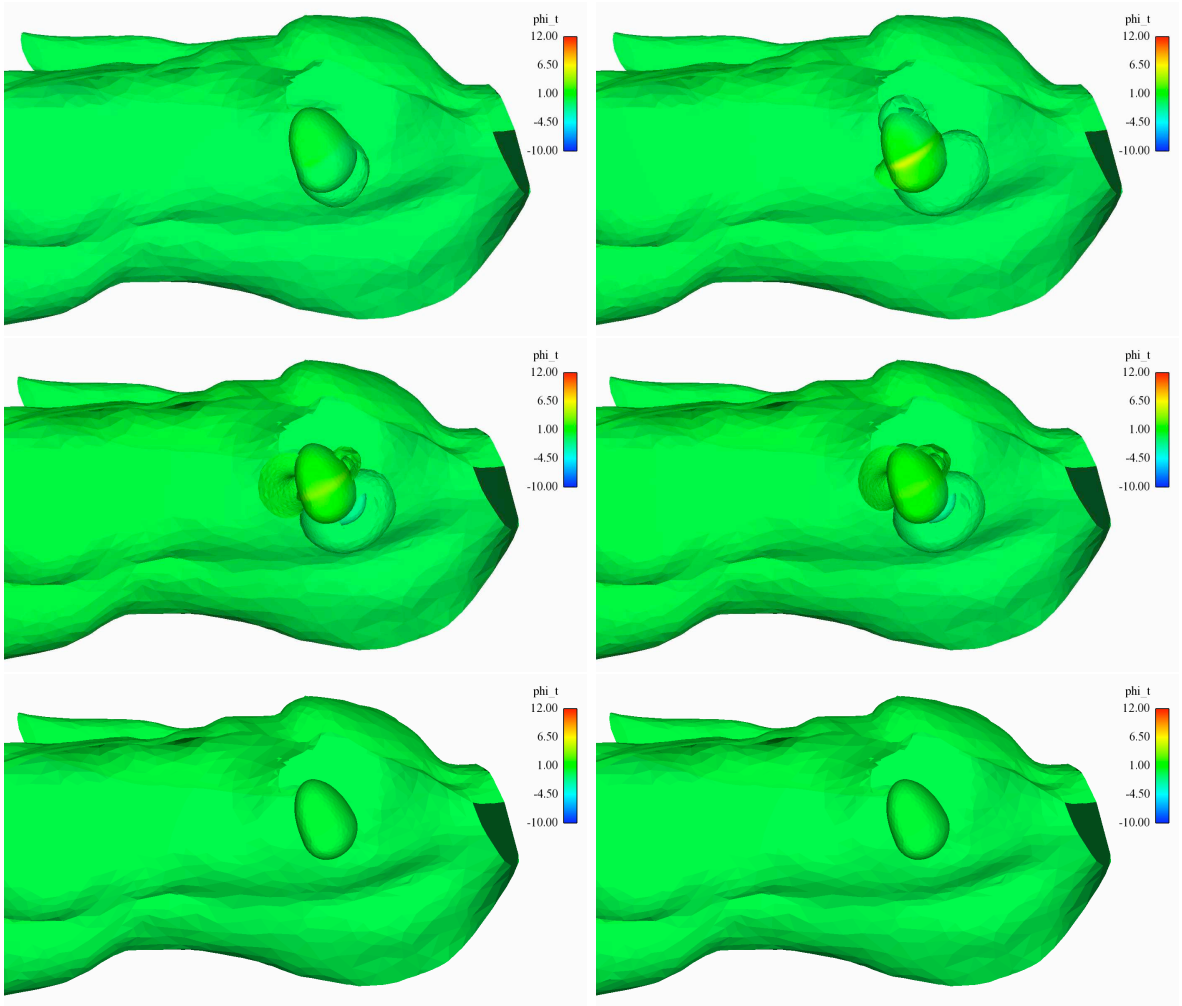

Figure 9.18: Simulation of a Healthy case: Snapshots torso potential u_T iso-surfaces in a cut of the torso, during the T-wave: Snapshot at times 100, 250, 320, 340, 400 and 450 ms (from left to right and from top to bottom).

The iso-surfaces of the torso potential in both QRS-complex and T-wave periods show the influence of the torso heterogeneity on the potential wave front in the torso. One can easily see this in the second snapshot in the QRS period, it is clear that the potential wave front takes the shape of the lungs. We can also see a slight influence of the bones in the fourth and the sixth snapshots.

9.5.2 Vectocardiogram

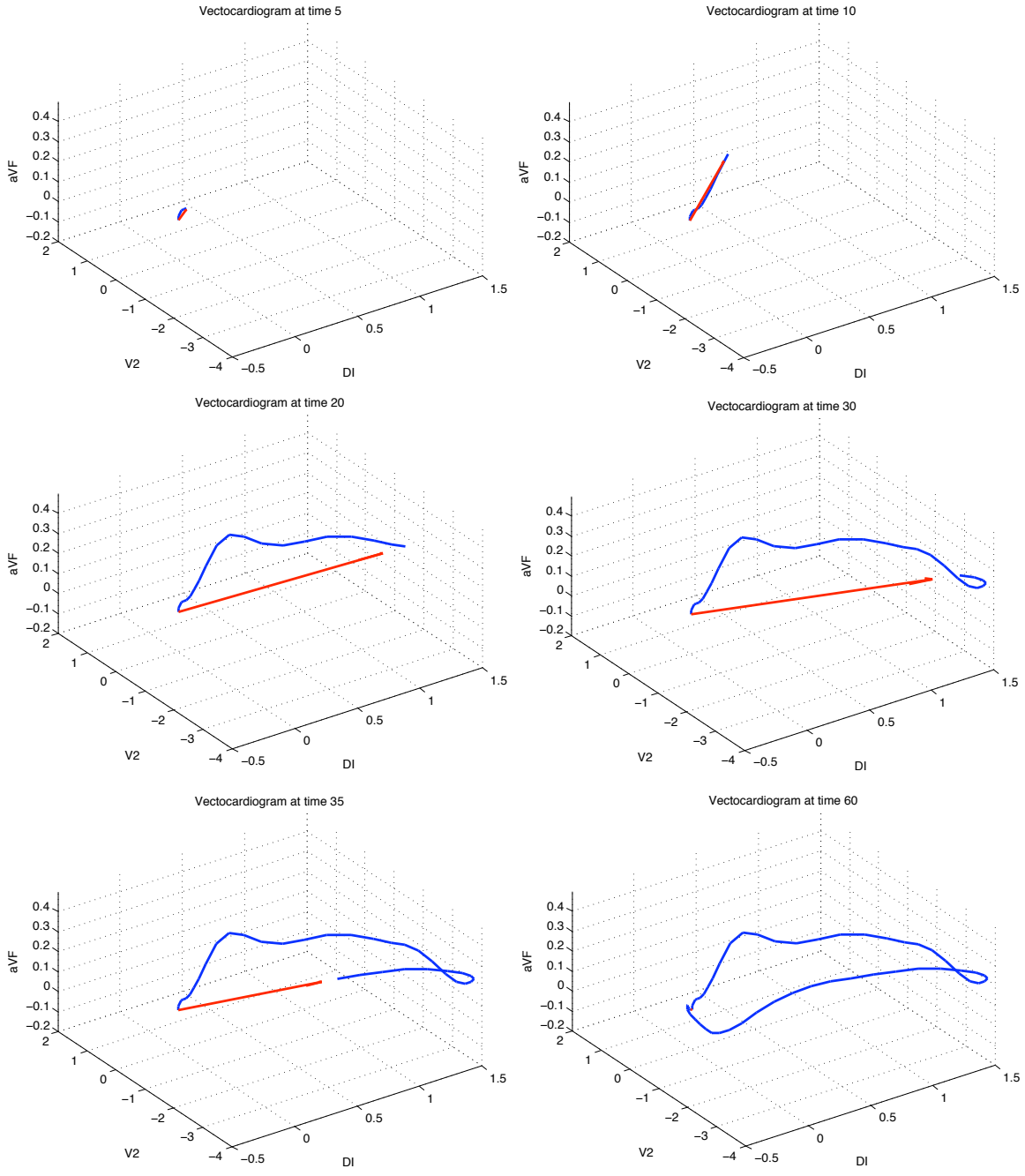

Figure 9.19: Simulation of a Healthy case: Snapshots the vectocardiogram trace during the QRS-complex period.

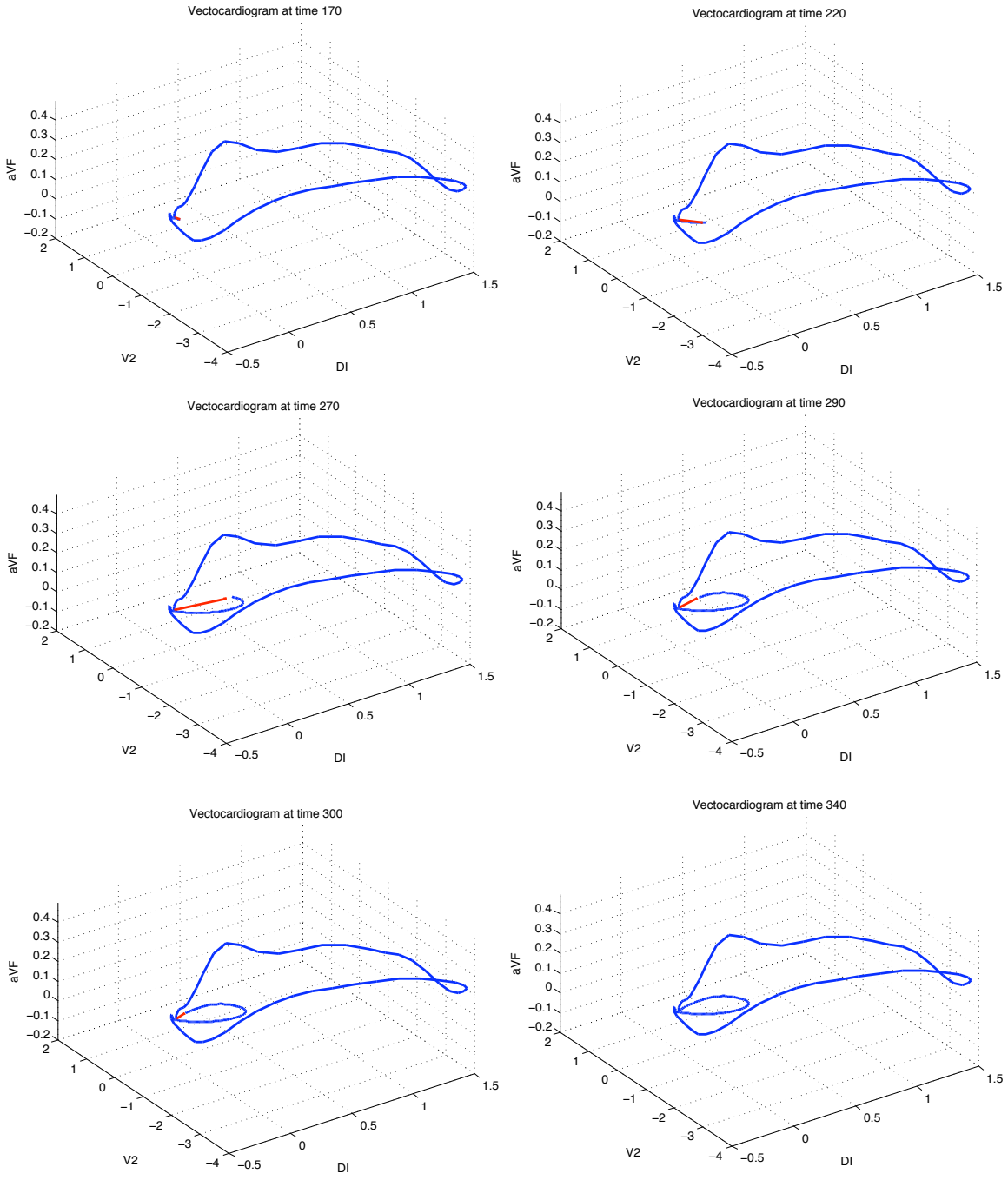

Figure 9.20: Simulation of a Healthy case: Snapshots the vectocardiogram trace during the T-wave period.

9.6 RBBB simulations

9.6.1 Spacial block

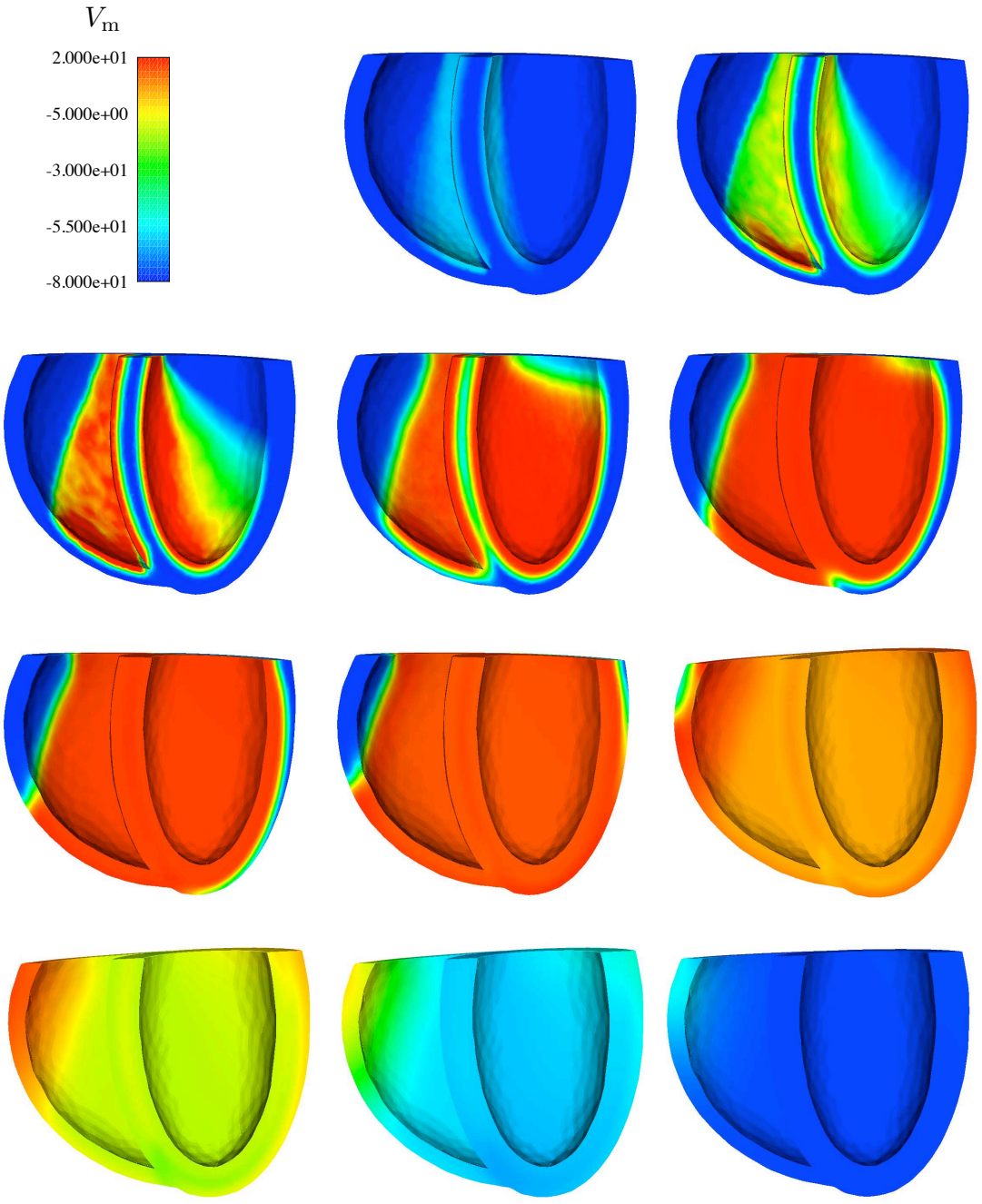

Figure 9.21: Simulation of RBBB: Snapshots of the action potential V_m in a cut of the analytical heart at times 1, 4, 6, 20, 40, 60, 80, 140, 200, 300 and 400 ms (from left to right and from top to bottom).

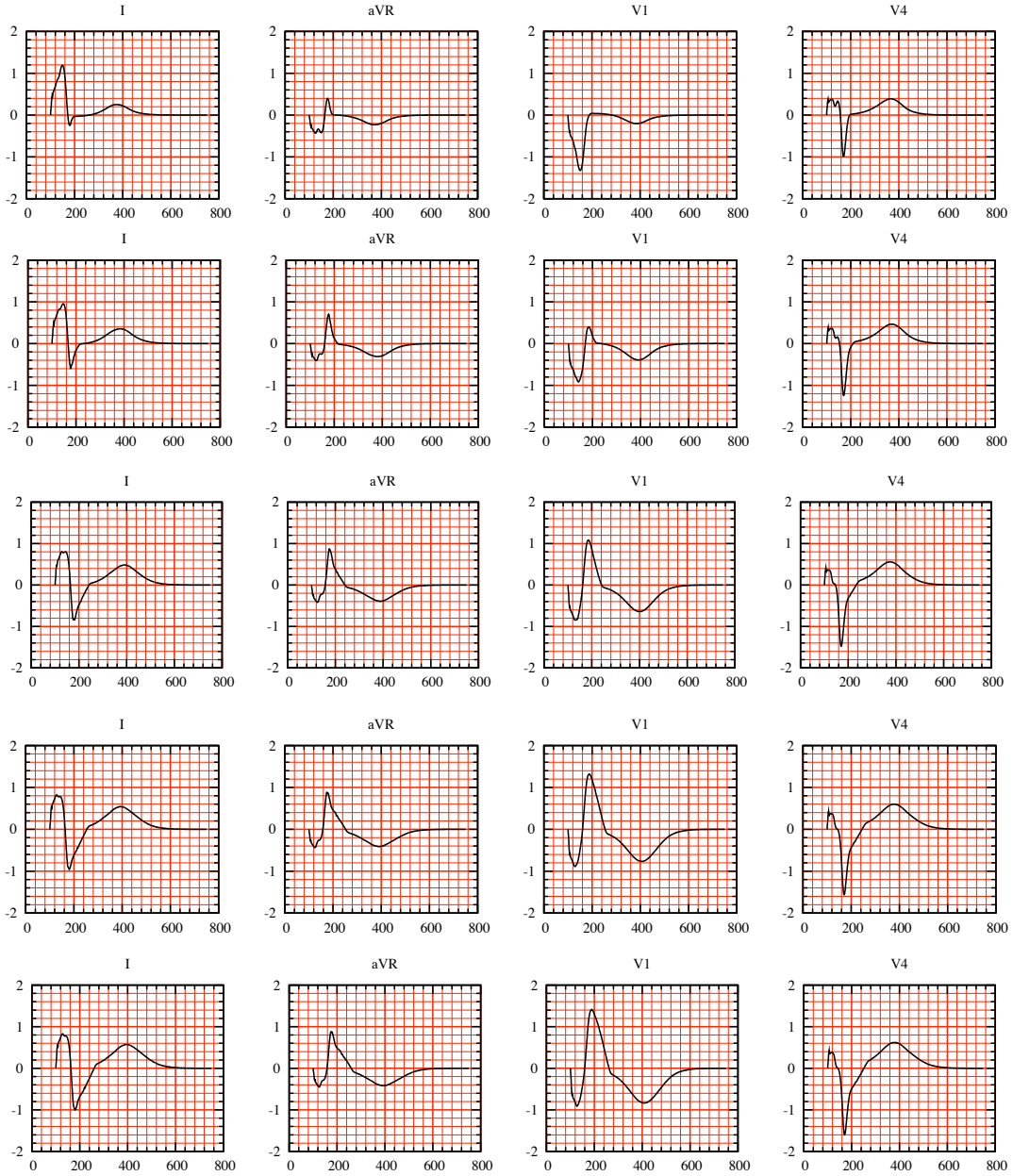

Figure 9.22: Diffrrent degrees of severity of RBBB ECG simulations using spacial block modeling. From the less sever to the most sever RBBB blocked at angle $\pi/3$, $\pi/4$, $\pi/6$, $\pi/8$ and $\pi/10$, (from top to bottom). Leads I, aVR, VI and V4 (from left to right). The RBBB criteria is clearly seen in the ECGs blocked at angles $\pi/4$, $\pi/6$, $\pi/8$ and $\pi/10$: The QRS durations in these ECGs exceed 140 ms and the duration between the beginning of the QRS complex and its last positive wave in V1 exceeds 40 ms.

9.6.2 Time delay

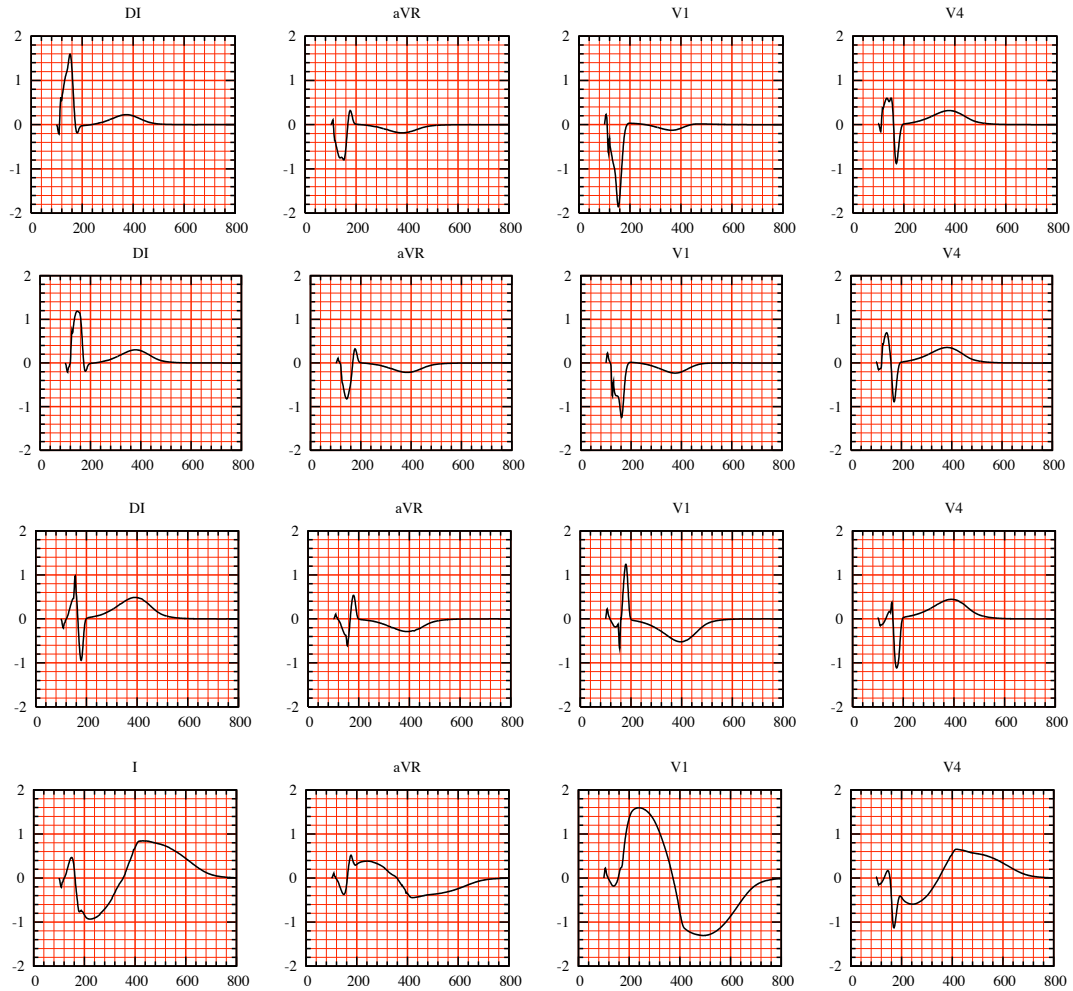

Figure 9.23: Diffrrent degrees of severity of RBBB ECG simulations generated using time delay of activating the right ventricle: RBBB-10, RBBB-20, RBBB-50 and RBBB-700 (from top to bottom). Leads I, aVR, VI and V4 (from left to right).

9.7 LBBB simulations

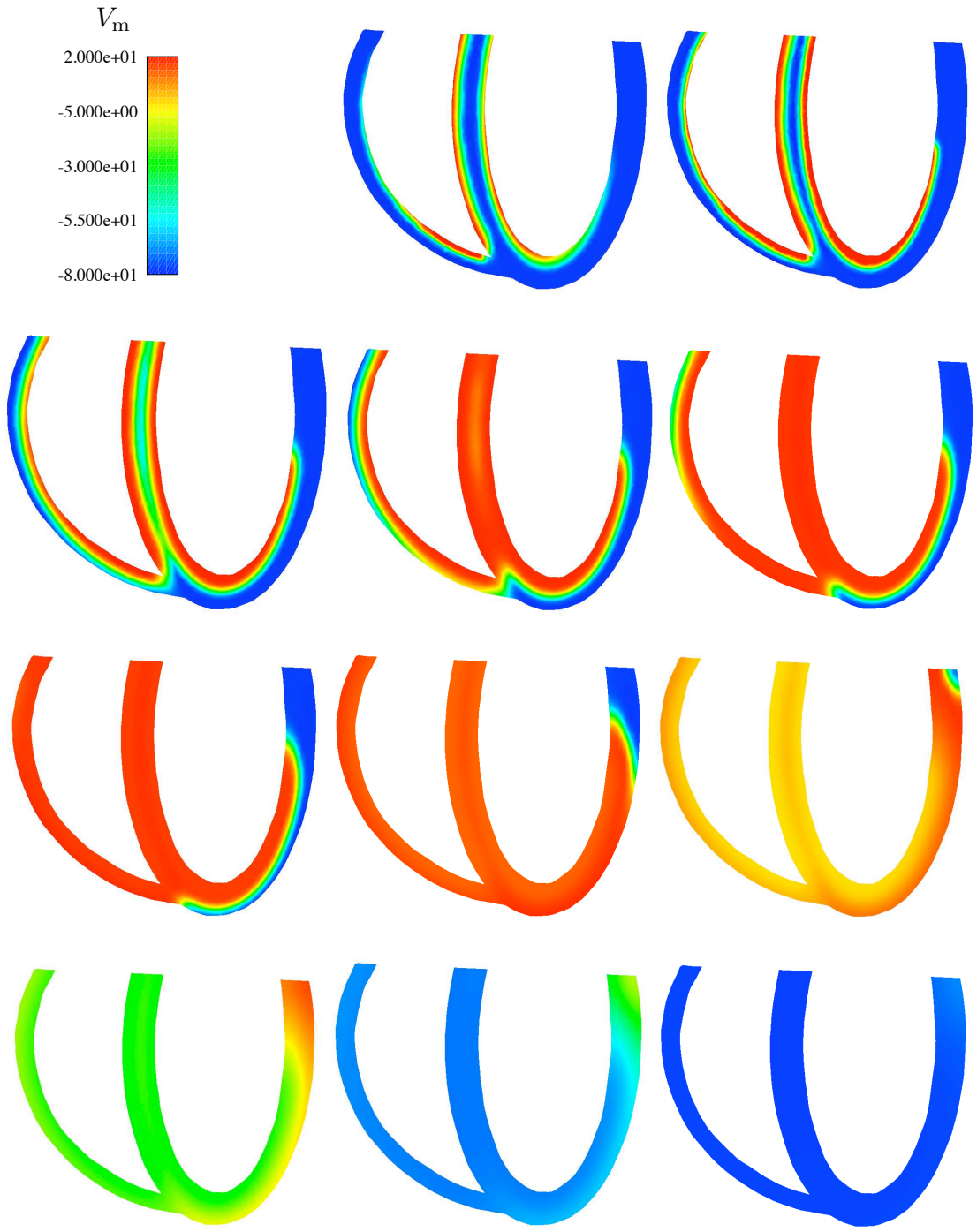

Figure 9.24: Simulation of LBBB using spacial block modeling at angle $\pi/3$: Snapshots of the action potential V_m in a cut of the analytical heart at times 5, 10, 20, 30, 40, 50, 80, 140, 200, 300 and 400 ms (from left to right and from top to bottom). On can see easily that the depolarization of the heart takes more than 140 ms that corresponds to a QRS duration exceeding 140 ms.

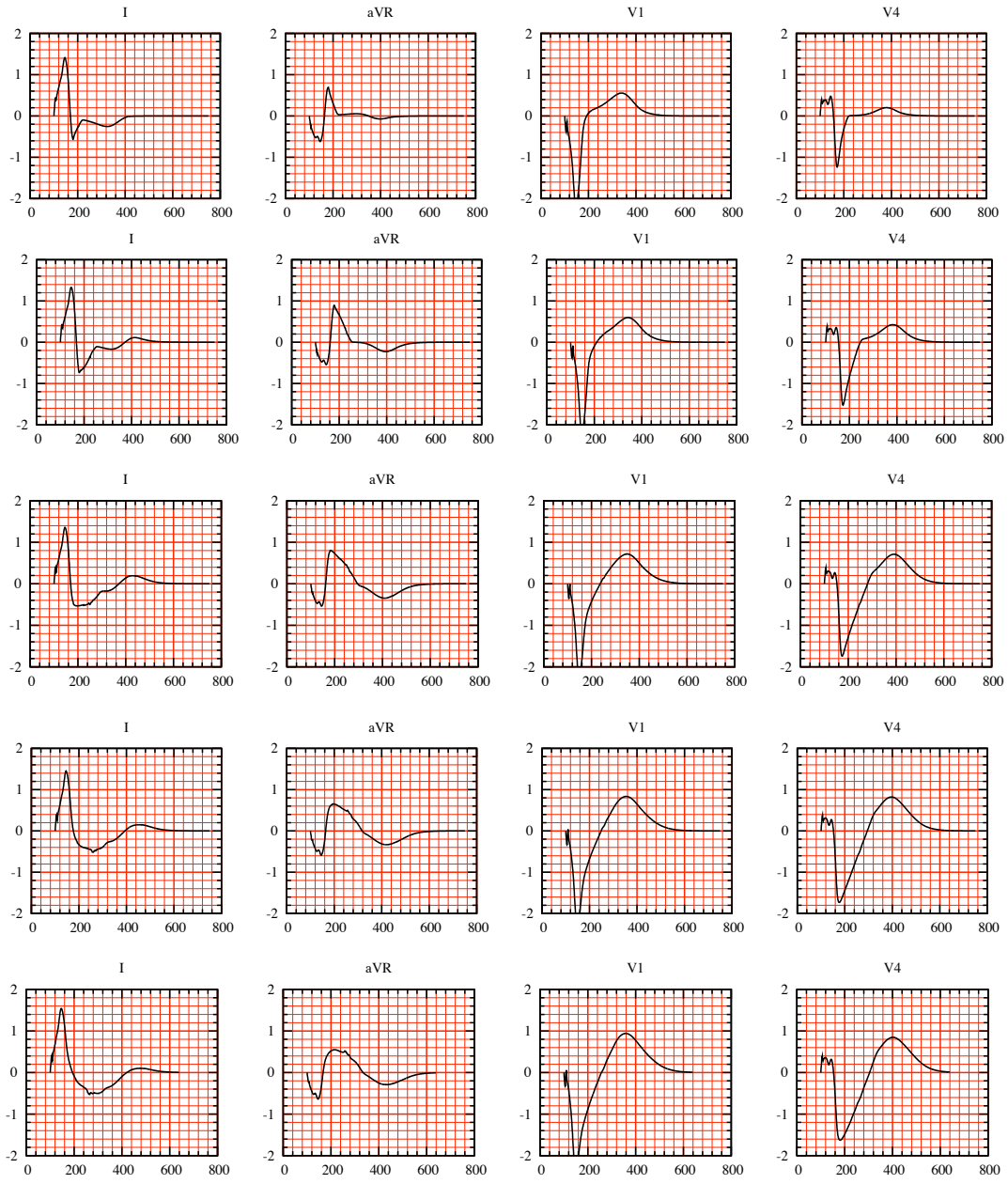

Figure 9.25: Diffrrent degrees of severity of LBBB ECG simulations using spacial block modeling. From the less sever to the most sever LBBB blocked at angle $\pi/3$, $\pi/4$, $\pi/6$, $\pi/8$ and $\pi/10$, (from top to bottom). Leads I, aVR, VI and V4 (from left to right). The LBBB criteria is clearly seen in all of ECGs: The QRS durations in these ECGs exceed 140 ms and the time interval between the beginning of the QRS and its latest positive peak in V6 is larger than 40 ms.

9.8 Simulation of arrhythmia

9.8.1 Ectopic sources

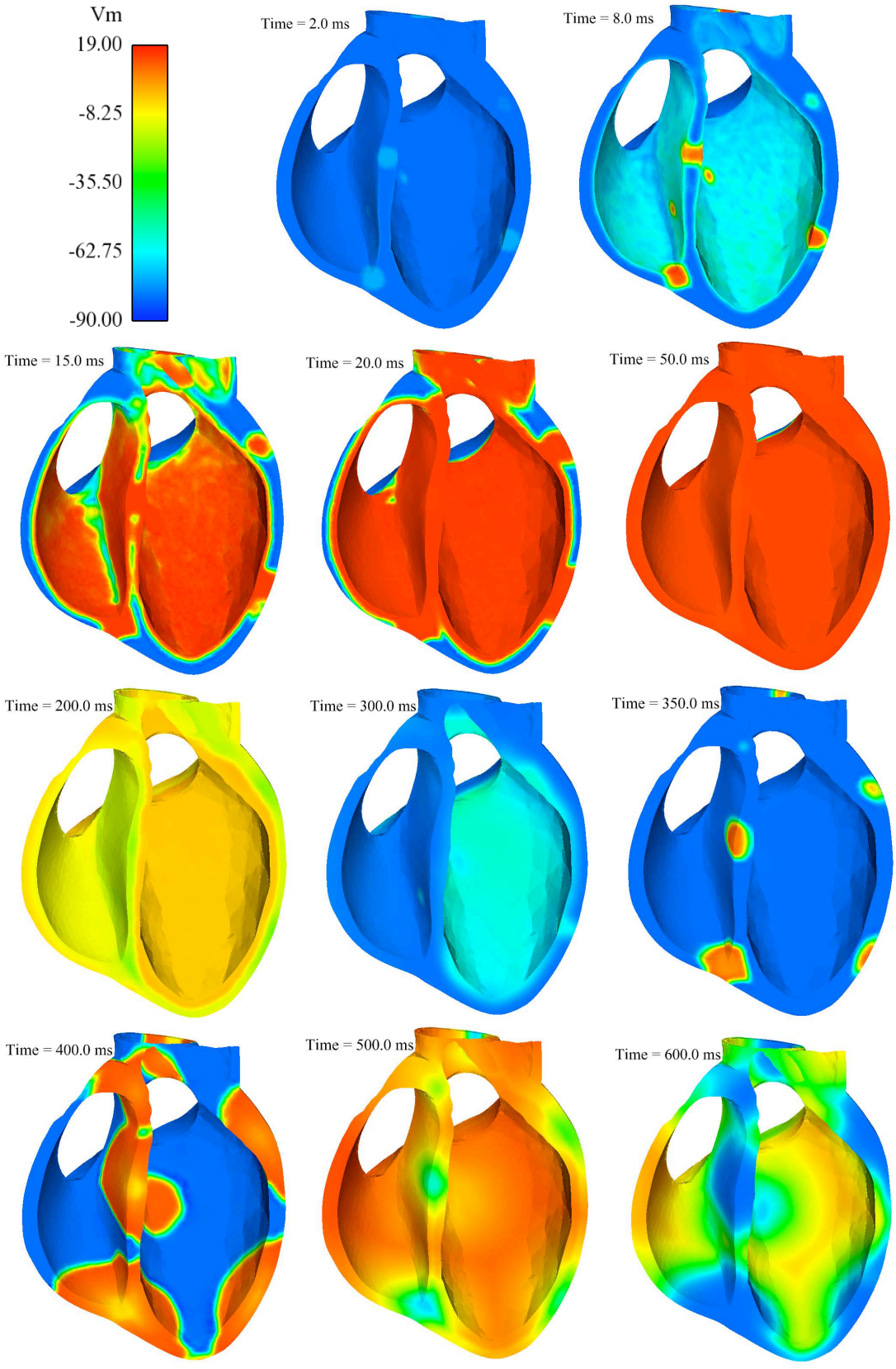

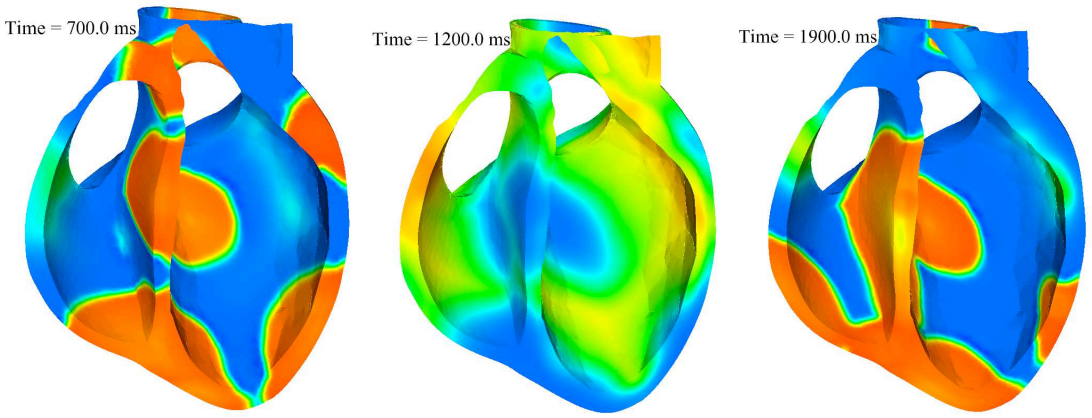

Figure 9.26: Snapshots of a ventricular tachycardia simulation generated using ectopic sources in the myocardium: The locations of the sources are fixed in time, the wave fronts at times 400, 700 and 1900 ms, for example, are similar. That is why the ECG signals are periodic.

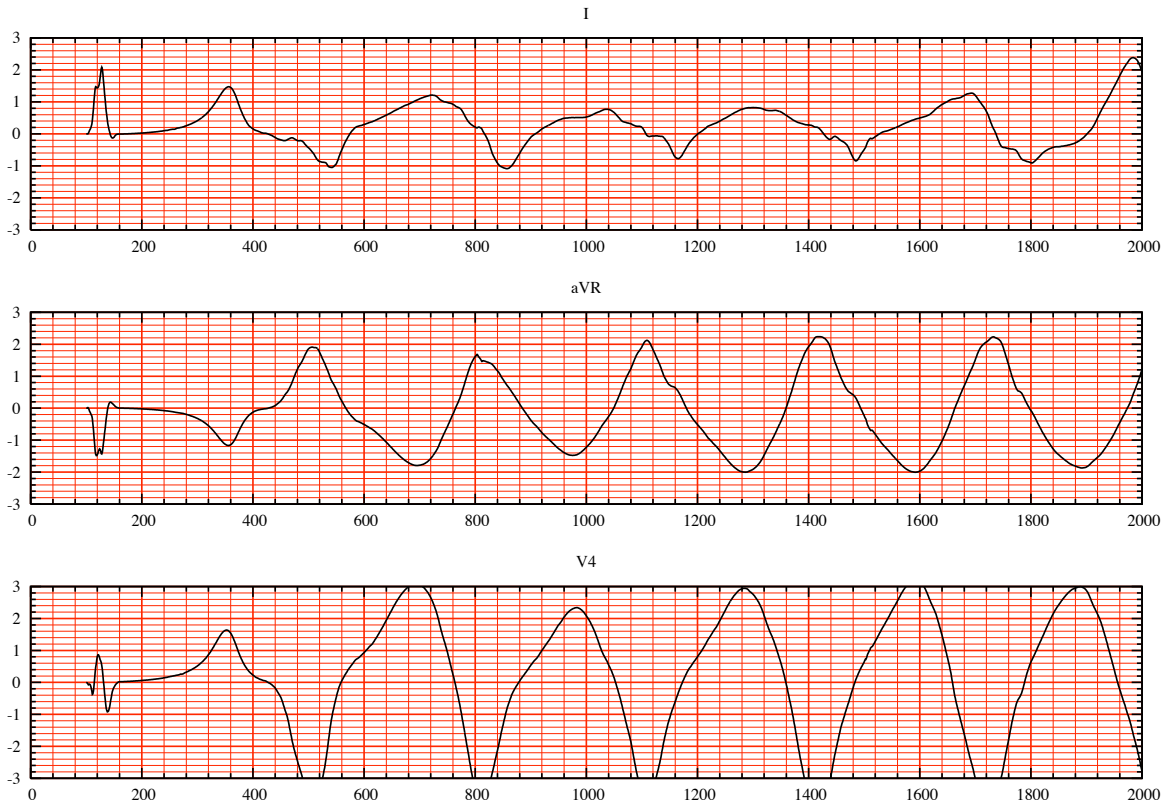

Figure 9.27: Simulated 12-leads ECG of the ventricular tachycardia corresponding to the simulation in Figure 9.26.

9.8.2 Re-entry simulations

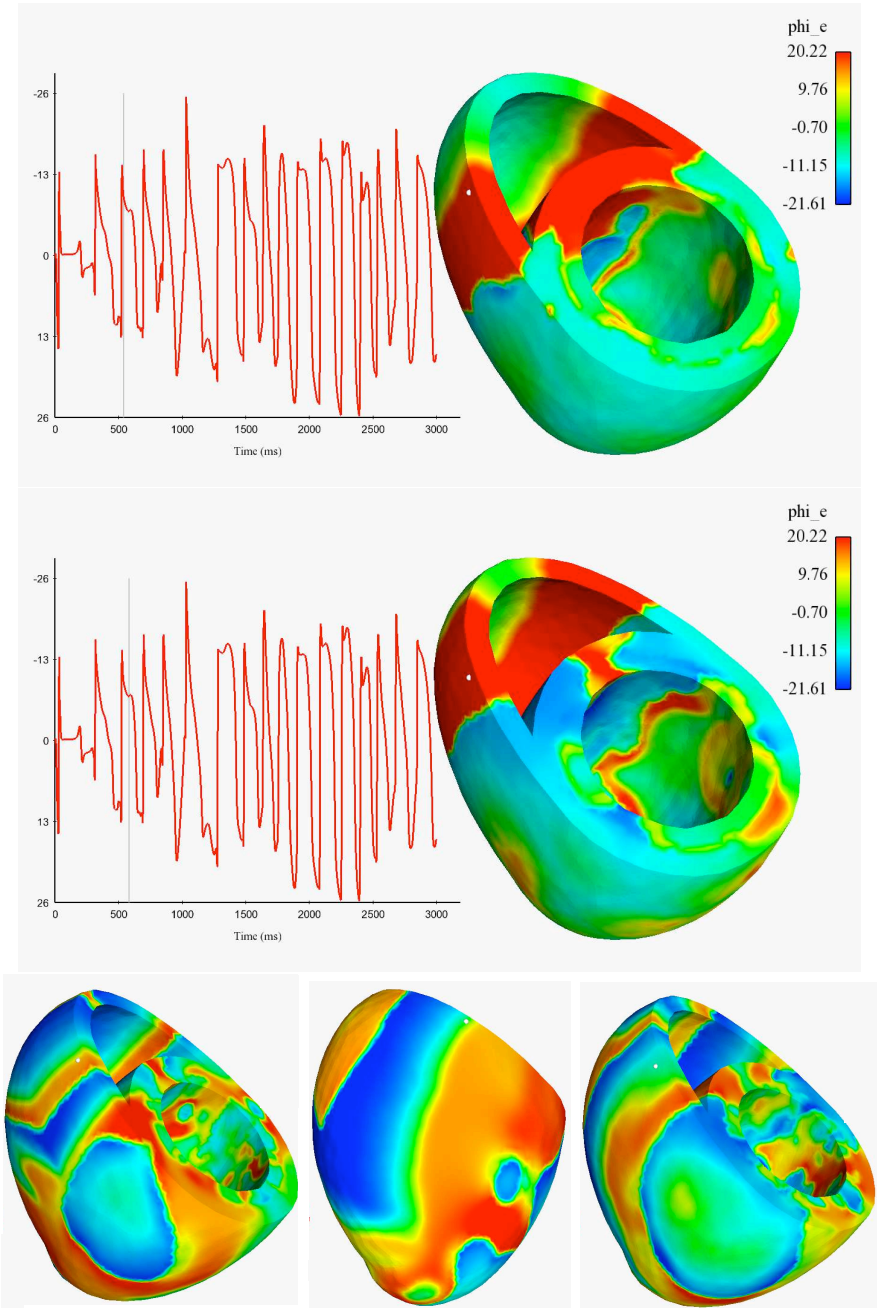

Figure 9.28: Snapshots of a re-entry simulation with a plot of the extracellular potential on a given location in the epicardium. Snapshots at times 540, 580, 1400, 2000 and 2500 ms (from top to bottom and from left to right).

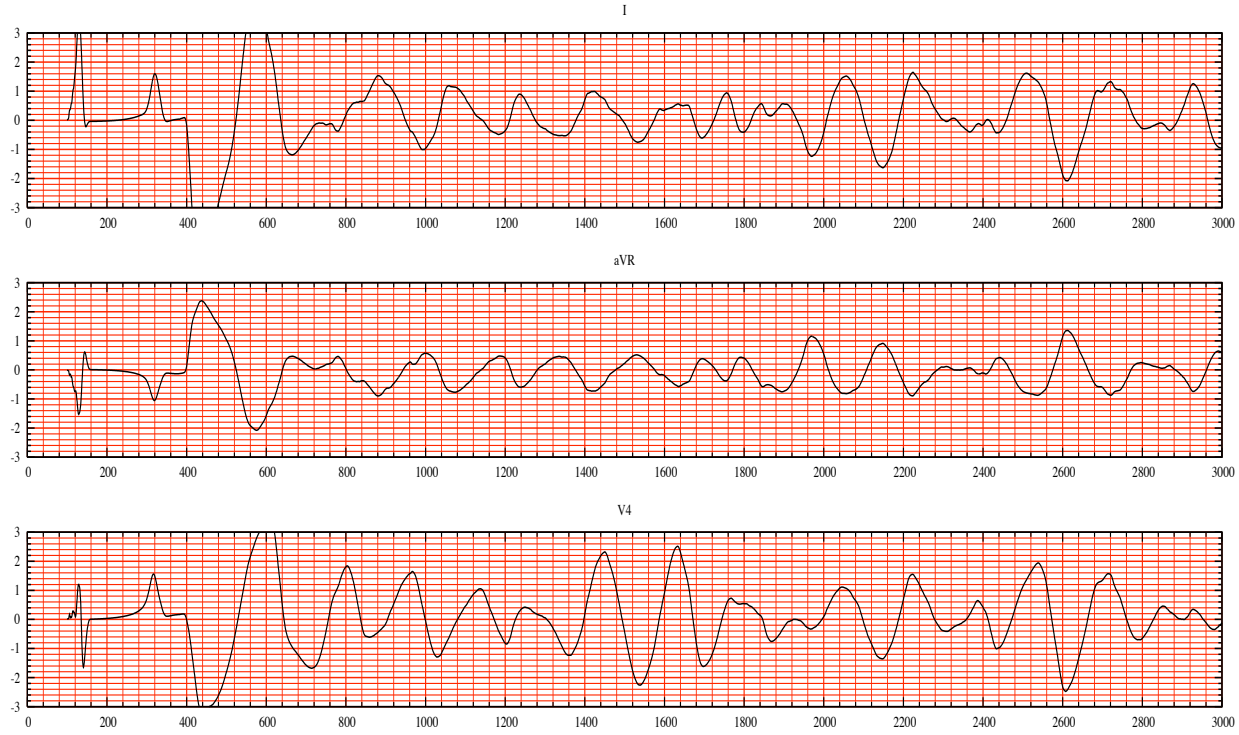

Figure 9.29: ECG simulation of re-entry during 3 seconds. From top to bottom: First lead, aVR and V4.

9.9 Mesh adaptivity: preliminary results

If we take a zoom of the R and S waves in Figure 5.31 (Chapter 5), we can see that there is a small delay between the ECG computed using the second and the third meshes. That could be explained by a "non-convergence" of the wave propagation celerity. To achieve this convergence one should use a very fine mesh of the heart: About 12 million nodes mesh were used in [Gul03] and 26 million heart nodes in [PDR$^+$06] to perform electrograms simulations and 12.5 million heart nodes for ECG simulations in [TDP$^+$04]. One of the solutions we propose is the mesh adaptivity technique: Adapting the mesh to the solution means the use a fine mesh in the zones where we have a lot of solution variation (dépolarization or repolarization wave front locations) and a coarse mesh where there is no a lot of variation of the solution. Recent works have been performed in this field by Belhamadia *et al.* [BFC04, Bel08, BFB08] for the mesh adaptivity or Colli Franzone *et al.* [CFDE$^+$06] for both mesh and time adaptivity. These works show the efficiency of using this technique in terms of computational cost of the monodomain problem for an isolated heart. Figure 9.30 shows snapshots of the action potential computed using the bidomain problem of an isolated heart with an isotropic mesh adaptivity. This work were performed with the collaboration of the Gamma project in INRIA. We have used the mesh adaptation tools (`metrix, yams, ghs3d,...,etc`). We use time-dependent adaptive remeshing: The mesh is updated each 4 ms, which allow to the electric wave to propagate in a fine mesh. The adaptation procedure during the time interval [1,4] ms for instance could be summarized as follows: We begin by computing the solution at times 1, 2, 3 and 4 ms using an initial mesh. After that we compute the metrics at each of the time steps and intersect them to obtain

new metric. This metric is used to generate a new mesh of the heart. After that, the solution at each of the time steps is interpolated on the new mesh. We iterate this procedure, by considering the new mesh as an initial mesh for the new iteration, until convergence. For more details about the mesh adaptation algorithm that we use, we refer to [Ala03, Los08]. The mesh adaptivity procedure was also performed on a realistic geometry of the heart see Figure 9.31. The geometrical model and all of the electrical model parameters used to produce this simulation are given in the section 6.5.1

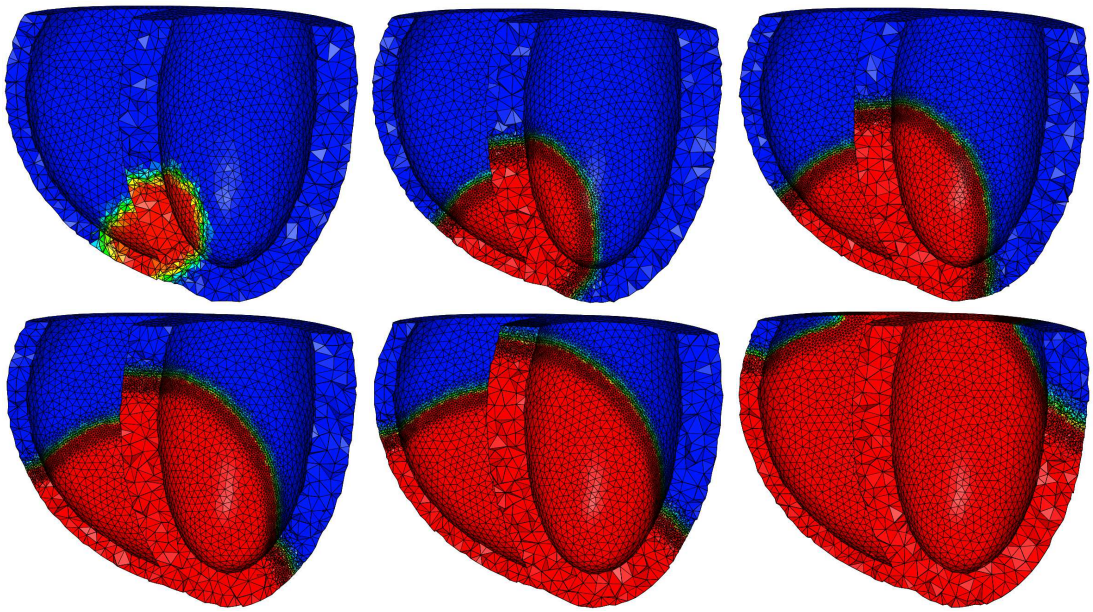

Figure 9.30: Snapshots of the action potential propagation at times $t = 4$, 16, 32, 48, 64 and 88 ms (from left to right and top to bottom). Illustration of the mesh adaptivity.

The results shown in Figure 9.30 and Figure 9.31 are performed using an *isotropic* mesh adaptivity which means that the edges of the volume element are almost equal. That is not necessary in case of wave spreading, the use of an *anisotropic* mesh adaptivity [Ala03, Los08] could provide more interesting results. That is one of our goals for forthcoming works.

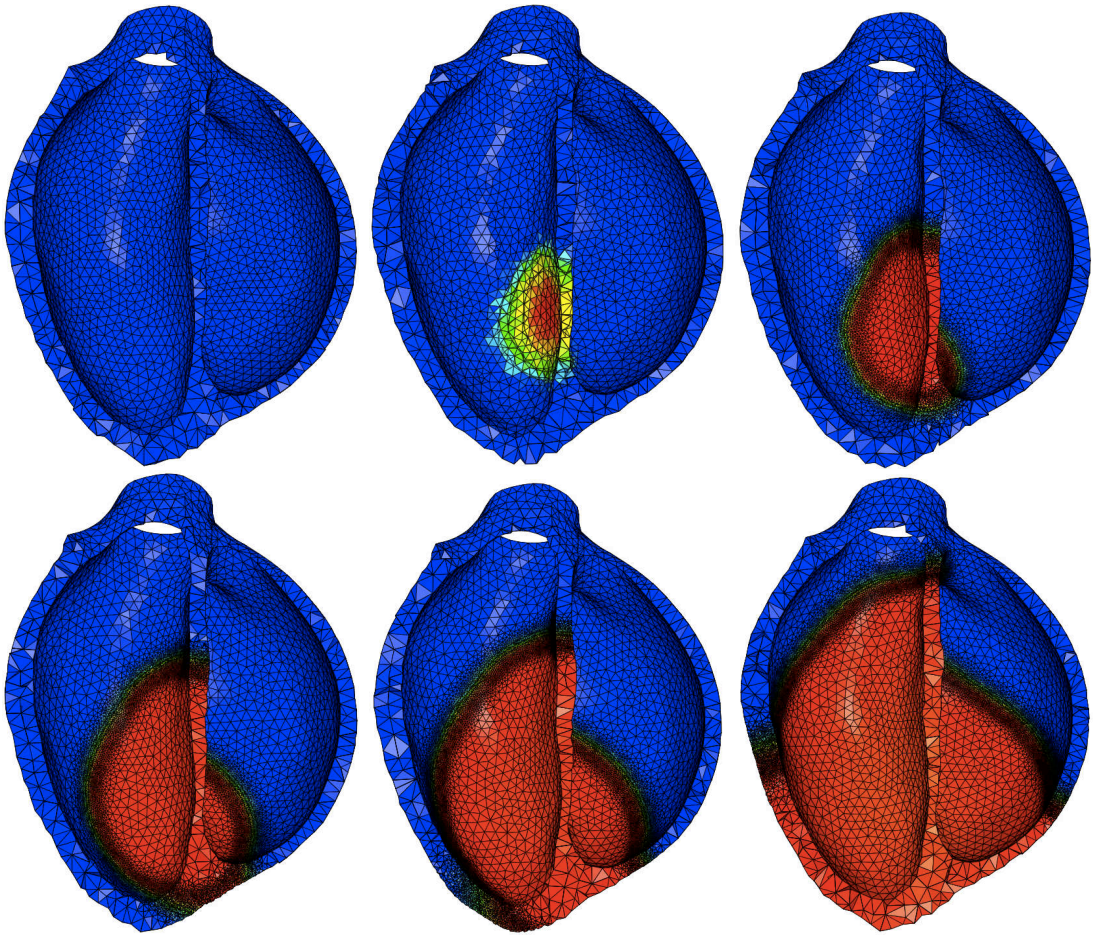

Figure 9.31: Snapshots of the Action potential propagation. The computation is performed with the mesh adaptivity prcedure

Bibliography

[ACF09] M. Astorino, F. Chouly, and M.A. Fernández. Robin Based Semi-Implicit Coupling in Fluid-Structure Interaction: Stability Analysis and Numerics. *SIAM J. Sci. Comput.*, 2009. To appear.

[Aeh06] B. Aehlert. *ECGs Made Easy.* Mosby Jems, Elsevier, third edition, 2006.

[AGPT08] M. Astorino, J.-F. Gerbeau, O. Pantz, and K. Traoré. Fluid-structure interaction and multi-body contact.Application to aortic valves. *Comp. Meth. Appl. Mech. Engng.*, 2008. DOI: 10.1016/j.cma.2008.09.012.

[Ala03] F. Alauzet. *Adaptation de maillage anisotrope en trois dimensions. Application aux simulations instationnaires en mécanique des fluides.* PhD thesis, Université Montpellier II, 2003.

[Ant06] C. Antzelevitch. Cellular basis for the repolarization waves of the ECG. *Ann. N. Y. Acad. Sci.*, 1080:268–281, 2006.

[AP96] R. Aliev and A. Panfilov. A simple two-variable model of cardiac excitation. *Chaos, Solitons and Fractals*, 7(3):293–301, 1996.

[ATP06] T.M. Austin, M.L. Trew, and A.J. Pullan. Solving the cardiac bidomain equations for discontinuous conductivities. *IEEE Trans. Biomed. Eng.*, 53(7):1265–72, 2006.

[BA05] J. Baerentzen and H. Aanaes. Signed distance computation using the angle weighted pseudo-normal. *IEEE Trans. Visual. Comput. Graph.*, 11(3):243–253, May 2005.

[BCF+09] M. Boulakia, S. Cazeau, M.A. Fernández, J.-F. Gerbeau, and N. Zemzemi. Mathematical Modeling of Electrocardiograms: A Numerical Study. Research Report RR-6977, INRIA, 2009.

[BCP09] Y. Bourgault, Y. Coudière, and C. Pierre. Existence and uniqueness of the solution for the bidomain model used in cardiac electrophysiology. *Nonlinear Analysis: Real World Applications*, 10(1):458 – 482, 2009.

[BCS01] J. Bestel, F. Clément, and M. Sorine. A biomechanical model of muscle contraction. In *Lectures Notes in Computer Science*, volume 2208. Eds W.J. Niessen and M.A. Viergever, Springer-Verlag, 2001.

[BEL03] Y. Bourgault, M. Ethier, and V.G. LeBlanc. Simulation of electrophysiological waves with an unstructured finite element method. *Mathematical Modelling and Numerical Analysis*, 37(4):649–661, 2003.

[Bel08] Y. Belhamadia. A time-dependent adaptive remeshing for electrical waves of the heart. *Biomedical Engineering, IEEE Transactions on*, 55(2):443–452, February 2008.

[BF09] E. Burman and M.A. Fernández. Stabilization of explicit coupling in fluid-structure interaction involving fluid incompressibility. *Comput. Methods Appl. Mech. Engrg.*, 198(5-8):766–784, 2009.

[BFB08] Y. Belhamadia, A. Fortin, and Y. Bourgault. Towards accurate numerical method for monodomain models using a realistic heart geometry. *Mathematical Biosciences*, 220(2):89Ð101, May 2008.

[BFC04] Y. Belhamadia, A. Fortin, and E. Chamberland. Three-dimensional anisotropic mesh adaptation for phase change problems. *Journal of Computational Physics*, 201:753–770, 2004.

[BFGZ07] M. Boulakia, M.A. Fernández, J.-F. Gerbeau, and N. Zemzemi. Towards the numerical simulation of electrocardiograms. In F.B. Sachse and G. Seemann, editors, *Functional Imaging and Modeling of the Heart*, volume 4466 of *Lecture Notes in Computer Science*, pages 240–249. Springer-Verlag, 2007.

[BFGZ08a] M. Boulakia, M. A. Fernández, J. F. Gerbeau, and N. Zemzemi. Direct and inverse problems in electrocardiography. In *Numerical Analysis and Applied Mathematics*, volume 1048, pages 113–117. AIP, 2008.

[BFGZ08b] M. Boulakia, M.A. Fernández, J.-F. Gerbeau, and N. Zemzemi. A coupled system of PDEs and ODEs arising in electrocardiograms modelling. *Applied Math. Res. Exp.*, 2008(abn002):28, 2008.

[BK06] M. Bendahmane and H.K. Karlsen. Analysis of a class of degenerate reaction-diffusion systems and the bidomain model of cardiac tissue. *Networks and Heterogeneous Media*, 1:185–218, 2006.

[BOCF08] A. Buen-Orovio, E. Cherry, and F. Fenton. Minimal model for human ventricular action potentials in tissue. *Journal of Theoretical Biology*, 253(3):544–560, August 2008.

[BP02] M. Buist and A. Pullan. Torso coupling techniques for the forward problem of electrocardiography. *Ann. Biomed. Eng.*, 30(10):1299–1312, 2002.

[BP03] Martin L. Buist and Andrew J. Pullan. The effect of torso impedance on epicardial and body surface potentials: A modeling study. *EEE Trans. Biomed. Eng.*, 50(7):816–824, 2003.

[BR77] G. Beeler and H. Reuter. Reconstruction of the action potential of ventricular myocardial fibres. *J. Physiol. (Lond.)*, 268:177–210, 1977.

[BRS77] R.C. Barr, M.3rd Ramsey, and M.S. Spach. Relating epicardial to body surface potential distributions by means of transfer coefficients based on geometry measurements. *IEEE Trans. Biomed. Eng.*, 24(1):1–11, 1977.

[Bur90] G. J. Burch. On a method of determining the value of rapid variations of a difference potential by means of a capillary electrometer. *Proc R Soc Lond (Biol) .*, 48(8):89–93, 1890.

[Car67] H. Cartan. *Calcul différentiel*. Hermann, Paris, 1967.

[CCAS08] R. Cohen, F. Cohen-Aubart, and P.-G. Steg. La péricardite aiguë en 2007 : un défi diagnostique. *Annales de Cardiologie et d'Angíologie*, 57(1):10 – 15, 2008.

[CFDE+06] P. Colli Franzone, P. Deuflhard, B. Erdmann, J. Lang, and L.F. Pavarino. Adaptivity in space and time for reaction-diffusion systems in electrocardiology. *SIAM Journal on Scientific Computing*, 28(3):942–962, 2006.

[CFG93] P. Colli Franzone and L. Guerri. Spread of excitation in 3-d models of the anisotropic cardiac tissue. I: Validation of the eikonal model. *Math. Biosci.*, 113(2):145–209, 1993.

[CFG+09a] D. Chapelle, M.A. Fernández, J.-F. Gerbeau, P. Moireau, J. Sainte-Maire, and N. Zemzemi. Numerical simulation of the electromechanical activity of the heart. In N. Ayache, H. Delingette, and M. Sermesant, editors, *Functional Imaging and Modeling of the Heart*, volume 5528 of *Lecture Notes in Computer Science*, pages 357–365. Springer-Verlag, 2009.

[CFG+09b] D. Chapelle, M.A. Fernández, J.-F. Gerbeau, P. Moireau, and N. Zemzemi. A 3D model for the electromechanical activity of the heart. Submitted, 2009.

[CFGPT98a] P. Colli Franzone, L. Guerri, M. Pennacchio, and B. Taccardi. Spread of excitation in 3-d models of the anisotropic cardiac tissue. II. Effects of fiber architecture and ventricular geometry. *Math. Biosci.*, 147(2):131–171, 1998.

[CFGPT98b] P. Colli Franzone, L. Guerri, M. Pennacchio, and B. Taccardi. Spread of excitation in 3-d models of the anisotropic cardiac tissue. III. Effects of ventricular geometry and fiber structure on the potential distribution. *Math. Biosci.*, 151:51Ð98, 1998.

[CFGT04] P. Colli Franzone, L. Guerri, and B. Taccardi. Modeling ventricular excitation: axial and orthotropic anisotropy effects on wavefronts and potentials. *Math. Biosci.*, 188(1):191–205, 2004.

[CFP04] P. Colli Franzone and L.F. Pavarino. A parallel solver for reaction-diffusion systems in computational electrocardiology. *Math. Models Methods Appl. Sci.*, 14(6):883–911, 2004.

[CFPST09] P. Colli Franzone, L.F. Pavarino, S. Scacchi, and B. Taccardi. Effects of anisotropy and transmural heterogeneity on the T-wave polarity of

simulated electrograms. In N. Ayache, H. Delingette, and M. Sermesant, editors, *Functional Imaging and Modeling of the Heart*, volume 5528 of *Lecture Notes in Computer Science*, pages 513–523. Springer-Verlag, 2009.

[CFPT05] P. Colli Franzone, L.F. Pavarino, and B. Taccardi. Simulating patterns of excitation, repolarization and action potential duration with cardiac bidomain and monodomain models. *Math. Biosci.*, 197(1):35–66, 2005.

[CFS02] P. Colli Franzone and G. Savaré. Degenerate evolution systems modeling the cardiac electric field at micro- and macroscopic level. In *Evolution equations, semigroups and functional analysis (Milano, 2000)*, volume 50 of *Progr. Nonlinear Differential Equations Appl.*, pages 49–78. Birkhäuser, 2002.

[Cia88] P.G. Ciarlet. *Mathematical Elasticity, Vol. I : Three-Dimensional Elasticity*. Studies in Mathematics and its Applications. North Holland, 1988.

[CNLH04a] J. Clements, J. Nenonen, P.K.J. Li, and B.M. Horacek. Acivation dynamics in anisotropic cardiac tissue via decoupling. *Annals of Biomedical Engineering*, 32(7):984–990, 2004.

[CNLH04b] J. Clements, J. Nenonen, P.K.J. Li, and B.M. Horacek. Activation dynamics in anisotropic cardiac tissue via decoupling. *Annals of Biomedical Engineering*, 32(7):984–990, 2004.

[CO06] C.E. Conrath and T. Opthof. Ventricular repolarization: an overview of (patho)physiology, sympathetic effects and genetic aspects. *Prog. Biophys. Mol. Biol.*, 92(3):269–307, Nov 2006.

[CPT06] Y. Coudière, C. Pierre, and R. Turpault. Solving the fully coupled heart and torso problems of electrocardiology with a 3d discrete duality finite volume method. submitted, 2006.

[dBM02] D. di Bernardo and A. Murray. Modelling cardiac repolarisation for the study of the T wave: effect of repolarisation sequence. *Chaos, Solitons & Fractals*, 13(8):1743–1748, 2002.

[DEA07] Laurent Dumas and Linda El Alaoui. How genetic algorithms can improve a pacemaker efficiency. In *GECCO '07: Proceedings of the 2007 GECCO conference companion on Genetic and evolutionary computation*, pages 2681–2686, New York, NY, USA, 2007. ACM.

[DFN85] D. Di-Francesco and D. Noble. Simulations of ionic currents and concentration changes. *Phil. Trans. R. Soc. Lond.*, pages 353–398, 1985.

[DL85] R. Dautray and J.-L. Lions. *Analyse mathématique et calcul numérique pour les sciences et les techniques, Tome 3*. Masson, Paris, 1985.

[DS05] K. Djabella and M. Sorine. Differential model of the excitation-contraction coupling in a cardiac cell for multicycle simulations. In *EMBEC'05*, volume 11, pages 4185–4190, Prague, 2005.

[DSL07] K. Djabella, M. Sorine, and M. Landau. A two-variable model of cardiac action potential with controlled pacemaker activity and ionic current interpretation. In *64th IEEE conference*, New Orleans, Louisiana USA, 2007.

[Dub89] D. Dubin. *Rapid Interpretation of EKG's*. Cover publishing Company, 1989.

[EB08] M. Ethier and Y. Bourgault. Semi-Implicit Time-Discretization Schemes for the Bidomain Model. *SIAM Journal on Numerical Analysis*, 46:2443, 2008.

[EFG+09] G. Ebrard, M.A. Fernández, J.-F. Gerbeau, F. Rossi, and N. Zemzemi. From intracardiac electrograms to electrocardiograms. models and metamodels. In N. Ayache, H. Delingette, and M. Sermesant, editors, *Functional Imaging and Modeling of the Heart*, volume 5528 of *Lecture Notes in Computer Science*, pages 524–533. Springer-Verlag, 2009.

[EG04] A. Ern and J.-L. Guermond. *Theory and practice of finite elements*, volume 159 of *Applied Mathematical Sciences*. Springer-Verlag, New York, 2004.

[EGR00] I.R. Efimov, R.A. Gray, and B.J. Roth. Virtual electrodes and deexcitation: new insights into fibrillation induction and defibrillation. *J. Cardiovasc. Electrophysiol.*, 11(3):339–353, 2000.

[Ein95] W. Einthoven. Ueber die form des menschlichen electrocardiogramms. *Arch f d Ges Physiol.*, 60:101–123, 1895.

[Ein01] W. Einthoven. Un nouveau galvanomètre. *Arch Neerl Sc Ex Nat.*, 6:625–633, 1901.

[Ein06] W. Einthoven. Le telecardiogramme. *Arch Int de Physiol.*, 4:132–164, 1906.

[FBR+87] M.R. Franz, K. Bargheer, W. Rafflenbeul, A. Haverich, and P.R. Lichtlen. Monophasic action potential mapping in human subjects with normal electrocardiograms: direct evidence for the genesis of the T wave. *Circulation*, 75(2):379–386, 1987.

[Fit61] R. Fitzhugh. Impulses and physiological states in theoretical models of nerve membrane. *Biophys. J.*, 1:445–465, 1961.

[FK98] F. Fenton and A. Karma. Vortex dynamics in three-dimensional continuous myocardium with fiber rotation: Filament instability and fibrillation. *Chaos*, 8(1):20–47, 1998.

[FPST08] P. Colli Franzone, L.F. Pavarino, S. Scacchi, and B. Taccardi. Modeling ventricular repolarization: Effects of transmural and apex-to-base heterogeneities in action potential durations. *Mathematical Biosciences*, 214(1-2):140 – 152, 2008. BICOMP 2008.

[Fre01] P. Frey. Yams: A fully automatic adaptive isotropic surface remeshing procedure. Technical report 0252, Inria, Rocquencourt, France, Nov. 2001.

[FZ09] M. A. Fernández and N. Zemzemi. Decoupled time-marching schemes in computational cardiac electrophysiology and ecg numerical simulation. Research Report RR-7022, INRIA, 2009.

[GBB+89] C.L. Grines, T.M. Bashore, H. Boudoulas, S. Olson, P. Shafer, and C.F. Wooley. Functional abnormalities in isolated left bundle branch block. the effect of interventricular asynchrony. *Circulation*, 79(4):845—853, 1989.

[GGMN+09] L. Gerardo-Giorda, L. Mirabella, F. Nobile, M. Perego, and A. Veneziani. A model-based block-triangular preconditioner for the bidomain system in electrocardiology. *J. Comp. Phys.*, 228:3625–3639, 2009.

[GHS90] P.L. George, F. Hecht, and E. Saltel. Fully automatic mesh generator for 3d domains of any shape. *Impact of Comp. in Sci. ans Eng.,*, 2:187–218, 1990.

[Gol06] A.L. Goldberger. *Clinical Electrocardiography: A Simplified Approach.* Mosby-Elsevier, 7th edition, 2006.

[GTEL91] L.S. Green, B. Taccardi, P.R. Ershler, and R.L. Lux. Epicardial potential mapping. effects of conducting media on isopotential and isochrone distributions. *Circulation*, 84(6):2513–2521, 1991.

[Gul88] R.M. Gulrajani. Models of the electrical activity of the heart and computer simulation of the electrocardiogram. *Crit. Rev. Biomed. Eng.*, 16(1):1–6, 1988.

[Gul03] R.M. Gulrajani. Computer heart models and the simulation of the electrocardiogram: newer strategies. In *25*th *Annual International Conference of the IEEE EMBS*, pages 17–21, 2003.

[HH52] A.L. Hodgkin and A.F. Huxley. A quantitative description of membrane current and its application to conduction and excitation in nerve. *J. Physiol.*, 117(4):500–544, 1952.

[HHLR94] N. Hooke, C.S. Henriquez, P. Lanzkron, and D. Rose. Linear algebraic transformations of the bidomain equations: implications for numerical methods. *Math. Biosci.*, 120(2):127–145, 1994.

[Hil38] A.V. Hill. The heat of shortening and the dynamic constants in muscle. *Proc. Roy. Soc. London (B)*, 126:136–195, 1938.

[HN84] T. Higuchi and Y. Nakaya. T wave polarity related to the repolarization process of epicardial and endocardial ventricular surfaces. *American Heart Journal*, 108(2):290–295, 1984.

[HR90] J.G. Heywood and R. Rannacher. Finite-element approximation of the nonstationary Navier-Stokes problem. IV. Error analysis for second-order time discretization. *SIAM J. Numer. Anal.*, 27(2):353–384, 1990.

[HTF01] T. Hastie, R. Tibshirani, and J. Friedman. *The elements of statistical learning*. Springer Series in Statistics. Springer-Verlag, New York, 2001. Data mining, inference, and prediction.

[Hui98] G. Huiskamp. Simulation of depolarization in a membrane-equations-based model of the anisotropic ventricle. *EEE Trans. Biomed. Eng.*, 5045(7):847–855, 1998.

[Hux57] A.F. Huxley. Muscle structure and theories of contraction. In *Progress in Biophysics and Biological Chemistry*, volume 7, pages 255–318. Pergamon press, 1957.

[IHR07] C. Igel, N. Hansen, and S. Roth. Covariance matrix adaptation for multi-objective optimization. *Evolutionary Computation*, 15(1):1–28, 2007.

[IT69] B. Irons and R.C. Tuck. A version of the aitken accelerator for computer implementation. *Int. J. Num. Meth. Engng.*, 1:275–277, 1969.

[KB98] J. P. Keener and K. Bogar. A numerical method for the solution of the bidomain equations in cardiac tissue. *Chaos*, 8(1):234–241, 1998.

[KHUM06] R.C.P. Kerckhoffs, S.N. Healy, T.P. Usyk, and A.D. McCulloch. Computational methods for cardiac electromechanics. *Proc. IEEE*, 94(4):769–783, 2006.

[KN93] W. Krassowska and J.C. Neu. Homogenization of syncitial tissues. *CRC Crit. Rev. Biomed. Eng.*, 21(2):137–199, 1993.

[KN94] W. Krassowska and J.C. Neu. Effective boundary conditions for syncitial tissues. *IEEE Trans. Biomed. Eng.*, 41(2):137–199, 1994.

[KSW+07] D.U.J Keller, G. Seemann, D.L. Weiss, D. Farina, J. Zehelein, and O. Dössel. Computer based modeling of the congenital long-qt 2 syndrome in the visible man torso: From genes to ECG. In *Proceedings of the 29th Annual International Conference of the IEEE EMBS*, pages 1410–1413, 2007.

[KV03] K. Kunisch and S. Volkwein. Galerkin proper orthogonal decomposition methods for a general equation in fluid dynamics. *SIAM Journal on Numerical Analysis*, 40(2):492–515, 2003.

[LBG+03] G. T. Lines, M. L. Buist, P. Grottum, A. J. Pullan, J. Sundnes, and A. Tveito. Mathematical models and numerical methods for the forward problem in cardiac electrophysiology. *Comput. Visual. Sci.*, 5(4):215–239, 2003.

[LGT03] G. Lines, P. Grottum, and A. Tveito. Modeling the electrical activity of the heart. a bidomain model of the ventricles embedded in a torso. *Comput. Visual. Sci.*, 5:195–213, 2003.

[LH91] L.J. Leon and B.M. Horácek. Computer model of excitation and recovery in the anisotropic myocardium. I. Rectangular and cubic arrays of excitable elements. *J. Electrocardiol.*, 24(1):1–15, 1991.

[Lin99] G. Lines. *Simulating the electrical activity in the heart.* PhD thesis, Department of Informatics, University of Olso, 1999.

[Los08] A Loseille. *Adaptation de maillage anisotrope 3D multi-échelles et ciblée à une fonctionnelle. Application à la prédiction haute-fidélité du bang sonique.* PhD thesis, Université Paris 6, 2008.

[LR91] C.H. Luo and Y. Rudy. A model of the ventricular cardiac action potential. Depolarisation, repolarisation,and their interaction. *Circ. Res*, 68(6):1501–1526, 1991.

[LR94] C. Luo and Y. Rudy. A dynamic model of the cardiac ventricular action potential. i. simulations of ionic currents and concentration changes. *Circ. Res.*, 74(6):1071–1096, 1994.

[LRA+82] W.C. Little, R.C. Reeves, J. Arciniegas, R.E. Katholi, and E.W. Rogers. Mechanism of abnormal interventricular septal motion during delayed left ventricular activation. *Circulation*, 65(7):1486—1491, 1982.

[LSH+09] S. Linge, J. Sundnes, M. Hanslien, G.T. Lines, and A. Tveito. Numerical solution of the bidomain equations. *Philos. Transact. A. Math. Phys. Eng. Sci.*, 367(1895):1931–1950, 2009.

[LT94] P. Le Tallec. Numerical methods for nonlinear three-dimensional elasticity. In P.G. Ciarlet and J.-L. Lions, editors, *Handbook of Numerical Analysis*, volume 3. Elsevier, 1994.

[LTS96] M.J. Lab, P. Taggart, and F. Sachs. Mechano-electric feedback. *Cardiovasc. Res.*, 32:1–2, 1996.

[Mac74] D.A. MacDonald. *Blood Flow in Arteries.* Edward Harold Press, 1974.

[Man20] H. Mann. A method of analyzing the electrocardiogram. *Arch Int Med.*, 25:283–294, 1920.

[Mar76] E.J. Marey. Des variations électriques des muscles et du coeur en particulier étudiées au moyen de l'électromètre de m lippman. *Comptes Rendus Hebdomadaires des Séances de l'Académie des sciences.*, 82:975–977, 1876.

[Mat42] C. Matteucci. Sur un phénomène physiologique produit par les muscles en contraction. *Ann Chim Phys.*, 6:339–341, 1842.

[MC04] M. Murillo and X.-C. Cai. A fully implicit parallel algorithm for simulating the non-linear electrical activity of the heart. *Numer. Linear Algebra Appl.*, 11(2-3):261–277, 2004.

[Moi08] P Moireau. *Filtering based data assimilation for second order hyperbolic PDE. Applications in cardiac mechanics.* PhD thesis, École Polytechnique, 2008.

[MP95] J. Malmivuo and R. Plonsey. Bioelectromagnetism. Principles and applications of bioelectric and biomagnetic fields. *Oxford University Press, New York*, 1995.

[MP09] Munteanu M. and L.F. Pavarino. Decoupled schwarz algorithms for implicit discretizations of nonlinear monodomain and bidomain systems. *Mathematical Models and Methods in Applied Sciences*, 19(7):1065–1097, 2009.

[MS03] C.C. Mitchell and D.G. Schaeffer. A two-current model for the dynamics of cardiac membrane. *Bulletin Math. Bio.*, 65:767–793, 2003.

[NAY62] J.S. Nagumo, S. Arimoto, and S. Yoshizawa. An active pulse transmission line stimulating nerve axon. *Proc. IRE*, 50:2061–2071, 1962.

[NK93] J.C. Neu and W. Krassowska. Homogenization of syncytial tissues. *Crit. Rev. Biomed. Eng.*, 21(2):137–199, 1993.

[NLT+06] Bjørn Fredrik Nielsen, Ola Marius Lysaker, Christian Tarrou, Joakim Sundnes, Xing Cai, and Kent-Andre Mardal. On the use of the bidomain equations for computing the transmembrane potential throughout the heart wall: An inverse problem. Presented at the Computers in Cardiology conference in Valencia, Spain, 2006.

[Nob62] D. Noble. A modification of the hodgkin-huxley equation applicable to purkinje fiber action and pacemaker potentials. *J Physiol .*, 160:317–352, 1962.

[NVKN98] D. Noble, A. Varghese, P. Kohl, and P. Noble. Improved guinea-pig ventricular cell model incorporating a diadic space, ikr and iks, and length- and tension-dependent processes. *Can. J. Cardiol.*, 14(1):123–134, 1998.

[OW00] M. Opper and O. Winther. *Advances in Large-Margin ClassiÞers. In: Gaussian Pro- cesses and SVM: Mean Field and Leave-One-Out, ch. 17.* MIT Press, Cambridge, 2000.

[Pag62] E. Page. Cat heart muscle in vitro. part iii. the extracellular space. *J. Gen. Physio.*, 46(1):201–213, 1962.

[PBC05] A.J. Pullan, M.L. Buist, and L.K. Cheng. *Mathematically modelling the electrical activity of the heart: From cell to body surface and back again.* World Scientific Publishing Co. Pte. Ltd., Hackensack, NJ, 2005.

[PBLV07] M. Potse, G. Baroudi, P.A. Lanfranchi, and A. Vinet. Generation of the t wave in the electrocardiogram: lessons to be learned from long-QT syndromes. In *Canadian Cardiovascular Congress*, 2007.

[PDG03] M. Potse, B. Dubé, and M. Gulrajani. ECG simulations with realistic human membrane, heart, and torso models. In *Proceedings of the 25th Annual Intemational Conference of the IEEE EMBS*, pages 70–73, 2003.

[PDR+06] M. Potse, B. Dubé, J. Richer, A. Vinet, and R. M. Gulrajani. A comparison of monodomain and bidomain reaction-diffusion models for action potential propagation in the human heart. *Biomedical Engineering, IEEE Transactions on*, 53(12):2425–2435, Dec. 2006.

[PDV09] M. Potse, B. Dubé, and A. Vinet. Cardiac anisotropy in boundary-element models for the electrocardiogram. *Med. Biol. Eng. Comput.*, 2009. DOI:10.1007/s11517-009-0472-x.

[Pie05] C. Pierre. *Modélisation et simulation de l'activité électrique du cœur dans le thorax, analyse numérique et méthodes de volumes finis.* PhD thesis, Laboratoire J. Leray, Université de Nantes, 2005.

[PS02] M. Pennacchio and V. Simoncini. Efficient algebraic solution of reaction-diffusion systems for the cardiac excitation process. *J. Comput. Appl. Math.*, 145(1):49–70, 2002.

[PS08] L.F. Pavarino and S. Scacchi. Multilevel additive schwarz preconditioners for the bidomain reaction-diffusion system. *SIAM J. Sci. Comput.*, 31(1):420–443, 2008.

[PSF06] M. Pennacchio, G. Savaré, and P. Colli Franzone. Multiscale modeling for the bioelectric activity of the heart. *SIAM J. Math. Anal.*, 37(4):1333–1370, 2006.

[QSS07] A. Quarteroni, R. Sacco, and F. Saleri. *Numerical mathematics*, volume 37 of *Texts in Applied Mathematics*. Springer-Verlag, Berlin, second edition, 2007.

[QV99] A. Quarteroni and A. Valli. *Domain decomposition methods for partial differential equations*. Numerical Mathematics and Scientific Computation. The Clarendon Press Oxford University Press, New York, 1999. Oxford Science Publications.

[RM94] J.M. Roger and A.D. McCulloch. A collocation-Galerkin finite element model of cardiac action potential propagation. *IEEE Trans. Biomed. Engr.*, 41(8):743–757, 1994.

[RPW+38] Barnes A. R., H. E. B. Pardee, P. D. White, F. N. Wilson, and C.C. Wolferth. A method of analyzing the electrocardiogram. *Am Heart J*, 15:235–239, 1938.

[RR04] M. Renardy and R. C. Rogers. *An introduction to partial differential equations*, volume 13 of *Texts in Applied Mathematics*. Springer-Verlag, New York, second edition, 2004.

[RS82] D.E. Roberts and A.M. Scher. Effects of tissue anisotropy on extracellular potential fields in canine myocardium in situ. *Circ. Res*, 50:342–351, 1982.

[Sac04] F.B. Sachse. *Computational Cardiology: Modeling of Anatomy, Electrophysiology and Mechanics*. Springer-Verlag, Berlin, 2004.

[Sca08] S. Scacchi. A hybrid multilevel schwarz method for the bidomain model. *Computer Methods in Applied Mechanics and Engineering*, 197(45-48):4051 – 4061, 2008.

[Sch69] O.H. Schmitt. Biological information processing using the concept of interpenetrating domains. In K.N. Leibovic, editor, *Information Processing in the Nervous System*. Springer-Verlag, 1969.

[SFWD99] F.B. Sachse, R. Frech, C.D. Werner, and O. Dossel. A model based approach to assignment of myocardial fibre orientation. *Computers in Cardiology 1999*, pages 145–148, 1999.

[SLC+06] J. Sundnes, G.T. Lines, X. Cai, B.F. Nielsen, K.-A. Mardal, and A. Tveito. *Computing the electrical activity in the heart*, volume 1 of *Monographs in Computational Science and Engineering*. Springer-Verlag, Berlin, 2006.

[SLMT02] J. Sundnes, G.T. Lines, K.A. Mardal, and A. Tveito. Multigrid block preconditioning for a coupled system of partial differential equations modeling the electrical activity in the heart. *Comput. Methods Biomech. Biomed. Engin.*, 5(6):397–409, 2002.

[SLT01] J. Sundnes, G.T. Lines, and A. Tveito. Efficient solution of ordinary differential equations modeling electrical activity in cardiac cells. *Math. Biosci.*, 172(2):55–72, 2001.

[SLT05] J. Sundnes, G.T. Lines, and A. Tveito. An operator splitting method for solving the bidomain equations coupled to a volume conductor model for the torso. *Math. Biosci.*, 194(2):233–248, 2005.

[SM00] N. Skouibine, K. Trayanova and P. Moore. A numerically efficient model for simulation of defibrillation in an active bidomain sheet of myocardium. *Math. Biosci.*, 166(1):85–100, 2000.

[SMC+06] M. Sermesant, Ph. Moireau, O. Camara, J. Sainte-Marie, R. Andriantsimiavona, R. Cimrman, D.L. Hill, D. Chapelle, and R. Razavi. Cardiac function estimation from mri using a heart model and data assimilation: advances and difficulties. *Med. Image Anal.*, 10(4):642–656, 2006.

[SMCCS06] J. Sainte-Marie, D. Chapelle, R. Cimrman, and M. Sorine. Modeling and estimation of the cardiac electromechanical activity. *Computers & Structures*, 84:1743–1759, 2006.

[SP76] J. B. Sanderson and F. Page. Expérimental results relating to the rhythmical and excitatory motions of the ventricle of the frog. *Proc R Soc Lond.*, 41:410–414, 1876.

[SP84] J. B. Sanderson and F. Page. On the electrical phenomena of the excitatory process in the heart of the tortoise, as investigated photographically. *J Physiol .*, 4(6):327–338, 1884.

[SPM08] S. Scacchi, L.F. Pavarino, and I. Milano. Multilevel Schwarz and Multigrid preconditioners for the Bidomain system. *Lecture Notes in Computational Science and Engineering*, 60:631, 2008.

[SR97] R.M. Shaw and Y. Rudy. Electrophysiologic effects of accute myocardial ischemia: Theoretical study of altered cell exitability and action potential duration. *Cardiovascular Research.*, 35:256–272, 1997.

[SS01] B. Scholkopf and A. J. Smola. *Learning with Kernels: Support Vector Machines, Regularization, Optimization, and Beyond*. Adaptive Computation and Machine Learning. MIT Press, Cambridge, MA, USA, 2001.

[SSN94] A.V. Shahidi, P. Savard, and R. Nadeau. Forward and inverse problems of electrocardiography: modeling and recovery of epicardial potentials in humans. *IEEE Trans. Biomed. Eng.*, 41(3):249–256, 1994.

[Ste78] H.J. Stetter. The defect correction principle and discretization methods. *Numer. Math.*, 29:425–443, 1978.

[Ste80] R.A. Stephenson. On the uniqueness of the square-root of a symmetric, positive-definite tensor. *J. Elasticity*, 10(2):213–214, 1980.

[TDP+04] M.-C. Trudel, B. Dubé, M. Potse, R.M. Gulrajani, and L.J. Leon. Simulation of qrst integral maps with a membrane-based computer heart model employing parallel processing. *IEEE Trans. Biomed. Eng.*, 51(8):1319–1329, 2004.

[Tho06] V. Thomée. *Galerkin finite element methods for parabolic problems*, volume 25 of *Springer Series in Computational Mathematics*. Springer-Verlag, Berlin, second edition, 2006.

[Tom00] K.A Tomlinson. *Finite element solution of an eikonal equation for excitation wavefront propagation in ventricular myocardium.* PhD thesis, The University of Auckland, New Zealand, 2000.

[TTNNP04] K. H. W. J. Ten Tusscher, D. Noble, P.J. Noble, and A. V. Panfilov. A model for human ventricular tissue. *Am J Physiol Heart Circ Physiol*, 286:1573–1589, 2004.

[Tun78] L. Tung. *A bi-domain model for describing ischemic myocardial D–C potentials*. PhD thesis, MIT, 1978.

[TW05] A. Toselli and O. Widlund. *Domain decomposition methods—algorithms and theory*, volume 34 of *Springer Series in Computational Mathematics*. Springer-Verlag, Berlin, 2005.

[VC07] E.J. Vigmond and C. Clements. Construction of a computer model to investigate sawtooth effects in the purkinje system. *IEEE Trans. Biomed. Engng.*, 54(3):389–399, 2007.

[vCD80] F.H. van Capelle and D. Durrer. Computer simulation of arrhythmias in a network of coupled excitable elements. *Circ. Res.*, 47:453–466, 1980.

[VCMP08] E.J. Vigmond, J. Clements, D.M. McQueen, and C.S. Peskin. Effect of bundle branch block on cardiac output: a whole heart simulation study. *Progress in Biophysics and Molecular Biology*, 97:520–542, 2008.

[Ven09] M. Veneroni. Reaction–diffusion systems for the macroscopic bidomain model of the cardiac electric field. *Nonlinear Analysis: Real World Applications*, 10(2):849–868, 2009.

[VWdSP+08] E.J. Vigmond, R. Weber dos Santos, A.J. Prassl, M Deo, and G. Plank. Solvers for the cardiac bidomain equations. *Progr. Biophys. Molec. Biol.*, 96(1-3):3–18, 2008.

[Wal87] A. D. Waller. A demonstration on man of electromotive changes accompanying the heart's beat. *J Physiol .*, 8(8):229–234, 1887.

[YA98] G.-X. Yan and C. Antzelevitch. Cellular basis for the normal T wave and the electrocardiographic manifestations of the long-QT syndrome. *Circulation*, 98:1928–1936, 1998.

[ZLRR95] J. Zeng, K.R. Laurita, D.S. Rosenbaum, and Y. Rudy. Tow components of the delayed rectifier k+ current in ventricular mycyte of the guinea pig type. *Circulation Research.*, 77:140–152, 1995.